



INSTITUTO  
SUPERIOR  
TÉCNICO

**UNIVERSIDADE TÉCNICA DE LISBOA**

**INSTITUTO SUPERIOR TÉCNICO**

**B-Fe-U ternary phase diagram and ternary  
compounds characterization**

**Marta Sofia Rosado Silva Dias**

**Dissertação para obtenção do Grau de Doutor em  
Engenharia de Materiais**

**Orientador : Doutor António Cândido Lampreia Pereira Gonçalves**

**Co-orientador : Doutora Patrícia Maria Cristovam Cipriano Almeida de  
Carvalho**

**Júri**

**Presidente : Presidente do Conselho Científico do IST**

**Vogais :**

**Doutor Rui Mário Correia da Silva Vilar**

**Doutor Rui Ramos Ferreira e Silva**

**Doutor António Cândido Lampreia Pereira Gonçalves**

**Doutor Rogério Anacleto Cordeiro Colaço**

**Doutor Alberto Eduardo Morão Cabral Ferro**

**Doutora Patrícia Maria Cristovam Cipriano Almeida de Carvalho**

**Maio 2011**

## Resumo

---

Este trabalho apresenta o diagrama de fases ternário B-Fe-U e a caracterização dos seus compostos ternários. O estudo do diagrama de fases engloba a projecção liquidus completa incluindo a natureza das linhas fronteiras que delimitam os campos de cristalização primária, a natureza e localização dos pontos invariantes, juntamente com três secções isotérmicas, a 780°C, 950°C e 1000°C e uma secção vertical ao longo da linha U:(Fe,B) = 1:5. O sistema ternário B-Fe-U compreende sete compostos binários e cinco compostos ternários os quais formam dezoito triângulos de compatibilidade e dezoito pontos de reacções ternárias. Foram realizadas medidas de refinamento de monocristal para os compostos  $UFe_3B_2$  e  $UFe_2B_6$ , sendo que o primeiro assume uma estrutura hexagonal do tipo  $CeCo_3B_2$  e o segundo uma estrutura ortorrômbica do tipo  $CeCr_2B_6$ . As medidas magnéticas foram realizadas para os compostos  $UFe_3B_2$ ,  $UFe_2B_6$  e  $UFeB_4$ . O composto  $UFe_3B_2$  apresenta um comportamento ferromagnético abaixo de 300 K enquanto o  $UFe_2B_6$  e  $UFeB_4$  são paramagnéticos entre 2-300K. Devido à complexidade das microestruturas das ligas ternárias, que impossibilitaram a extracção de monocristais, os compostos  $UFeB_4$ ,  $UFe_4B$  e  $U_2Fe_{21}B_6$  foram estudados usando difracção de electrões retrodifundidos. O  $U_2Fe_{21}B_6$  assume uma estrutura cúbica do tipo  $Cr_{23}C_6$  e o  $UFe_4B$  adopta uma estrutura hexagonal similar à do  $CeCo_4B$ . O composto  $UFeB_4$  apresenta um estrutura com crescimento cooperativo entre duas estruturas ortorrômbicas,  $YCrB_4$  e  $ThMoB_4$ .

Palavras chave: Microestrutura, reacção ternária, projecção liquidus, liga.



## Abstract

---

This work presents the B-Fe-U ternary phase diagram and characterizes the ternary borides of the system. The phase diagram study comprises the complete liquidus projection, including the *cotectic* and *reaction* boundary lines that delimit primary crystallization fields, the nature and position of the ternary invariants points, as well as three isothermal sections, at 700°C, 950°C and 1100°C, and a vertical section along  $U:(Fe,B) = 1:5$ . The B-Fe-U system comprises seven binary compounds and five ternary compounds, all with limited solubility, which form eighteen compatibility triangles and corresponding eighteen ternary reactions. Single-crystal refinement was performed on  $UFe_3B_2$  and  $UFe_2B_6$  ternary compounds which present a hexagonal  $CeCo_3B_2$ -type and orthorhombic  $CeCr_2B_6$ -type structures, respectively. Magnetic measurements were studied for the  $UFe_3B_2$ ,  $UFe_2B_6$  and  $UFeB_4$  ternary compounds.  $UFe_3B_2$  is ferromagnetic below 300K, while  $UFe_2B_6$  and  $UFeB_4$  are paramagnetic between 2-300K. Due to the complexity of the ternary alloys microstructure  $UFeB_4$ ,  $UFe_4B$  and  $U_2Fe_{21}B_6$  could not be extracted as single-crystals and were investigated by electron-backscattered diffraction.  $U_2Fe_{21}B_6$  assumes a cubic  $Cr_{23}C_6$ -type structure and  $UFe_4B$  adopts a structure related to the hexagonal  $CeCo_4B$ -type structure. The  $UFeB_4$  compound consists of an intergrowth between  $YCrB_4$ - and  $ThMoB_4$ -type structures.

Keywords: Microstructure, ternary reaction, liquidus projection, alloy



## Acknowledgements

---

During the long four years that took this thesis to complete, I received the help and support of many people and institutions.

First of all, I am particularly indebted to my supervisors Doctor Patrícia Carvalho and Doctor António Gonçalves for their suggestions, support during these four years of research, to write this never ending story, bore my explanations and their incentive.

I thank to FCT the PhD SFRH/BD/21539/2005 fellowship incorporated in the Program GRICES/EGIDE 2007-2008 and FCT/POCTI, Portugal, under Nr. QUI/46066/2002.

I am also thankful to the Laboratoire de Chimie du Solide et Inorganique Moléculaire, in Rennes, France, specially to Doctor Henri Noel, Doctor Olivier Tougait and Doctor Mathew Pasturel, which allowed me to stay for few periods to use the DTA and EPMA apparatus providing me with all the data and facilities I needed.

I am also thankful to Doctor Nuno Franco for high temperature X-ray measurements and to Doctor Umesh Vinaica and Doctor Ana Paula Dias for DTA measurements.

I wish to thank to QES group including specially to Doctor Isabel Santos to perform single-crystals X-ray measurements, and to Doctor Laura Pereira to perform magnetic studies.

I wish to express my gratitude to my colleges who gave me a hand and counsel: Margarida Henriques and Yuriy Verbovytsky from ITN and Daniela Nunes from IST.

I wish to express my gratitude to my friends Marta Santos, Carina Neto, Rute Vitor, Adelaide Carvalho, Augusta Antunes and Sergio Magalhães to their friendship and encouragement.

Special thanks to Mónica Afonso and Sandrina Oliveira for their friendship, patience, encouragement and support all the time and for the good time that we spent together in these years.

I am also thankful my friends to Susana Gomes and Filipa Rodrigues to their friendship and encouragement.

I would like to express my gratitude to all those who gave me the possibility to complete this thesis.

I would like to thank my parents Esperança and Fernando for educating me, for their love and encouragement to pursue my interests, and my brother André, and Priscila for their love.

Special thanks to God who gives me the courage to face this challenge and give the opportunity to write this thesis.

My final thanks go to husband David and my son Josué, who in addition to love and care have given me the emotional balance I needed in order to face this personal challenge. Without them this work would never have come into existence.

I love you.

Marta

## Contents

---

### Chapter 1 – Introduction

---

1.1 Designations and nomenclature	3
1.2 Motivation	4
1.3 Background	6
1.3.1 Ternary phase diagrams	6
1.3.2 Types of magnetic behavior	15
1.4 State of the Art	22
1.4.1 B-T-U systems: isothermal sections, compounds and phase equilibria	22
1.4.2 Ternary boron-metal- <i>f</i> -elements systems: liquidus projections	27
1.4.3 Magnetic properties of actinide compounds	28
1.5 References	31

---

### Chapter 2 – Working principles and methods

---

2.1 X-ray Diffraction	37
2.1.1 Powder X-ray diffraction (PXRD)	45
2.1.2 Single crystal X-ray diffraction	48
2.2 Scanning electron microscopy (SEM)	50
2.2.1 Energy dispersive X-ray spectroscopy (EDS)	53
2.2.2 Wavelength dispersive spectroscopy (WDS)	55
2.3 Electron backscattered diffraction (EBSD)	56
2.4 Differential thermal analysis (DTA)	58
2.5 Superconducting quantum interference device (SQUID)	59
2.6 Experimental details	60
2.6.1 Alloys preparation and heat treatments	60
2.6.2 PXRD	63
2.6.3 Single crystal X-ray diffraction	63
2.6.4 SEM, EDS, WDS and EBSD	64
2.6.5 DTA and heating curves	65

2.6.6 High temperature X-ray diffraction (HTXRD)	66
2.6.7 Magnetic Measurements	66
2.8 References	67

---

### **Chapter 3 – Ternary phase diagram**

---

3.1. Introduction	71
3.2. State of the art	72
3.3. Results	76
3.3.1 WDS results	77
3.3.2 Liquidus Projection	79
3.3.2.1 B-rich section	80
3.3.2.2 0%>U>30% and 21%>B>50% (at.%) section	102
3.3.2.3 Fe-rich section	121
3.3.2.4 U-rich section	146
3.3.3 Complete liquidus projection	159
3.3.3.1 Total reaction scheme	160
3.3.4 Isothermal sections	161
3.3.5 Vertical section along the U:(Fe,B) = 1:5 line	164
3.4 References	165

---

### **Chapter 4 – Ternary compounds characterization**

---

4.1 UFeB <sub>4</sub>	170
4.1.1 Results and Discussion	171
4.2 UFe <sub>2</sub> B <sub>6</sub>	178
4.2.1 Results and Discussion	178
4.3 UFe <sub>3</sub> B <sub>2</sub>	184
4.3.1 Results and Discussion	185
4.4 UFe <sub>4</sub> B	191
4.4.1 Results and Discussion	191

4.5 $U_2Fe_{21}B_6$	199
4.5.1 Results and Discussion	199
4.6 References	203

---

## **Chapter 5 – Concluding remarks and future work**

---

5.1 Concluding remarks and future work	209
--	-----

---

## **Appendix 1**

---

Appendix 1	213
------------	-----



## Figure Index

---

Figure	Pages
1.1 – Isothermal sections of a class I four-phase equilibrium showing (a) the three high temperature triangles and (b) the low temperature triangle.	8
1.2 – Temperature-composition ternary phase diagram illustrating a class I four-phase equilibrium.	9
1.3 – Isothermal sections of a class II ternary reaction; (a) the two high temperature tie triangles, (b) two tie lines $\alpha L$ and $\beta\gamma$ divide the isothermal trapezium at the reaction temperature (c) the two low-temperature tie triangles.	10
1.4 – Temperature-composition diagram illustrating a class II four-phase equilibrium.	11
1.5 – Isothermal sections of a class III four-phase equilibrium; (a) high temperature tie-triangle and (b) three low-temperature tie-triangles.	11
1.6 – Temperature-composition diagram of a class III four-phase equilibrium.	12
1.7 – Boundary lines involved in (a) class I ternary reaction, (b) class II ternary reaction and (c) class III ternary reaction.	13
1.8 – Solidification path of composition X in the B-C-A ternary diagram.	14
1.9 – Typical curves of $M(B)$ for a ferromagnetic, paramagnetic, ferrimagnetic, antiferromagnetic and diamagnetic materials.	16
1.10 – The inverse of $\chi$ as a function of T for systems exhibiting Curie and Curie-Weiss behavior.	18
1.11 – Magnetization as a function of magnetic field strength for $T < T_C$ , after cooling the sample from above $T_C$ . The magnetization saturation ( $M_s$ ), the remnant magnetization ( $M_{rem}$ ) and the coercive field ( $H_C$ ) are identified.	19
1.12 – Magnetization as a function of temperature for the $LaCuO_3$ sample which is first cooled in $H=0$ , a field is then applied and data is collected on warming (ZFC) and again	21

on cooling (FC) keeping the magnetic field.

1.13 – Schematic diagrams showing how the atomic moments in a ferromagnetic, 22  
antiferromagnetic and ferromagnetic are aligned.

---

2.1 – (a) Diffraction from a lattice row along the  $x$ -axis. The incident and diffracted beams 38  
are at  $\alpha_0$  and  $\alpha_n$  to the row. The path difference between the diffracted beams is  $AB - CD$ .  
(b) The incident and diffracted beam directions and the path difference between the  
diffracted beams expressed in vector notation.

2.2 – Three Laue cones representing the directions of the diffracted beams from a lattice 38  
row along the  $x$ -axis with  $0\lambda$  ( $h = 0$ ),  $1\lambda$  ( $h = 1$ ) and  $2\lambda$  ( $h = 2$ ) path differences.

2.3 – The condition for reflection in Bragg's law. 40

2.4 – Ewald's sphere construction for a set of planes at a Bragg angle. 40

2.5 – The scattering of X-rays from an atom. 42

2.6 – Transitions that give rise to the various X-ray lines. 45

2.7 – Schematic of an X-ray diffractometer with Bragg-Brentano geometry. 46

2.8 – Method to mount a stable crystal on a glass fiber. 48

2.9 – A goniometer head, showing the various possible adjustments that can be made in 49  
order to center the crystal with the X-ray beam.

2.10 – Schematic diagram of a scanning electron microscope. 51

2.11 – (a) Elastically scattered primary electron deflected back out of the specimen, the 52  
electron is termed as a backscattered electron (BSE), (b) Inelastically scattered primary  
electron with transfer of energy to the specimen atom resulting in a secondary electron  
emission (SE).

2.12 – Penetration of electrons into a bulk specimen. 53

2.13 – Configuration of sample, analytical crystal and detector on the Rowland circle within the wavelength dispersive spectrometer.	56
2.14 – a) Origin of Kikuchi lines by elastic scattering of the primary electrons followed by Bragg's diffraction on (hkl) lattice planes, (b) sample position and EBSD detector.	57
2.15 – Schematic illustration of DTA furnace.	58
2.16 – Composition of the alloys investigated (pentagonal grey shapes) and the position of binary and ternary compounds in the B-Fe-U system (black circles).	61
<hr/>	
3.1 – Equilibrium B-Fe binary phase diagram.	72
3.2 – Equilibrium B-U binary phase diagram.	73
3.3 – Equilibrium Fe-U binary phase diagram.	74
3.4 – Isothermal section of U-Fe-B at 800 °C.	75
3.5 – Experimental powder X-ray diffractograms of (a) as-cast 77B:8Fe:15U (b) as-cast 67B:22Fe:11U (UFe <sub>2</sub> B <sub>6</sub> stoichiometry) and (c) annealed 66B:17Fe:17U (UFeB <sub>4</sub> stoichiometry) alloys (respectively Nr. 1, 3, 5) where the presence of, respectively, UB <sub>4</sub> , UFe <sub>2</sub> B <sub>6</sub> and UFeB <sub>4</sub> is clearly evident. Dotted lines represent simulations for these compounds. UFe <sub>2</sub> B <sub>6</sub> crystallizes with CeCr <sub>2</sub> B <sub>6</sub> -type structure and UFeB <sub>4</sub> crystallizes with a structure related to the YCrB <sub>4</sub> one, which were assumed in the simulated diffratogram.	80
3.6 – BSE images of (a) 77B:8Fe:15U, (b, c) 67B:22Fe:11U (UFe <sub>2</sub> B <sub>6</sub> stoichiometry), (d) 66B:17Fe:17U (UFeB <sub>4</sub> stoichiometry), (e) 50B:25Fe:25U and (f) 43B:55Fe:2U (respectively Nr. 1, 3, 5, 12, 18) alloys. Black arrows point to (a) A/D interface, (c) E/F interface, (d) A/E interface, (e) E/B interface and (f) E/G interface. In (a) the dashed black arrow points to F/D interface, the dashed white arrow points to D/G interface, the solid grey arrow points to A/F interface and the solid white arrow points to F/G interface. Phase labeling is listed in Table 3.1.	82
3.7 – Heating curves for representative B-rich samples, (a) 77B:8Fe:15U (b) 67B:22Fe:11B (UFe <sub>2</sub> B <sub>6</sub> stoichiometry), (c) 66B:17Fe:17B (UFeB <sub>4</sub> stoichiometry) as-cast alloys (respectively, Nr.1, 3 and 5).	84

- 3.8 – Liquidus projection diagram in the B-rich section showing R1<sub>III</sub>, R2<sub>III</sub>, R3<sub>II</sub>, R4<sub>II</sub>, R5<sub>I</sub> and R6<sub>II</sub> where the solid lines represent the solid phases in equilibrium and dashed lines indicate the liquid composition. 97
- 3.9 – Liquidus projection diagram in the B-rich section showing R1<sub>III</sub>, R2<sub>III</sub>, R3<sub>II</sub>, R4<sub>II</sub>, R5<sub>I</sub> and R6<sub>II</sub> together with 77B:8Fe:15U, 67B:22Fe:11U (UFe<sub>2</sub>B<sub>6</sub> stoichiometry), 66B:17Fe:17U (UFeB<sub>4</sub> stoichiometry), 50B:25Fe:25U and 43B:55Fe:2U alloys positions (respectively Nr.1, 3, 5, 12 and 18), where the dashed lines represent the liquid composition. The grey lettering indicates the primary crystallization fields of the compounds. 98
- 3.10 – Solidification path for alloys 77B:8Fe:15U, 67B:22Fe:11U (UFe<sub>2</sub>B<sub>6</sub> stoichiometry), 66B:17Fe:17U (UFeB<sub>4</sub> stoichiometry) alloys (respectively Nr.1, 3 and 5). 100
- 3.11 – Reaction scheme at the B-rich section of the liquidus projection 101
- 3.12 – Experimental powder X-ray diffractograms of (a) annealed 50B:25Fe:25U, (b) annealed 43B:55Fe:2U (b) as-cast 33B:50Fe:17U (UFe<sub>3</sub>B<sub>2</sub> stoichiometry) alloys (respectively Nr. 12, 18 and 25), where the presence of UB<sub>2</sub>, UFeB<sub>4</sub> and UFe<sub>3</sub>B<sub>2</sub> is clearly evident. UFeB<sub>4</sub> crystallizes with a structure related to the YCrB<sub>4</sub> one and UFe<sub>3</sub>B<sub>2</sub> crystallizes in a CeCo<sub>3</sub>B<sub>2</sub>-type structure. These structures were assumed in the simulated diffratogram. Dotted lines represent simulations for these compounds. The symbols indicate reflections of other phases; UFeB<sub>4</sub> - stars; UFe<sub>2</sub> - crosses, UFe<sub>3</sub>B<sub>2</sub> - solid circles, UFe<sub>4</sub>B - solid squares, Fe<sub>2</sub>B - open squares, FeB - open circles. 102
- 3.13 – BSE images showing microstructures observed in (a) as-cast 50B:25Fe:25U alloy (Nr.12), (b) as-cast 43B:55Fe:2U alloy (Nr.18), (c) as-cast 38B:52Fe:10U alloy (Nr.22), (d, e) respectively, as-cast and annealed 40B:40Fe:20U alloy (Nr.21), and (f) as-cast 33B:50Fe:17U alloy (Nr.25). The black arrow in (a) indicates the E/M interface and in (f) indicate regions M. The white arrow in (a) indicates regions BM. The phase labeling is given in Table 3.1. 104
- 3.14 – DTA curves for representative 0%>U>30% and 21%>B>50% (at.%) section as-cast: (a) 38B:52Fe:10U and (b) 33B:50Fe:17U (UFe<sub>3</sub>B<sub>2</sub> stoichiometry) alloys (Nr. 22 and 25). 106
- 3.15 – Liquidus projection in the 0%<U<30% and 21%<B<50% (at%) section showing 116

the approximate position of R7<sub>II</sub>, R8<sub>III</sub>, R9<sub>II</sub> and R10<sub>II</sub>. The solid lines represent the solid phases in equilibrium and dashed lines indicate the liquid composition in the liquidus surface boundary lines.

3.16 – Liquidus projection of the 0%>U>30% and 21%>B>50% (at.%) section showing the position R7<sub>II</sub>, R8<sub>III</sub>, R9<sub>II</sub> and R10<sub>II</sub> together with the position of 50B:25Fe:25U, 43B:55Fe:2U, 40B:40Fe:20U, 38B:52Fe:10U, 34B:60Fe:6U and 33B:50Fe:17U (UFe<sub>3</sub>B<sub>2</sub> stoichiometry) alloys (respectively Nr.12, 18, 21, 22, 24 and 25) where the dashed lines represent the liquid composition at the liquidus surface boundary lines. The grey lettering indicates the primary crystallization fields of the compounds. 117

3.17 – Solidification path for 38B:52Fe:10U and 33B:50Fe:17U alloys (respectively Nr.22 and 25). 119

3.18 – Reaction scheme in the 0%>U>30% and 21%>B>50% (at.%) section of the B-Fe-U diagram. 120

3.19 – Representative experimental powder X-ray diffractograms of Fe-rich alloys: (a) as-cast 23B:62Fe:15U (Nr.30), (b) annealed 21B:76Fe:3U (Nr.31), (c) annealed 10B:80Fe:10U (Nr.43), where the presence of, respectively, UFe<sub>3</sub>B<sub>2</sub>, U<sub>2</sub>Fe<sub>21</sub>B<sub>6</sub> and UFe<sub>4</sub>B is evident. The dotted lines represent simulations for these compounds. UFe<sub>3</sub>B<sub>2</sub> crystallizes with CeCo<sub>3</sub>B<sub>2</sub>-type structure, U<sub>2</sub>Fe<sub>21</sub>B<sub>6</sub> crystallizes with a Cr<sub>23</sub>C<sub>6</sub> type-structure and UFe<sub>4</sub>B crystallizes with a structure related to the CeCo<sub>4</sub>B one. These structures were assumed in the simulated diffratogram. The symbols indicate reflections of other phases present in the alloys; UFe<sub>2</sub> - crosses, UFe<sub>4</sub>B - solid squares, UFe<sub>3</sub>B<sub>2</sub> - solid circles, α-Fe - open circles, Fe<sub>2</sub>B - open squares. 122

3.20 – BSE images showing microstructures of the (a) as-cast 17B:73Fe:10U alloy (Nr. 36), (b) as-cast and (c) annealed 17B:66Fe:17U (UFe<sub>4</sub>B stoichiometry) alloy (Nr.37), (d) as-cast 15B:80Fe:5U alloy (Nr.39), (e) as-cast and (f) annealed 9B:87Fe:4U (Nr.44) alloy. The phase labelling is given in Table 3.1. 124

3.21 – DTA curves for representative Fe-rich as-cast: (a) 17B:73Fe:10U, (b) 17B:66Fe:17U (UFe<sub>4</sub>B stoichiometry) and (c) 9B:87Fe:4U alloys (Nr. 36, 37 and 44). 125

3.22 – HTXRD results of α-Fe to γ-Fe transformation. 126

3.23 – Liquidus projection diagram in the part the Fe-rich section showing R11<sub>III</sub>, R12<sub>II</sub>, R13<sub>III</sub>, R14<sub>II</sub>, R15<sub>II</sub> and R16<sub>I</sub> where the solid lines represent the solid phases in equilibrium 141

and dashed lines indicate the liquid composition.

3.24 – Liquidus projection diagram in the Fe-rich section showing R11<sub>II</sub>, R12<sub>II</sub>, R13<sub>III</sub>, R14<sub>II</sub>, R15<sub>II</sub> and R16<sub>I</sub> together with 17B:73Fe:10U, 17B:66Fe:17U (UFe<sub>4</sub>B stoichiometry), 15B:80Fe:5U, 11B:78Fe:11U, 10B:80Fe:10U, 9B:87Fe:4U, and 7B:79Fe:14U alloys positions (respectively, Nr. 36, 37, 39, 41, 43, 44 and 47) where the dashed lines represent the liquid composition. The grey lettering indicates the primary crystallization fields of the compounds. 142

3.25 – Solidification path for alloys 17B:73Fe:10U, 17B:66Fe:17U (UFe<sub>4</sub>B stoichiometry) and 9B:87Fe:4U alloys (respectively, Nr. 36, 37 and 44). 144

3.26 – Reaction scheme corresponding to the Fe-rich section of the liquidus projection of the B-Fe-U diagram. 145

3.27 – Representative experimental X-ray powder diffractograms of U-rich alloys: (a) annealed 30B:4Fe:66U (Nr.27) (b) as-cast 9B:6Fe:85U (Nr.46), (c) as-cast 5B:50Fe:45U (Nr.50) where UB<sub>2</sub>, α-U and UFe<sub>2</sub> are clearly evident. The dotted lines represent the simulations for UB<sub>2</sub>, α-U and UFe<sub>2</sub>. The symbols indicate reflections of other phases; U<sub>6</sub>Fe - stars; UFe<sub>2</sub> - crosses, UO<sub>2</sub> - open circles and UB<sub>2</sub> – close circles. 146

3.28 – BSE images showing microstructures observed in (a) as-cast 9B:12Fe:79U alloy (Nr.45), (b) is a magnified detail of 9B:12Fe:79U alloy (Nr.45), (c) as-cast 16B:43Fe:40U alloy (Nr.38), (d) low and (e) high magnification of as-cast 9B:6Fe:85U alloy (Nr.46) and (f) annealed 9B:6Fe:85U alloy (Nr.46). The pits observed in the U dendrites in (d) and (e) (regions N) result from a slight overetching. 148

3.29 – DTA curves for representative U-rich section (a) as-cast 16B:44Fe:40U alloys (Nr. 38), (b) as-cast 9B:12Fe:79U alloys (Nr. 45), (c) as-cast 9B:6Fe:85U alloys (Nr. 46). 149

3.30 – Liquidus projection diagram in the U-rich section showing R17<sub>II</sub> and R18<sub>I</sub> where the solid lines represent the solid phases in equilibrium and dashed lines indicate the liquid composition together with 30B:20Fe:50U, 30B:4Fe:66U, 16B:44Fe:40U, and 9B:12Fe:79U alloys position (respectively, Nr.26, 27, 38 and 45) alloys. The grey lettering indicates the primary crystallization fields of the compounds. 155

3.31 – Solidification path for alloys 16B:43Fe:40U, 9B:12Fe:79U and 9B:6Fe:85U alloys position (respectively, Nr. 38, 45 and 46). 157

3.32 – Reaction scheme corresponding to the U-rich section of the liquidus projection of 158

the B-Fe-U diagram.

- 3.33 – Liquidus projection diagram in the B-Fe-U ternary diagram showing all the ternary reactions, where solid lines represent the solid phases in equilibrium and dashed lines indicate the liquid composition (see appendix 1). 159
- 3.34 – Reaction scheme of the liquidus projection of the B-Fe-U diagram. 160
- 3.35 – Isothermal section at 780°C of the B-Fe-U ternary phase diagram, where solid lines represent the solid phases in equilibrium. 161
- 3.36 – Isothermal section at 950°C of the B-Fe-U ternary phase diagram, where solid lines represent the solid phases in equilibrium. 162
- 3.37 – Isothermal section at 1100°C of the B-Fe-U ternary phase diagram, where solid lines represent the solid phases in equilibrium. 163
- 3.38 – Isopleth at 16.67 at.% U. The squares indicate intersections with boundary reactions in the liquidus projection. 164
- 

- 4.1 – (a) Experimental powder X-ray diffraction pattern of the annealed an 66B:17Fe:17U (UFeB<sub>4</sub> stoichiometry) alloy, (b) simulation for the YCrB<sub>4</sub>-type structure and (c) simulation for the ThMoB<sub>4</sub>-type structure (the stars indicate reflections indexed to UB<sub>4</sub>). 172
- 4.2 – BSE image showing light and dark layers in the UFeB<sub>4</sub> phase (as-cast 50B:25Fe:25U alloy) characteristic of a random intergrowth when observed edge-on. 173
- 4.3 – (a) BSE image showing light and dark layers in the UFeB<sub>4</sub> phase (as-cast 50B:25Fe:25U alloy), (b) Experimental EBSD pattern of the UFeB<sub>4</sub> phase. The arrows indicate diffraction rings centered on low-index zone axes of a crystallographic plane parallel to the planar. 174
- 4.4 – (a) Experimental EBSD pattern of the UFeB<sub>4</sub> compound and simulations with 40 indexed planes for (b) YCrB<sub>4</sub>-type and (c) ThMoB<sub>4</sub>-type structures (MAD = 0.406 and 175

0.398°, respectively). The arrows indicate concentric diffraction rings associated with the crystallographic plane corresponding to the planar defects.

- 4.5 – Temperature dependence of the inverse susceptibility for the annealed 66U:17Fe:17B alloy (UFeB<sub>4</sub> stoichiometry) at 3T. The upturn at 30K results most likely from ferromagnetic impurities. 177
- 4.6 – Magnetic field dependence of the magnetization for the annealed 66U:17Fe:17B alloy (UFeB<sub>4</sub> stoichiometry) at 2K. 177
- 4.7 – Experimental PXRD of the annealed 67B:22Fe:11U (UFe<sub>2</sub>B<sub>6</sub> stoichiometry) alloy, and simulation for the CeCr<sub>2</sub>B<sub>6</sub>-type structure (stars – UFeB<sub>4</sub>; crosses – UB<sub>4</sub>). 178
- 4.8 – Projections of the UFe<sub>2</sub>B<sub>6</sub> on along (a) [100], (b) [010] and (c) [001]. 181
- 4.9 – Coordination polyhedra for (a) U atom, (b) Fe atom and (c) B<sub>2</sub> atom and d) B<sub>1</sub> atom. 182
- 4.10 – Temperature dependence of the magnetic susceptibility of UFe<sub>2</sub>B<sub>6</sub> at compound at 5 Tesla. 183
- 4.11 – Experimental powder X-ray diffraction patterns of (a) annealed 33B:50Fe:17U (UFe<sub>3</sub>B<sub>2</sub> stoichiometry) alloy, (b) Czochralski pulled 23B:62Fe:15U alloy, and (c) simulation for UFe<sub>3</sub>B<sub>2</sub> phase with the CeCo<sub>3</sub>B<sub>2</sub>-type structure (star – UFeB<sub>4</sub>, black circles – UFe<sub>4</sub>B and cross- $\alpha$ -Fe). 185
- 4.12 – Projections of the UFe<sub>3</sub>B<sub>2</sub> structure along (a) [100] and (b) [001] showing the unit cell. 187
- 4.13 – Coordination polyhedra for (a) U atom, (b) Fe atom and (c) B atom. 188
- 4.14 – Temperature dependence of the magnetization M (T) for the UFe<sub>3</sub>B<sub>2</sub> compound taken in a field of 1 T. The inset shows the ZFC and FC curves in a field of 0.01 T. 189
- 4.15 – Magnetization dependence on applied field for UFe<sub>3</sub>B<sub>2</sub> at different temperatures. 190

- 4.16 – Experimental powder X-ray diffraction pattern of the annealed 10B:80Fe:10U alloy 192  
together with a simulation for  $\text{UFe}_4\text{B}$  with the  $\text{CeCo}_4\text{B}$ -type structure (pentagons -  $\text{UFe}_2$ ,  
circle -  $\text{UFe}_3\text{B}_2$ ; square -  $\alpha\text{-Fe}$ ).
- 4.17 – (a) BSE image of the annealed 10B:80Fe:10U alloy and (b) U and (c) Fe X-ray 193  
maps.
- 4.18 – (a) Experimental  $\text{UFe}_4\text{B}$  EBSD pattern of grain 1 and simulations for (b)  $\text{CeCo}_4\text{B}$ - 195  
type structure (MAD =  $0.301^\circ$ ), (c)  $\text{Ce}_3\text{Co}_{11}\text{B}$ -type structure (MAD =  $0.304^\circ$ ) (d)  
 $\text{Ce}_2\text{Co}_7\text{B}_3$ -type structure (MAD =  $0.302^\circ$ ), (e)  $\text{Ni}_3\text{Nd}_{13}\text{B}_2$ -type structure (MAD =  $0.303^\circ$ )  
and (f)  $\text{Lu}_5\text{Ni}_{19}\text{B}_6$ -type structure (MAD =  $0.302^\circ$ ). The simulations were performed for 60  
reflecting planes. The dashed lines indicate simulated bands absent in the experimental  
patterns.
- 4.19 – (a) Experimental  $\text{UFe}_4\text{B}$  EBSD pattern of grain 2 and simulations for (b)  $\text{CeCo}_4\text{B}$ - 196  
type structure (MAD =  $0.225^\circ$ ), (c)  $\text{Ce}_3\text{Co}_{11}\text{B}$ - type structure (MAD =  $0.235^\circ$ ), (d)  
 $\text{Ce}_2\text{Co}_7\text{B}_3$ - type structure (MAD =  $0.308^\circ$ ), (e)  $\text{Ni}_3\text{Nd}_{13}\text{B}_2$ -type structure (MAD =  $0.335^\circ$ )  
and (f)  $\text{Lu}_5\text{Ni}_{19}\text{B}_6$ -type structure (MAD =  $0.335^\circ$ ). The simulations were performed for 60  
reflecting planes. The dashed lines indicate simulated bands absent in the experimental  
patterns.
- 4.20 – (a) Experimental  $\text{UFe}_4\text{B}$  EBSD pattern of grain 3 and simulations for (b)  $\text{CeCo}_4\text{B}$ - 197  
type structure (MAD =  $0.372^\circ$ ), (c)  $\text{Ce}_3\text{Co}_{11}\text{B}$ -type structure (MAD =  $0.397^\circ$ ), (d)  
 $\text{Ce}_2\text{Co}_7\text{B}_3$ -type structure (MAD =  $0.283^\circ$ ), (e)  $\text{Ni}_3\text{Nd}_{13}\text{B}_2$ -type structure (MAD =  $0.390^\circ$ )  
and (f)  $\text{Lu}_5\text{Ni}_{19}\text{B}_6$ -type structure (MAD =  $0.381^\circ$ ). The simulations were performed for 60  
reflecting planes. The dashed lines indicate simulated bands absent in the experimental  
patterns.
- 4.22 – Experimental powder X-ray diffraction pattern of annealed 15B:80Fe:5U alloy 200  
together with a simulation for  $\text{U}_2\text{Fe}_{21}\text{B}_6$  with the  $\text{Cr}_{23}\text{C}_6$ -type structure (crosses -  $\text{UFe}_4\text{B}$ ;  
star -  $\text{Fe}_2\text{B}$ ; circles -  $\text{UFe}_3\text{B}_2$ ; square -  $\alpha\text{-Fe}$ ).
- 4.23 – (a) BSE image of the annealed 15B:80Fe:5U alloy and (b) U and (c) Fe X-ray 201  
maps.
- 4.24 – Experimental EBSD patterns of the annealed 15B:80Fe:5U alloy (a)  $\text{U}_2\text{Fe}_{21}\text{B}_6$  - grain 1, 202  
(b)  $\text{U}_2\text{Fe}_{21}\text{B}_6$  - grain 2 (c)  $\text{U}_2\text{Fe}_{21}\text{B}_6$  - grain 3 (d)  $\text{UFe}_3\text{B}_2$ , (e)  $\text{Cr}_{23}\text{B}_6$ -type simulation (grain 1,  
MAD =  $0.357^\circ$ ), (f)  $\text{Cr}_{23}\text{B}_6$ -type simulation (grain 2, MAD =  $0.488^\circ$ ), (g)  $\text{Cr}_{23}\text{B}_6$ -type

simulation (grain 3,  $MAD = 0.345^\circ$ ) (h)  $CeCo_3B_2$ -type simulation ( $MAD = 0.296^\circ$ ). The simulations were performed for 60 reflecting planes.

## Tables Index

---

Table	Pages
2.1 – Crystals used in WDS spectrometers.	55
2.2 – Correspondence between alloy number and composition.	62
<hr/>	
3.1 – Phases, cotectic and ternary mixtures labeling and WDS results.	78
3.2 – Boundary lines for R1 <sub>III</sub> , R2 <sub>III</sub> , R3 <sub>II</sub> , R4 <sub>II</sub> , R5 <sub>I</sub> and R6 <sub>II</sub> ternary reaction points associated with the four-phase configuration.	96
3.3 – Boundary lines for R7 <sub>II</sub> , R8 <sub>III</sub> , R9 <sub>II</sub> and R10 <sub>II</sub> ternary reaction points associated with the four-phase configuration.	115
3.4 – Boundary lines for R11 <sub>III</sub> , R12 <sub>II</sub> , R13 <sub>III</sub> and R14 <sub>II</sub> ternary reaction points associated with the four-phase configuration.	139
3.5 – Boundary lines for R15 <sub>II</sub> and R16 <sub>I</sub> ternary reaction points associated with the four-phase configuration.	140
3.6 – Boundary lines for R17 <sub>II</sub> and R18 <sub>I</sub> ternary reaction points associated with the four-phase configuration.	154
<hr/>	
4.1 – Crystal data and structure refinement for UFe <sub>2</sub> B <sub>6</sub> single crystal.	179

4.2 – Atomic positions and thermal parameters (nm <sup>2</sup> ) for the UFe <sub>2</sub> B <sub>6</sub> compound obtained from single X-ray crystal diffraction.	180
4.3 – Selected interatomic distances (d, nm) for atoms in the UFe <sub>2</sub> B <sub>6</sub> compound.	180
4.4 – Crystal data and structure refinement for the UFe <sub>3</sub> B <sub>2</sub> single crystals extracted from the annealed 33B:50Fe:17U (UFe <sub>3</sub> B <sub>2</sub> stoichiometry) alloy.	186
4.5 – Atomic positions and thermal parameters (nm <sup>2</sup> ) for the UFe <sub>3</sub> B <sub>2</sub> compound obtained from single X-ray crystal diffraction	187
4.6 – Interatomic distances (nm) for atoms in the UFe <sub>3</sub> B <sub>2</sub> crystal.	187
4.7 – Lattice parameters adjusted from the PXRD data for the CeCo <sub>4</sub> B-, Ce <sub>3</sub> Co <sub>11</sub> B-, Ce <sub>2</sub> Co <sub>7</sub> B <sub>3</sub> -, Ni <sub>3</sub> Nd <sub>13</sub> B <sub>2</sub> - and Lu <sub>5</sub> Ni <sub>19</sub> B <sub>6</sub> -type structures together with simulated planes absent in experimental patterns.	198

## Acronyms

---

BSE – Backscattered Electrons  
CCD – Charge Coupled Device  
CGS – Centimeter, Gauss, Second  
DTA – Differential Thermal Analysis  
DSC – Differential Scanning Calorimetry  
EBSD – Electron Backscattered Electrons Diffraction  
EDS – Energy Dispersive X-ray Spectroscopy  
EPMA – Electron Probe Microanalyzer  
FC – Field-Cooled  
HTXRD – High temperature X-ray diffraction  
IF – Induction Furnace  
LIF – Lithium Fluoride  
HOLZ – High Order Laue Zone  
MAD – Mean Angle Deviation  
MPMS – Magnetic Property Measurement System  
OPS – Oxide Polishing Suspension  
PET – Pentaerythritol  
PXRD – Powder X-ray diffraction  
TAP – Thallium Acid Phthallate  
SEM – Scanning Electron Microscope  
SE – Secondary Electrons  
SI – International System  
SQUID – Superconducting Quantum Interference Device  
WDS – Wavelength Dispersive Spectroscopy  
ZFC – Zero Field-Cooled



## Symbols

---

A – actinide element

Å – angstroms

λ – electron λ

Γ – generic component

a – interatomic distance in the row along x-axis

**A** – type of layer

$a_i$  – parameter in the Cromer and Mann formula

**a** – translation vector from one lattice site to the next along x-axis

**a\*** – translation vector from one lattice site to the next along x\*-axis in reciprocal lattice

A – transmission factor

**A'** – type of layer

AB – path between A and B points

ab – plane composed by a and b axis

AC – distance between electron λ and point C

ΓC – distance between Γ and C components in the ternary phase diagram

AD – distance between electron λ and point D

ΓN – distance between Γ component and point N in the ternary phase diagram

at% – atomic percentage

α – alpha phase; origin of the outer electrons that will fill the vacancy in X-ray

$\alpha_n$  – angle between the diffracted beam and x-axis

$\alpha_0$  – angle between the incident beam and x-axis; zero order semi-apex angle

$\alpha_1$  – first order semi-apex angle; origin of the outer electrons that will fill the vacancy and correspondent level of energy

$\alpha_2$  – second order semi-apex angle; origin of the outer electrons that will fill the vacancy and correspondent level of energy

$\alpha L$  – tie line between  $\alpha$  and liquid phases

$B$  – Debye-Waller temperature factor

$B$  – electron  $B$

$\mathcal{B}$  – generic component

$b$  – interatomic distance in the row along y-axis

$B$  – magnetic induction

$\mathbf{b}$  – translation vector from one lattice site to the next along y-axis

$\mathbf{b}^*$  – translation vector from one lattice site to the next along y-axis in reciprocal lattice

$b_i$  – parameter in the Cromer and Mann formula

$\mathcal{BCA}$  – ternary phase diagram triangle

$\beta_n$  – angle between the diffracted beam and y-axis

$\beta_0$  – angle between the incident beam and y-axis

$\beta$  – beta phase; origin of the outer electrons that will fill the vacancy in X- ray

$\beta\gamma$  – tie line between  $\beta$  and  $\gamma$  phases

$^{\circ}\text{C}$  – Celsius degrees

$C$  – Curie constant

$c$  – interatomic distance in the row along z-axis

$\mathcal{C}$  – generic component

$C$  – number of constrains

$C$  – number of components

$\mathbf{c}$  – translation vector from one lattice site to the next along z-axis

$c$  – speed of the light; parameter in the Cromer and Mann formula

$\mathbf{c}^*$  – translation vector from one lattice site to the next along z-axis in reciprocal lattice

$C_{st}$  – composition standard

CD – path between C and D points

$C_rO$  – distance between the origin of the reciprocal lattice and the centre of the Ewald's sphere

$C_rP$  – distance between the point P in the reciprocal lattice and the centre of the Ewald's sphere

Cmcm –crystalline space group Nr.63

$d_{hkl}$  – interplanar distance

$\Delta T$  – temperature difference

$\Delta f'$  – real part of atomic scattering factor

$e$  – charge on the electron

eV – electron Volt

emu – electromagnetic unit

exp – exponential function

$f_0$  – atomic scattering factor

$f$  – effective scattering from an atom

$F$  – number of degrees of freedom

$F_{hkl}$  – structure factor

$F_c$  – structure factor calculated

$F_o$  – structure factor observed

Fm  $\bar{3}m$  –crystalline space group Nr.225

$\phi$  – phase angle of the scattered wave

$\phi$  – single-crystal X-ray angle

$\gamma$  – gamma phase; origin of the outer electrons that will fill the vacancy in X- ray

$\gamma_n$  – angle between the diffracted beam and z-axis

$\gamma_0$  – angle between the incident beam and z-axis

G – gauss

g – gram

$Goof$  – goodness of fit in single crystal refinement

$\mathbf{g}$  – reciprocal lattice vector

H – applied magnetic field

h – hours

$h$  – Miller indice

$H_c$  – coercive field

$i$  – generic element

$I$  – Stoner parameter

$I_0$  – intensity of incident beam

$I^{obs}$  – observed intensity

$I_{st}$  – peak intensity for the  $i$  element in the standard sample

$I_i$  – measured peak intensity

$I_{hkl}$  – scattered intensity

Immm –crystalline space group Nr.71

$j$  – generic atom

k – Boltzman constant

$\mathbf{K}$  – diffraction vector

$k$  – Miller index

$K$  – scale factor

K – shell containing the inner vacancy

$K_i$  – correction factor

$K\alpha$  – transition from the L to the K shells

$K\beta$  – transition from the M to the K shells

L – liquid; shell containing the inner vacancy

$L$  – Lorentz factor

$l$  – Miller index

$l_k$  – boundary line, where k denotes the number sequence

$\lambda$  – wavelength

M – magnetization; M shell containing the inner vacancy

m – temperature maximum

$\mathcal{M}$  – ternary phase diagram point

mbar – milibar

$m_e$  – mass of the electron

mg – milligrams

$m_{hkl}$  – plane multiplicity factor

min –minute

$\mathcal{M}\mathcal{N}$ – distance between  $\mathcal{M}$  and  $\mathcal{N}$  points in the ternary phase diagram

$M_{\text{rem}}$ – remnant magnetization

$M_s$  – saturation magnetization

$\mathcal{M}\mathcal{X}$  – distance between  $\mathcal{M}$  and alloy composition  $\mathcal{X}$  in the ternary phase diagram

$\mu_B$  – magneton Bohr

$\mu\text{m}$  – micrometers

$\mu_0$  – vacuum permeability

$n$  – integer designated as order of diffraction

N – N shell containing the inner vacancy

$\mathcal{N}$  – ternary phase diagram point

$N$  – total number of used points

nA – nanoampere

$n(E_F)$  – electronic density of states at the Fermi energy level

$MC$  – distance between point  $M$  and  $C$  component in the ternary phase diagram

nm – nanometers

Nr. – number

O – origin of the reciprocal lattice

$\odot$  – ternary phase diagram point

Oe – oersted

OP – distance between the origin of the reciprocal lattice and point P

**P** – point where the diffracted beam intercepts the Ewald's sphere

$P$  – polarization factor; number of refined parameters

$\mathcal{P}$  – pressure

$P(u, v, w)$  – electronic density in Patterson function

$P6mmm$  –crystalline space group Nr.191

$Pnma$  –crystalline space group Nr.51

$\pi$  – ratio of circle's circumference to its diameter

$r$  – distance from the scattering electron to the detector

$R_I$  – class I invariant reaction

$R_{II}$  – class II invariant reaction

$R_{III}$  – class III invariant reaction

$R_{Bragg}$  – Bragg residual value

$R_{exp}$  – expected residual value

$R_{ij}$  – numbering sequence that follows the ternary reaction order

$R_p$  – profile residual value

$R_{wp}$  – weighted-profile residual value

$R_y$  – residual value in Rietveld refinement

$\rho(xyz)$  – electronic density distribution

$S$  – goodness of fit in Rietveld refinement

$\mathbf{S}$  – unit vector along the direction of the diffracted beam; diffracted wave vector

$\mathbf{S}_0$  – unit vector along the direction of the incident beam; incident wave vector

$T$  – temperature; Tesla

$T$  – transition metal element

$T_C$  – Curie temperature

$T_N$  – Neel temperature

$\theta$  – scattering or diffracting angle

$\theta_{CW}$  – Curie-Weiss Temperature

$u$  – mean-square vibration amplitude of the atom; atomic position

$u$  – boron fraction

$U_{eff}$  – effective intra-atomic Coulomb correlation

$v$  – atomic position

$v$  – iron fraction

$V$  – volume

$W$  –  $5f$  bandwidth

$w$  – atomic position

$w$  – uranium fraction

$w_i$  – statistical weight

$w_P$  – intensity weight

$wR$  – weighted residual

$\bar{X}$  – beam scattering coherently from electrons  $\mathbb{A}$

$\hat{X}$  – beam scattering coherently from electrons  $\mathbb{B}$

$\chi$  – magnetic susceptibility; single-crystal X-ray angle

$x_j$  – atomic position for  $j$  atom

$x_m$  – atomic position for atom  $m$

$\mathcal{X}\mathbb{N}$  – distance between alloy composition  $\mathcal{X}$  and point  $\mathbb{N}$  in the ternary phase diagram

$\bar{Y}$  – beam scattering coherently from electrons  $\mathbb{A}$  at  $0^\circ$  angle

$\hat{Y}$  – beam scattering coherently from electrons  $\mathbb{B}$  at  $0^\circ$  angle

$y_i^{cal}$  – calculated intensities

$y_i^{obs}$  – experimental intensities

$y_j$  – atomic position for  $j$  atom

$y_m$  – atomic position for atom  $m$

$Z$  – atomic number

$\bar{Z}$  – beam scattering coherently from electrons  $\mathbb{A}$  at non-zero angle

$\hat{Z}$  – beam scattering coherently from electrons  $\mathbb{B}$  at non-zero angle

$z_j$  – atomic position for  $j$  atom

$z_m$  – atomic position for atom  $m$

N.B.:

Chemical element symbols have not been listed nor as SI units.

***List of Publications related to this thesis:***

M. Dias, P.A. Carvalho, O. Sologub, O. Tougait, H. Noël, C. Godart, E. Leroy, A.P. Gonçalves. "Isothermal Section at 950°C of the U-Fe-B ternary system", *Intermetallics*, 15, 3 (2007) 413-418.

M. Dias, P.A. Carvalho, O. Sologub, L.C.J. Pereira, I.C Santos, A.P. Gonçalves, "Studies on the new  $UF_2B_6$  phase" *Journal of Alloys and Compounds*, 492 (1-2) (2010) L13.

M. Dias, P.A. Carvalho, A.P. Dias, M. Bohn, N. Franco, O. Tougait, H. Noël, A.P. Gonçalves "Cascade of Peritectic Reactions in the B-Fe-U system", *Journal of Phase Equilibria and Diffusion*, 31(2) (2010) 104.

M. Dias, P.A. Carvalho, M. Bohn, O. Tougait, H. Noël, A.P. Gonçalves, "Liquidus projection of the B-Fe-U diagram: boron-rich section", *Journal of Alloy and Compounds*, (2011) (submitted).

M. Dias, P.A. Carvalho, M. Bohn, O. Tougait, H. Noël, A.P. Gonçalves, "Liquidus projection of the B-Fe-U diagram: the  $0\% < U < 30\%$  and  $21\% < B < 50\%$  section", *Journal of Alloy and Compounds*, 2011 (submitted).

M. Dias, P.A. Carvalho, U. Vinaica, O. Tougait, H. Noël, A.P. Gonçalves, "Liquidus projection of the B-Fe-U diagram: the iron-rich section", *Journal of Alloy and Compounds*, 2011 (in preparation).

M. Dias, P.A. Carvalho, U. Vinaica, O. Tougait, H. Noël, A.P. Gonçalves, "The B-Fe-U (Boron – Iron – Uranium) System: uranium-rich section and global update" *Journal of Alloy and Compounds*, 2011 (in preparation).

M. Dias, P.A. Carvalho, I.C.Santos, O.Tougait, L. Havela, A.P. Gonçalves, "EBSD and magnetic studies on the  $UF_2B_4$  compound", *Intermetallics*, 2011 (in preparation).

M. Dias, P.A. Carvalho, L.C.J. Pereira, I.C.Santos, O.Tougait, A.P. Gonçalves "Crystal structure and magnetism of the  $UF_3B_2$  compound", *Intermetallics*, 2011 (in preparation).

M. Dias, P.A. Carvalho, A.P. Gonçalves, "EBSD studies on iron-rich  $U_xFe_yB_z$  compounds", *Intermetallics*, 2011 (in preparation).

Título: Diagrama de fases ternário do sistema B-Fe-U e caracterização dos compostos ternários

Ramo: Engenharia de Materiais

## Resumo

Este trabalho apresenta o diagrama de fases ternário B-Fe-U e a caracterização dos seus compostos ternários. O estudo do diagrama de fases engloba a projecção liquidus completa incluindo a natureza das linhas fronteiras que delimitam os campos de cristalização primária, a natureza e localização dos pontos invariantes, juntamente com três secções isotérmicas, a 780°C, 950°C e 1000°C e uma secção vertical ao longo da linha  $U:(Fe,B) = 1:5$ . O sistema ternário B-Fe-U compreende sete compostos binários e cinco compostos ternários os quais formam dezoito triângulos de compatibilidade e dezoito pontos de reacções ternárias. Foram realizadas medidas de refinamento de monocristal para os compostos  $UFe_3B_2$  e  $UFe_2B_6$ , sendo que o primeiro assume uma estrutura hexagonal do tipo  $CeCo_3B_2$  e o segundo uma estrutura ortorrômbica do tipo  $CeCr_2B_6$ . As medidas magnéticas foram realizadas para os compostos  $UFe_3B_2$ ,  $UFe_2B_6$  e  $UFeB_4$ . O composto  $UFe_3B_2$  apresenta um comportamento ferromagnético abaixo de 300 K enquanto o  $UFe_2B_6$  e  $UFeB_4$  são paramagnéticos entre 2-300K. Devido à complexidade das microestruturas das ligas ternárias, que impossibilitaram a extracção de monocristais, os compostos  $UFeB_4$ ,  $UFe_4B$  e  $U_2Fe_{21}B_6$  foram estudados usando difracção de electrões retrodifundidos. O  $U_2Fe_{21}B_6$  assume uma estrutura cúbica do tipo  $Cr_{23}C_6$  e o  $UFe_4B$  adopta uma estrutura hexagonal similar à do  $CeCo_4B$ . O composto  $UFeB_4$  apresenta um estrutura com crescimento cooperativo entre duas estruturas ortorrômbicas,  $YCrB_4$  e  $ThMoB_4$ .

Palavras chave: Microestrututura, reacção ternária, projecção liquidus, liga.

Title: B-Fe-U ternary phase diagram and ternary compounds characterization

Àrea: Materials Engeneering

### Abstract

This work presents the B-Fe-U ternary phase diagram and characterizes the ternary borides of the system. The phase diagram study comprises the complete liquidus projection, including the *cotectic* and *reaction* boundary lines that delimit primary crystallization fields, the nature and position of the ternary invariants points, as well as three isothermal sections, at 700°C, 950°C and 1100°C, and a vertical section along  $U:(Fe,B) = 1:5$ . The B-Fe-U system comprises seven binary compounds and five ternary compounds, all with limited solubility, which form eighteen compatibility triangles and corresponding eighteen ternary reactions. Single-crystal refinement was performed on  $UFe_3B_2$  and  $UFe_2B_6$  ternary compounds which present a hexagonal  $CeCo_3B_2$ -type and orthorhombic  $CeCr_2B_6$ -type structures, respectively. Magnetic measurements were studied for the  $UFe_3B_2$ ,  $UFe_2B_6$  and  $UFeB_4$  ternary compounds.  $UFe_3B_2$  is ferromagnetic below 300K, while  $UFe_2B_6$  and  $UFeB_4$  are paramagnetic between 2-300K. Due to the complexity of the ternary alloys microstructure  $UFeB_4$ ,  $UFe_4B$  and  $U_2Fe_{21}B_6$  could not be extracted as single-crystals and were investigated by electron-backscattered diffraction.  $U_2Fe_{21}B_6$  assumes a cubic  $Cr_{23}C_6$ -type structure and  $UFe_4B$  adopts a structure similar to the hexagonal  $CeCo_4B$ -type structure. The  $UFeB_4$  compound consists of an intergrowth between  $YCrB_4$ - and  $ThMoB_4$ - type structures.

Keywords: Microstructure, ternary reaction, liquidus projection, alloy

---

# Chapter 1

---



## **Chapter 1 – Introduction**

### **1.1 Designations and nomenclature**

The terms ‘rare earths’ and ‘lanthanides’ designate a series of 14 metallic elements with atomic numbers between 58 and 71, which follow lanthanum ( $Z=57$ ), in the sixth row and IIIB group of the Periodic Table. The atomic number increases in the series through successive filling of the internal  $4f$  orbital [1]. As a result of the internal orbital filling, the members of the series have analogous valence structures and closely resemble in chemical characteristics. Furthermore, due to electronic similarities, scandium ( $Z = 21$ ) and yttrium ( $Z = 39$ ), in the same group of the Periodic Table, are frequently considered rare earths.

The ‘actinides’ are a family of 14 chemical elements with atomic numbers between 90 and 103, which follow actinium ( $Z = 89$ ) and include U ( $Z = 92$ ), in the seventh row and IIIB group of the Periodic Table. The atomic number increases in the series through successive filling of the  $5f$  orbital [2]. These large elements present radioactive decay and, as with the rare earths, their interesting properties result from the especial electronic structure of the  $f$  orbital. For this reason both rare earths and actinides are frequently referred to as  $f$ -elements.

The current work follows the commonly accepted alphabetical order of the constituent elements for the designation of ternary diagrams and alloys [3], i.e., B-Fe-U. Nevertheless, for the borides designation the nomenclature of ternary rare earth and actinide compounds will be used instead i.e.;  $R_xT_yD_z$  and  $A_xT_yD_z$ , where R denotes rare-earth, A an actinide, T a transition metal and D another element, which in the present case is B (see for example [4]).

## **1.2 Motivation**

The information currently available on phase diagrams of *f*-element ternary borides consists essentially of isothermal sections. The reports on B-T-R systems cover combinations involving all lanthanides, however in the case of B-T-A only a reduced set of combinations (A = Th, U or Pu) [5] exists in the literature [6]. In fact, for a large number of B-T-A systems merely a few compounds have been identified and no information on the phase diagram is reported. In both instances the materials have been typically prepared by conventional arc-melting techniques and characterized by X-ray powder diffraction in the as-cast and annealed conditions. Magnetic properties have been investigated using polycrystalline monophasic materials, and only when available have single-crystals been used for a structural characterization of the compounds. However, most of these studies have not involved any microstructural characterization, local diffraction or chemical analysis. Nevertheless, the existence of homogeneity ranges, structural disorder and phase transitions are known to play an important role on the resulting physical properties [5]. Furthermore, although *f*-element compounds are frequently sensitive to sample preparation methods, namely to solidification conditions and heat treatments, modest consideration has been given to these aspects in most of the systems investigated.

The interaction between the different sublattices in compounds of general  $R_xT_yB_z$  and  $A_xT_yB_z$  forms can lead to unique ground states and other physical phenomena worth investigating from a fundamental point of view:

- As an example, the B-Rh-R ternary systems have been extensively studied in connection with the interplay between superconductivity and magnetism, as in the case of  $ErRh_4B_4$  [7]; as well as due to unusual magnetic properties such as the anomalous ferromagnetism observed for  $RRh_3B_2$  [8].
- Additionally, other ternary compounds of the  $R_xT_yB_z$  and  $A_xT_yB_z$  types (T= Fe, Co) have received considerable attention due to their potential applications as super-magnets. Generally, for high T concentrations these compounds are ferromagnetic with a relatively high Curie temperature [9], and moreover the presence of the *f*-element can lead to the strong magnetic

anisotropy involved in super-magnetism, of which the behavior of  $\text{Nd}_2\text{Fe}_{14}\text{B}$  is a paradigm [10].

Generic uranium-based compounds present frequently atypical physical properties due the high spatial extension of the  $5f$  orbitals. Good examples are the coexistence of superconductivity and ferromagnetism in the  $\text{UGe}_2$  compound [11] and the complex magnetic structure of  $\text{UFe}_4\text{Al}_8$  [12]:

- In the case of  $\text{UGe}_2$ , the superconductivity under pressure is on the border of itinerant ferromagnetism; superconductivity is observed below 1 K in a limited pressure range, and seems to arise from the same electrons that produce band magnetism [11].  $\text{UGe}_2$  single crystal investigations [13, 14] showed also a highly anisotropic ferromagnetism below 52 K, with an easy direction parallel to the  $c$ -axis of the orthorhombic structure. The small saturation moment ( $1.43\mu_{\text{B}}/\text{U}$ ) and the relatively large specific heat indicate that  $\text{UGe}_2$  is a heavy fermion ferromagnet.
- The  $\text{UFe}_4\text{Al}_8$  compound of the  $\text{ThMn}_{12}$ -type structure exhibits a ferromagnetic behavior below 150K [12]. Magnetization measurements on a single crystal revealed high anisotropy with an easy magnetization  $ab$  plane. The iron atoms in  $\text{UFe}_4\text{Al}_8$  are mainly antiferromagnetically ordered, however, a small canting of these iron moments induces a magnetic moment in the uranium atoms, leading to a complex magnetic ground state for this compound [15].

Usually intermetallic uranium borides do not present magnetic ordering. The only reported exceptions are  $\text{URh}_3\text{B}_z$  ( $z \sim 1$ ) [16] and  $\text{UNi}_4\text{B}$  [17]:

- The  $\text{URh}_3\text{B}_x$  structure is based on the structure of the cubic  $\text{URh}_3$  compound which is a temperature-independent paramagnet [18] where the  $5f$  electrons are itinerant. However,  $\text{URh}_3\text{B}$  exhibits Curie-Weiss susceptibility and orders antiferromagnetically at 9.8 K [16] suggesting a more local nature of its  $5f$  electrons.
- The  $\text{UNi}_4\text{B}$  compound was first reported as crystallizing in the hexagonal  $\text{CeCo}_4\text{B}$ -type structure and to order antiferromagnetically below  $T_{\text{N}} = 20$  K [19]. Neutron diffraction experiments suggested that it consisted of two

uranium sub-systems, one involving  $2/3$  of the uranium atoms, with moments having antiferromagnetic interactions in a triangular symmetry in the easy hexagonal basal plane, the other  $1/3$  consisting of uranium atoms with free moments due to geometrical frustration [17]. However, recent X-ray diffraction investigations performed on an  $\text{UNi}_4\text{B}$  single crystal indicate that this compound crystallizes in the orthorhombic  $Cmcm$  space group, with four distinct uranium positions [20], which most probably determines its peculiar magnetic structure.

The study of B-T-U systems and their compounds is therefore an extremely interesting and largely unexplored field of research. A detailed knowledge of the phase diagrams is essential for a proper understanding of the solidification behaviour of these materials, which reflects the thermodynamic characteristics of the compounds involved. Furthermore, the phase diagrams are necessary for a correct selection of the synthesis method of each intermetallic compound, namely for establishing suitable single-crystal growth and heat-treatment conditions.

### **1.3 Background**

#### **1.3.1 Ternary phase diagrams**

At constant pressure ternary phase diagrams are represented by triangular prisms in which the temperature is plotted on the vertical axis against the three components compositions on the base of the prism. The intersection of two liquidus surfaces is a boundary line. A liquidus surface portion enclosed by a series of boundary lines is designated as primary crystallization field. The straight line connecting phases in equilibrium with adjacent primary crystallization fields, and whose liquidus surface intersection forms a boundary line, is called an Alkemade line. A tie line is a straight line joining two phases with specific composition at a given temperature. A tie triangle is a three-phase region at fixed temperature consisting of mixtures of the phases represented by the triangle corners. The location of the tie lines can be visualized by reference to isothermal (horizontal) sections cut through the

temperature-composition diagram at a series of temperature levels. Due to the seemingly resemble to binary diagrams, vertical sections, also known as isopleths, are widely used. A binary congruent compound in a ternary system can form a quasi-binary diagram with one of the other components of the ternary diagram. In this case, the vertical section joining the two compounds is equivalent to a binary phase diagram, which divides the ternary diagram into two independent parts. Ternary liquidus projections can be constructed by projecting the three-dimensional liquidus surface and its boundary lines onto the compositional base of the ternary phase diagram.

The thermodynamic basis of equilibrium diagrams is the phase rule of Willard Gibbs [21], which defines equilibrium conditions in terms of the number of phases and system components:

$$F = C - P + 2$$

where  $F$  is the degrees of freedom,  $C$  is the number of components, and  $P$  the number of phases. For a ternary system ( $C = 3$ ) at constant pressure, the phase rules states:

$$F = 4 - P$$

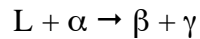
meaning that four-phase equilibria are invariant. These ternary four-phase equilibria are divided in three classes [22].

### **Boundary line types and ternary reaction geometry**

There are two types of boundary lines: (i) *cotectic* along which two phases co-precipitate; (ii) *reaction* along which one solid phase reacts with the liquid to produce another solid phase. At each point the boundary type is determined from the tangent: if the tangent intersects the Alkemade line, then the boundary line is *cotectic*, if it intersects its extension, the boundary line is of *reaction* type. When a boundary line that separates the  $\alpha$  and  $\beta$  primary crystallization fields, crosses the respective Alkemade line (joining  $\alpha$  and  $\beta$  in equilibrium) the temperature achieves there a maximum.

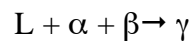
A class I invariant reaction ( $R_I$ ) involves three converging boundary lines (Figure 1.1 (a)); a class II invariant reaction ( $R_{II}$ ) presents two converging boundary lines and a diverging one, (Figure 1.1 (b)); a class III invariant reaction ( $R_{III}$ ) presents a converging boundary line and two diverging ones (Figure 1.1 (c)) [22,23].

A class II ternary reaction with the following equation:



requires the boundary lines between the  $\alpha$  and  $\beta$  and between the  $\alpha$  and  $\gamma$  crystallization fields to be converging to the invariant point, while the boundary line between the  $\beta$  and  $\gamma$  crystallization fields must be diverging.

A class III ternary reaction with the following equation:



requires a boundary line between the  $\alpha$  and  $\beta$  crystallization fields to be converging to the invariant point, whereas the boundary lines between the  $\gamma$  and  $\beta$  and between the  $\alpha$  and  $\gamma$  crystallization fields must be diverging.

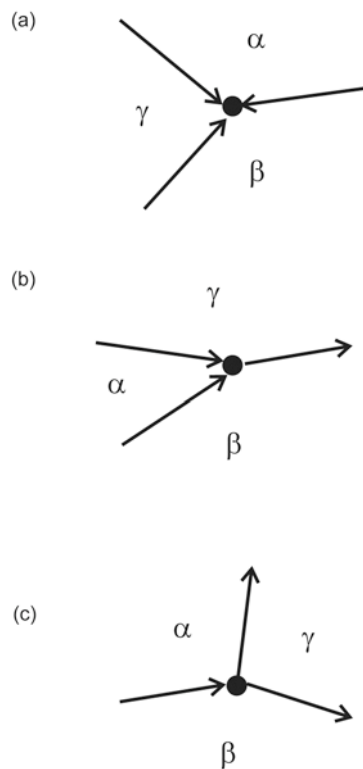
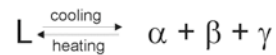


Figure 1.1 – Boundary lines involved in (a) class I ternary reaction ( $R_I$ ), (b) class II ternary reaction ( $R_{II}$ ) and (c) class III ternary reaction ( $R_{III}$ ).

### Class I ternary four-phase equilibrium (ternary eutectic reaction)

Ternary eutectic reactions occur by “isothermal” decomposition of a liquid into three different solid phases:



Three tie-triangles,  $L + \alpha + \beta$ ,  $L + \alpha + \gamma$ ,  $L + \beta + \gamma$  (Figure 1.2 (a)), descend from high temperature and terminate on an  $\alpha + \beta + \gamma$  tie-triangle connecting the composition of the three solid phases participating in the reaction (Figure 1.2 (b)). One-phase regions,  $\alpha$ ,  $\beta$  and  $\gamma$ , are situated at the corners of the solid phases tie-triangle. At the reaction temperature the liquid composition lies at a point  $L$  within this triangle, which defines the invariant reaction point, where the liquidus surfaces of the three solid phases meet at the lowest melting point of the neighborhood. Notice that at the ternary reaction temperature there is an isothermal four-phase triangle, i.e., any alloy located inside the  $\alpha + \beta + \gamma$  tie-triangle will consist of four phases. A class I equilibrium is illustrated in the ternary diagram of Figure 1.3.

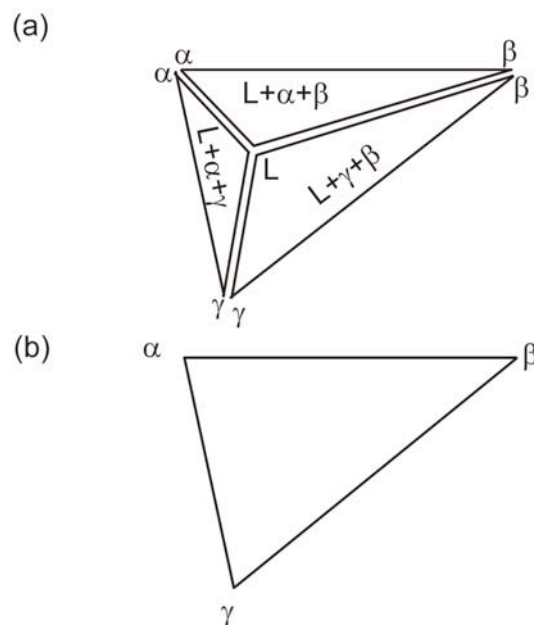


Figure 1.2 – Isothermal sections of a class I four-phase equilibrium showing (a) the three high temperature triangles and (b) the low temperature triangle.

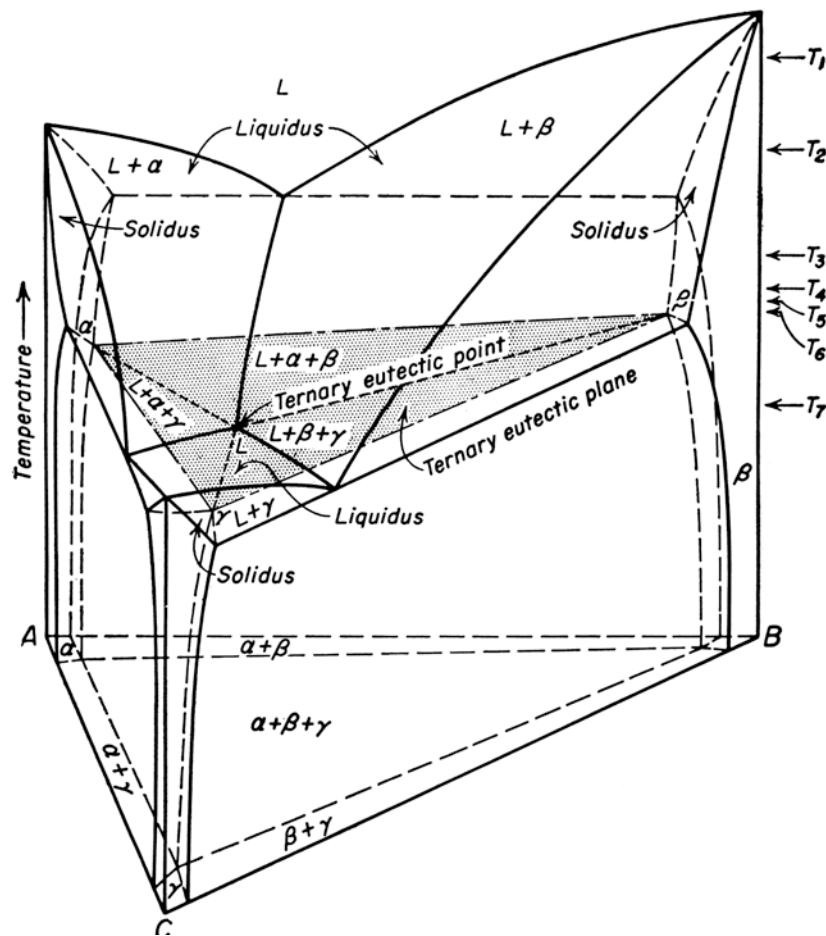
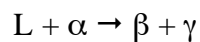


Figure 1.3 – Temperature-composition ternary phase diagram illustrating a class I four-phase equilibrium [22].

### Class II ternary four-phase equilibrium (ternary tributary reaction)

A class II four-phase equilibrium is represented by the following equation:



In this case two tie-triangles  $L + \alpha + \beta$  and  $L + \alpha + \gamma$  descend from higher temperature (Figure 1.4 (a)) and terminate on two new tie-triangles,  $\alpha + \beta + \gamma$  and  $L + \beta + \gamma$ , that descend to lower temperature. At the reaction temperature the four tie-triangles form a trapezium (Figure 1.4 (b)) where any alloy will consist of four phases at the reaction temperature (Figure 1.4 (c)). The two  $L + \alpha + \beta$  and  $L + \alpha + \gamma$  domains

join along a common tie line  $\alpha L$  to form the four phase trapezium, and upon cooling this figure divides along the tie-line  $\beta\gamma$  to form two new tie-triangles,  $\alpha + \beta + \gamma$  and  $L + \beta + \gamma$ . The intersection of  $\alpha L$  with  $\beta\gamma$  defines the invariant reaction point. A class II equilibrium is illustrated in the ternary diagram of Figure 1.5.

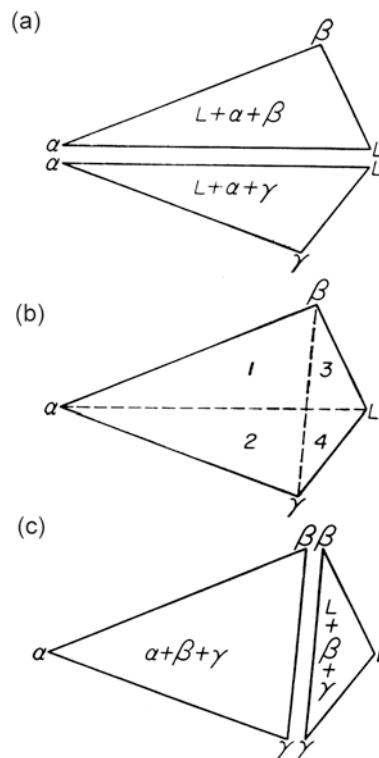


Figure 1.4 – Isothermal sections of a class II ternary reaction; (a) the two high temperature tie triangles, (b) two tie lines  $\alpha L$  and  $\beta\gamma$  divide the isothermal trapezium at the reaction temperature (c) the two low temperature tie triangles [22].

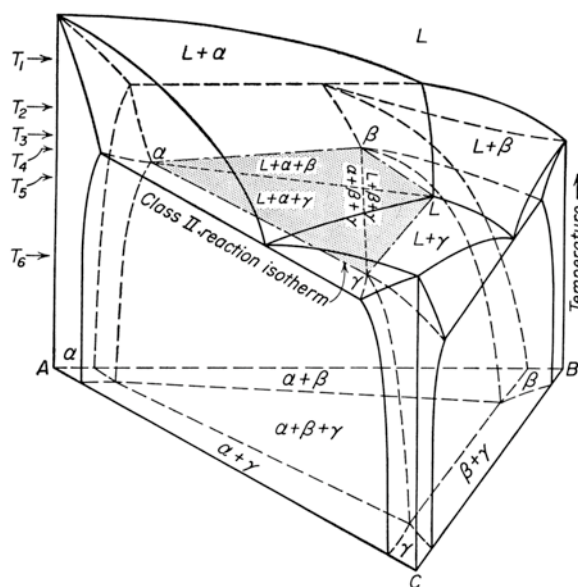
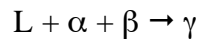


Figure 1.5 – Temperature-composition diagram illustrating a class II four-phase equilibrium [22].

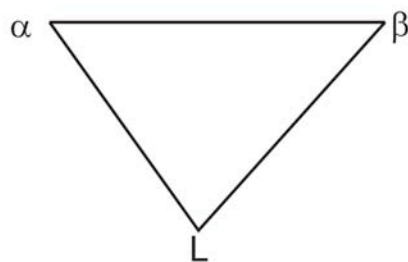
### Class III ternary four-phase equilibrium (ternary distributary reaction)

A class III four-phase equilibrium is represented by the following equation:



Here three phases interact isothermally upon cooling to form one new phase. Three phases  $\alpha$ ,  $\beta$  and L located at the corners of a tie-triangle combine to form the  $\gamma$  phase, whose composition lies within the tie-triangle and defines the invariant reaction point. Beneath the reaction temperature three tie-triangles,  $\alpha + \beta + \gamma$ ,  $L + \alpha + \gamma$ , and  $L + \beta + \gamma$ , are issued (Figure 1.6 (b)). A class III equilibrium is illustrated in the ternary diagram of Figure 1.7.

(a)



(b)

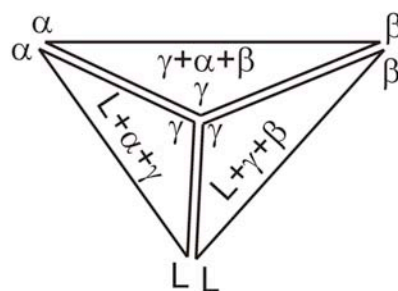


Figure 1.6 – Isothermal sections of a class III four-phase equilibrium; (a) high temperature tie-triangle and (b) three low-temperature tie-triangles.

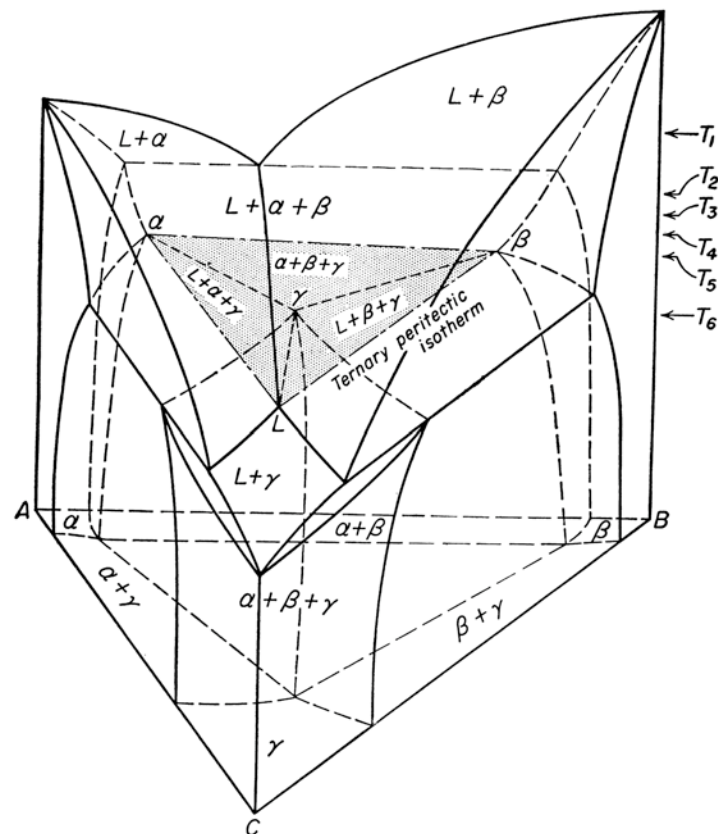


Figure 1.7 – Temperature-composition diagram of a class III four-phase equilibrium [22].

### Solidification paths

Consider the liquidus surface projection shown in Figure 1.8 which involves primary phases of pure  $\mathcal{A}$ ,  $\mathcal{B}$  and  $\mathcal{C}$  elements with limited mutual solubility. When alloy  $\mathcal{X}$  is cooled down crystals of  $\mathcal{C}$  begin to precipitate when the temperature is below the liquidus temperature. As the temperature is lowered, crystals of  $\mathcal{C}$  continue to precipitate, and the composition of the liquid moves along a straight line away from  $\mathcal{C}$ , because  $\mathcal{C}$  is precipitating and the liquid becomes impoverished in  $\mathcal{C}$  and enriched in  $\mathcal{A}$  and  $\mathcal{B}$ . At a given temperature the liquid of composition  $\mathcal{X}$  intersects the boundary line at point  $\mathcal{O}$ . Since in this case the boundary line is converging to a class I ternary reaction, it necessarily has a *cotectic* nature. Therefore, crystals of  $\mathcal{A}$  will then co-precipitate with crystals of  $\mathcal{C}$  and the liquid path will follow the *cotectic* boundary line towards point  $\mathcal{M}$ . The overall composition of the solid phases precipitated during

this interval will be a mixture of  $\mathcal{A}$  and  $\mathcal{C}$ . At point  $\mathcal{M}$ , the bulk composition of the solid phases so far precipitated through the cooling process lies at point  $\mathcal{N}$  (the extension of the straight line from  $\mathcal{M}$  through the initial composition  $\mathcal{X}$ ) [24]. The phase proportions can be determined through the lever rule:

$$\% \text{ solid} = (\text{distance } \mathcal{M}\mathcal{X} / \text{distance } \mathcal{M}\mathcal{N}) * 100$$

$$\% \text{ liquid} = (\text{distance } \mathcal{X}\mathcal{N} / \text{distance } \mathcal{M}\mathcal{N}) * 100$$

The solid consists of  $\mathcal{A}$  crystals and  $\mathcal{C}$  crystals with the following proportions:

$$\% \text{ phase } \mathcal{A} = (\text{distance } \mathcal{N}\mathcal{C} / \text{distance } \mathcal{A}\mathcal{C}) * 100$$

$$\% \text{ phase } \mathcal{C} = (\text{distance } \mathcal{A}\mathcal{N} / \text{distance } \mathcal{A}\mathcal{C}) * 100$$

The final solid must consist of  $\mathcal{A} + \mathcal{B} + \mathcal{C}$  crystals since the initial composition lies in the triangle  $\mathcal{B}\mathcal{C}\mathcal{A}$ .

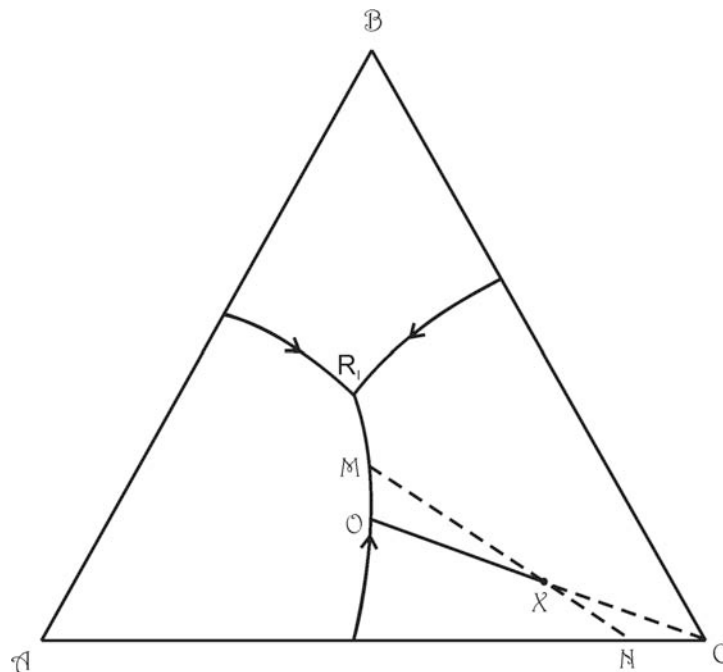


Figure 1.8 – Solidification path of composition  $\mathcal{X}$  in the  $\mathcal{B}$ - $\mathcal{C}$ - $\mathcal{A}$  ternary diagram that presents a ternary eutectic reaction ( $\mathcal{R}_1$ ).

**1.3.2 Types of magnetic behavior**

The origin of magnetism lies on the orbital motion of electrons, on the spin motion of unpaired electrons and on how the magnetic moments of individual atoms interact with one another. A material's magnetic moment is a measure of the overall tendency of the individual atomic moments to align with an external magnetic field (H). Therefore, the magnetic behavior of a material can be investigated with a magnetometer through controlled magnetization of samples. The relation between the applied magnetic field, H, the sample magnetization, M, and the magnetic induction, B, in the SI and CGS systems is:

SI	CGS
$B = \mu_0 (H + M)$	$B = H + 4\pi M$
SI units	CGS units
B – tesla (T)	B – gauss (G)
H – ampere/metro (A/m)	H – oersted (Oe)
M – ampere/metro (A/m)	M – gauss (G)
$\mu_0 = 4\pi \times 10^{-7}$ – henry/metro (H/m)	

By studying how the magnetization, M, responds to an applied magnetic field, M(H), and on how it changes with temperature, M(T), it is possible to classify the type of magnetic behavior in five categories: diamagnetism, paramagnetism, ferromagnetism, ferrimagnetism and antiferromagnetism [25]. Typical magnetization curves for each behavior type are presented in Figure 1.9.

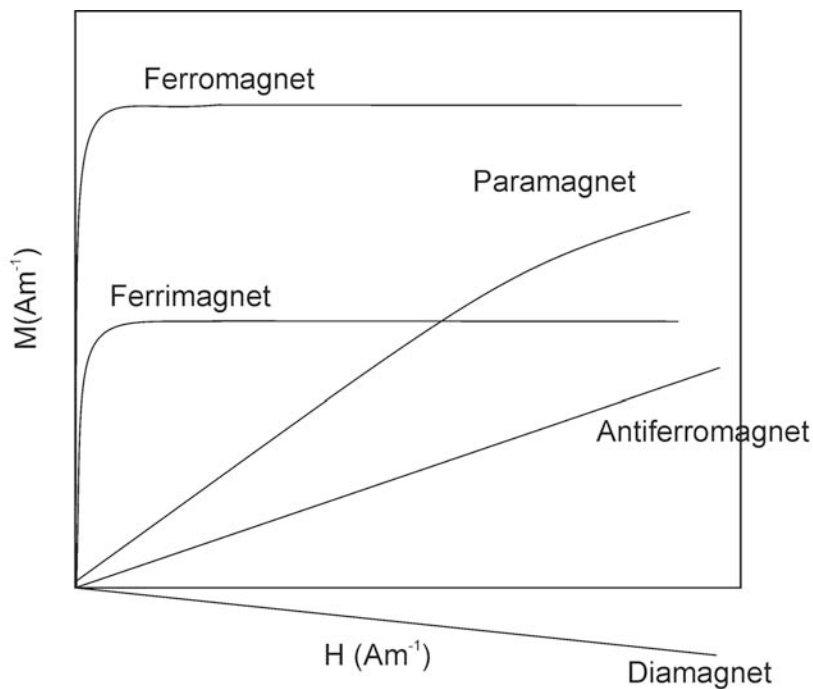


Figure 1.9 – Typical curves of  $M(H)$  for a ferromagnetic, paramagnetic, ferrimagnetic, antiferromagnetic and diamagnetic materials.

### **Diamagnetism**

The orbital motion of electrons creates minute atomic current loops, which produce magnetic fields. When an external magnetic field is applied to a material, these current loops tend to align in such a way as to oppose the magnetic applied field. This may be viewed as an atomic version of Lenz's law: induced magnetic fields tend to oppose the change which created them. All materials are inherently diamagnetic, but if the atoms have some net magnetic moment as in paramagnetic materials, or if there is long-range ordering of atomic magnetic moments, as in the other types of magnetic behavior, these stronger effects are dominant. Diamagnetism is therefore a residual effect, which is manifested when the other types magnetic behavior are absent. Materials in which this effect is the only magnetic response are called diamagnetic. When a diamagnetic material is exposed to an external magnetic applied field  $H$ , a small negative linear magnetization is produced  $M(H)$  (Figure 1.9) and thus the magnetic susceptibility ( $\chi=M/H$ ) is negative.

## Paramagnetism

In paramagnetic materials, some of the atoms have a net magnetic moment due to the spin of unpaired electrons in partially filled orbitals. In the presence of an external magnetic field there is a partial alignment of these atomic moments with the direction of the magnetic field, resulting in a positive induced magnetization (Figure 1.9) and positive susceptibility. However, the magnetization induced is diminute since the external magnetic field orients a small fraction of the spins. This fraction is proportional to the field strength, which explains the linear dependency.

In ideal paramagnetism, the atomic magnetic moments do not interact with one another and are randomly oriented in the absence of an external magnetic field due to thermal agitation, resulting in a zero net magnetic moment. This ideal behavior is termed Curie-type. However, if there is some, albeit weak, energy exchange between neighboring atomic moments they may interact and spontaneously align or anti-align, as well as react to an external magnetic field. This behavior is termed Curie-Weiss.

Curie-type paramagnetism has a particular temperature dependence and is described by the Curie law  $\chi(T) = C/T$ , where  $C$  is the Curie constant. The Curie-Weiss magnetic susceptibility is given by the Curie Weiss law  $\chi = C / (T - \theta_{CW})$ , where  $\theta_{CW}$  is the Curie-Weiss Temperature. The magnetic susceptibility is related to the exchange strength and its sign depends on whether the interaction tends to align adjacent moments in the same direction or opposite to each other. For  $\theta_{CW} > 0$  the exchange coupling between neighboring moments contributes to align them in the same direction, for  $\theta_{CW} < 0$  the interaction between moments tends to align them opposite to one another (Figure 1.10).

In a material where only the conduction electrons are contributing to the paramagnetism,  $\chi$  is low and temperature independent. This behavior is called Pauli paramagnetism. On the other hand when  $\chi$  is temperature dependent according to  $\chi \propto 1/T$ , the behavior is called Langevin paramagnetism.

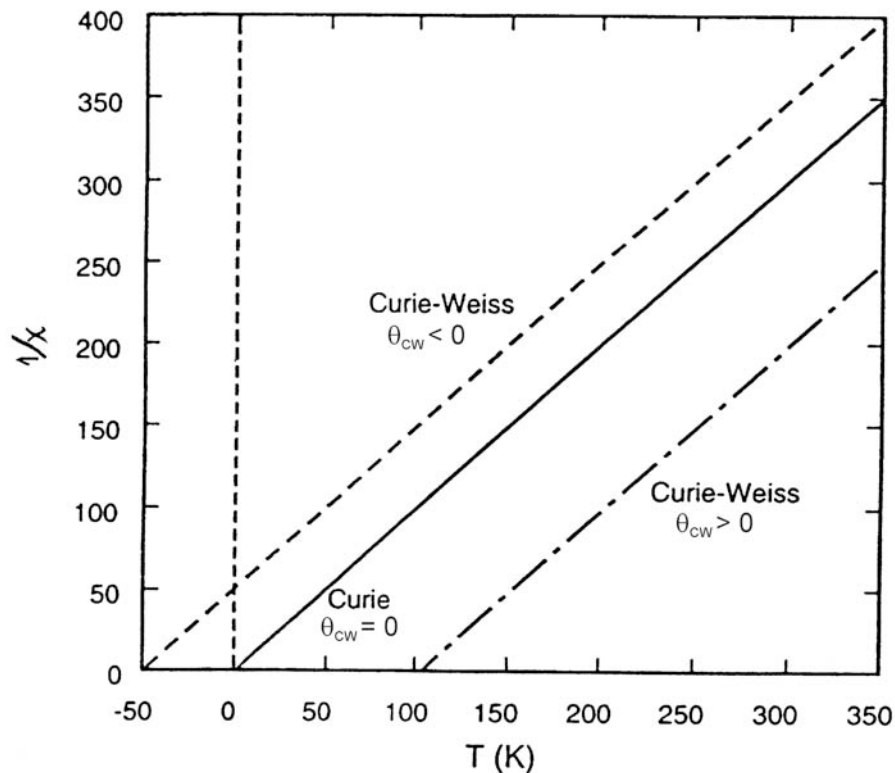


Figure 1.10 – The inverse of  $\chi$  as a function of  $T$  for systems exhibiting Curie and Curie-Weiss behavior [25].

## Ferromagnetism

In ferromagnetic materials the atoms have a net magnetic moment due to the spin of unpaired electrons in partially filled orbitals and the atomic moments have very strong magnetic interactions. These interactions are produced by electronic short-range exchange forces and induce parallel alignment of the atomic magnetic moments. The  $M(H)$  curve for a ferromagnet is not linear and the behavior is frequently irreversible, leading to hysteresis (see Figure 1.11). When  $H$  is increased the magnetization gradually reaches a maximum value known as the saturation magnetization,  $M_s$ . As  $H$  is reduced back to zero from saturation, a different curve is usually followed and  $M$  does not return to zero. The magnetization value for zero  $H$  is the remnant magnetization  $M_{rem}$ . The applied magnetic field in the opposite direction required to bring magnetization to zero is called coercive field, and is usually denoted by  $H_c$ .

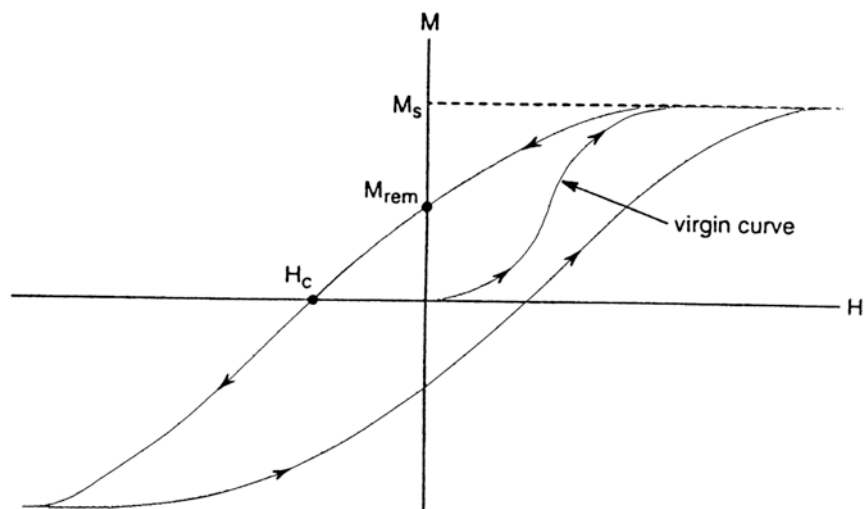


Figure 1.11 – Magnetization as a function of applied magnetic field for  $T < T_C$ , after cooling the sample from above  $T_C$ . The magnetization saturation ( $M_s$ ), the remnant magnetization ( $M_{rem}$ ) and the coercive field ( $H_c$ ) are identified [25].

Thermally demagnetized ferromagnetic materials (virgin curve, see Figure 1.11) present numerous magnetic domains, and within each domain the individual atomic moments are aligned with one another. These multi-domain configurations form closed-field loops inside the material, which result in a net magnetization close to zero under equilibrium conditions due to magnetostatic energy minimization. The regions separating magnetic domains are called domain walls, where the magnetization rotates coherently from the direction in one domain to that in the next domain. When a magnetic field is applied to such materials the atomic magnetic moments gradually align with the external magnetic field and the multi-domain structure is progressively converted into one domain (full saturated sample). The gradual moment rotation occurs first for domains where the atomic magnetic moments have a component along the applied field direction, and in the case of anisotropic materials full saturation requires the moments to turn away from their preferred crystallographic direction. Subsequently, when the applied field is reduced the atomic moments tend to rotate back to the previous directions producing a multi-domain structure. However, domain wall motion is usually blocked to some extent by wall pinning in crystalline defects, like grain boundaries or inclusions, and

magnetostatic equilibrium conditions may not be attained. As a result the material will present remanent magnetization at  $H = 0$  and a coercive field of opposite direction will be required for full demagnetization ( $M = 0$ ).

When heated above its Curie temperature, a multi-domain ferromagnetic material undergoes a phase transition, and the uniform magnetization within the domains spontaneously disappears: each atomic magnetic moment acquires its own direction, independent from its neighbors (paramagnetic state). Upon cooling from above the Curie temperature in zero magnetic field strength, a ferromagnetic material will generally show a diminute overall magnetization due to spontaneous formation of domains in near equilibrium conditions (thermally demagnetized).

Information on irreversibility due to hindered domain wall mobility, and on magnetic transitions at low fields can be obtained through zero-field cooled (ZFC) and field cooled (FC) procedures (Figure 1.12). The measurements are performed by cooling the sample to a low temperature in  $H = 0$ . A constant weak magnetic field is then applied and the magnetization is measured as a function of temperature up to the highest desired temperature, yielding the ZFC data. Subsequently the sample is cooled in the same magnetic field to the lowest temperature and the magnetization is again measured as a function of temperature, yielding the FC data. In the case presented in Figure 1.12, the ZFC curve shows a net magnetization close to zero in the absence of the applied field at the lowest temperature, indicating an originally thermally demagnetized state. As the temperature rises the atomic moments align gradually with the applied field by taking advantage of the thermal vibrations. This behavior evidences domain wall pinning, since for negligible pinning the spin rotation occurs swiftly when the weak field is applied even at low temperatures. The ensuing low magnetization observed in the ZFC curve occurs when the material assumes a paramagnetic state above the Curie temperature (around 150 K in Figure 1.12) and the atomic moments spontaneously acquire a random orientation. Subsequently, by cooling in the same field (FC), the moments rotate towards the applied field when the Curie temperature is again approached. The net magnetization attained below the Curie temperature depends on the thermal vibration sensitivity (in the case of Figure 1.12 saturation is not reached even at 0 K).

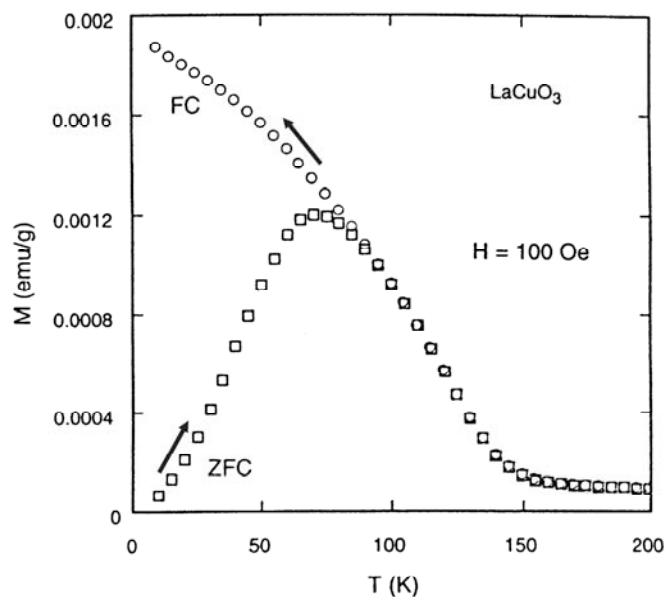


Figure 1.12 – Magnetization as a function of temperature for the  $\text{LaCuO}_3$  sample which is first cooled in  $H = 0$ , a field is then applied and data is collected on warming (ZFC) and again on cooling (FC) keeping the magnetic field [25].

### Antiferromagnetism

In anti-ferromagnetic materials adjacent atomic magnetic moments are aligned in opposite directions to each other (Figure 1.13). As the moments of neighboring atoms tend to cancel, the net magnetization is relatively small. The  $M(B)$  behavior is similar to that observed for paramagnets (see Figure 1.9); however the origin of antiferromagnetic behavior is quite different since it involves long range magnetic order. Antiferromagnets present a phase transition at a given  $T$  denominated as Néel temperature  $T_N$ . Above  $T_N$  materials are often paramagnetic, exhibiting a Curie-Weiss behavior,  $\chi = C/(T-\theta_{CW})$  with  $\theta_{CW} < 0$ .

## Ferrimagnetism

Ferrimagnets and ferromagnets have similar  $M(H)$  and  $M(T)$  behavior (Figure 1.9). However, at the atomic level ferrimagnets are more similar to antiferromagnets as adjacent magnetic moments are coupled in opposite directions. The larger of the two magnetic moments tends to align with the external magnetic field while the smaller tends to align opposite to the field direction (Figure 1.13).

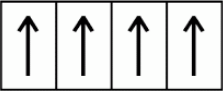
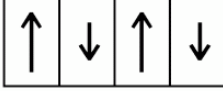
Type	Arrangement	Lattice	Resultant
true ferromagnetic (Fe, Ni, Co)	alignment within lattice		
antiferromagnetic	sublattices, A & B, aligned but antiparallel, equal		(none)
ferrimagnetic	sublattices, A & B, aligned antiparallel, unequal		

Figure 1.13 – Schematic diagrams showing how the atomic moments in a ferromagnetic, antiferromagnetic and ferrimagnetic are aligned [26].

## 1.4 State of the art

### 1.4.1 B-T-U systems: isothermal sections, compounds and phase equilibria

Limited studies on B-T-U (T = transition metal) systems have been carried out during the seventies and eighties of the XX century. This research was mainly devoted to the investigation of magnetic and other physical properties of the compounds, with only a few reports on isothermal sections [5]. It is likely that the high melting temperature of the borides associated with the low uranium diffusivity rendered difficult the synthesis of this type of materials, discouraging their study. An overview on reported ternary systems containing uranium and boron with different transition metals is presented below. For an appropriate comparison of the structures, their stability, and

magnetic behavior of the compounds, ternary systems containing transition metals belonging to the 4<sup>th</sup> period (where Fe is included) between V and Ni and belonging to the 6<sup>th</sup> group (Mo and W) have been selected since these ternary systems present compounds similar to those found in the B-Fe-U ternary system [5].

### **B-V-U ternary system**

Investigations on the B-V-U ternary system revealed the formation of UVB<sub>4</sub>, with the YCrB<sub>4</sub>-type structure [27,28]. The alloys with the compound stoichiometric composition were produced using an arc furnace under argon atmosphere, in one case the materials were subsequently annealed at 800°C during 500 h [27]; in another case powders of the elemental mixture were cold pressed and annealed at 1700°C for 1h [28]. The compounds were characterized using powder X-ray diffraction (PXRD). No phase diagram information has been published on the system and no magnetic measurements were performed for this compound.

### **B-Cr-U ternary system**

Research on the boron-rich part of the B-Cr-U system has shown the existence of the UCrB<sub>4</sub> ternary compound, with the YCrB<sub>4</sub>-type structure [29, 30, 31]. The phase relations in the isothermal section at 800°C have been determined by Valyovka et al. [29]. The alloys were prepared by arc-melting uranium pieces and compacted powder mixtures of chromium and boron under an argon atmosphere. PXRD phase analysis was used to confirm the equilibrium of UCrB<sub>4</sub> with the UB<sub>4</sub>, Cr<sub>3</sub>B<sub>4</sub> and CrB binary compounds [29]. Magnetic studies were also performed on the ternary compound, which exhibits a paramagnetic Curie-Weiss behavior between 80-300K [30].

### **B-Mn-U ternary system**

Studies on the B-Mn-U ternary system revealed the existence of the UMnB<sub>4</sub> compound with the YCrB<sub>4</sub>-type structure [5]. The compound was synthesized by arc furnace under an argon atmosphere and was annealed at 1700°C for 1h. The

characterization of the compound was carried out by PXRD and magnetic measurements performed on a polycrystalline single-phase sample prepared by annealing mixed powders of Mn and  $UB_4$  at  $900^\circ\text{C}$  for 48h followed by further annealing at  $1200^\circ\text{C}$  for 12h. The compound showed a practically temperature-independent paramagnetic behavior between 80-300 K and at 300 K the susceptibility was reported to be  $5.26 \times 10^{-6} \text{ emu.g}^{-1}$  [30].

### **B-Co-U ternary system**

Early work on the ternary B-Co-U system established the existence of four ternary compounds,  $U_2Co_{21}B_6$ , with the  $W_2Cr_{21}B_6$ -type structure [32],  $UCo_4B$ , with the  $CeCo_4B$ -type structure [33],  $UCo_3B_2$ , with the  $CeCo_3B_2$ -type structure [33] and  $UCoB_4$ , with the  $YCrB_4$ -type structure [27]. The uranium-rich corner of the isothermal section at  $800^\circ\text{C}$  and  $600^\circ\text{C}$  was later studied by Valyovka and Kuz'ma using PXRD data [34]. The alloys were prepared by arc melting uranium pieces together with compacts of powder mixtures of cobalt and boron. The melted buttons were then annealed at  $800^\circ\text{C}$  and  $600^\circ\text{C}$  for 500h. This study confirmed the presence of the previous compounds and established the existence of  $U_3Co_7B_2$ , with the  $Dy_3Ni_7B_2$ -type structure, and  $UCo_4B_4$ , with the  $CeCo_4B_4$ -type structure [34].

Magnetic susceptibility measurements were performed for  $UCoB_4$  in the 80-300 K temperature range [29]. This compound shows a paramagnetic behavior with a magnetic susceptibility at 300 K of  $3.2 \times 10^{-6} \text{ emu.g}^{-1}$ . A temperature independent enhanced Pauli paramagnetic behavior was found for the  $UCo_3B_2$  compound [35]. The magnetic susceptibility at 4K and 300K was reported to be  $3.2 \times 10^{-6} \text{ emu.g}^{-1}$  and  $2.9 \times 10^{-6} \text{ emu.g}^{-1}$ , respectively. The variations in  $\chi$  data were reported to  $UO_2$  impurities.

### **B-Ni-U ternary system**

The systematic investigation of the  $600^\circ\text{C}$  and  $800^\circ\text{C}$  isothermal sections in the U-rich corner of the B-Ni-U ternary system revealed the existence of three compounds,

UNiB<sub>4</sub> with the ErNiB<sub>4</sub>-type structure [33], U<sub>2</sub>Ni<sub>21</sub>B<sub>6</sub>, with the W<sub>2</sub>Cr<sub>21</sub>B<sub>6</sub>-type structure and UNi<sub>4</sub>B with the CeCo<sub>4</sub>B-type structure [31, 32]. The phase equilibria have been determined from PXRD of alloys prepared by arc melting uranium pieces together with compacted powder mixtures of nickel and boron, followed by annealing at 600°C and 800°C for 500h. UNi<sub>4</sub>B was first reported to crystallize with the hexagonal CeCo<sub>4</sub>B-type structure and to order antiferromagnetically below  $T_N = 20$  K [36]. Further work has been carried out on this compound due to its unique magnetic structure as described above.

### **B-Mo-U ternary system**

The boron-rich corner of the B-Mo-U ternary system was investigated for the first time by Rogl et al [27], who identified two compounds, UMoB<sub>4</sub> and U<sub>2</sub>MoB<sub>6</sub>. In order to complete the phase equilibria in the isothermal section at 1000°C Valyovka and Kuz'ma investigated further the system and found two new compounds, UMo<sub>2</sub>B<sub>6</sub> [37] and UMo<sub>4</sub>B<sub>4</sub> [33], and established the structures of U<sub>2</sub>MoB<sub>6</sub> and UMoB<sub>4</sub> as being, respectively, of Y<sub>2</sub>ReB<sub>6</sub>-type and YCrB<sub>4</sub>-type. The phase equilibria in the B-Mo-U ternary system have been determined by PXRD analysis of 48 alloys prepared by arc melting solid pieces of uranium together with compacted powder mixtures of molybdenum and boron. The material was then annealed at 1000°C for 500 h. The U<sub>2</sub>MoB<sub>6</sub> compound was not found in pure due to UB<sub>2</sub> contamination, which may indicate that U<sub>2</sub>MoB<sub>6</sub> forms by a peritectic-like reaction between the liquid and UB<sub>2</sub>. Recently a new compound, U<sub>5</sub>Mo<sub>10</sub>B<sub>24</sub>, has been found in the system [38]. Single crystals were extracted from material prepared by arc-melting the pure elements and the structure was determined from X-ray data as belonging to the *Pmmn* space group.

### **B-W-U ternary system**

Investigations on the B-W-U ternary system were carried out by Valyovka and Kuz'ma [33] and Rogl et al [27]. The phase equilibria at 1000°C have been established by Valkyovka et al. [39] by means of PXRD analysis. For this study 34 ternary alloys were prepared by arc-melting pieces of uranium with compacted mixtures of tungsten and boron powders, followed by annealing at 1000°C for 500 h.

Employing similar techniques, i.e. arc-melting and annealing in high vacuum at 1400 to 1700°C for 1 to 36h, the formation of two compounds,  $UWB_4$  and  $U_2WB_6$ , was established [27].  $UWB_4$  was found to crystallize with the orthorhombic  $ThMoB_4$ -type structure and  $U_2WB_6$  with the  $Y_2ReB_6$ -type structure. A common feature to these two compounds is the presence of planar networks of boron atoms. The  $Y_2ReB_6$  structure, which is characterized by a planar network composed of seven, six, and five-member rings, occupies an intermediate position between the  $YCrB_4$  and  $AlB_2$  structures [36]. The U-W-B ternary system is the first in which the  $ThMoB_4$ - $Y_2ReB_6$ - $AlB_2$  morphotropic transition of structure types has been observed; the transition is possible due to the fact that in the  $ThMoB_4$  structure the boron atoms are joined together in a network consisting of five- and seven-member rings (as in the case of  $YCrB_4$ ).

#### **1.4.2 Ternary boron-metal-*f*-element systems: liquidus projections**

Reports on the experimental determination of liquidus projections of ternary boride systems are limited and usually pertain to systems based essentially on transition metals, such as B-Ti-Ni [40] and B-Sn-Ti [41]. Regarding ternary *f*-elements boride systems, only the liquidus projections of B-Fe-R systems (R= Pr and Nd) have been reported [42, 43]:

- In the B-Fe-Pr case the samples were prepared in an arc furnace under an argon atmosphere by melting iron powder, praseodymium pieces and boron pieces. The samples were subsequently annealed at 873 K or 1273 K for 30 days. Microstructural observations were carried out by scanning electron microscopy (SEM) complemented by energy-dispersive spectroscopy (EDS). Powder X-ray diffraction (PXRD), magnetic measurements and differential thermal analysis (DTA) were also used to characterize the materials produced. The Pr-Fe-B phase diagram in the low boron region was presented and discussed in terms of four vertical sections, a liquidus projection and a Scheil diagram. Three ternary reactions and two maximum temperatures were found in the region [42].

- As for the B-Fe-Nd ternary system the alloys were prepared in an induction furnace from neodymium, boron and iron pieces [43]. The materials were melted together under an argon atmosphere, and each molten button was heated to a temperature 100 °C above the respective liquidus temperature and directly casted in an iron mold. In order to identify the phases present in the as-cast specimens and their phase equilibria relations, a metallographical investigation was carried out using optical microscopy, SEM, PXRD, wavelength dispersive spectroscopy (WDS) and DTA. The phase diagram has been investigated in the Nd-poor region where three phases coexist with the liquid:  $\alpha$ -Fe,  $\text{Fe}_2\text{B}$  and  $\text{Nd}_2\text{Fe}_7\text{B}_6$ . Two liquidus surface boundary lines  $\text{L} \rightarrow \text{Fe} + \text{Fe}_2\text{B}$  and  $\text{L} \rightarrow \text{Fe}_2\text{B} + \text{Nd}_2\text{Fe}_7\text{B}_6$  join and form the ternary reaction:  $\text{L} + \text{Fe}_2\text{B} \rightarrow \alpha\text{-Fe} + \text{Nd}_2\text{Fe}_7\text{B}_6$ . Furthermore, a ternary eutectic reaction,  $\text{L} \rightarrow \text{Fe} + \text{Nd}_2\text{Fe}_{14}\text{B} + \text{Nd}_2\text{Fe}_7\text{B}_6$  was also established and both  $\text{Nd}_2\text{Fe}_7\text{B}_6$  and  $\text{Nd}_2\text{FeB}_3$  have been identified as congruent compounds.

In spite of the limited experimental reports, the increasing importance of metallic fuel for nuclear plants triggered the theoretical calculation of ternary phase diagrams based on compound thermodynamic properties [44]. A dual effort was undertaken in this approach:

- Thermodynamic phase diagram calculations, including solidus and liquidus surfaces, have been carried out using the Calphad and Thermocalc software packages, for example, for the C–Pu–U [45], Zr–Pu–U [46] and Zr–Fe–U [47] ternary systems. This allows for a thermodynamic description of ternary systems through extrapolation of binary diagrams and can be used as guidance for experimental work.
- A detailed experimental knowledge of the thermodynamic properties of all phases involved in the ternary diagrams is required for the phase diagram calculations. This type experimental assessment is being extensively carried out for several decades [48, 49]. However, the advances are relatively slow as this is only possible when single-phase, or preferably single-crystal, samples can be produced. Experimental determination of solidus and liquidus

temperatures for selected alloys have also been carried out to validate the ternary diagram calculations [48].

### **1.4.3 Magnetic properties of actinide compounds**

The central feature of the actinides group is the progressive filling of the  $5f$  orbital, which results in an increasing orbital localization from light to heavy actinides and induces two distinct types of magnetic behavior [50]:

- The magnetic behavior of light actinides (between Th to Pu) is similar to the  $d$  elements one. In this case the energy levels of  $5f$  orbitals are closer to the  $6d$  and  $7s$  ones [51, 52] and hybridization phenomena of type  $d-f$  and  $s-f$  can occur with the participation of  $5f$  electrons in chemical bonds. Moreover the large radial extension of  $5f$  orbitals causes an overlap between the wave functions forming a conduction band with an itinerant behavior [53].
- For heavy actinides (between Am to Cf) a localized behavior, similar to the one of rare earths, is observed. The decrease of the  $5f$  orbitals energy together with his contraction decreases the probability of hybridization.

A relation between the delocalization of the  $5f$  states and the interatomic distances of the actinide atoms was first proposed by Hill, who pointed out that uranium, neptunium and plutonium could be divided into magnetic ordered and paramagnetic subgroups, depending on the interactinide distance  $d_{An-An}$ , the critical value being about 0.34 nm for uranium [54]. Below this value the compound is paramagnetic due to the direct  $5f-5f$  overlapping between neighboring atoms (itinerant state). Above this value a magnetic ordered state exists, which is a result of higher localized  $5f$  states (localized state).

The behavior of  $f$  electrons, between itinerant and localized, has been discussed under two frameworks: the Stoner theory (itinerant magnetism) and the Mott-Hubbard theory (localized magnetism) [50]:

- In the Stoner theory, magnetic ordering is possible in a band scheme when spin polarization becomes energetically favorable. For a ferromagnetism case, the condition for ordering is:  $I \times n(E_F) > 1$ . Where  $I$ , called the Stoner parameter, is related with the exchange interaction between the electrons with opposite spins in the band, and  $n(E_F)$  is the electronic density of states at the Fermi energy level.
- The Mott and Hubbard theory considers the following criterion for magnetic ordering:

$$W < U_{eff}$$

Where  $W$  is the  $5f$  bandwidth and  $U_{eff}$  the effective intra-atomic Coulomb correlation. If the bandwidth decreases below a critical value, then a sudden transition takes place (Mott transition), driving the system from a paramagnetic state into a magnetic ordered one.

A typical behavior of compounds with high U-content is a weak temperature independent magnetic susceptibility (Pauli paramagnetism). This fact indicates a low density of states at  $E_F$  in which the uranium atoms are close together and their  $5f$ - $5f$  wave function overlaps considerably [55].

For uranium compounds with  $d$ -elements, the hybridization tends to decrease along the transition metals each period. For  $d$ -elements at the beginning of the period  $5f$ - $d$  hybridization occurs and the compounds have a paramagnetic behavior. The transition metals at the end of the period present much higher electronegativity than U. In this case the transition element  $d$ -orbital is pushed to higher energies decreasing thus the  $5f$ - $d$  overlap. This leads to weaker  $5f$ - $d$  hybridization and a consequent tendency for to  $5f$  localization, which is manifested as magnetic ordering [55].

Wave function studies show that for uranium compounds with  $p$ -elements (including boron), the size of the ligand determines the strength of the  $5f$ - $p$  hybridization, which should be less significant for larger  $p$  ligands within the same group of the periodic table [55]. In the uranium compounds, the  $5f$ - $p$  hybridization between uranium and boron atoms depends on the crystallographic structure. Boron is a diamagnetic

element as does not contribute for atomic magnetic moments of the materials. Although its presence changes the crystallographic structure and influences the magnetic properties. For uranium compounds with low B-content, boron acts as an interstitial atom, whereas in uranium compounds with high B-content the boron atoms form a three-dimensional network.

In summary the magnetic behavior of the actinides is diverse, ranging from Pauli paramagnetism to complex magnetic structures, as non-collinear and incommensurate. This type of behavior (complex magnetic structures) is originated from competition between the interactions of two or more magnetic sublattices with different intrinsic magnetic exchange types.

### **1.5 References:**

- [1] F. H. Spedding, “Handbook on the Physics and Chemistry of Rare Earths”, Vol. 1 (eds. K. A. Gschneidner Jr, L. Eyring,), North-Holland, (1996).
- [2] J. P. Desclaux and A.J. Freeman, “Handbook on the Physics and Chemistry of The Actinides”, Vol. 1 (eds. A.J. Freedman and G.L. Lander), North-Holland (1984).
- [3] Phase Diagrams, “Metals Handbook”, Vol.3, 7th edition, New-York, ASM.
- [4] W. Suski, “Handbook on the Physics and Chemistry of Rare Earths”, Vol. 22 (eds. K. A. Gschneidner Jr, L. Eyring), North-Holland (1996).
- [5] P. Rogl, “Handbook on the Physics and Chemistry of the Actinides”, (eds. A.J. Freeman and C. Keller), North-Holland, Amsterdam (1991) 75-154.
- [6] YuB. Kuzma, N. F. Chaban, “Binary and ternary systems containing boron” Handbook, (eds. Metallurgy), Moscow (1990) (in Russian) 317.
- [7] J. L. Genicon, A. Sulpice, R. Tournier, B. Chevalier, J. Etourneau, *Journal of Physique-Lettres*, 44 (1983) L725-L732.
- [8] Y. Kitaoka, Y. Kishimoto, K. Asayama, T. Kohara, K. Takeda, R. Vijayaraghavan, S. K. Malik, S. K. Dhar, D. Rambabu, *Journal of Magnetic Materials*, 52 (1985) 449-451.
- [9] Y. C. Yang, X. D. Zhang, S. L. Ge, Q. Pan, Y. F. Ding, *Proceeding of the Six International Symposium on Magnetic Anisotropy and Coercivity in Rare-Earth-Transition-Metal Alloys*, Carnegie Mellon University Press: Pittsburgh, (1990) 191.
- [10] B. Johansson, H. L. Skiver, *Journal of Magnetic Materials*, 29 (1982) 217.
- [11] SS. Saxena, P. Agarwal, K. Ahilan, F. M. Groshe, R. K. W. Haselwimmer, M. J. Steiner, et al. *Nature*, (2000) 406-587.
- [12] A. Baran, W.Suski, T. Mydlarz , *Journal of the Less Common Metals*, 96 (1984) 269-273.
- [13] A. Menovsky, F. R. de Boer, P.H. Frings, J. J. M. Franse, in: “High Field Magnetism”, (ed. M. Date) North- Holland, Amsterdam, (1983) 189.
- [14] Y. Onuki, I. Ukon, S. W. Yun, I. Umehara, K. Satoh, T. Fukuhara, H. Sato, S. Takayanagi, M. Shikama and A. Ochiai, *Journal of Physics Society, Japan*, 61 (1992) 293.

- [15] J. A. Paixão, B. Lebech, A. P. Gonçalves, P. J. Brown, G. H. Lander, P. Burlet, A. Delapalme and J. C. Spirlet, *Physical Review B*, 55 (1997) 14370-14377.
- [16] Z. Zolnierok, D. Kaczorowski, *Journal of Magnetic Materials*, 63- 4 (1987) 178.
- [17] S. A. M. Mentink, A. Drost, G. J. Nieuwenhuys, E. Frikkee. A. A. Menovsky, J.A. Mydosh, *Physics Review Letters*, 73 (1994) 1031.
- [18] J. W. Nellis, A. R. Harvey, M. B. Brodsky, “AIP Conf. Proc. no. 10, Magnetism and Magnetic Materials” (Eds. C. D. Graham and J. J. Rhyne) (1972) 1076.
- [19] S. A. M. Mentink, H. Nakotte, A. de Visser, A. A. Menovsky, G. J. Nieuwenhuys, J. A. Mydosh, *Physica B*, 186-188 (1993) 270.
- [20] Y. Haga, A. Oyamada, T. D. Matsuda, S. Ikeda, Y. Ounki, *Physica B*, 403 (2008) 900.
- [21] J. W. Gibbs, “The Collected Works of J. Willard Gibbs”, Vol. I, (eds Longmans, Green and Co.), New York, (1928) 54.
- [22] F. N. Rhines, “Phase Diagrams in Metallurgy Their Development and Application” McGraw-Hill, USA, (1956) 159.
- [23] A. Prince, “Alloy phase equilibria”, Elsevier Pub.Co., Amsterdam, New York, (1966).
- [24] <http://www.tulane.edu/~sanelson/geol212/ternaryphdiag.htm>
- [25] M. McElfresh, “Fundamentals of Magnetism and Magnetic Materials and Magnetic Materials Featuring Quantum Designs, Magnetic Property Measurement system” – Quantum Design, (1994).
- [26] [http://gravmag.ou.edu/mag\\_rock/mag\\_rock.html](http://gravmag.ou.edu/mag_rock/mag_rock.html)
- [27] P. Rogl and H. Nowotny, *Monatshefte für Chemie*, 106 (1975) 381.
- [28] I. P. Valyovka, and Yu. B. Kuz’ma, *Dopovidi Akademii Nauk Ukrainskoi SSR*, Ser, A (7) (1975) 652.
- [29] R. Sobczak and P. Rogl, *Journal of Solid State Chemistry*, 27 (1979) 343-348.
- [30] I. P. Valyovka, and Yu. B. Kuz’ma, *Poroskov, Metallurgiya*, 5 (1984) 98-100.
- [31] E. Ganglberger, H. Nowotny and F. Benesovsky, *Monatshefte für Chemie*, 96 (1965) 1144.
- [32] Yu. B. Kuz’ma, Yu. V. Vorosshilov and E. E. Cherkashin, *Inorganic Materials (Izv. Akad. Nauk. SSSR)*, 1 (1965) 1017.

- [33] I. P. Valyovka, and Yu. B. Kuz'ma, *Dopovidi Akademii Nauk Ukrainskoi SSR, Ser. A* (11), (1974) 1029.
- [34] I. P. Valyovka, and Yu. B. Kuz'ma, *Inorganic Materials (Izv. Akad. Nauk. SSSR)* 14 (3) (1978) 469.
- [35] K. N. Yang, M. S. Torikachvili, M. B. Maple and H. C. Ku, *Journal of Applied Physics*, 57, 1 (1985) 3140.
- [36] S. A. M. Mentink, H. Nakotte, A. de Visser, A. A. Menovsky, G. J. Nieuwenhuys, J. A. Mydosh, *Physica B*, 186-188 (1993) 270.
- [37] I. P. Valyovka, and Yu. B. Kuz'ma, *Russian Powder Metalurgy and Metal Ceramics*, 288, (12) (1986) 986.
- [38] T. Konrad, W. Jeitschko, *Journal of Alloys and Compounds*, 233, 1-2 (1996), L3.
- [39] I. P. Valyovka and Yu. B. Kuz'ma, *Russian Powder Metalurgy and Powder Ceramics*, 224, 8 (1981) 71.
- [40] J. A. Ajaó, *Journal of Alloys and Compounds*, 493,1-2 (2010) 314.
- [41] A. A. Bondar, T. Ya. Velikanova, D. B. Borysov, L. V. Artyukh, O. O. Bilous, M. P. Burka, O. S. Fomichov, N. I. Tsyganenko and S. O. Firstov, *Journal of Alloys and Compounds*, 400, 1-2 (2005) 202.
- [42] A. C. Neiva, A. P. Tschiptschin and F. P. Missell, *Journal of Alloys and Compounds*, 217, 2 (1995) 273.
- [43] Y. Matsuura, S. Hirose, H. Yamamoto, S. Fujimura; M. Sagawa *Japanese Journal of Applied Physics, Part 2 (ISSN 0021-4922)*, 24 (1985) L635.
- [44] <http://www.lib.utexas.edu/chem/info/thermo.html>
- [45] E. Fischer, *Calphad*, 33, 3 (2009) 487.
- [46] L. Leibowitz, E. Veleckis, R.A. Blomquist, A.D. Pelton, *Journal of Nuclear Materials*, 154, 1 (1988) 145.
- [47] A.D. Pelton, P.K. Talley, L. Leibowitz, R.A. Blomquist, *Journal of Nuclear Materials*, 210, 3 (1994) 324.
- [48] P.J. Spencer, "Computer Coupling of phase Diagrams and Thermochemistry", 32, 1 (2008) 1.
- [49] <http://www.thermocalc.com>
- [50] J-M. Fournier, T. Robert, "Handook of the Physics and Chemistry of the Actinides", Elsevier, Chapter 2 (1985) 31.

[51] J.P. Desclaux, A. J. Freeman in “Handook of the Physics and Chemistry of the Actinides”, (eds A.J. Freeman and G.H. Lander), Vol.1, North Holland, Chapter 1 (1984) 31.

[52] A. J. Freeman and D.D Koelling in “ The Actinides: Electronic Structure and Related Properties”, (eds A. J. Freeman and J. B. Darby), Vol.1, Chapter 2, Academic Press, (1974).

[53] V. Sechovsky, L. Havela, in “Ferromagnetic Materials”- A Handbook on the Properties of Magnetically Ordered Substances” (eds. E .P. Wohlfarth and and K. H. J. Buschow) Vol IV, Chapter IV (North-Holland Publ.Co., Amsterdam) (1988) 309.

[54] H. H. Hill, “Plutonium and Other Actinides 1970”, (eds. W. N. Miner, AIME New York), (1970) 2.

[55] V. Sechovsky, L. Havela, *Physica Scripta*, T45 (1992) 99.

---

## **Chapter 2**

---



## **Chapter 2 – Working principles and methods**

This chapter presents a brief description of the techniques and methods used. The working principles, as well as practical aspects, parameter values and operative details that have been essential to accomplish the experimental and theoretical work will be discussed.

### **2.1 X-ray diffraction**

X-ray diffraction has been used in two research lines (i) fingerprint identification of crystalline phases present in the materials studied and (ii) determination and refining of crystalline structures.

#### **Geometry of diffraction**

In 1912 Von Laue discovered that crystals act as diffraction gratings, i.e. a crystal may be considered to be built up of scattering centres arranged in rows. Constructive interference of waves scattered from adjacent atoms (Figure 2.1(a)) requires the path difference  $(AB - CD)$  to equal a whole number of wavelengths, i.e:

$$(AB - CD) = (\cos \alpha_n - \cos \alpha_0).a = h \lambda$$

where  $\alpha_n$  and  $\alpha_0$  are the angles between, respectively, the diffracted and incident beams and the  $x$ -axis,  $a$  is the interatomic distance in the row and  $h$  is an integer. This is known as the first Laue equation that may be expressed in vector notation: let  $\mathbf{S}$  and  $\mathbf{S}_0$  be unit vectors along, respectively, the directions of the diffracted and incident beams, and let  $\mathbf{a}$  be the translation vector from one lattice site to the next (Figure 2.1 (b)), the path difference  $(\cos \alpha_n - \cos \alpha_0).a$  is therefore  $(\mathbf{S} - \mathbf{S}_0).\mathbf{a}$  and the first Laue equation may be written as:

$$(\mathbf{S} - \mathbf{S}_0).\mathbf{a} = h \lambda$$

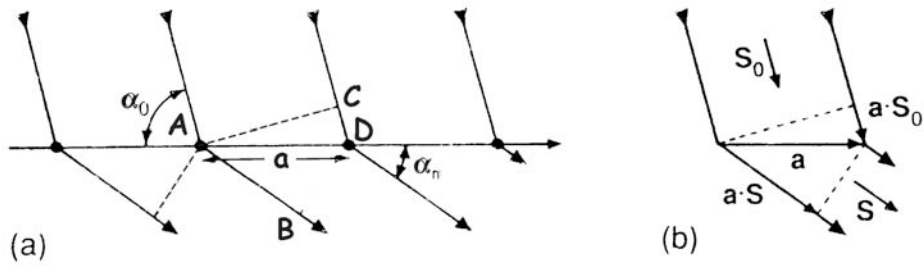


Figure 2.1 – (a) Diffraction from a lattice row along the  $x$ -axis. The incident and diffracted beams are at  $\alpha_0$  and  $\alpha_n$  to the row. The path difference between the diffracted beams is  $AB - CD$ . (b) The incident and diffracted beam directions and the path difference between the diffracted beams expressed in vector notation [1].

Figure 2.1 shows the diffracted beam at angle  $\alpha_n$  below the atom row, yet the same path difference is obtained if the diffracted beam lies in the plane of the paper at angle  $\alpha_n$  above the atom row or indeed out of the plane of the paper. Hence all diffracted beams with the same path difference occur at the same angle to the row, i.e. the diffracted beams of the same order all lie on the surface of a cone - called Laue cone - centred on the atom row with semi-apex angle  $\alpha_n$ . This situation is illustrated in Figure 2.2 which shows three Laue cones with semi-apex angle  $\alpha_0$  (zero order,  $h = 0$ ), semi-apex angle  $\alpha_1$  (first order,  $h = 1$ ) and semi-apex angle  $\alpha_2$  (second order,  $h = 2$ ) [1].

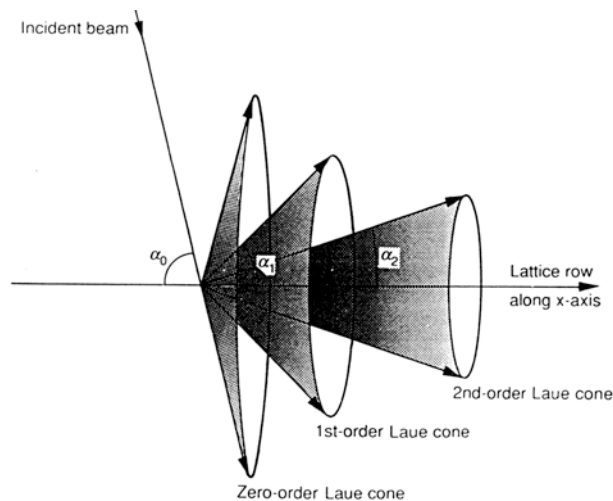


Figure 2.2 – Three Laue cones representing the directions of the diffracted beams from a lattice row along the  $x$ -axis with  $0\lambda$  ( $h = 0$ ),  $1\lambda$  ( $h = 1$ ) and  $2\lambda$  ( $h = 2$ ) path differences [1].

The analysis can be repeated for the atom rows along the y and z-axes, yielding, respectively, the second and third Laue equations:

$$(\cos \beta_n - \cos \beta_0) \cdot b = (\mathbf{S} - \mathbf{S}_0) \cdot \mathbf{b} = k \lambda$$

$$(\cos \gamma_n - \cos \gamma_0) \cdot c = (\mathbf{S} - \mathbf{S}_0) \cdot \mathbf{c} = l \lambda$$

where the angles  $\beta_n$ ,  $\beta_0$ ,  $\gamma_n$  and  $\gamma_0$ , the interatomic distances  $b$  and  $c$ , and the integers  $k$  and  $l$  are defined in the same way as for  $\alpha_n$ ,  $\alpha_0$ ,  $a$  and  $h$ . Considering a diffraction vector defined as  $\mathbf{K} = (\mathbf{S} - \mathbf{S}_0) / \lambda$ , diffraction occurs when simultaneously:

$$\mathbf{K} \cdot \mathbf{a} = h$$

$$\mathbf{K} \cdot \mathbf{b} = k$$

$$\mathbf{K} \cdot \mathbf{c} = l$$

The solution to these equations is:

$$\mathbf{K} = h \cdot \mathbf{a}^* + k \cdot \mathbf{b}^* + l \cdot \mathbf{c}^*$$

where  $h$ ,  $k$  and  $l$  are the Miller indices of an  $(h k l)$  plane in real space and  $\mathbf{a}^*$ ,  $\mathbf{b}^*$  and  $\mathbf{c}^*$  are a new set of vectors which are related to  $\mathbf{a}$ ,  $\mathbf{b}$  and  $\mathbf{c}$  according to:

$$\mathbf{a}^* \cdot \mathbf{a} = 1 \quad \mathbf{a}^* \cdot \mathbf{b} = 0 \quad \mathbf{a}^* \cdot \mathbf{c} = 0$$

$$\mathbf{b}^* \cdot \mathbf{a} = 0 \quad \mathbf{b}^* \cdot \mathbf{b} = 1 \quad \mathbf{b}^* \cdot \mathbf{c} = 0$$

$$\mathbf{c}^* \cdot \mathbf{a} = 0 \quad \mathbf{c}^* \cdot \mathbf{b} = 0 \quad \mathbf{c}^* \cdot \mathbf{c} = 1$$

Constructive interference occurs then when  $\mathbf{K} = \mathbf{g}$ , which defines a point in the reciprocal lattice.

Bragg simplified Von Laue's mathematical description of X-ray interference by envisaging diffraction in terms of reflections from crystal planes (Figure 2.3) and considering that for constructive interference the path difference between waves,  $2d_{hkl} \sin \theta$ , must equal a whole number of wavelengths:

$$n \lambda = 2d_{hkl} \sin \theta$$

Bragg's law provides then the condition for a plane wave to be diffracted by a family of lattice planes where  $n$  is an integer designated as order of diffraction,  $\lambda$  is the wavelength of incident wave,  $d_{hkl}$  is the spacing between the planes in the atomic lattice, and  $\theta$  is the angle between the incident ray and the scattering planes.

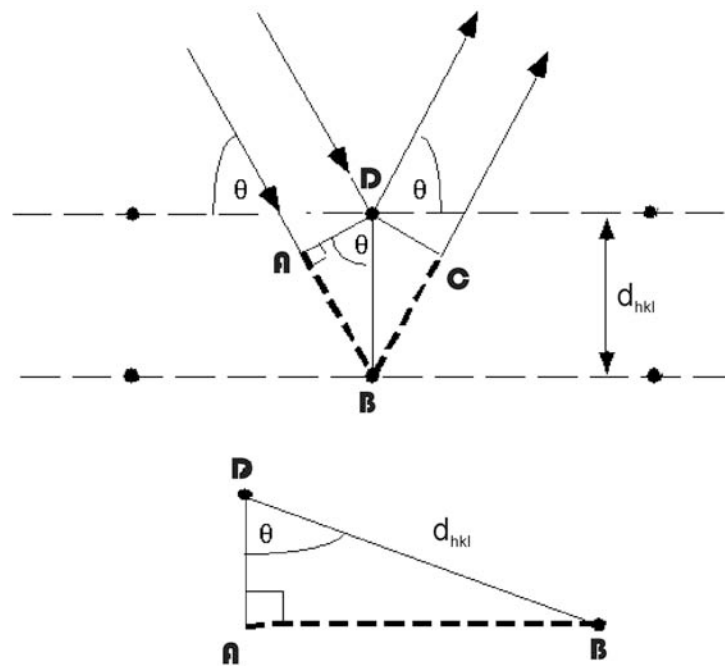


Figure 2.3 – The condition for reflection in Bragg's law.

A graphic method of solving Bragg's equation was proposed by Ewald: the crystal is placed at the center of a reflection sphere with a radius of  $1/\lambda$  (Figure 2.4), the origin of the reciprocal lattice is situated at  $O$ , the incident wave vector  $S_0$  is  $C_rO$ , the diffracted wave vector  $S$  is  $C_rP$  and the angle between them is  $2\theta$ .

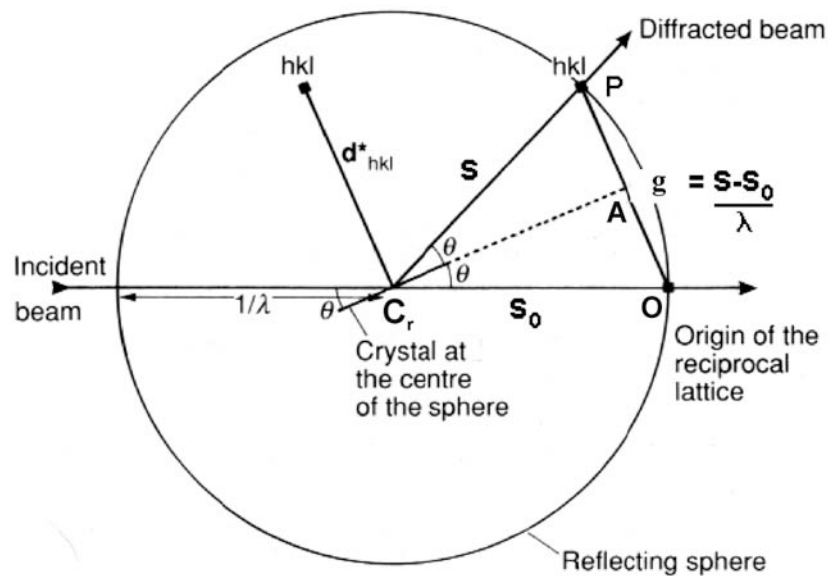


Figure 2.4 – Ewald's sphere construction for a set of planes at a Bragg angle [2].

$\mathbf{OP}$  is a reciprocal lattice  $\mathbf{g}$  and has thus magnitude  $1/d_{hkl}$ . Since the incident and diffracted wave vectors have magnitude  $1/\lambda$ , the condition  $\mathbf{OP} = \mathbf{g}$  corresponds to  $2\sin\theta/\lambda = 1/d_{hkl}$ , which is equivalent to Bragg's law for a first order diffraction ( $n=1$ ). This means that the diffracted wave vector  $\mathbf{S}$ , will satisfy the diffraction condition if  $\mathbf{OP} = \mathbf{C}_r\mathbf{P} - \mathbf{C}_r\mathbf{O} = (\mathbf{S} - \mathbf{S}_0)/\lambda$  is a reciprocal lattice vector  $\mathbf{g}$ , i.e., if:

$$\mathbf{g} = (\mathbf{S} - \mathbf{S}_0) / \lambda = \mathbf{K}$$

which is equivalent to Laue's equations.

### Intensity of diffraction

Thompson showed that the scattered intensity from an electron is given by [3]:

$$I = \frac{I_0 e^4}{m_e^2 r^2 c^4} \frac{1 + \cos^2(2\theta)}{2}$$

where  $I_0$  is the intensity of incident beam,  $e$  is the charge of the electron,  $m_e$  is the mass of the electron,  $c$  is the speed of the light,  $r$  is the distance from the scattering electron to the detector and  $\theta$  is the angle of scattering. In coherent scattering, an incident electromagnetic wave interacts with the many electrons of an atom and, in turn, the induced vibration scatters the wave. Figure 2.5 shows the  $X$  and  $X'$  waves being coherently scattered by electrons A and B. At an angle of  $0^\circ$  the scattered waves  $Y$  and  $Y'$  are exactly in phase, however at any non-zero angle the waves show destructive interference, for example,  $Z'$  travels CB-AD farther than  $Z$  [3].

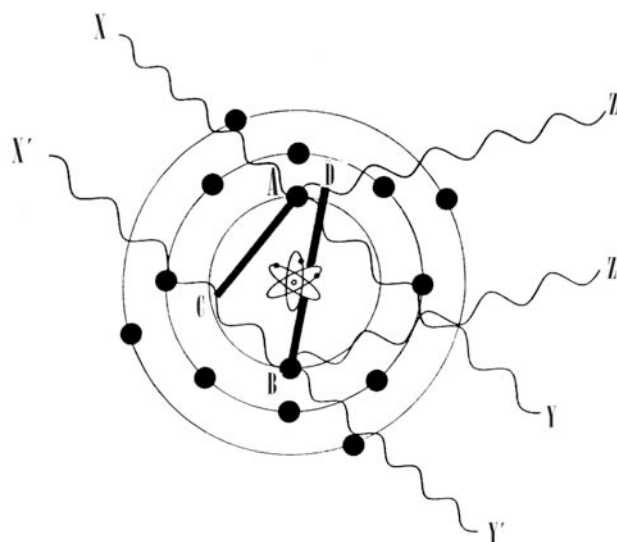


Figure 2.5 – The scattering of X-rays from an atom [3].

Since the atomic dimensions are of the same order of magnitude as X-ray wavelengths, this path difference causes partial destructive interference and lowers the resultant amplitude for increasing scattering angles. The phenomenon is described by the atomic scattering factor, which can be defined by a parametric function proposed by Cromer and Mann [4]:

$$f_0 = \sum_{i=1}^4 a_i e^{-b_i(\sin\theta/\lambda)^2} + c$$

The  $a_i$ ,  $b_i$  and  $c$  parameters together with the calculated atomic scattering factor for each element of the periodic table as a function of  $\sin\theta/\lambda$  are given in the International Tables for Crystallography.

Scattering by an atom is influenced by two additional phenomena:

- In coherent scattering, the electron acts as an oscillator under the stimulation of the incident radiation. However, when the frequency is high enough to cause the electron to oscillate away from the nucleus, ionization occurs. Since there is then a finite quantum probability that the electron could exist in these states, there will be a slight delay as it oscillates back toward the nucleus. This *anomalous scattering* will induce a phase shift in the scattered wave. The

effective scattering from an atom involves hence an additional real part ( $\Delta f'$ ) and an imaginary term ( $\Delta f''$ ):

$$|f|^2 = (f_0 + \Delta f')^2 + (\Delta f'')^2$$

- The second phenomenon, *thermal motion*, has been treated by Debye (1913), and later by Waller (1928), by introducing a temperature factor in the atomic scattering factor:

$$f = f_0 \exp\left(-\frac{B \sin^2 \theta}{\lambda^2}\right)$$

where  $B = 8\pi^2 u^2$  is the Debye-Waller factor, directly related to  $u^2$ , the mean-square vibration amplitude of the atom which depends on  $kT$ , the thermal energy available.

Due to periodicity X-ray scattering by a crystal can be analyzed by considering a single unit cell. The scattering amplitude from each atom is given by  $f$  with the phase of the scattered wave depending on the atom location in the cell. In order to sum the contributions from all atoms in the cell, each scattered wave is represented by a complex vector:

$$f \exp(i\phi) = f \cos(\phi) + f i \sin(\phi)$$

where  $\phi$  is the phase angle of the scattered wave, with the component arising from the  $j$  atom being given by:

$$\phi_j = 2\pi(hx_j + ky_j + lz_j)$$

The terms  $h$ ,  $k$  and  $l$  designate the planes and  $x_j$ ,  $y_j$  and  $z_j$  are the atomic positions for  $j$  atom. The resultant diffracted wave for any set of Bragg planes is described by the structure factor:

$$F_{hkl} = \sum_{j=1}^{\text{number of atoms}} f_j \exp[2\pi i(hx_j + ky_j + lz_j)]$$

The scattered intensity  $I_{hkl}$  is related to the structure factor of the corresponding  $hkl$  reflection through:

$$I_{hkl} = K L P A m_{hkl} |F_{hkl}|^2$$

$K$  is a scale factor,  $L$  is the Lorentz factor which depends on the geometry of the X-ray diffraction technique,  $P$  is the polarization factor that depends on the particular experimental setup,  $A$  the transmission factor and  $m_{hkl}$  is the plane multiplicity factor.

### **Production of X-rays**

X-rays are generated in a cathode tube where through a thermoionic effect a tungsten filament (cathode) emits electrons that are accelerated toward a target (anode) by a potential difference. The accelerated electrons ionize the target atoms that produce characteristic X-rays: an electron is removed from an inner shell and the vacancy is subsequently filled by an electron from an outer shell, with a concomitant emission of a photon with energy corresponding to the shell energy difference that is *characteristic* of the target atoms (usually Cu, Fe, Mo and Cr). The characteristic X-rays are labeled as K, L, M, or N to denote the shell containing the inner vacancy. An additional designation,  $\alpha$ ,  $\beta$  or  $\gamma$  refers to the origin of the outer electrons that will fill the vacancy: a  $K\alpha$  photon is produced when a transition from the L to the K shells occurs, a  $K\beta$  photon is produced when a transition from the to M a K shells occurs, etc. Furthermore, since within each shells there are multiple levels of energy, a further designation,  $\alpha_1$ ,  $\alpha_2$  etc, is required (Figure 2.6). The X-rays emitted by the target atoms leave the cathode tube through beryllium windows, are subsequently filtered so that only  $K\alpha$  remains, and are directed toward the sample [5].

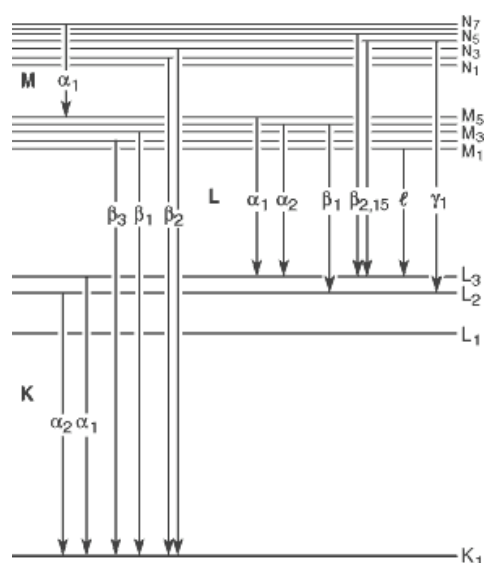


Figure 2.6 --Transitions that give rise to the various X-ray lines.

### **2.1.1 Powder X-ray diffraction (PXRD)**

In the PXRD method a sample is ground to a fine powder with random crystallographic orientation and placed in a sample holder mounted on a goniometer stage. Divergent  $K\alpha$  rays exit the source and are collimated and focused on the sample. Following the diffraction process, the rays are refocused at the detector slit and recorded by the X-ray detector. The incident X-ray beam and diffracted beam slits move on a circle centered on the sample (see Figure 2.7). The angle between the incident and Bragg diffracted beams is equal to  $2\theta$ , whereas the sample is at  $\theta$  to the incident X-ray beam. This is called the Bragg-Bretano geometry. Typically data is collected for  $2\theta$  between  $10^\circ$  and  $70^\circ$  [6].

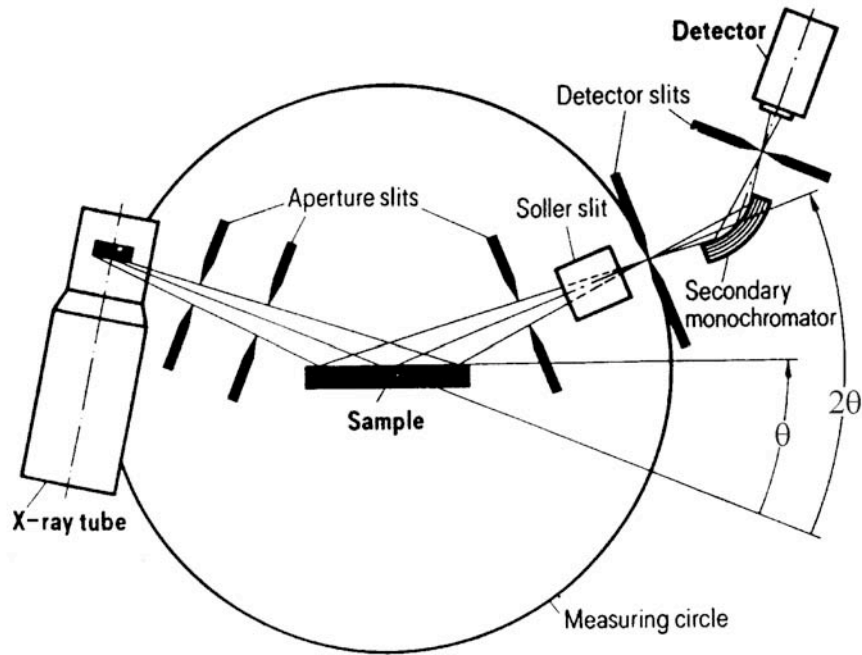


Figure 2.7 – Schematic of an X-ray diffractometer with Bragg-Brentano geometry [3].

The series of sharp intensity peaks detected as a function of the  $2\theta$  angle are unique for any given crystalline structure [6]. The  $d$ -spacing corresponding to each peak can be then obtained by solving Bragg's law for the appropriate values of  $\lambda$  and  $\theta$ .

Powder diffraction data can be analyzed using the Rietveld method in which intensities calculated based on a crystalline structure model ( $y_i^{cal}$ ) are adjusted point-to-point to the whole experimental intensities ( $y_i^{obs}$ ). The fitting algorithm minimizes the residuals,  $R_y$ , based on a least-squares approach:

$$R_y = \sum_i w_i (y_i^{obs} - y_i^{cal})^2$$

where,  $w_i = 1/y_i^{obs}$  is the statistic weight associated with the relative peak intensity. The mathematical function used to describe the intensity profiles is based on gaussian, lorentzian, voigt or pseudo-voigt distributions. The calculated intensity depends on a series of variables:

- instrumental characteristics (displacement parameters concerning goniometer misadjustments, experimental geometry, detector characteristics);
- structural parameters (unit-cell parameters, atomic positions, occupancy, thermal vibrations);
- microstructural parameters (mean crystallite size, microstrain, defects);
- sample parameters (preferred orientation, residual stress, thickness, transparency, absorption, phase fractions).

The efficiency of this methodology is limited by the overlap of neighboring peaks and the number of variables considered.

The quality of a Rietveld refinement is quantified by the following parameters: profile residual  $R_p$ , weighted-profile residual  $R_{wp}$ , expected residual  $R_{exp}$ , goodness of fit  $S$ , and Bragg residual  $R_{Bragg}$ . The former are given, respectively, by:

$$R_p = 100 \frac{\sum_{i=1,n} |y_i^{obs} - y_i^{cal}|}{\sum_{i=1,n} |y_i^{obs}|}$$

$$R_{wp} = 100 \sqrt{\frac{\sum_i w_i (y_i^{obs} - y_i^{cal})^2}{\sum_i w_i (y_i^{obs})^2}}$$

where  $w_i$ , refer to the statistic weight. The expected residual factor  $R_{exp}$  hints on what should be expected from the experimental data:

$$R_{exp} = 100 \sqrt{\frac{(N - P + C)}{\sum_i w_i (y_i^{obs})^2}}$$

where  $N$  is the total number of used points,  $P$  is the number of refined parameters and  $C$  is the number of constrains. For a high goodness of fit the value of  $R_{wp}$  should be similar to the  $R_{exp}$  value, therefore:

$$S = \frac{R_{wp}}{R_{exp}}$$

The Bragg residual factor  $R_{Bragg}$  shows the relation between the calculated intensities for the diffraction peaks ( $hkl$ ) and the observed intensities and is given by the expression:

$$R_{Bragg} = \frac{\sum_{hkl} |I^{obs} - I^{cal}|}{\sum_{hkl} I^{obs}}$$

where  $I^{obs}$  correspond to a value of intensity calculated from  $y_i^{obs}$ . Acceptable refinements are associated with residuals in the of 1-5% range.

### **2.1.2. Single crystal X-ray diffraction**

The method consists of three general stages: (a) experimental measurement of both the intensity and the angular position for a large fraction of the diffracted beams; (b) tentative deduction of the atomic arrangement (structure solution); (c) refinement of the tentative atomic arrangement in accordance with the experimental intensities (structure refinement).

The crystal is glued to a glass fiber fixed onto a brass pin and is then placed on a goniometer head that rotates (Figure 2.8). The goniometer device allows aligning the crystal with the X-ray beam (Figure 2.9). The diffracted beams are intercepted by a detector to produce a diffraction pattern of regularly spaced reflections [7].

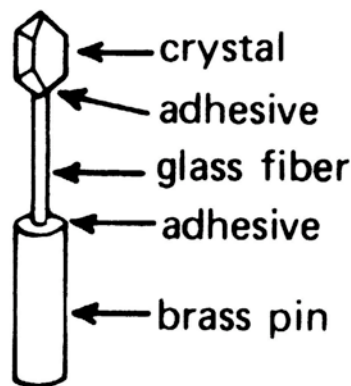


Figure 2.8 – Method to mount a stable crystal on a glass fiber [7].

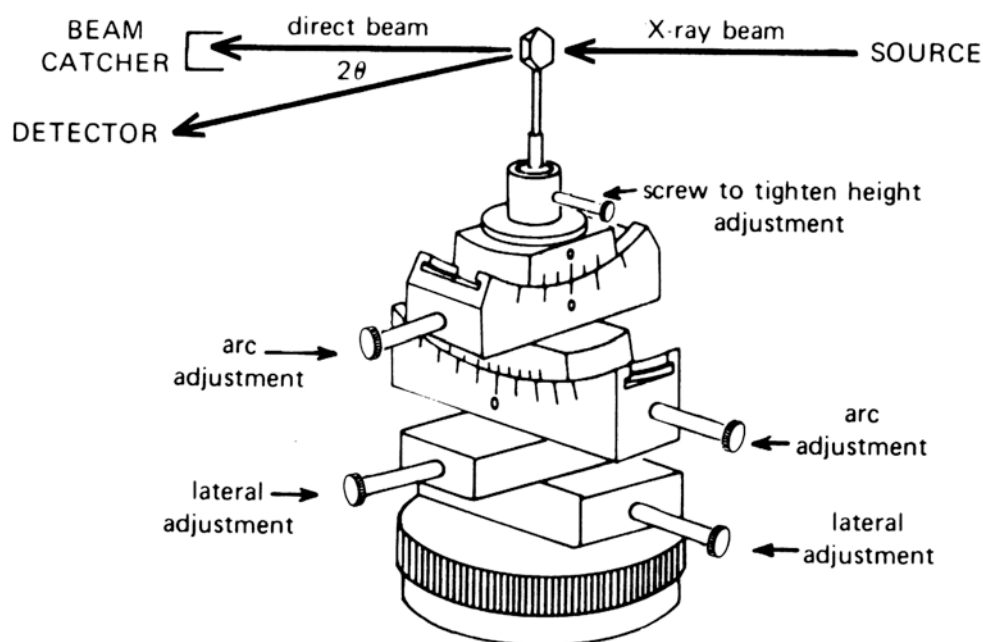


Figure 2.9 – A goniometer head, showing the various possible adjustments that can be made in order to center the crystal with the X-ray beam [7].

For the tentative deduction of the crystal structure, the experimental two-dimensional diffraction pattern is converted into a three-dimensional model of the electron density distribution in the crystal, which is expressed as the inverse Fourier transform of the structure factors:

$$\rho(xyz) = \frac{1}{V} \sum_{h,k,l} F(hkl) \cdot \exp[-2\pi(hx_m + ky_m + lz_m)]$$

The atoms are then situated in the cell based on the electronic density maxima obtained using the Patterson method, in which a map is produced from the Fourier transform of the intensities (Patterson function):

$$P(u, v, w) = \sum_{hkl} |F_{hkl}|^2 e^{-2\pi i(hu + kv + lw)}$$

Since the Patterson function is proportional to the squared structure factor the contribution of the heavy atoms tends to be enhanced.

The parameters used in the structure refinement are adjusted for each reflection in order to minimize the expression  $\sum w (F_o^2 - F_c^2)^2$ , where  $F_o$  and  $F_c$  are the structure factors observed and calculated, respectively, and  $w$  is the intensity weight. The results of the structure refinement yield a list of the atom positions in the unit cell, shape of the anisotropic intensity center for each atom (thermal parameters), distance and angle between nearest neighbors. The quality of a solution is assessed by the values of  $R$ ,  $wR$ , and  $Goof$ :

- The R-value, given by  $R = \sum ||F_o| - |F_c|| / \sum |F_o|$ , reveals the agreement between the calculated and observed models. Values less than 5% are considered acceptable solutions; high-quality samples will often result in R-values lower than 2.5%.
- The weighted residual  $wR$  refers to the normalized differences between the squared  $F$ -values and results in a higher value than  $R$ .
- The "goodness of fit" of the solution,  $Goof$ , accounts for the residuals, the number of reflections and the used parameters. At the final refinement, the  $Goof$  value should approach 1.

## **2.2 Scanning electron microscopy (SEM)**

The scanning electron microscope is a versatile instrument for microstructural examination due to the associated microanalysis and diffraction techniques and to its high resolution. Values of the order of 1 nm are currently quoted for commercial instruments. The basic components of these microscopes are: electron gun, lens system, detectors, imaging and recording system and the electronics associated with them. Figure 2.10 shows the schematic diagram of a scanning electron microscope.

A beam of electrons is produced in the electron gun by a thermal emission source, such as a heated tungsten filament, or by a field emission cathode. The electron beam follows a helicoidal path through the microscope column, which is held in vacuum. The

beam is condensed by the first condenser lens, used to both form the beam and limit the amount of current in the beam. It works in conjunction with the condenser aperture to eliminate high-angle electrons. The second condenser lens forms a thin, tight, coherent beam. A selectable objective aperture further eliminates high-angle electrons from the beam. The final lens, the objective, focuses the scanning beam onto the specimen. A set of coils scans the beam over the sample surface, dwelling on points for a period of time determined by the scan speed.

Electrons are deflected by collisions with the specimen atoms. These collisions can be either elastic, when the electron is deflected but no energy interchange occurs, or inelastic, when the electron supplies energy to the atom. These interactions are responsible for different signal types: backscattered electrons, secondary electrons, X-Rays, Auger electrons, cathodoluminescence [7].

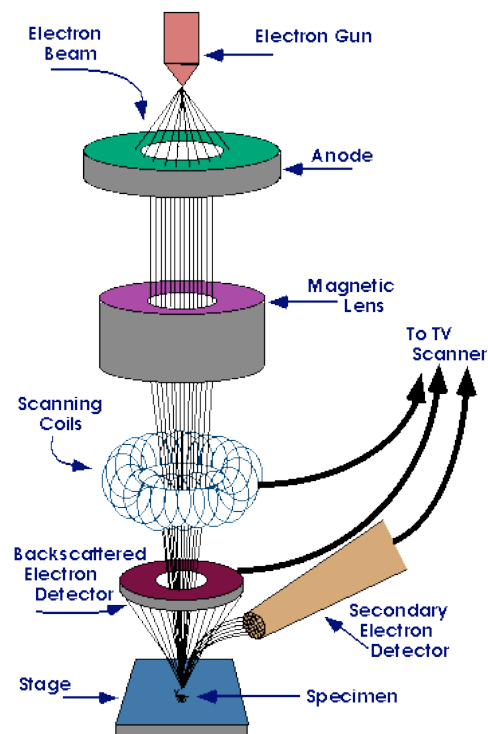


Figure 2.10 – Schematic diagram of a scanning electron microscope. [8]

Elastic interactions occur when a beam electron collides with the electric field of the nucleus of an atom, resulting in a change in direction of the primary electron without a significant change in energy ( $< 50$  eV). If the elastically scattered electron is deflected back out of the specimen, the electron is termed as backscattered (Figure 2.11 (a)). Backscattered electrons (BSE) have hence an energy range from 50 eV to nearly the incident beam energy [7].

Inelastic interactions occur when a primary electron collides with the electric field of an atom electron cloud, resulting in an energy transfer to the atom and a potential expulsion of an electron from that atom as a secondary electron (SE). SE electrons by definition have an energy less than 50 eV. If the vacancy created by the SE emission is filled with an electron from a higher-level shell, an X-ray characteristic of that energy transition is produced [7].

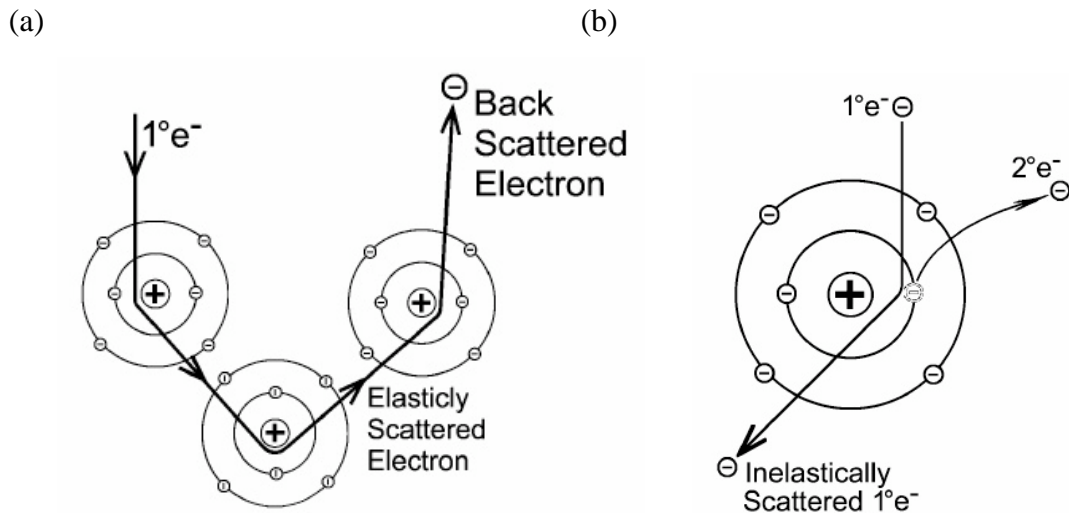


Figure 2.11 – (a) Elasticly scattered primary electron deflected back out of the specimen, the electron is termed as a backscattered electron (BSE), (b) Inelastically scattered primary electron with transfer of energy to the specimen atom resulting in a secondary electron emission (SE) [7].

Secondary and backscattered electrons have different maximum escape depths (Figure 2.12): due to their low energy, SE electrons can only escape from 5-50 nm below the surface; BSE can escape from a depth a hundred times greater. As a result the secondary

electron signal reveals the sample topography with high spatial resolution. SE electrons are detected by an Everhart-Thornley detector which is a scintillator-photomultiplier [7]. The BSE signal is sensitive to the local atomic number and therefore is able to reveal contrast between phases with different composition. In order to maximize the collection solid angle the backscattered electron detector is situated above the sample in a "doughnut" type arrangement, with the electron beam passing through the hole of the doughnut [7]. In both cases the resulting signal is rendered into a two-dimensional intensity distribution.

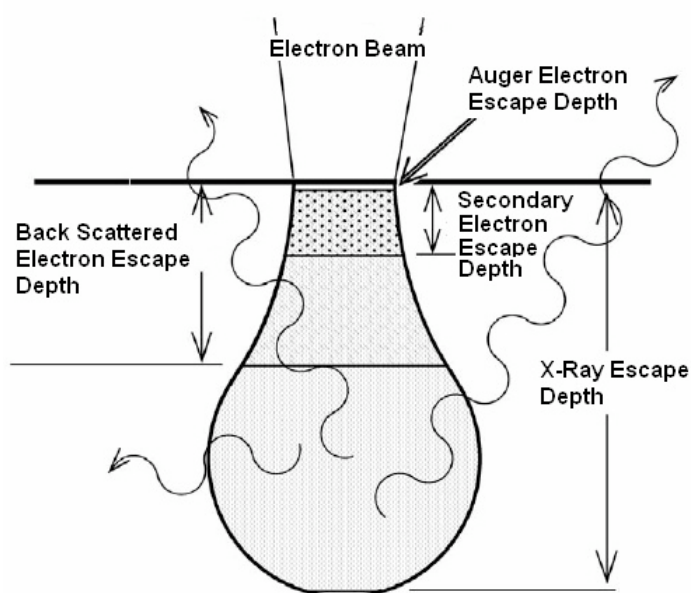


Figure 2.12 – Penetration of electrons into a bulk specimen [7].

### **2.2.1 Energy dispersive X-ray spectroscopy (EDS)**

This microanalysis technique, usually coupled with scanning electron microscopy, detects characteristic X-rays resulting from the interaction of the primary electron beam with the sample atoms. The X-ray emission process is analogous to the one described in Figure 2.6 [9]. The detector is typically a lithium-drifted silicon, solid-state device. When an incident X-ray strikes the detector, it creates a charge pulse that is converted to a voltage pulse that is proportional to the energy of the X-ray. The signal is then sent

to a multichannel analyzer where the pulses are sorted by voltage. A spectrum of counts versus X-ray energy is then generated, where the channels corresponding to the characteristic X-rays can be identified to qualitatively determine the elemental composition of the sample. Elements ranging from that of sodium to uranium can be detected. The minimum detection limits vary from approximately 0.1 to a few atom percent, depending on the element and the sample matrix [9]. Several X-ray maps can be recorded simultaneously using image brightness intensity as a function of the local relative concentration of the element(s) present with a lateral spatial resolution of about 1  $\mu\text{m}$ .

Once the intensities of the characteristic X-rays have been determined, the next challenge is to use this information to compute the elemental composition of the specimen. The intensities obtained depend on three matrix effects and must be corrected:

- Atomic Number correction: The probability of production of an X-ray by an incident electron must account for the probability of backscattering and the average depth of X-ray production, which depend in a complicated manner upon the beam voltage and the average atomic number of the specimen.
- Absorption correction: The probability that an X-ray, once produced, will exit the specimen and reach the detector depends upon the absorption of the overlying material. Each element is characterized by a set of absorption coefficients for X-rays of various energies, and the overall absorption for a specific energy depends thus upon the composition of the specimen as well as the length of the path the exiting X-ray.
- Fluorescence correction: When an emitted characteristic X-ray is absorbed by another matrix element, the absorbing element may be excited and decay with emission of its own characteristic X-ray. This process, called *secondary fluorescence* results thus in an intensity enhancement for the fluorescent element and a concomitant intensity decrease corresponding to the primarily excited atom.

In quantitative EDS microanalysis, samples of known composition  $C_{st}$  are used as standards and the concentration of an  $i$  element  $C_i$  in a studied can be inferred from the peak intensity ratio  $I_i / I_{st}$  :

$$C_i / C_{st} = K I_i / I_{st}$$

where  $I_i$  is the peak intensity measured in the sample and the  $I_{st}$  is the peak intensity for the  $i$  element in the standard.  $K$  is the correction factor that includes the three matrix effects [10]. In semi-quantitative analysis theoretical models are used to account for the ‘ZAF’ matrix corrections. However, the relative errors associated with standardless analysis are higher.

### **2.2.2 Wavelength dispersive spectroscopy (WDS)**

The wavelength dispersive spectrometer is usually coupled with an SEM imaging system and requires dedicated instruments designated by electron microprobe micro-analyzer (EPMA). The spectrometer uses diffraction to sort by wavelength the characteristic X-rays emitted by the sample. The X-rays are selected using analytical crystals with specific lattice spacing positioned at specific  $\theta$  angles. Only the wavelengths that satisfy Bragg's law are allowed to pass on to the detector (Figure 2.13). Crystals with different  $d_{hkl}$  values must therefore be used to cover the whole wavelength range (see Table 2.1). The analytical crystals are bent in order to focus the X-ray beam on the sample and on the detector and are situated in the Rowland circle to maximize the collection efficiency of the spectrometer (Figure 2.13).

Name	Abbreviation	$d_{hkl}$ (Å)	Wavelength range (Å)
Lithium fluoride	LIF	2.013	0.8-3.2
Pentaerythritol	PET	4.371	1.8-7.0
Thallium acid phthallate	TAP	12.95	5.1-21.0

Table 2.1- Crystals used in WDS spectrometers [6].

The X-rays are detected in a “proportional counter” consisting of a gas-filled tube with a coaxial anode wire: X-rays ionize gas atoms producing free electrons, which move to the anode while the positive ions move out the cathode; each detected photon produces a charge pulse proportional to the photon energy; the pulses are counted and plotted against the X-ray wavelength [6].

WDS requires standard reference materials in concentrations similar to the materials to investigate and is typically used for quantitative spot analysis. The composition of unknown samples is determined by comparing the intensities obtained from the studied samples with those from the standard reference materials. This technique is complementary to EDS, although wavelength dispersive spectrometers have significantly higher spectral resolution and enhanced quantitative potential.

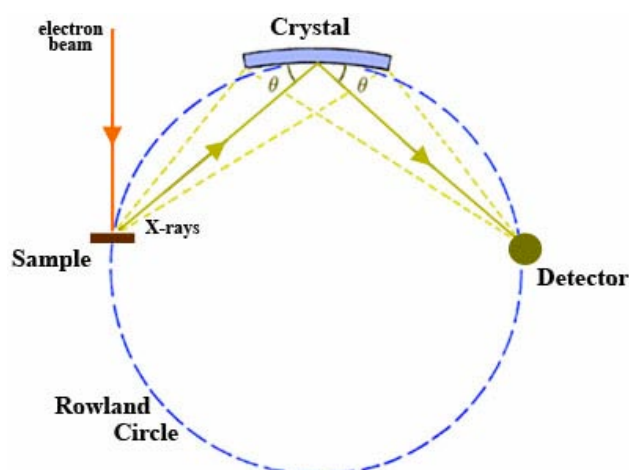


Figure 2.13 – Configuration of sample, analytical crystal and detector on the Rowland circle within the wavelength dispersive spectrometer [11].

### **2.3 Electron backscattered diffraction (EBSD)**

Local crystallographic information can be obtained with this diffraction technique using scanning electron microscopes. The primary electron beam is directed at a point of interest on the sample surface, diffuse elastic scattering in all directions causes the electrons to diverge from a point just below the sample surface and to impinge upon

crystal planes in a continuous range of angles. Whenever the Bragg condition is satisfied by a family of lattice planes, two Kossel cones are produced. The source of electron scattering can be considered to be the plane lying between the cones as shown in Figure 2.14 (a). Collection of the Kossel cones pattern is relatively straightforward: the polished sample is tilted to a relatively high angle inside the microscope (typically 70°) to maximize collection; the diffracted cones are intersected and imaged using a phosphor screen attached to a sensitive camera. The whole pattern consists of pairs of parallel lines where each pair or “Kikuchi band” has a distinct width and corresponds to a distinct family of crystallographic planes. Band intersections correspond to low-index zone axes. Since the pattern formed is characteristic of the crystal structure it can be used to discriminate between different phases, measure the crystal orientation, grain boundary misorientations, and provide information about local crystalline perfection [12]. Software can be used to automatically locate the positions of individual Kikuchi bands, compare these to theoretical data of the relevant phase and rapidly calculate the 3-D crystallographic orientation.

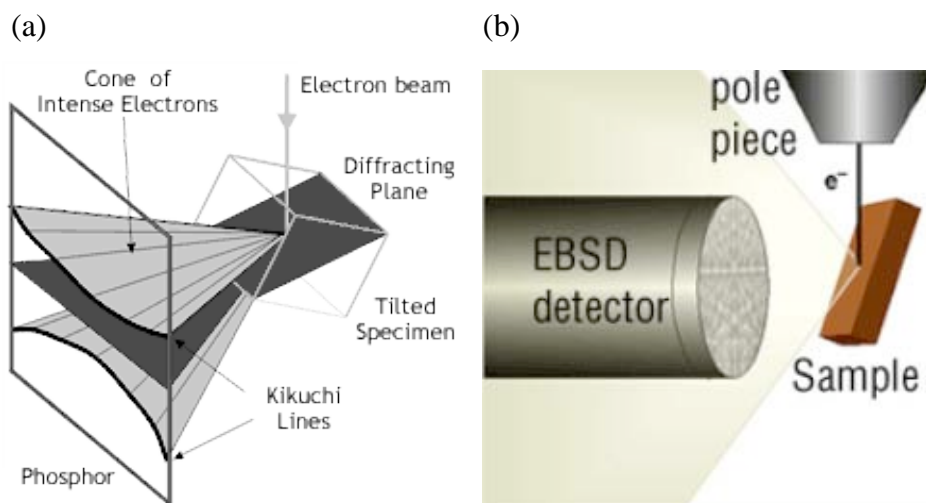


Figure 2.14 – (a) Origin of Kikuchi lines by elastic scattering of the primary electrons followed by Bragg’s diffraction on  $(hkl)$  lattice planes, (b) sample position and EBSD detector [13].

## **2.4 Differential thermal analysis (DTA)**

In differential thermal analysis the material under study and an inert reference are submitted to identical thermal cycles, while recording the temperature difference between them. The temperature difference is derived from the voltage difference between the sample and the reference thermocouples, and is then plotted against time or temperature. Changes in the sample, either exothermic or endothermic, can be detected relative to the inert reference. The minimum temperature difference that can be measured by DTA is 0.01 K [14].

The key components of a DTA equipment are as follows (Figure 2.15): (a) sample holder comprising thermocouples, (b) furnace, (c) temperature programmer and (d) recording system. The furnace should provide a stable and sufficiently large hot-zone and must be able to respond rapidly to commands from the temperature programmer. A temperature programmer is essential in order to obtain constant heating rates. The equipment uses a pair of crucibles that are supported by a pair of vertical thermocouples (differential thermocouple). After both crucibles are placed on top of the differential thermocouple stalks, the furnace is lowered over the crucibles, and the furnace is heated and cooled according to the programmed thermal cycle. The differential thermocouple output (heat flow in micro-volts or differential temperature) is displayed on a PC monitor as a function of time or temperature. High purity alumina is a standard DTA crucible material. Zirconia and yttria crucibles can be used for highly reactive metals [15]. The apparatus works under inert gas as helium or argon.

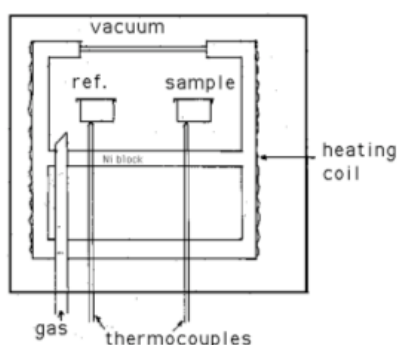


Figure 2.15 – Schematic illustration of DTA furnace [15].

The onset of the DTA peak gives the start temperature of the transformation, which is usually inferred from the DTA curve derivative. On heating, melting requires an input of heat and the downward peak is endothermic, whereas on cooling, freezing releases heat and the upward peak is exothermic. A similar interpretation is used for any other phase transformations occurring during the thermal cycle. Larger sample masses produce larger peak signals (deflection from the baseline) and are therefore more easily detected. However, the larger masses also delay the temperature at which the signal returns to the baseline, rendering detection of closely spaced thermal events more difficult. Sample shape is also a significant factor to take into account since the thermal contact area between the sample and the cup will change during the melting process [16].

### **2.5 Superconducting quantum interference device (SQUID)**

SQUID magnetometers are used to measure extremely weak magnetic fields. The main components of the magnetometer are: (a) superconducting magnet; (b) superconducting detection coil which is coupled inductively to the sample and (c) the SQUID. The superconducting magnet is a solenoid and a uniform magnetic field is produced along the axial cylindrical bore of the coil. The superconducting detection coil system is placed in the uniform magnetic field of the solenoidal superconducting magnet.

A measurement is done by moving the sample through the superconducting detection coils. The magnetic moment of the sample induces then an electric current in the superconducting detection coil. Since the sample is moving inside the superconducting detection coils will induce a variation on the magnetic flux, which is proportional to the sample magnetization. Therefore since the magnetic flux is quantified on the SQUID, this variation will change the intensity of the current proportional to the magnetic flux in order to keep constant the magnetic flux inside the loop. The SQUID acts as a magnetic flux-to-voltage converter enabling to measure the sample magnetization.

## **2.6 Experimental details**

### **2.6.1 Alloys preparation and heat treatments**

Crystal growing of actinides and their compounds requires special methods due to the difficulties arising from handling problems (radioactivity, toxicity, scarcity, high reactivity) and the need for high working temperatures (typically 2000 °C). Since uranium is not commercially available the element used in the present work has been provided from French, Czech and American collaboration groups.

B-Fe-U alloys were prepared by melting together the elements (purity > 99 at.%) in an arc furnace equipped with a cold crucible under an argon atmosphere. The surface of uranium pieces was deoxidized in diluted nitric acid prior to melting. In order to ensure homogeneity, the samples were melted at least three times before quenching to room temperature. The mass loss after solidification proceeding was lower than 1 wt.%. In order to check reproducibility, the alloy production was often repeated. Figure 2.16 represents the position in the ternary diagram of the 51 alloys investigated in the present work. The alloys have been sorted by decreasing boron contents followed by decreasing iron contents and the correspondence between the numbers and the nominal uB:vFe:wU compositions can be found in Table 2.2.

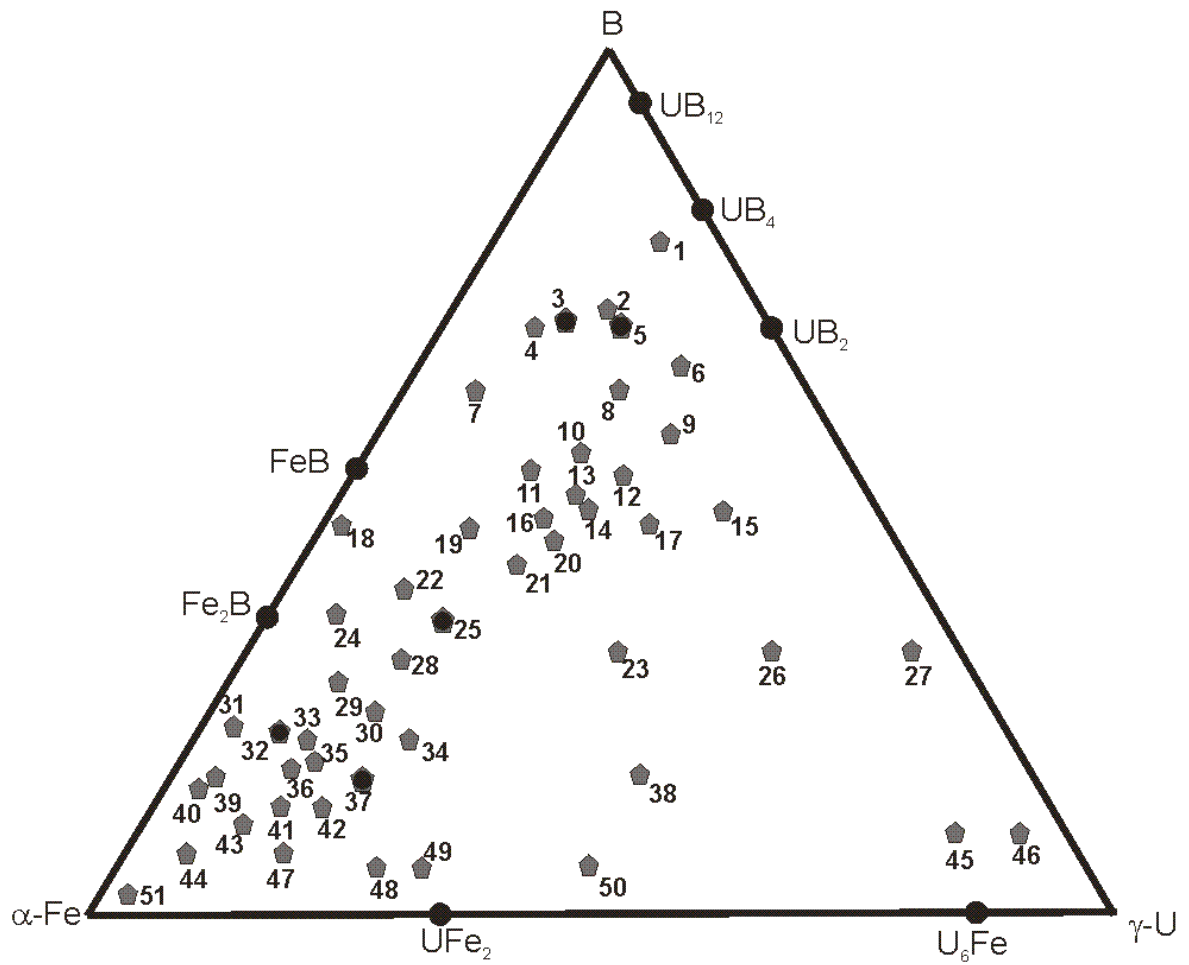


Figure 2.16 – Composition of the alloys investigated (pentagonal grey shapes) and the position of binary and ternary compounds in the B-Fe-U system (black circles).

Nr.	uB:vFe:wU composition ( $U_xFe_yB_z$ compound stoichiometry)	Nr	uB:vFe:wU composition ( $U_xFe_yB_z$ compound stoichiometry)
1	77B:8Fe:15U	27	30B:4Fe:66U
2	69B:13Fe:18U	28	29B:57Fe:14U
3	67B:22Fe:11U ( $UFe_2B_6$ )	29	27B:64Fe:9U
4	66B:25Fe:9U	30	23B:62Fe:15U
5	66B:17Fe:17U ( $UFeB_4$ )	31	21B:76Fe:3U
6	63B:13Fe:24U	32	21B:72Fe:7U ( $U_2Fe_{21}B_6$ )
7	60B:35Fe:5U	33	20B:70Fe:10U
8	60B:20Fe:20U	34	20B:60Fe:20U
9	54B:18Fe:28U	35	18B:70Fe:12U
10	52B:27Fe:21U	36	17B:73Fe:10U
11	50B:33Fe:17U	37	17B:66Fe:17U ( $UFe_4B$ )
12	50B:25Fe:25U	38	16B:44Fe:40U
13	47B:30Fe:23U	39	15B:80Fe:5U
14	46B:30Fe:24U	40	14B:83Fe:3U
15	46B:19Fe:30U	41	11B:78Fe:11U
16	45B:35Fe:20U	42	11B:72Fe:17U
17	44B:25Fe:29U	43	10B:80Fe:10U
18	43B:55Fe:2U	44	9B:87Fe:4U
19	43B:43Fe:14U	45	9B:12Fe:79U
20	43B:35Fe:23U	46	9B:6Fe:85U
21	40B:40Fe:20U	47	7B:79Fe:14U
22	38B:52Fe:10U	48	5B:70Fe:25U
23	35B:35Fe:30U	49	5B:67Fe:28U
24	34B:60Fe:6U	50	5B:50Fe:45U
25	33B:50Fe:17U ( $UFe_3B_2$ )	51	2B:96Fe:2U
26	30B:20Fe:50U		

Table 2.2 – Correspondence between alloy number and composition.

The large cooling rate associated with the arc furnace ( $10^2$  K/s) obstructs the solid-state diffusion and promotes the existence of liquid at temperatures below the equilibrium solidification temperature. Therefore, microstructures evidence extended solidification paths, which to enable to study the liquidus surface and establish its boundary lines and ternary reactions. However nucleation may be retarded or even suppressed for specific phases and/or metastable phases may crystallize. Annealing treatments at 650°C during 15 days for uranium-rich samples and at 950°C during 60 days for iron-rich samples we used to confirm the equilibrium phases. However, due to the high melting temperature of some of the borides and to the low diffusivity of uranium, significant changes in the microstructures towards an equilibrium configuration could not be observed. Consequently, the (metastable) equilibrium phase diagram could only be inferred from as-cast microstructures.

### **2.6.2 PXRD**

PXRD data was obtained from the as-cast and annealed samples and were collected at room temperature with monochromatic Cu K $\alpha$  radiation using an Inel CPS 120 diffractometer, equipped with a position-sensitive detector covering 120° in 2 $\theta$  with a resolution of 0.03°, and a Panalytical X'Pert diffractometer with a 2 $\theta$ -step size of 0.02° from 10° to 70°. The Powder Cell software package [17] was used to simulate diffractograms for comparison with experimental data.

Due to the fact that the Fe-rich and U-rich alloys are extremely soft, these materials were difficult to reduce to powder. This led to some degree of preferred crystallographic orientation that rendered laborious the phase identification by PXRD.

### **2.6.3 Single crystal X-ray diffraction**

A single crystal of the UFe<sub>2</sub>B<sub>6</sub> phase was analyzed with a Bruker AXS APEX CCD X-ray diffractometer equipped with an Oxford Cryosystem at 150 K using Mo radiation K $\alpha$  ( $\lambda = 0.71073 \text{ \AA}$ ) and  $\omega$  and  $\phi$  scan mode. Data collection, refinement and data reduction were carried out using the SMART and SAINT software packages [18]. A semi-empirical absorption correction was carried out with SADABS [19]. The structures were solved by direct methods using SIR97 [20] and refined by fullmatrix least-squares methods with the SHELX-97 [21] program using the built in atomic scattering factors and the WINGX software package [22].

A single-crystal of the UFe<sub>3</sub>B<sub>2</sub> phase was analysed with a Bruker Kappa CCD diffractometer using Mo radiation K $\alpha$  ( $\lambda = 0.71073 \text{ \AA}$ ) at room temperature. The unit-cell parameters, orientation matrix as well as the crystal quality were derived from 10 frames recorded at  $\chi = 0$  using a scan of 1° in  $\phi$ . The COLLECT software package [23] was used to infer more data than a hemisphere. Data reduction and reflection indexing were performed with the DENZO routine of the Kappa CCD software package [23].

The scaling and merging of redundant measurements of the different data sets as well as the cell refinement were also performed with DENZO.

The crystal structures and polyhedra of both phases were represented using DIAMOND 2.1 [24].

#### **2.6.4 SEM, EDS, WDS and EBSD**

As-cast and annealed microstructures were observed in secondary and backscattered electron modes (respectively, SE and BSE) on polished and etched surfaces using a JEOL JSM-7001F field emission gun scanning electron microscope equipped for energy dispersive spectroscopy (EDS) and HKL Oxford EBSD detector. The samples were polished with 6, 3 and 1  $\mu\text{m}$  diamond suspensions and etched with a commercial alumina suspension (OPS).

The EDS spectroscopy technique was primarily used for efficient X-ray map collection, whereas (quantitative) analysis for phase identification was carried out with a Cameca SX100 electron probe microanalyzer (EPMA) equipped with five wavelength dispersive spectrometers. In the EPMA instrument a multilayer Mo-B<sub>4</sub>C crystal with a large interplanar distance ( $2d=210.36$  nm) is used to detect boron, a lithium fluoride (LIF) crystal ( $2d=4.03$  nm) is used to detect uranium and a pentaerythriol (PET) crystal ( $2d=8.75$  nm) is used to detect iron. These elements were analyzed simultaneously through the  $BK\alpha$ ,  $UM\beta$  and  $FeK\alpha$  transitions with an acceleration voltage of 15 kV, a beam current of 20 nA, and using CeB<sub>6</sub>, UC and  $\alpha$ -Fe as standards. The typical beam size was  $\sim 100$  nm and the interaction volume was  $\sim 1 \mu\text{m}^3$ . The X-phi correction software package was used to calculate the relative element proportions [25]. Quantitative analyses were performed in 13 representative alloys and each phase was analyzed in more than 6 randomly selected points.

EBSD patterns were collected from as-cast and annealed samples. Candidate crystal structures, consistent with the compositional information, were selected from the

literature. The interzonal angles observed in the patterns were then compared with those simulated. The HKL Channel 5 software [26] was used for phase identification and index determination of the designated zones. The program calculates the reflected planes having significant intensity and automatically suggests solutions ranked by lowest “mean angular deviation” (MAD) that is an index of “goodness of fit”. MAD solutions under 1° are considered desirable for accurate solutions. The resolution of the EBSD was about 5  $\mu\text{m}$ . The Carine Crystallography software package [27] was used to simulate the reciprocal lattice in order to infer the crystallographic indexes of planar defects. Samples for EBSD acquisition were further polished with a 0.1 $\mu\text{m}$  diamond suspension prior to etching with OPS.

#### **2.6.5 DTA and heating curves**

DTA measurements were carried out for 30 alloys up to 1600°C using a Setaram DTA Labsys and Setaram Setsys Evolution 16/18 DTA/DSC with sample masses of 30-120 mg, employing open alumina crucibles and a permanent argon flow. The curves were normalized for mass and the transition temperatures were determined from the derivative curves. The heating rates optimized for clear peak evidence versus acquisition efficiency were 5 and 10°C/min. The difference in temperature measured for the same transformations at different heating/cooling rates enabled to estimate that the undercooling/overheating ( $\Delta T$ ) values were below 5 °C. Since the DTA cooling rates were significantly different from the ones of the solidification methods used, the heating curves (and not the cooling curves) were systematically scrutinized and related with the as-cast microstructures, i.e., the sequence of phase transformations during heating was related to the reversed solidification path inferred from the multiphase microstructures. The DTA curves analysis is based on the theoretical discussion presented in reference [28].

The high melting temperatures of the alloys in the B-rich corner rendered limited the use of DTA facilities. This obstacle was overcome by obtaining heating curves up to 2000 °C at 10 W/min in an induction furnace (IF) coupled with an optical pyrometer.

Due to the samples radioactivity the amounts processed had to be kept to a minimum (100-200 mg), which in turn conditioned the signal/noise ratio in the heating curves obtained with the pyrometer measurements. Heating and cooling experiments enabled to infer undercooling/superheating values below 20°C. The heating curves analysis is based on the theoretical discussion presented in reference [28]. The transition temperatures were obtained from the derivative curve.

### **2.6.6 High temperature X-ray diffraction (HTXRD)**

HTXRD was used to further characterize the phase transformations detected by DTA up to 980°C, namely the  $\alpha$ -Fe to  $\gamma$ -Fe transition. The Cu K $\alpha$  line was collimated with a Göbel mirror and a divergent slit of 1x10 mm<sup>2</sup>, and filtered with a Ge (111) two-crystal monochromator. X-ray diffractograms were collected on polished surfaces with typical 11x9 mm<sup>2</sup> areas. The measurements were made continuously during heating at a rate of 5 °C/min under a vacuum of 10<sup>-4</sup> mbar using a MBraun ASA 50M PSD detector with an acquisition time of 12 s in the 41° to 48° 2 $\theta$  range. The temperature was measured with a thermocouple welded to the sample surface and checked with a micro-optical pyrometer (PYRO 95). Above 800 °C, the temperature deviations detected with the pyrometer remained below 1%.

### **2.6.7 Magnetic measurements**

Preliminary magnetization measurements of the 67B:22Fe:11U (UFe<sub>2</sub>B<sub>6</sub> stoichiometry) sample (Nr.3) and 23B:62Fe:15U (Nr.30) were done on a fixed powder using a S700X SQUID magnetometer (Cryogenic Ltd.) in the 2-300K temperature range and under applied fields up to 6T.

## **2.8 References**

- [1] C. Hammond, “ The basis of Crystallographic and Diffraction ”, International Union of Crystallography, Oxford University Press, (1997), 127.
- [2] [http://capsicum.me.utexas.edu/ChE386K/html/ewald\\_construction.htm](http://capsicum.me.utexas.edu/ChE386K/html/ewald_construction.htm)
- [3] E. Lifsthin, “ X-ray Characterization of Materials ”, Wiley-VCH, Germany (1999), 39.
- [4] D. T. Cromer, D. Liberman, Journal of Chemical Physics, 53 (1970) 1891-1898.
- [5] V. D. Scott, G. Love and S. J. B. Reed, “Quantitative Electron-Probe Microanalysis”, 2<sup>nd</sup> Edition, Ellis Horwood, Britain (1995) 22.
- [6] [http://serc.carleton.edu/research\\_education/geochemsheets/techniques/XRD.htm](http://serc.carleton.edu/research_education/geochemsheets/techniques/XRD.htm)
- [7] B. Hafner, “Scanning Electron Microscopy Primer”, Characterization Facility, University of Minnesota-Twin Cities, (2007).
- [8] <http://www.mokkka.hu/drupal/en/node/8881>
- [9] <http://www.mcswiggen.com/TechNotes/WDSvsEDS.htm>
- [10] A. Ul-Hamid, H. M. Tawancy, A. I. Mohammed, S. S. Al-Jaroudi, N. M. Abbas, Materials Characterization, 56 (2006) 192.
- [11] [http://serc.carleton.edu/research\\_education/geochemsheets/wds.html](http://serc.carleton.edu/research_education/geochemsheets/wds.html)
- [12] V. Randle, O. Engler, “Introduction to texture and Analysis macrotexture, microtexture and Orientation Mapping”, CRC press, Florida, USA, (2000) 127-130.
- [13] [http://nanoscience.huji.ac.il/unc/sem\\_basics.htm](http://nanoscience.huji.ac.il/unc/sem_basics.htm)
- [14] T.Hatakeyama, F.X.Quin, “Thermal Analysis, Fundamentals and Applications to Polymer Science”, 2<sup>nd</sup> Edition, Wiley, England, (1999) 6.
- [15] H. Bhadeshia, University of Cambridge, Materials Science & Metallurgy, seminar.
- [16] W. J. Boettinger, U. R. Kattner K.-W. Moon, J. H. Perepezko, “DTA and Heat-flux DSC Measurements of Alloy Melting and Freezing”, special Publications, Washington, 2006, 11.
- [17] G. Nozle, W. Kraus, Powder Cell for Windows, Version 2.2, Federal Institute for Materials Research and Testing, Berlin, Germany (1999).
- [18] Bruker, SMART and SAINT, BrukerAXS Inc., Madison, Wisconsin, USA, (2004).

- [19] G. M. Sheldrick, SADABS, BrukerAXS Inc., Madison, Wisconsin, USA, (2004).
- [20] A. Altomare, M.C. Burla, M. Camalli, G. Cascarano, G. Giacovazzo, A. Guagliardi, A.G.G. Moliterni, G. Polidori, R. Spagna, *J. Appl. Crystallogr.* 32 (1999) 115.
- [21] G. M. Sheldrick, SHELXL97, Program for Crystal Structure and Refinement University of Gottingen, Germany, (1997).
- [22] L. J. Farrugia, *Journal of Applied Crystallography* 32 (1999) 837.
- [23] Bruker-AXS, in: Collect, Denzo, Scalepack, Sortav. Kappa CCD Program Package, Bruker AXS, Delft, The Netherlands (1998).
- [24] W. T. Pennington, *Journal of Applied Crystallography* 32 (1999) 1028-1029.
- [25] C. Merlet, *Microchimica Acta* 114/115 (1994) 363–376.
- [26] <http://www.oxinst.eu/products/microanalysis/ebsd/ebsd-acquisition-software/Pages/channel5.aspx>
- [27] <http://carine.crystallography.pagespro-orange.fr/>
- [28] T. Gödeke, “Ableitung des Kristallisationspfades in ternären Glussledierungen”, Max Planck Institut für Metallforschung, Stuttgart, Germany.

---

## **Chapter 3**

---



## **Chapter 3 – Ternary phase diagram**

### **3.1 Introduction**

This chapter describes solidification paths in the B-Fe-U ternary phase diagram. The boundary lines, which delimit primary crystallization fields and delineate the liquidus projection, are identified. In addition, three isothermal sections are presented together with a vertical section evidencing a cascade of peritectic-like reactions. The binary diagrams and a previous proposal for a ternary isothermal section are reviewed in detail below.

### 3.2 State of the art

#### Binary systems

Binary B-Fe, B-U and Fe-U diagrams are available in the literature [1-3]:

**B-Fe.** This phase diagram has been reviewed in ref. [4] and is presented in Figure 3.1. Two binary compounds, FeB (FeB-type structure) and Fe<sub>2</sub>B (CuAl<sub>2</sub>-type structure) exist in equilibrium in the system [5]. However, four other compounds, claimed to be metastable, have also been reported, Fe<sub>3</sub>B (Fe<sub>3</sub>C-type-structure), Fe<sub>7</sub>B (unknown type-structure), Fe<sub>9</sub>B (W-type structure) and FeB<sub>2</sub> (AlB<sub>2</sub> type-structure) [6 - 9].

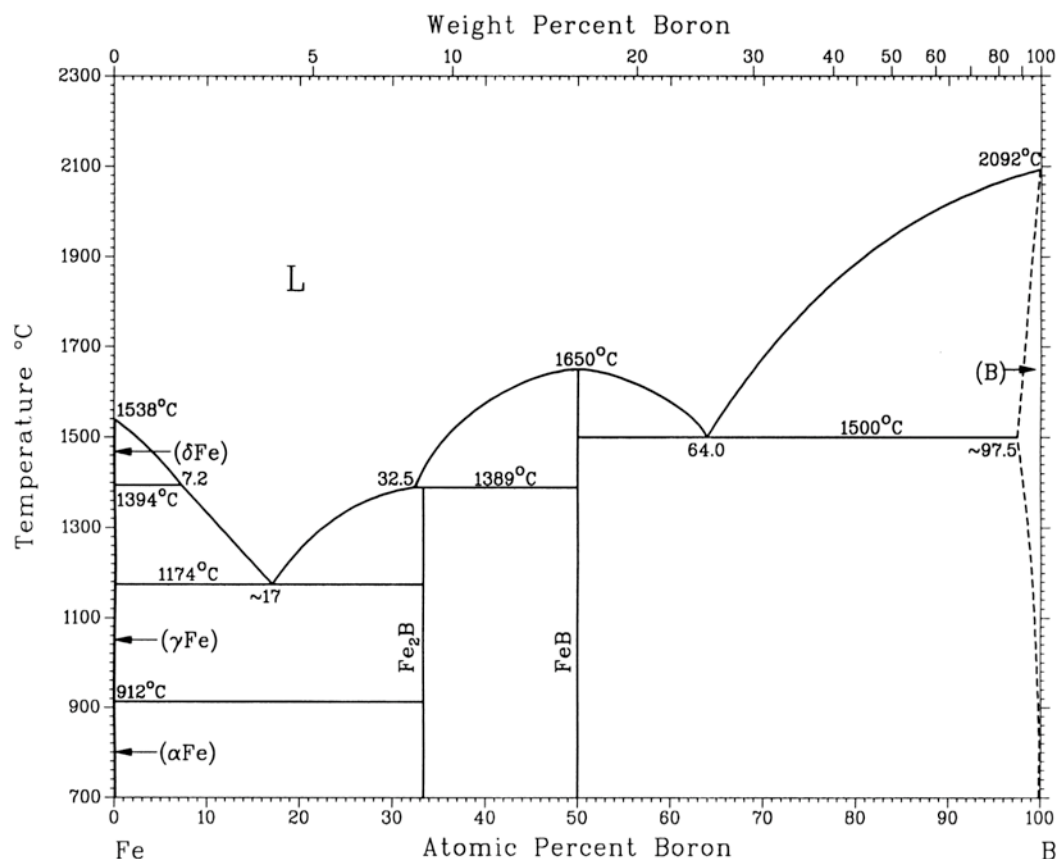


Figure 3.1 – Equilibrium B-Fe binary phase diagram [1].

**B-U.** The boron-uranium system was studied in the late fifties [10] and since then only minor modifications have been proposed to the phase diagram (Figure 3.2) [11]. Three binary phases have been identified,  $UB_2$  ( $AlB_2$ -type structure),  $UB_4$  ( $ThB_4$ -type structure) and  $UB_{12}$  ( $UB_{12}$ -type structure), all melting congruently at high temperatures and having negligible solubility ranges [12,13].

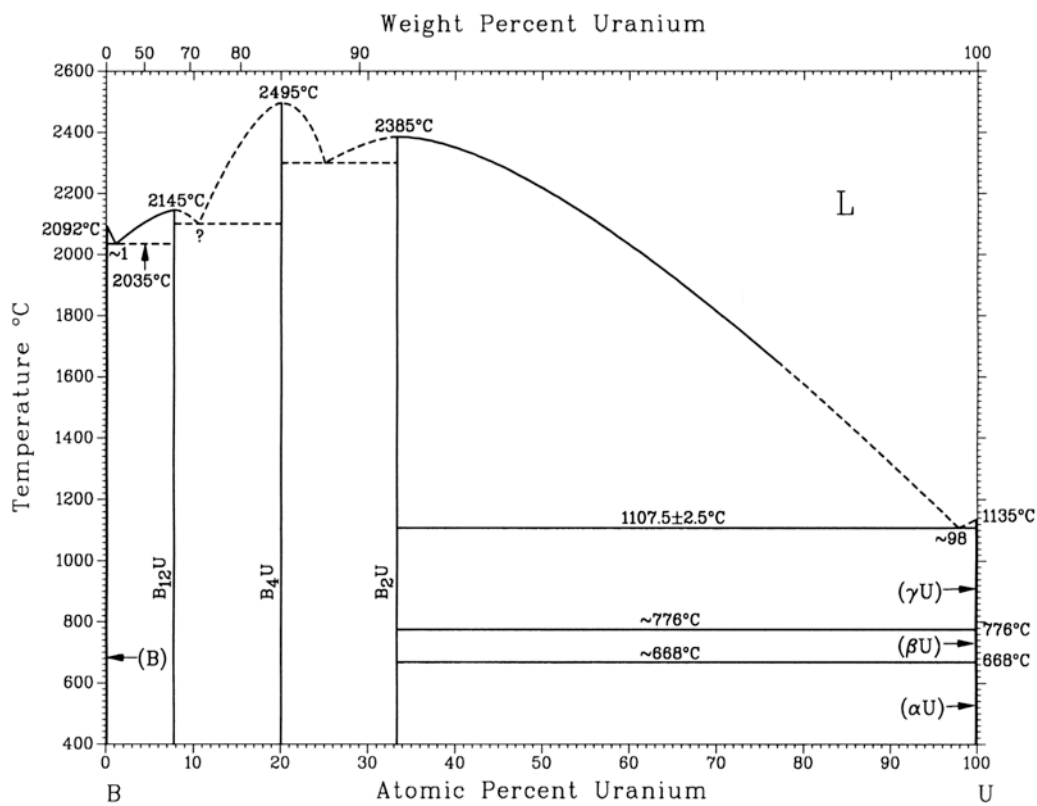


Figure 3.2 – Equilibrium B-U binary phase diagram [2].

**Fe-U.** This diagram is well known and the last revised version, shown in Figure 3.3, has been considered in the current work [14]. Two binary intermetallic compounds exist in the system,  $\text{UFe}_2$  ( $\text{MgCu}_2$ -type structure) and  $\text{U}_6\text{Fe}$  ( $\text{U}_6\text{Mn}$ -type structure), both without significant solubility ranges. Thermodynamic properties of the phases have also been reported [15-17].

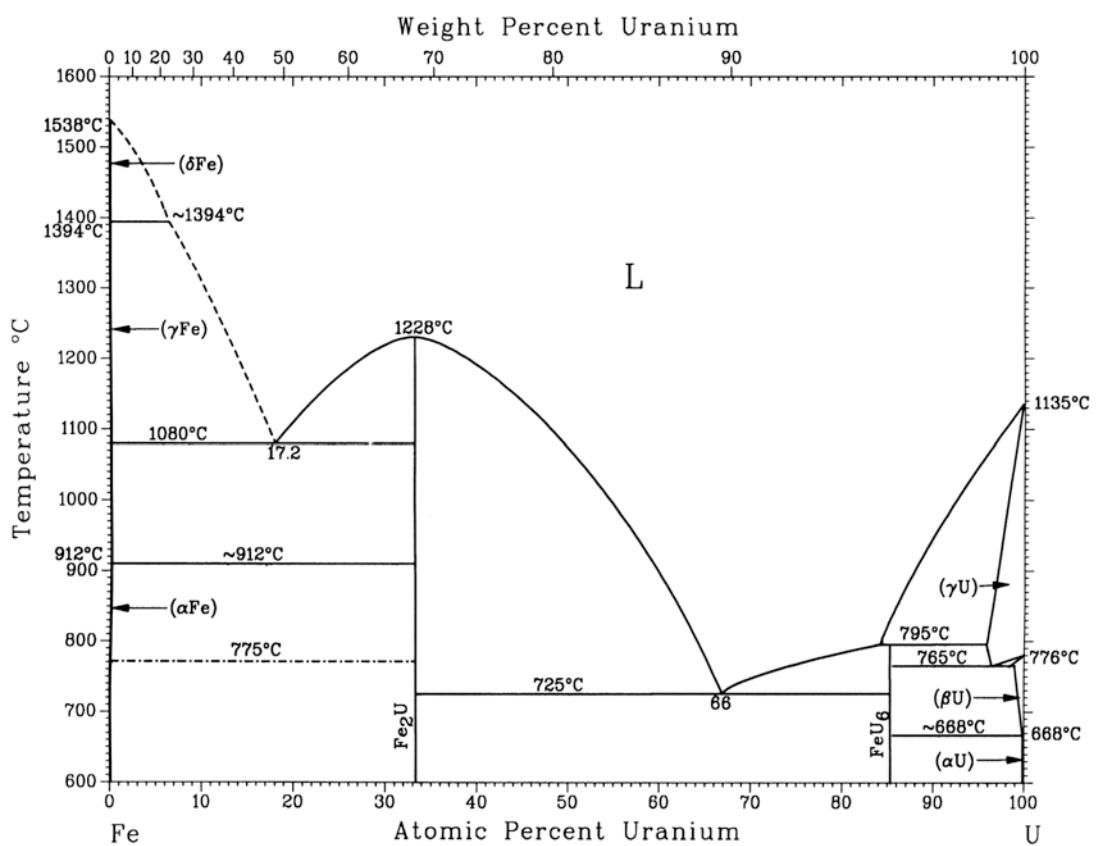


Figure 3.3 – Equilibrium Fe-U binary phase diagram [3].

**Ternary diagram**

Results on the B-Fe-U ternary diagram were previously reported by Valyovka et al. [18,19], who have identified only the  $\text{UFeB}_4$  and  $\text{UFe}_3\text{B}_2$  ternary compounds, and have proposed (incomplete) compatibility triangles in the isothermal section at 800 °C (Fig 3.4).

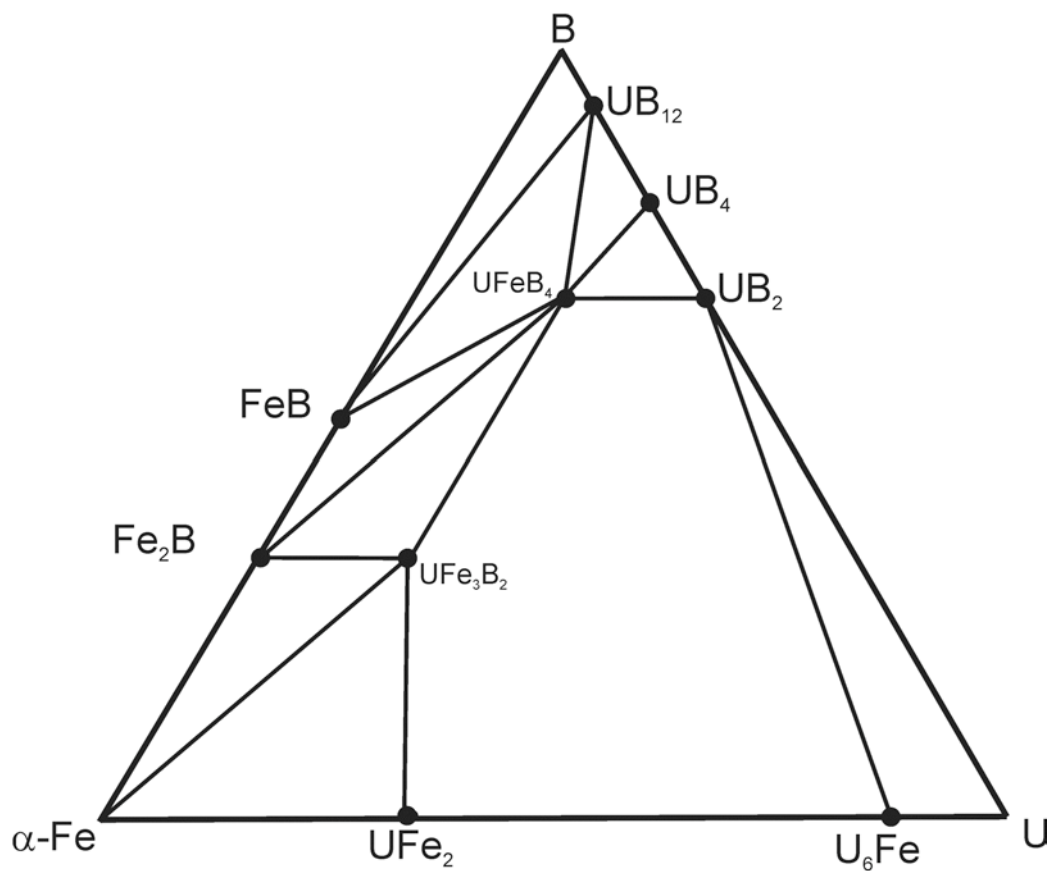


Figure 3.4 – Isothermal section of U-Fe-B at 800 °C [18,19].

### **3.3 Results**

The current systematic study of uB:vFe:wU alloys by PXRD and SEM/EDS revealed, in addition to  $\text{UFeB}_4$  and  $\text{UFe}_3\text{B}_2$  [18,19], the presence of three other ternary compounds: (i)  $\text{UFe}_4\text{B}$ , with a hexagonal structure closely related to the  $\text{CeCo}_4\text{B}$ -type structure ( $a = 0.4932(1)$  nm and  $c = 0.7037(2)$  nm); (ii)  $\text{U}_2\text{Fe}_{21}\text{B}_6$ , with a cubic  $\text{Cr}_{23}\text{C}_6$ -type structure ( $a = 1.0766(4)$  nm); and (iii)  $\text{UFe}_2\text{B}_6$  with the  $\text{CeCr}_2\text{B}_6$ -type structure ( $a = 0.3137(6)$  nm,  $b = 0.6181(11)$  nm,  $c = 0.8225(17)$  nm). The compounds through characterization is described in Chapter 4.

The B-Fe-U diagram is presented and discussed in four parts: B-rich section,  $0\% > \text{U} > 30\%$  and  $21\% > \text{B} > 50\%$  (at.%) section, Fe-rich section and U-rich section. The system comprises seven binary compounds and five ternary compounds, all with limited solubility ranges, which form 18 compatibility triangles and corresponding 18 ternary reactions. Selection of the appropriate compatibility triangle configurations from all possible combinations has been carried out based on microstructural observations combined with WDS and EDS analyses obtained from as-cast and annealed alloys.

The assumption of equilibrium conditions at bi and triphasic solid/liquid interfaces in binary alloys is valid for the cooling rates used in the current work [20]. If analogous equilibrium conditions are assumed for triphasic solid/liquid interfaces in ternary alloys, then the intimate microstructural contact between two solid phases in as-cast ternary alloys can be associated with an Alkemade line and a corresponding liquidus boundary line. The compatibility triangles between the limited solubility compounds in the B-Fe-U system and their ternary reactions have hence been inferred from two by two combinations of three phases presenting recurrent interfaces between them. Whenever possible the microstructures have been used to discuss the nature of the boundary lines [21].

Due to the high melting temperature of B-rich alloys, the annealing treatments did not induce significant changes in the microstructures. Consequently, the equilibria

(possibly metastable) at the B-rich section could only be inferred from the interfaces created during solidification. On the other hand, significant microstructural changes, such as globalization, grain growth and volume fraction variations, could be detected in annealed microstructures of the 0%>U>30% and 21%>B>50% (at.%), Fe-rich and U-rich sections. Consequently, in the latter sections the evolution of the annealed microstructures was used to complement the information on the phase equilibria inferred from the interfaces created during solidification.

WDS results are presented in 3.3.1. The liquidus projection is discussed in 3.3.2, where the position of the ternary reactions, as well as the configuration and direction of boundary lines, are proposed based on temperature considerations and microstructural observations. Indeed, all ternary reactions are discussed in terms of (i) representative microstructures evidencing the involved boundary lines; (ii) direction and nature of the boundary lines superimposed on the compatibility triangles; and (iii) corresponding four phase equilibrium triangles. PXRD, HTXRD, heating curves and DTA data are also presented in 3.3.2. Three representative isothermal sections and a specific vertical section are presented in 3.3.4 and 3.3.5, respectively.

### **3.3.1 WDS results**

The WDS results obtained for each phase observed in the microstructures are listed in Table 3.1, where an alphabetic phase/mixture labeling is also presented. The letters were assigned following the sequence of melting points/ranges as determined by DTA and heating curves. The phase mixtures originating from cooperative growth (i.e., resulting from *cotectic* boundary lines and ternary eutectic reactions) were labelled by a combination of the letters corresponding to the constituent phase.

Letter	Phase, <i>cotectic</i> mixture or ternary eutectic mixture	WDS results (at%)
A	UB <sub>4</sub>	-----
B	UB <sub>2</sub>	-----
C	B	-----
D	UB <sub>12</sub>	-----
E	UFeB <sub>4</sub>	U <sub>1.00</sub> Fe <sub>1.07(8)</sub> B <sub>4.42(6)</sub>
F	UFe <sub>2</sub> B <sub>6</sub>	U <sub>1.00</sub> Fe <sub>2.16(2)</sub> B <sub>6.18(9)</sub>
G	FeB	Fe <sub>1.00(7)</sub> B <sub>1.00(1)</sub>
H	UFe <sub>3</sub> B <sub>2</sub>	U <sub>1.00</sub> Fe <sub>3.14(4)</sub> B <sub>2.12(0)</sub>
J	α-Fe (previous γ-Fe)	-----
K	Fe <sub>2</sub> B	Fe <sub>1.88(3)</sub> B <sub>1.00(3)</sub>
L	Liquid	-----
M	UFe <sub>2</sub>	U <sub>1.00</sub> Fe <sub>1.97(4)</sub>
N	α-U	-----
O	UFe <sub>4</sub> B	U <sub>1.00</sub> Fe <sub>5.37(9)</sub> B <sub>1.14(8)</sub>
P	U <sub>2</sub> Fe <sub>21</sub> B <sub>6</sub>	U <sub>1.00</sub> Fe <sub>13.75(5)</sub> B <sub>4.54(1)</sub>
Q	U <sub>6</sub> Fe	-----
S	γ-U	-----
T	non-identified iron-rich phase	-----
CG	FeB + B	-----
EK	UFeB <sub>4</sub> + Fe <sub>2</sub> B	-----
HK	UFe <sub>3</sub> B <sub>2</sub> + Fe <sub>2</sub> B	-----
HM	UFe <sub>3</sub> B <sub>2</sub> + UFe <sub>2</sub>	-----
BM	UB <sub>2</sub> + UFe <sub>2</sub>	-----
KO	Fe <sub>2</sub> B + UFe <sub>4</sub> B	-----
MO	UFe <sub>2</sub> + UFe <sub>4</sub> B	-----
PO	U <sub>2</sub> Fe <sub>21</sub> B <sub>6</sub> + UFe <sub>4</sub> B	-----
JM	α-Fe + UFe <sub>2</sub> (previous γ-Fe + UFe <sub>2</sub> )	-----
JO	α-Fe + UFe <sub>4</sub> B (previous γ-Fe + UFe <sub>4</sub> B )	-----
MQ	UFe <sub>2</sub> + U <sub>6</sub> Fe	-----
JMO	α-Fe + UFe <sub>2</sub> + UFe <sub>4</sub> B (previous γ-Fe + UFe <sub>2</sub> + UFe <sub>4</sub> B )	-----
BMR	UB <sub>2</sub> + UFe <sub>2</sub> + U <sub>6</sub> Fe	-----

Table 3.1 – Phases, *cotectic* and ternary mixtures labeling and WDS results.

### **3.3.2 Liquidus projection**

The interfaces present in the microstructures, which originate from liquidus boundaries, have been used to determine the Alkemade lines defining each compatibility triangle. The ternary reactions to/from which the boundary lines converge/diverge are introduced by decreasing temperature order, and designated by  $R_{ij}$ , where  $i=1,2,\dots,18$  corresponds to the temperature sequence and  $j=I,II,III$  describes the reaction class. The boundary lines are denoted by  $l_k$ , where  $k=1, 2,\dots, 32$  refers to the numbering sequence that follows the ternary reaction order albeit with an additional criterion: in cases where two boundary lines are diverging from a ternary reaction (class III) a lower order is attributed to the line converging to the next highest temperature ternary reaction; in cases where two boundary lines are converging to a ternary reaction (class II) a lower order is attributed to the line originating from the previous ternary reaction of highest temperature. The dashed liquidus lines and the associated binary reactions present in the binary diagrams [1-3] have been assumed true in the liquidus projection construction. Microstructures of 15 alloys were used to evidence the boundary lines associated with each ternary reaction. The direction of decreasing temperature is indicated by an arrowhead on each boundary line.

### 3.3.2.1 B-rich section

The B-rich section of the ternary phase diagram comprehends two ternary reactions of class III (R1<sub>III</sub>, R2<sub>III</sub>), two ternary reactions of class II (R3<sub>II</sub>, and R6<sub>II</sub>) and two ternary reaction of class I (R4<sub>I</sub> and R5<sub>I</sub>).

#### PXRD

Figure 3.5 shows the experimental diffractograms of representative alloys, where the ternary and binary compounds on the B-rich section were best evidenced. The PXRD diffractogram obtained for the as-cast 77B:8Fe:15U alloy (Nr.1) shows that it is essentially constituted by  $UB_4$ . The diffractogram of the as-cast 67B:22Fe:11U alloy (Nr.3,  $UFe_2B_6$  stoichiometry) points to a predominance of the  $UFe_2B_6$  phase, however,  $UFeB_4$  peaks are also present. The diffractogram of the annealed 66B:17Fe:17U alloy (Nr.5,  $UFeB_4$  stoichiometry) shows major peaks indexed to  $UFeB_4$ , although the presence of  $UB_4$  can also be inferred. These results indicate that the  $UFeB_4$  liquidus field is close to its stoichiometric composition.

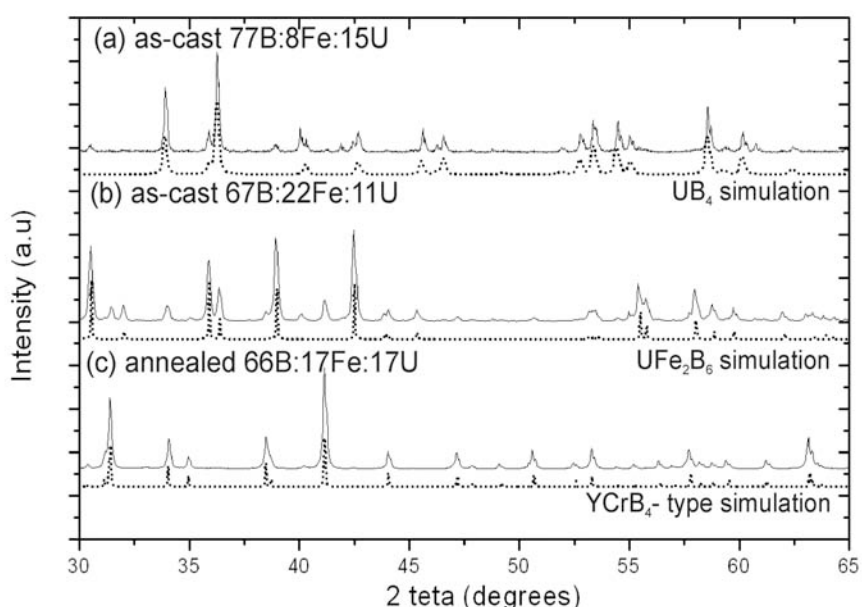


Figure 3.5 – Experimental powder X-ray diffractograms of (a) as-cast 77B:8Fe:15U (b) as-cast 67B:22Fe:11U ( $UFe_2B_6$  stoichiometry) and (c) annealed 66B:17Fe:17U ( $UFeB_4$  stoichiometry) alloys (respectively Nr. 1, 3, 5) where the presence of, respectively,  $UB_4$ ,  $UFe_2B_6$  and  $UFeB_4$  is evident. Dotted lines represent simulations for these compounds:  $UFe_2B_6$  crystallizes with  $CeCr_2B_6$ -type structure and  $UFeB_4$  crystallizes with a structure related to the  $YCrB_4$  one.

### Microstructures

Microstructures of five as-cast alloys will be used to evidence the boundary lines associated with each ternary reaction.

The microstructure of the 77B:8Fe:15U alloy (Nr.1) presents four distinct regions, designated as A, D, F and G (Figure 3.6 (a)). WDS and EDS results indicate that these regions correspond, respectively, to  $UB_4$ ,  $UB_{12}$ ,  $UFe_2B_6$  and FeB, which is in agreement with the PXRD results considering the apparent volume fraction of each phase.

The microstructure of the 67B:22Fe:11U (Nr. 3,  $UFe_2B_6$  stoichiometry) alloy presents six differentiated regions, designated as A, E, F, D, G and GC (Figures 3.6 (b) and (c)). WDS, EDS and PXRD results indicate that these phases correspond to, respectively,  $UB_4$ ,  $UFeB_4$ ,  $UFe_2B_6$ ,  $UB_{12}$  and FeB, while GC is a FeB + B *cotectic* mixture.

The microstructure of the 66B:17Fe:17U alloy (Nr.5,  $UFeB_4$  stoichiometry) presents three regions, designated by A, E and T (Figure 3.6 (d)). WDS and EDS analysis showed that these regions correspond, respectively, to  $UB_4$ ,  $UFeB_4$  and an iron-rich phase in agreement with the PXRD results by considering the apparent volume fraction of each phase (Figure 3.5 (c); notice that the low volume fraction of the iron-rich phase justifies an impaired detection by PXRD).

The microstructure of the 50B:25Fe:25U alloy (Nr.12) presents four different regions, designated by B, E, M and H (Figure 3.6 (e)). WDS, EDS and PXRD results indicated that the phases correspond, respectively, to  $UB_2$ ,  $UFeB_4$ ,  $UFe_2$  and  $UFe_3B_2$ . The primary solidification of  $UB_2$  occurring for the 50B:25Fe:25U alloy (Nr.12) implies an extended crystallization field for this compound.

The microstructure of the 43B:55Fe:2U alloy (Nr.18) presents four regions; E, G, K and EK (Figure 3.6 (f)). WDS, EDS and PXRD analyses indicate that these regions correspond, respectively, to  $UFeB_4$ , FeB,  $Fe_2B$ , while EK corresponds to  $UFeB_4$  +  $Fe_2B$  *cotectic* mixture.

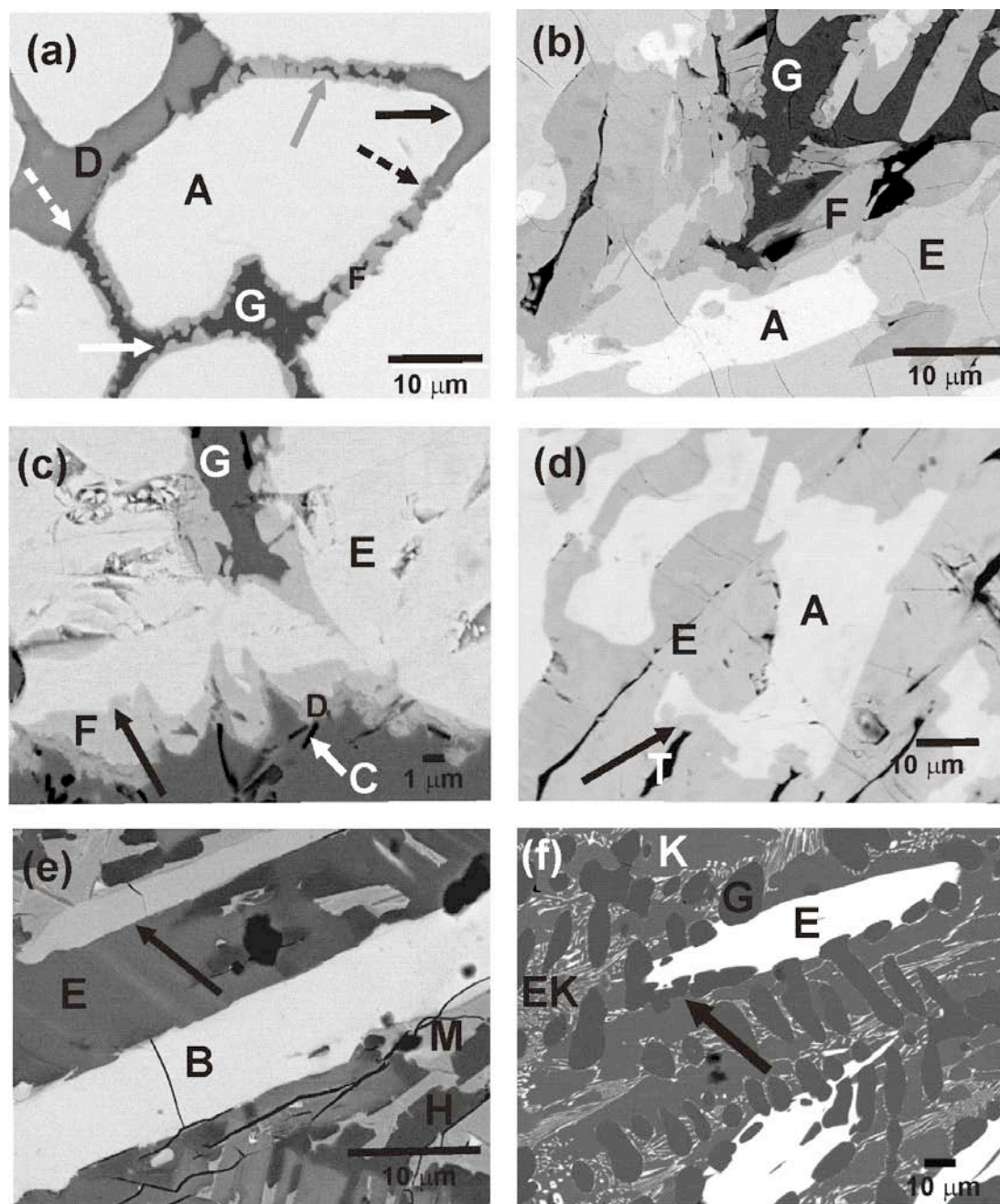


Figure 3.6 – BSE images of (a) 77B:8Fe:15U, (b, c) 67B:22Fe:11U ( $\text{UFe}_2\text{B}_6$  stoichiometry), (d) 66B:17Fe:17U ( $\text{UFeB}_4$  stoichiometry), (e) 50B:25Fe:25U and (f) 43B:55Fe:2U (respectively Nr. 1, 3, 5, 12, 18) alloys. Solid black arrows point to (a) A/D interface, (c) E/F interface, (d) A/E interface, (e) E/B interface and (f) E/G interface. In (a) the dashed black arrow points to the F/D interface, the dashed white arrow points to the D/G interface, the solid grey arrow points to the A/F interface and the solid white arrow points to the F/G interface. The white arrow in (c) indicates a C region. Phase labeling is listed in Table 3.1. The T phase in (d) could not be analyzed due to its reduced dimensions but X-ray maps showed a high iron content.

### Transition temperatures

Figure 3.7 presents heating curves obtained with an optical IR bichromatic pyrometer while heating 77B:8Fe:15U (Nr.1), 67B:22Fe:11U (Nr.3,  $\text{UFe}_2\text{B}_6$  stoichiometry) and 66B:17Fe:17U (Nr.5,  $\text{UFeB}_4$  stoichiometry) as-cast alloys in an induction furnace up to 2000 °C. The heating rate used for each alloy was selected for an optimized detection of the phase transitions. Heating and cooling experiments enabled to infer undercooling/superheating values below 20 °C. The assigning of specific phase transformations to the transitions detected in the curve derivatives was carried out based on the sequential melting of the phases and *cotectic* mixtures present in the microstructures and on their apparent volume fractions.

The heating curve of the 77B:8Fe:15U (Nr.1) alloy exhibited transitions at 1470 °C, 1580 °C and 1730 °C. The predominant phase in the microstructure is  $\text{UB}_4$  with a more modest presence of  $\text{UB}_{12}$ ,  $\text{UFe}_2\text{B}_6$  and FeB (see Figure 3.6 (a)). However, since this alloy is situated close to the binary diagram, melting of  $\text{UB}_4$  is likely to have occurred above 2000 °C and the observed transitions are not related to this compound. Taking into account the apparent solidification sequence (see Figure 3.6 (a)), the first transition at 1470 °C corresponds to FeB melting (possibly together with  $\text{UFe}_2\text{B}_6$  melting); the transition at 1560 °C corresponds to  $\text{UFe}_2\text{B}_6$  melting (possibly together with  $\text{UB}_{12}$  melting); and the one at 1730 °C to  $\text{UB}_{12}$  melting.

The heating curve of the 67B:22Fe:11U (Nr.3,  $\text{UFe}_2\text{B}_6$  stoichiometry) alloy exhibited four transitions. The predominant phases are:  $\text{UB}_4$ ,  $\text{UFeB}_4$ ,  $\text{UFe}_2\text{B}_6$  and FeB in solidification sequence order (see Figure 3.6 (b) and (c)). Therefore, the first transition, at 1410 °C, corresponds to melting of FeB (or possibly an eutectic mixture involving this phase); the next transition at 1470 °C to the ensuing  $\text{UFe}_2\text{B}_6$  melting (possibly together with  $\text{UB}_{12}$  melting); the next transition at 1560 °C to melting of  $\text{UFeB}_4$ , and the last transition at 1700 °C to the succeeding  $\text{UB}_4$  melting.

The heating curve of the 66B:17Fe:17U (Nr.5,  $\text{UFeB}_4$  stoichiometry) alloy exhibited three transitions. In the solidification sequence order the phases present in the microstructure are  $\text{UB}_4$ ,  $\text{UFeB}_4$  and an iron-rich phase (Figure 3.6 (d)). Therefore, the first transition at 1470 °C corresponds to melting of the iron-rich phase; the next transition at 1660 °C to melting of the predominant  $\text{UFeB}_4$ ; and the last transition at 1700 °C to melting of primary  $\text{UB}_4$ .

The alloys Nr.3 and 5 where  $\text{UB}_4$  melted at ~1700 °C are situated far away from the compound stoichiometric composition. This indicates that the temperature transition detected at 1730 °C for alloy Nr.1, which is situated much closer to the stoichiometric  $\text{UB}_4$  composition ( $T_m = 2495$  °C [2]), is likely to correspond to melting of  $\text{UB}_{12}$  and not to melting of  $\text{UB}_4$ .

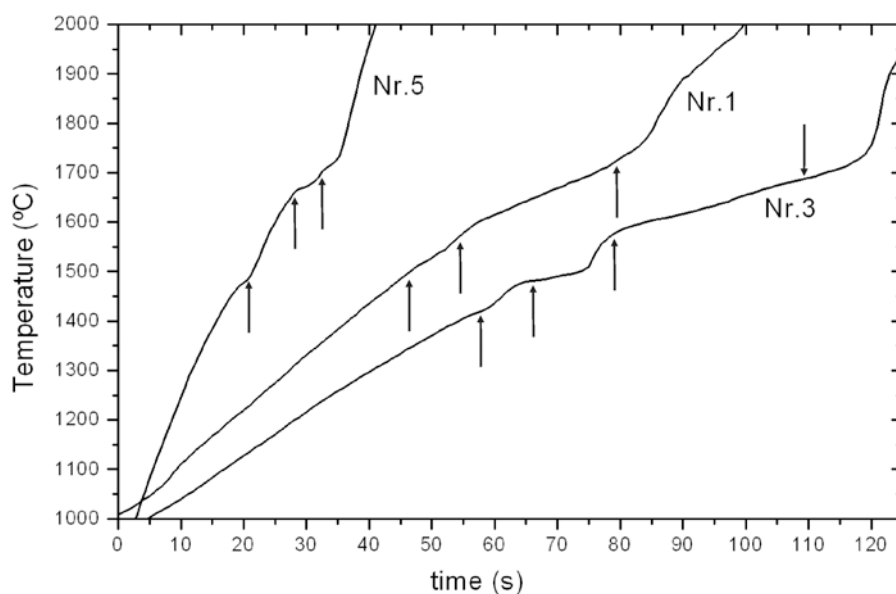


Figure 3.7 – Heating curves for representative B-rich alloys, (a) 77B:8Fe:15U (b) 67B:22Fe:11B ( $\text{UFe}_2\text{B}_6$  stoichiometry), (c) 66B:17Fe:17B ( $\text{UFeB}_4$  stoichiometry) as-cast alloys (respectively, Nr.1, 3 and 5).

**UB<sub>4</sub>-UB<sub>2</sub>-UFeB<sub>4</sub>****Compatibility triangle**

Two boundary lines can be inferred from the interfaces between UB<sub>4</sub> (regions A) and UFeB<sub>4</sub> (regions E), and between UB<sub>2</sub> (regions B) and UFeB<sub>4</sub> (regions E) (Figure 3.6 (d) and (e), respectively). A third boundary line originating in the binary B-U diagram [2] separates the UB<sub>4</sub> and UB<sub>2</sub> liquidus surfaces. These boundary lines imply the existence of an UB<sub>4</sub>-UB<sub>2</sub>-UFeB<sub>4</sub> compatibility triangle, and therefore of a ternary reaction involving the three phases.

**R<sub>1III</sub> ternary reaction**

The alloys in the UB<sub>4</sub>-UB<sub>2</sub>-UFeB<sub>4</sub> compatibility triangle (Nr.1, 3 and 5) showed evidence of UB<sub>4</sub>, UB<sub>2</sub> and UFeB<sub>4</sub> at the initial solidification stages, yet these phases tended to be absent at the final solidification regions. In addition, their heating curves exhibit the highest transition temperatures (~1700 °C). As a result, the R<sub>1</sub> ternary reaction corresponds to either a class II or a class III configuration, and not to a class I reaction, which would produce a local minimum in the liquidus surface. Furthermore, only the UB<sub>4</sub>/UB<sub>2</sub> boundary line (l<sub>1</sub>) is converging to the invariant ternary reaction from the binary diagram [2], while the UB<sub>4</sub>/UFeB<sub>4</sub> (l<sub>2</sub>) and UB<sub>2</sub>/UFeB<sub>4</sub> (l<sub>3</sub>) boundary lines, that cannot originate from (non-existing) higher temperature ternary reactions, must be diverging. As a result, R<sub>1</sub> is a class III ternary reaction and therefore lies outside the UB<sub>2</sub>-UB<sub>4</sub>-UFeB<sub>4</sub> compatibility triangle.

Since UB<sub>4</sub> and UB<sub>2</sub> are both congruent compounds, the boundary line separating their liquidus surfaces is of *cotectic* nature:



The dendritic morphology of UB<sub>4</sub> (regions A) in Figure 3.6 (d) indicates that primary crystallization in the 66B:17Fe:17U alloy (Nr.5, UFeB<sub>4</sub> stoichiometry) occurred with this phase. The fine discontinuities and concave recesses observed in the dendrite

arms of  $UB_4$  (see black arrow in Figure 3.6 (d)) suggest that these dendrites (regions A) were partly consumed during solidification of the surrounding phase and therefore that  $UFeB_4$  (regions E) was formed by a *reaction* boundary line:



The boundary line  $l_3$  can have either a *cotectic* or *reaction* nature [21,22], which could not be established from the microstructures.

The proposed equation for the ternary reaction is:

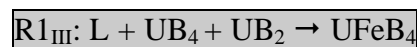


Table 3.2 presents the  $R1_{III}$  ternary reaction equation (left column), the boundary lines at the invariant point (centre column) and the four-phase equilibrium configuration (right column). At  $R1_{III}$  three phases interact isothermally upon cooling to form a new phase, i.e.,  $UB_4$ ,  $UB_2$ , and  $L(R1_{III})$ , located at the vertices of a horizontal triangular reaction plane, combine to form  $UFeB_4$ , whose composition lies inside the triangle (see right column of Table 3.2). The three-phase field  $UB_4 + UB_2 + L$  descends from higher temperatures to the ternary peritectic temperature, and three-phase regions  $UB_4 + L + UFeB_4$ ,  $UB_2 + L + UFeB_4$  and  $UB_4 + UB_2 + UFeB_4$  are issued beneath and proceed to lower temperatures. The ternary reaction configuration demands the  $UB_4$ - $UB_2$ - $UFeB_4$  triangle to lie inside the  $UB_4$ - $UB_2$ - $L(R1_{III})$  one at the ternary reaction temperature, which roughly positions the  $R1_{III}$  ternary reaction.

**UB<sub>4</sub>-UFeB<sub>4</sub>-UFe<sub>2</sub>B<sub>6</sub>****Compatibility triangle**

The intimate microstructural contact between UB<sub>4</sub> and UFeB<sub>4</sub> (respectively, regions A and E in Figure 3.6 (b)), UB<sub>4</sub> and UFe<sub>2</sub>B<sub>6</sub> (respectively, regions A and F in Figure 3.6 (a)) and UFeB<sub>4</sub> and UFe<sub>2</sub>B<sub>6</sub> (respectively, regions E and F in Figure 3.6 (c)) implies the existence of an UB<sub>4</sub>-UFeB<sub>4</sub>-UFe<sub>2</sub>B<sub>6</sub> compatibility triangle and a corresponding ternary reaction involving the three phases.

**R<sub>2III</sub> ternary reaction**

The UB<sub>4</sub>/UFeB<sub>4</sub> boundary line (l<sub>2</sub>) that stems from the higher temperature R1<sub>III</sub> is converging to R2. The other two boundary lines involving UFe<sub>2</sub>B<sub>6</sub> must diverge from R2 toward lower temperature ternary reactions, as there are no higher temperature invariant points from where they can originate. As a result, R2 is a class III ternary reaction, to where only l<sub>2</sub> is converging and from where both UB<sub>4</sub>/UFe<sub>2</sub>B<sub>6</sub> (l<sub>5</sub>) and UFeB<sub>4</sub>/UFe<sub>2</sub>B<sub>6</sub> (l<sub>6</sub>) boundary lines are diverging. Therefore, this invariant point lies outside the UB<sub>4</sub>-UFeB<sub>4</sub>-UFe<sub>2</sub>B<sub>6</sub> compatibility triangle.

As discussed for R1<sub>III</sub> the l<sub>2</sub> boundary line presents a *reaction* nature:



The microstructure of the 77B:8Fe:15U alloy (Nr.1) evidences consumption of UB<sub>4</sub> in association with UFe<sub>2</sub>B<sub>6</sub> formation (see grey arrow in Figure 3.6 (a)), which demonstrates a *reaction* nature for l<sub>5</sub>:



The microstructure of the 67B:22Fe:11U alloy (Nr.3, UFe<sub>2</sub>B<sub>6</sub> stoichiometry) suggests UFeB<sub>4</sub> encapsulation in association with UFe<sub>2</sub>B<sub>6</sub> formation (see black arrow in Figure 3.6 (c)), which is compatible with a *reaction* nature for l<sub>6</sub>:



The proposed equation for the ternary reaction is:



Table 3.2 presents the  $\text{R2}_{\text{III}}$  ternary reaction equation (left column), the boundary lines at the invariant point (centre column) and the four-phase equilibrium configuration (right column). At  $\text{R2}_{\text{III}}$  three phases interact isothermally upon cooling to form a new phase, i.e.,  $\text{UB}_4$ ,  $\text{UFeB}_4$  and  $\text{L}(\text{R2}_{\text{III}})$ , located at the vertices of a horizontal triangular reaction plane, combine to form  $\text{UFe}_2\text{B}_6$ , whose composition lies inside the triangle (see right column of Table 3.2). The three-phase field  $\text{UB}_4 + \text{UFeB}_4 + \text{L}$  descends from higher temperatures to the ternary peritectic temperature, and three-phase regions  $\text{UFeB}_4 + \text{UFe}_2\text{B}_6 + \text{L}$ ,  $\text{UB}_4 + \text{UFe}_2\text{B}_6 + \text{L}$  and  $\text{UB}_4 + \text{UFeB}_4 + \text{UFe}_2\text{B}_6$  are issued beneath and proceed to lower temperatures. The ternary reaction configuration demands the  $\text{UB}_4$ - $\text{UFeB}_4$ - $\text{UFe}_2\text{B}_6$  triangle to lie inside the  $\text{UB}_4$ - $\text{UFeB}_4$ - $\text{L}(\text{R2}_{\text{III}})$  one, which roughly positions the  $\text{R2}_{\text{III}}$  ternary reaction.

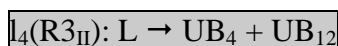
**UB<sub>4</sub>-UB<sub>12</sub>-UFe<sub>2</sub>B<sub>6</sub>****Compatibility triangle**

The intimate microstructural contact observed in Figure 3.6 (a) to (c) between UB<sub>4</sub> (regions A) and UFe<sub>2</sub>B<sub>6</sub> (regions F), UB<sub>4</sub> (regions A) and UB<sub>12</sub> (regions D), and UFe<sub>2</sub>B<sub>6</sub> (regions F) and UB<sub>12</sub> (regions D) implies the existence of an UB<sub>4</sub>-UB<sub>12</sub>-UFe<sub>2</sub>B<sub>6</sub> compatibility triangle and a corresponding ternary reaction involving the three phases.

**R<sub>3II</sub> ternary reaction**

The binary UB<sub>4</sub> + UB<sub>12</sub> eutectic in the B-U phase diagram occurs at 2145 °C [2], which is higher than the transition temperatures detected in the heating curves of the B-Fe-U alloys. Therefore the UB<sub>4</sub>/UB<sub>12</sub> boundary line (l<sub>4</sub>) converges to the lower temperature R<sub>3</sub> from the binary diagram. Likewise, the UB<sub>4</sub>/UFe<sub>2</sub>B<sub>6</sub> boundary line (l<sub>5</sub>), which stems from the higher temperature R<sub>2III</sub> ternary reaction, converges to R<sub>3</sub>. The UB<sub>12</sub>/UFe<sub>2</sub>B<sub>6</sub> boundary line (l<sub>11</sub>) must diverge from R<sub>3</sub> toward a lower temperature ternary reaction, as there is no higher temperature invariant point from where it can originate. This configuration corresponds to a class II ternary reaction lying outside the UB<sub>4</sub>-UB<sub>12</sub>-UFe<sub>2</sub>B<sub>6</sub> compatibility triangle [21, 22].

The boundary line between the UB<sub>4</sub> and UB<sub>12</sub> liquidus surfaces cannot assume a *reaction* nature due to the congruent melting of the compounds, and is therefore converging to R<sub>3III</sub> with a *cotectic* nature:



As discussed for R<sub>2III</sub> the l<sub>5</sub> boundary line presents a *reaction* nature:



The microstructures of the 77B:8Fe:15U (Nr.1) and 67B:22Fe:11U (Nr.3, UFe<sub>2</sub>B<sub>6</sub> stoichiometry) alloys show that UFe<sub>2</sub>B<sub>6</sub> (regions F) forms prior to UB<sub>12</sub> (regions D)

(see Figure 3.6 (a) and (c). Therefore,  $\text{UFe}_2\text{B}_6$  cannot originate from a *reaction* transition involving  $\text{UB}_{12}$  consumption. On the other hand,  $\text{UB}_{12}$  is a congruent compound that cannot originate from a *reaction* transition involving  $\text{UFe}_2\text{B}_6$  consumption. As a result, the  $l_{11}$  boundary line must necessarily present a *cotectic* nature:



The proposed equation for the ternary reaction is:



Table 3.2 presents the  $\text{R3}_{\text{II}}$  ternary reaction equation (left column), the boundary lines at the invariant point (centre column) and the four-phase equilibrium configuration (right column). At  $\text{R3}_{\text{II}}$  two phases,  $\text{UB}_4$  and  $\text{L}(\text{R3}_{\text{II}})$ , interact to form two other phases,  $\text{UB}_{12}$  and  $\text{UFe}_2\text{B}_6$ . Two three-phase regions,  $\text{UB}_4 + \text{UFe}_2\text{B}_6 + \text{L}$  and  $\text{UB}_4 + \text{UB}_{12} + \text{L}$ , descend from higher temperatures toward the four-phase reaction plane, where they meet to form a horizontal trapezium,  $\text{UB}_4 + \text{UB}_{12} + \text{UFe}_2\text{B}_6 + \text{L}$ , where the four phases are in equilibrium. Below this temperature two other three-phase regions form,  $\text{UB}_4 + \text{UB}_{12} + \text{UFe}_2\text{B}_6$  and  $\text{UB}_{12} + \text{UFe}_2\text{B}_6 + \text{L}$ . The  $\text{UB}_4$  crystallization field is delimited by the lines converging to  $\text{R3}_{\text{II}}$  indicating that the ternary reaction is situated across  $\text{UB}_4$  on the left side of the  $\text{UFe}_2\text{B}_6$ - $\text{UB}_{12}$  Alkemade line to allow the formation of the low temperature  $\text{UB}_{12}$ - $\text{UFe}_2\text{B}_6$ - $\text{L}$  triangle. This trapezium configuration shows that  $\text{R3}_{\text{II}}$  lies in the  $\text{UB}_{12}$ - $\text{UFe}_2\text{B}_6$ - $\text{FeB}$  compatibility triangle.

**UB<sub>12</sub>-UFe<sub>2</sub>B<sub>6</sub>-FeB****Compatibility triangle**

The intimate microstructural contact observed in Figure 3.6 (a) between UFe<sub>2</sub>B<sub>6</sub> and UB<sub>12</sub> (regions F and D, respectively), UFe<sub>2</sub>B<sub>6</sub> and FeB (regions F and G, respectively), and UB<sub>12</sub> and FeB (regions D and G, respectively) implies the existence of an UB<sub>12</sub>-UFe<sub>2</sub>B<sub>6</sub>-FeB compatibility triangle and a corresponding ternary reaction involving the three phases.

**R<sub>4I</sub> ternary reaction**

The UFe<sub>2</sub>B<sub>6</sub>/UB<sub>12</sub> boundary line (l<sub>11</sub>) stems from the higher temperature R<sub>3II</sub> ternary reaction and converges to R<sub>4</sub>. As discussed for R<sub>3II</sub>, this line is *cotectic* and its nature is not expected to change since it generates compounds with limited solubility. The fact that the extension of a *cotectic* boundary line must cross the corresponding Alkemade line [21,22] positions R<sub>4</sub> to the left of the UFe<sub>2</sub>B<sub>6</sub>/FeB Alkemade line. Only a class I ternary reaction, situated in the UB<sub>12</sub>-UFe<sub>2</sub>B<sub>6</sub>-FeB compatibility triangle, is compatible with this requirement. Therefore, the UB<sub>12</sub>/FeB (l<sub>12</sub>) and UFe<sub>2</sub>B<sub>6</sub>/FeB (l<sub>13</sub>) boundary lines converge also to R<sub>4</sub>.

The l<sub>12</sub> boundary line cannot assume a *reaction* nature due to congruent melting of the compounds, and is therefore converging to R<sub>4I</sub> with a *cotectic* nature:



The l<sub>13</sub> boundary line is also *cotectic* since UFe<sub>2</sub>B<sub>6</sub> solidifies prior to FeB (Figure 3.6 (a) to (c)) and therefore cannot form by a *reaction* transition involving FeB consumption:



The proposed equation for the ternary reaction is:

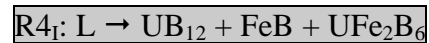


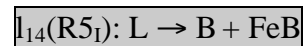
Table 3.2 presents the  $R4_1$  ternary reaction equation (left column), the boundary lines at the invariant reaction (centre column) and the four-phase equilibrium configuration (right column). The ternary reaction  $R4_1$  involves an isothermal decomposition of the liquid phase into three different solid phases:  $UB_{12}$ ,  $UFe_2B_6$  and  $FeB$ . The three-phase fields  $UB_{12} + FeB + L$ ,  $UB_{12} + UFe_2B_6 + L$  and  $UFe_2B_6 + FeB + L$ , separated by boundary lines, terminate on the ternary eutectic plane  $UB_{12} + UFe_2B_6 + FeB + L$ . The three-phase field  $UB_{12} + UFe_2B_6 + FeB$  forms below the ternary eutectic temperature.

**B-UB<sub>12</sub>-FeB****Compatibility triangle**

The intimate microstructural contact observed in Figure 3.6 (a) to (c) between B (regions C) and FeB (regions G), and between UB<sub>12</sub> (regions D) and FeB (regions G), together with the boundary line between the B and UB<sub>12</sub> crystallization fields (originating from the B-U diagram [2]), implies the existence of an B-UB<sub>12</sub>-FeB compatibility triangle and a corresponding ternary reaction involving the three phases.

**R<sub>5I</sub> ternary reaction**

The B, UB<sub>12</sub> and FeB phases, that melt congruently and have extremely limited solubilities, form necessarily a ternary eutectic inside the B-UB<sub>12</sub>-FeB compatibility triangle, to where the three boundary lines converge with a *cotectic* nature. Consequently, the B/UB<sub>12</sub> (I<sub>15</sub>) and B/FeB (I<sub>14</sub>) boundary lines that stem from the binary diagrams [2,1] converge to R<sub>5I</sub>. Furthermore, the UB<sub>12</sub>/FeB boundary line (I<sub>12</sub>) crosses the respective Alkemade line, where it reaches a maximum temperature “m”, and subsequently converges to R<sub>5I</sub>. Therefore:



The proposed equation for the ternary reaction is:



Table 3.2 presents the R<sub>5I</sub> ternary reaction equation (left column), the boundary lines at the invariant point (centre column) and the four-phase equilibrium configuration (right column). The ternary reaction R<sub>5I</sub> involves an isothermal decomposition of the liquid phase into three different solid phases: UB<sub>12</sub>, B and FeB. The three-phase fields UB<sub>12</sub> + FeB + L, UB<sub>12</sub> + B + L and B + FeB + L are separated by binary *cotectic* boundary lines and terminate on the ternary eutectic plane UB<sub>12</sub> + B + FeB + L. The three-phase field UB<sub>12</sub> + B + FeB forms below the ternary eutectic temperature. Microstructural evidence of this ternary (divorced) eutectic can be found in the 67B:22Fe:11U alloy (Nr.3) microstructures (Figure 3.6 (c)).

**UFeB<sub>4</sub>-UFe<sub>2</sub>B<sub>6</sub>-FeB****Compatibility triangle**

The intimate microstructural contact observed in Figure 3.6 (a), (c) and (f) between UFeB<sub>4</sub> and UFe<sub>2</sub>B<sub>6</sub> (regions E and F, respectively), UFe<sub>2</sub>B<sub>6</sub> and FeB (regions F and G, respectively), and UFeB<sub>4</sub> and FeB (regions E and G, respectively) implies the existence of an UFeB<sub>4</sub>-UFe<sub>2</sub>B<sub>6</sub>-FeB compatibility triangle and a corresponding ternary reaction involving the three phases.

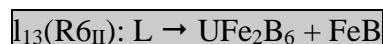
**R6<sub>II</sub> ternary reaction**

The UFeB<sub>4</sub>/UFe<sub>2</sub>B<sub>6</sub> boundary line (*l*<sub>6</sub>), that stems from the higher temperature R3<sub>II</sub>, converges to the R6 ternary reaction. Moreover, the *l*<sub>16</sub> boundary line, which separates the UFeB<sub>4</sub> and FeB crystallization fields, must diverge from R6 toward a lower temperature ternary reaction, as there is no higher temperature invariant point from where it can originate. This fact dismisses a class I ternary reaction and implies that R6 lies outside the UFeB<sub>4</sub>-UFe<sub>2</sub>B<sub>6</sub>-FeB compatibility triangle. The four-phase equilibrium geometry consistent with a class III reaction of the types L + FeB + UFeB<sub>4</sub> → UFe<sub>2</sub>B<sub>6</sub> or L + FeB + UFe<sub>2</sub>B<sub>6</sub> → UFeB<sub>4</sub>, would position R6 close to R3<sub>II</sub> or R1<sub>III</sub>, respectively. Since this is not compatible with the previously defined liquidus surface configuration, a class II ternary reaction has been inferred for R6. As a result, *l*<sub>13</sub> converges both to R4<sub>I</sub> and R6<sub>II</sub> since it crosses the respective Alkemade line where it reaches a temperature maximum “m”.

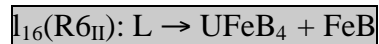
As discussed for R2<sub>III</sub>, the *l*<sub>6</sub> boundary line presents a *reaction* nature. Therefore:



As discussed for R4<sub>I</sub>, the *l*<sub>13</sub> boundary line presents a *cotectic* nature. Therefore:



The  $\text{UFeB}_4/\text{FeB}$  boundary line ( $I_{16}$ ) has a *cotectic* nature since  $\text{FeB}$  is a congruent compound and  $\text{UFeB}_4$ , which solidifies prior to  $\text{FeB}$  (Figure 3.6 (b) and (f)), cannot form by a *reaction* transition through  $\text{FeB}$  consumption:



The proposed equation for the ternary reaction is:

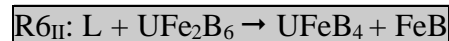


Table 3.2 presents the  $R6_{II}$  ternary reaction equation (left column), the boundary lines at the invariant reaction (centre column) and the four-phase equilibrium configuration (right column). At  $R6_{II}$  two phases,  $\text{UFe}_2\text{B}_6$  and  $L(R6_{II})$ , interact to form  $\text{UFeB}_4$  and  $\text{FeB}$ . Two three-phase regions,  $\text{UFeB}_4 + \text{UFe}_2\text{B}_6 + L$  and  $\text{UFe}_2\text{B}_6 + \text{FeB} + L$ , descend from higher temperatures toward the four-phase reaction plane, where they meet to form a horizontal trapezium,  $\text{UFeB}_4 + \text{UFe}_2\text{B}_6 + \text{FeB} + L$ , where the four phases are in equilibrium. Below this temperature two other three-phase regions form,  $\text{UFeB}_4 + \text{UFe}_2\text{B}_6 + \text{FeB}$  and  $\text{UFeB}_4 + \text{FeB} + L$ . The  $\text{UFe}_2\text{B}_6$  crystallization field is delimited by the lines converging to  $R6_{II}$  indicating that the ternary reaction is situated across  $\text{UFe}_2\text{B}_6$  below the  $\text{UFeB}_4\text{-FeB}$  Alkemade line to allow the formation of the low temperature  $\text{UFeB}_4\text{-FeB-L}$  triangle. This trapezium configuration shows that  $R6_{II}$  lies in the  $\text{UFeB}_4\text{-FeB-Fe}_2\text{B}$  compatibility triangle.

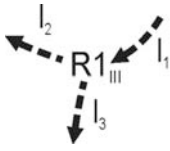
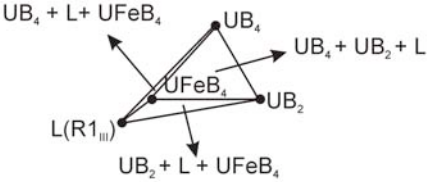
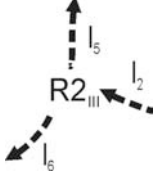
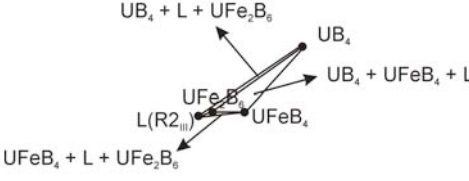
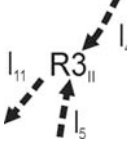
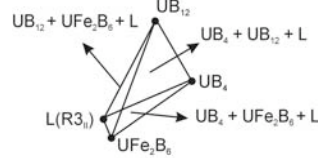
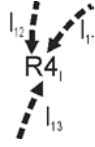
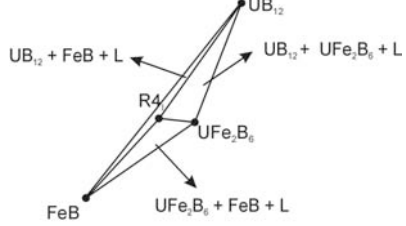
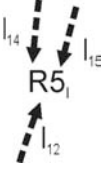
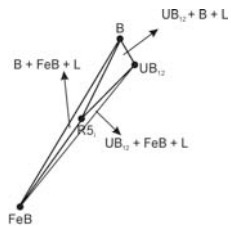
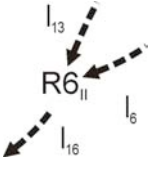
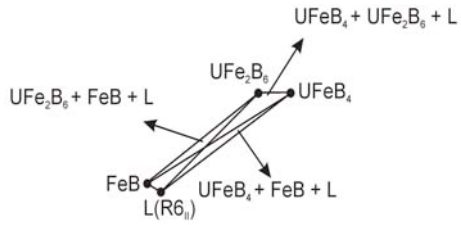
Boundary lines associated with ternary reactions	Four-phase configuration
$L + UB_4 + UB_2 \rightarrow UFeB_4$ 	$I_1(R1_{III}): L \rightarrow UB_4 + UB_2$ (from binary diagram [2]) $I_2(R1_{III}): L + UB_4 \rightarrow UFeB_4$ (regions A $\rightarrow$ regions E) $I_3(R1_{III}): UB_2/UFeB_4$ (regions B/regions E) 
$L + UB_4 + UFeB_4 \rightarrow UFe_2B_6$ 	$I_2(R2_{III}): L + UB_4 \rightarrow UFeB_4$ (regions A $\rightarrow$ regions E) $I_5(R2_{III}): L + UB_4 \rightarrow UFe_2B_6$ (regions A $\rightarrow$ regions F) $I_6(R2_{III}): L + UFeB_4 \rightarrow UFe_2B_6$ (regions E $\rightarrow$ regions F) 
$L + UB_4 \rightarrow UB_{12} + UFe_2B_6$ 	$I_4(R3_{II}): L \rightarrow UB_4 + UB_{12}$ (from binary diagram [2]) $I_5(R3_{II}): L + UB_4 \rightarrow UFe_2B_6$ (regions A $\rightarrow$ regions F) $I_{11}(R3_{II}): L \rightarrow UB_{12} + UFe_2B_6$ (regions F + regions D) 
$L \rightarrow UB_{12} + UFe_2B_6 + FeB$ 	$I_{11}(R3_{II}): L \rightarrow UB_{12} + UFe_2B_6$ (regions F + regions D) $I_{12}(R4_I): L \rightarrow UB_{12} + FeB$ (region D + region G) $I_{13}(R4_I): L \rightarrow FeB + UFe_2B_6$ (region F + region D) 
$L \rightarrow B + UB_{12} + FeB$ 	$I_{12}(R5_I): L \rightarrow UB_{12} + FeB$ (regions D + regions G) $I_{14}(R5_I): L \rightarrow B + FeB$ (from binary diagram [1]) $I_{15}(R5_I): L \rightarrow UB_{12} + B$ (from binary diagram [2]) 
$L + UFe_2B_6 \rightarrow UFeB_4 + FeB$ 	$I_6(R2_{III}): L + UFeB_4 \rightarrow UFe_2B_6$ (regions E $\rightarrow$ regions F) $I_{13}(R6_{II}): L \rightarrow UFe_2B_6 + FeB$ (regions F + regions G) $I_{16}(R6_{II}): L \rightarrow UFeB_4 + FeB$ (regions E + regions G) 

Table 3.2 – Boundary lines for R1<sub>III</sub>, R2<sub>III</sub>, R3<sub>II</sub>, R4<sub>I</sub>, R5<sub>I</sub> and R6<sub>II</sub> ternary reactions associated with the four-phase configuration.

### Liquidus projection

Figure 3.8 presents the liquidus projection at the B-rich section together with the Alkemade lines defining the phase equilibria. Figure 3.9 shows the position of alloys Nr.1, 3, 7, 5, 12 and 18. The grey lettering indicates primary crystallization fields.

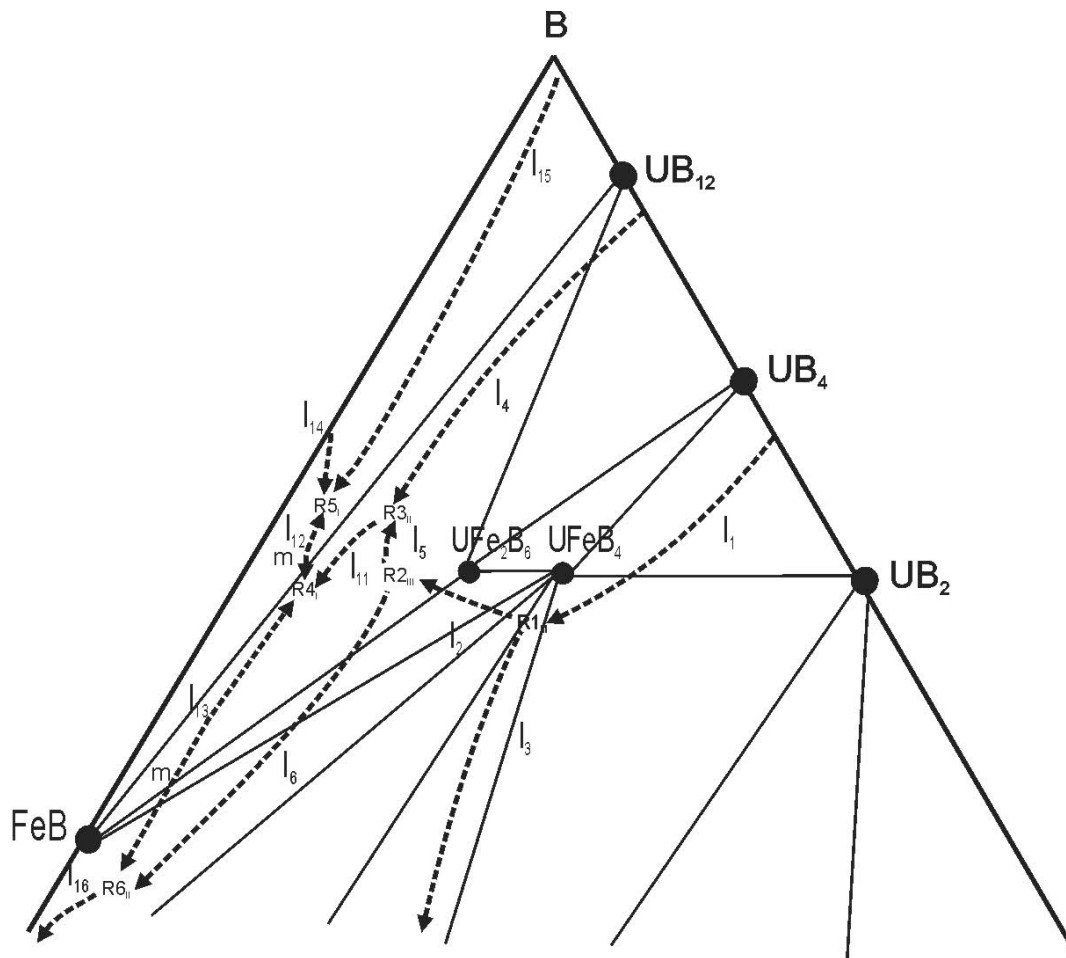


Figure 3.8 – Liquidus projection in the B-rich section showing R1<sub>III</sub>, R2<sub>III</sub>, R3<sub>II</sub>, R4<sub>I</sub>, R5<sub>I</sub> and R6<sub>II</sub> where solid lines represent Alkemade lines and dashed lines indicate the liquid composition at the boundary lines.



### Solidification path

Figure 3.10 shows the solidification path of the alloys whose microstructures have been described.

In agreement with the liquidus surface proposed, the solidification path followed by the 66B:17Fe:17U (Nr.5,  $\text{UFeB}_4$  stoichiometry) alloy can be described as:  $L \rightarrow \text{UB}_4$  (regions A)  $\rightarrow \text{UFeB}_4$  (regions E)  $\rightarrow$  iron rich phase (regions T) (Figure 3.6 (d)). The primary solidification of  $\text{UB}_4$  implies that this alloy is situated inside the  $\text{UB}_4$  crystallization field, which is delimited by the  $l_1$  and  $l_2$  boundary lines. According to the detected transition temperatures (Figure 3.7), solidification of  $\text{UB}_4$  (above  $l_2$ ) occurred at 1700 °C and formation of  $\text{UFeB}_4$  (below  $l_2$ ) occurred at 1660 °C. This suggests that the two transitions are proximal (see Figure 3.10). The fact that  $l_2$  is diverging from  $\text{R1}_{\text{III}}$  enables to infer that this ternary reaction occurs at  $T > 1660$  °C.

The solidification path of the 67B:22Fe:11U alloy (Nr.3,  $\text{UFe}_2\text{B}_6$  stoichiometry) was:  $L \rightarrow \text{UB}_4$  (regions A)  $\rightarrow \text{UFeB}_4$  (regions E)  $\rightarrow \text{UFe}_2\text{B}_6$  (regions F)  $\rightarrow \text{UFe}_2\text{B}_6$  (regions F) +  $\text{UB}_{12}$  (regions D) +  $\text{FeB}$  (regions G)  $\rightarrow \text{UB}_{12}$  (regions D) +  $\text{FeB}$  (regions G) + B (regions C) (Figure 3.6 (b) and (c)). The primary solidification of  $\text{UB}_4$  indicates that the alloy is situated inside the crystallization field of this compound. According to the transition temperatures (Figure 3.7), solidification of  $\text{UB}_4$  (above  $l_2$ ) occurred at 1700 °C; formation of  $\text{UFeB}_4$  (below  $l_2$ ) occurred at 1560 °C; formation of  $\text{UFe}_2\text{B}_6$  (below  $l_6$ ) occurred at 1470 °C. This implies that  $\text{R4}_{\text{I}}$  occurs at  $T < 1470$  °C. Solidification ended in the ternary  $\text{R5}_{\text{I}}$  eutectic at 1410 °C due to the proximity of the  $\text{R4}_{\text{I}}$  and  $\text{R5}_{\text{I}}$  reactions and possible local composition variations. Since  $l_2$  converges to  $\text{R2}_{\text{III}}$  this ternary reaction occurs at  $T \sim 1560$  °C. The fact that the solidification path of alloy Nr.3 crosses both  $l_2$  and  $l_6$  is consistent with their *reaction* nature and indicates that  $\text{R2}_{\text{III}}$  is situated to the left of alloy Nr.3 (Figure 3.10).

According to liquidus surface proposed, the solidification path followed by the 77B:8Fe:15U (Nr.1) alloy was:  $L \rightarrow \text{UB}_4$  (regions A)  $\rightarrow \text{UB}_4$  (regions A) +  $\text{UB}_{12}$  (regions D)  $\rightarrow \text{UB}_{12}$  (regions D) +  $\text{UFe}_2\text{B}_6$  (regions F)  $\rightarrow \text{UFe}_2\text{B}_6$  (regions F) +  $\text{FeB}$

(regions G) (Figure 3.6 (a)). According to the results presented in Figure 3.7,  $UB_4$  solidified at  $T > 2000$  °C;  $UB_4 + UB_{12}$  ( $l_4$ ) formed at 1730 °C;  $UFe_2B_6 + UB_{12}$  ( $R_{3II}$  and  $l_{11}$ ) solidified at 1560 °C; and  $UFe_2B_6 + UB_{12} + FeB$  ( $R_{4I}$ ) formed at 1470 °C.

Since  $l_6$  diverges from  $R_{2II}$ , where  $T \sim 1560$  °C, and converges to  $R_{6II}$ , this latter ternary reaction occurs at  $T < 1560$  °C.

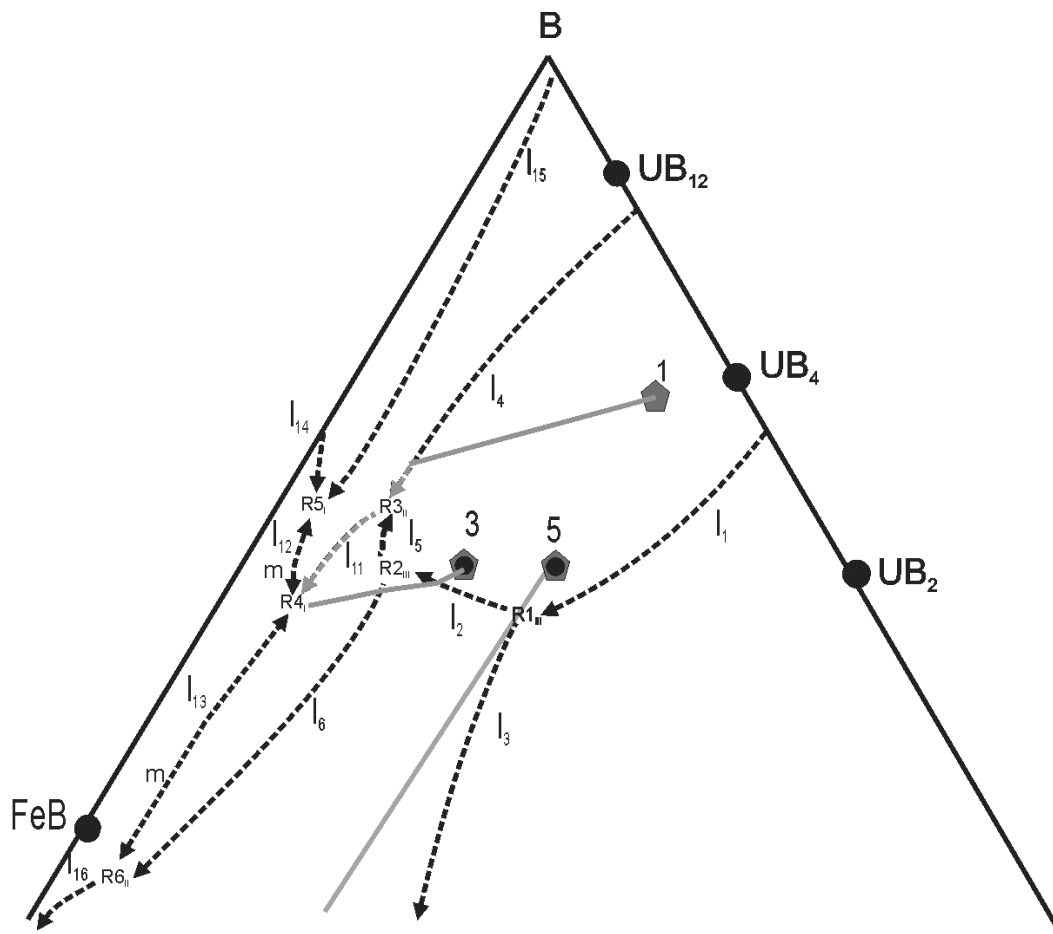


Figure 3.10 – Solidification path for alloys 77B:8Fe:15U, 67B:22Fe:11U ( $UFe_2B_6$  stoichiometry), 66B:17Fe:17U ( $UFeB_4$  stoichiometry) alloys (respectively Nr.1, 3 and 5). Dashed lines represent the liquid composition at the boundary lines.

## Reaction scheme

Figure 3.11 shows the reaction scheme of the B-rich section with indication of the transition temperatures. The ternary reactions are presented by decreasing temperature order, together with the binary reactions stemming from the B-Fe and B-U binary phase diagrams. U-Fe binary reactions do not converge to the ternary reactions discussed above, and therefore have not been represented. The arrowed lines represent the boundary lines that diverge/converge from the ternary reactions. The low temperature regions issued from the ternary reactions are listed underneath each ternary reaction equation. Temperature maxima, represented by “m”, exist in the  $I_{12}$  boundary line, which joins  $R5_I$  and  $R4_I$ , and in the  $I_{13}$  boundary line, which joins  $R4_I$  and  $R6_{II}$ .

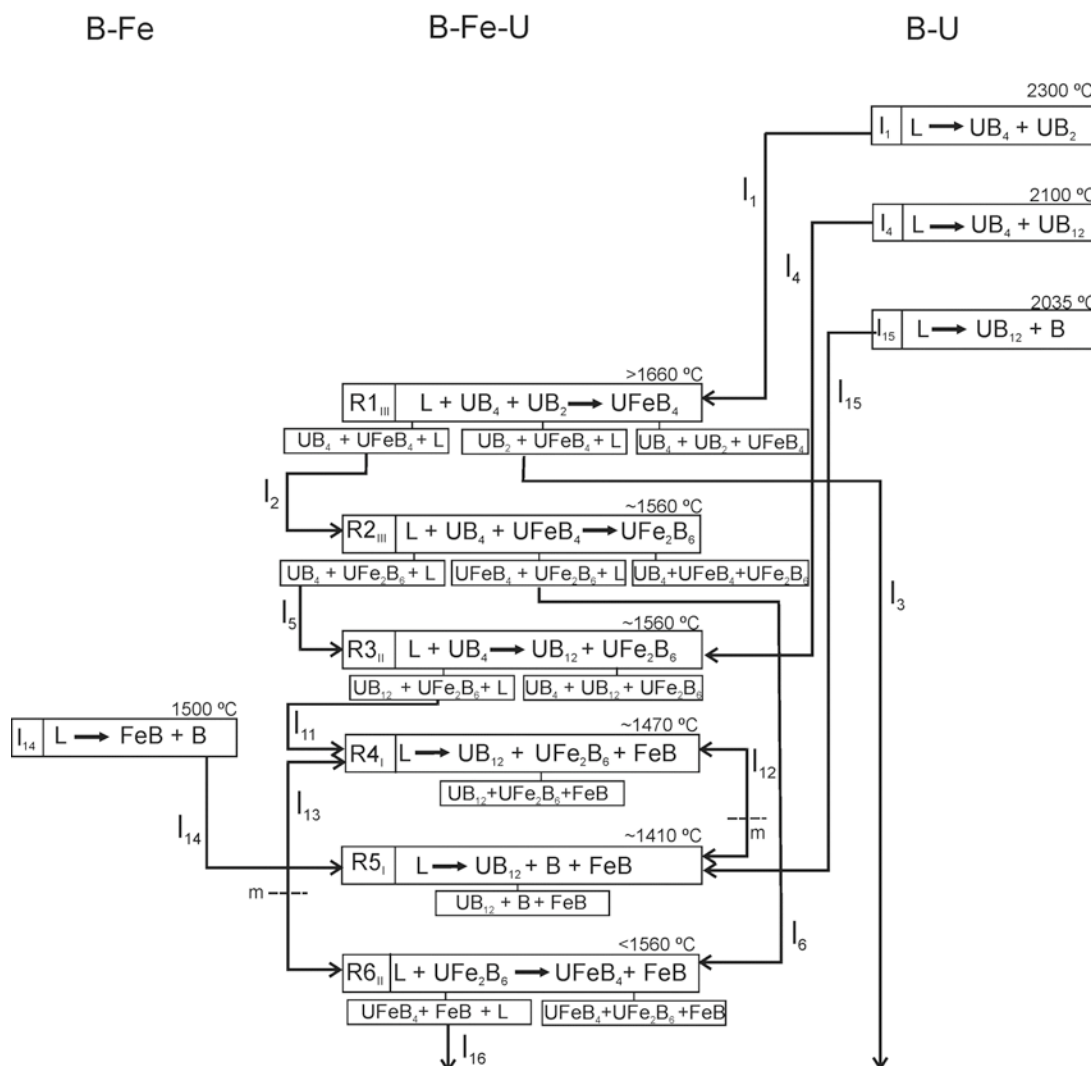


Figure 3.11 – Liquidus reaction scheme at the B-rich section.

### 3.3.2.2 0%>U>30% and 21%>B>50% (at.%) section

The 0%>U>30% and 21%>B>50% (at.%) section of the ternary phase diagram comprehends one ternary reaction of class III (R8<sub>III</sub>) and three ternary reactions of class II (R7<sub>II</sub>, R9<sub>II</sub>, R10<sub>II</sub>).

#### PXRD

Figure 3.12 shows experimental diffractograms of representative alloys evidencing the ternary and binary compounds present in the 0%>U>30% and 21%>B>50% (at.%) section. The PXRD diffractogram obtained for the annealed 50B:25Fe:25U alloy (Nr.12) shows that  $UB_2$  is the predominant phase, with a minor presence of  $UFeB_4$ ,  $UFe_2$  and  $UFe_3B_2$ . The diffractogram of the annealed 43B:55Fe:2U alloy (Nr.18) shows peaks of  $UFeB_4$  and  $Fe_2B$  with a minor presence of  $FeB$ . The diffractogram of the as-cast 33B:50Fe:17U alloy (Nr.25) shows major peaks of  $UFe_3B_2$  although the presence of  $UFeB_4$ ,  $UFe_4B$  and  $UFe_2$  can also be inferred.

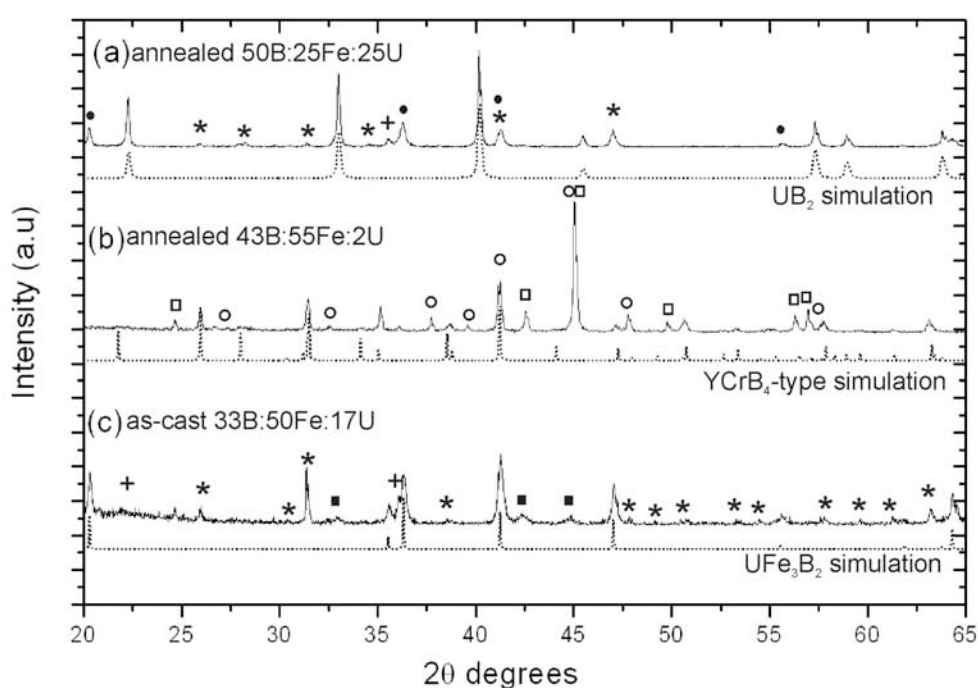


Figure 3.12 – Experimental powder X-ray diffractograms of (a) annealed 50B:25Fe:25U, (b) annealed 43B:55Fe:2U (b) as-cast 33B:50Fe:17U ( $UFe_3B_2$  stoichiometry) alloys (respectively Nr. 12, 18 and 25), where the presence of  $UB_2$ ,  $UFeB_4$  and  $UFe_3B_2$  is evident. Dotted lines represent simulations:  $UFeB_4$  crystallizes with a structure related to the  $YCrB_4$  one and  $UFe_3B_2$  crystallizes with a  $CeCo_3B_2$ -type structure. Symbols:  $UFeB_4$  - stars;  $UFe_2$  - crosses,  $UFe_3B_2$  - solid circles,  $UFe_4B$  - solid squares,  $Fe_2B$  - open squares,  $FeB$  - open circles.

### Microstructures

Microstructures of five alloys in as-cast and/or annealed conditions have been used to evidence the boundary lines and compatibility triangles in this section of the diagram.

The microstructure of the as-cast 50B:25Fe:25U alloy (Nr.12) presents five regions, designated by B, E, M, H and BM (Figure 3.13 (a)). WDS, EDS and PXRD results indicated that the phases correspond, respectively, to  $UB_2$ ,  $UFeB_4$ ,  $UFe_2$  and  $UFe_3B_2$ , while BM correspond to  $UB_2 + UFe_2$  *cotectic* mixture. Annealing did not induce significant changes in the microstructure.

The microstructure of the as-cast 43B:55Fe:2U (Nr.18) alloy (Figure 3.13 (b)) presents four regions, E, G, K and EK. WDS and EDS analyses indicate that these regions correspond, respectively, to  $UFeB_4$ ,  $FeB$  and  $Fe_2B$  while EK is an  $UFeB_4 + Fe_2B$  *cotectic* mixture, in agreement with PXRD results. The annealed microstructure did not evidence significant changes.

The microstructure of the as-cast 40B:40Fe:20U alloy (Nr.21), shown in Figure 3.13 (c), exhibits four differentiated regions, E, H, M and HM. WDS, EDS and PXRD analyses indicate that these regions correspond, respectively, to  $UFeB_4$ ,  $UFe_3B_2$  and  $UFe_2$  while HM is an  $UFe_3B_2 + UFe_2$  *cotectic* mixture. The annealed microstructure of the same alloy, shown in Figure 3.13 (d), evidences globulization of the *cotectic* constituents. Furthermore, both the microstructural and PXRD results show that during the heat treatment the volume fraction of the  $UFe_3B_2$  compound (regions H) increased at expenses of  $UFeB_4$  (regions E) reduction.

The microstructure of the as-cast 38B:52Fe:10U (Nr.22) alloy shown in Figure 3.13 (e) presents five regions, designated as E, H, K, JO and JMO. WDS, EDS and PXRD results indicate that these phases correspond, respectively, to  $UFeB_4$ ,  $UFe_3B_2$ , and  $Fe_2B$ , while JO is an  $\alpha\text{-Fe} + UFe_4B$  *cotectic* mixture and JMO corresponds to the ternary  $\alpha\text{-Fe} + UFe_2 + UFe_4B$  eutectic mixture. The 34B:60Fe:6U alloy (Nr.24) presents a similar microstructure albeit with a lower volume fraction of  $UFeB_4$  (regions E).

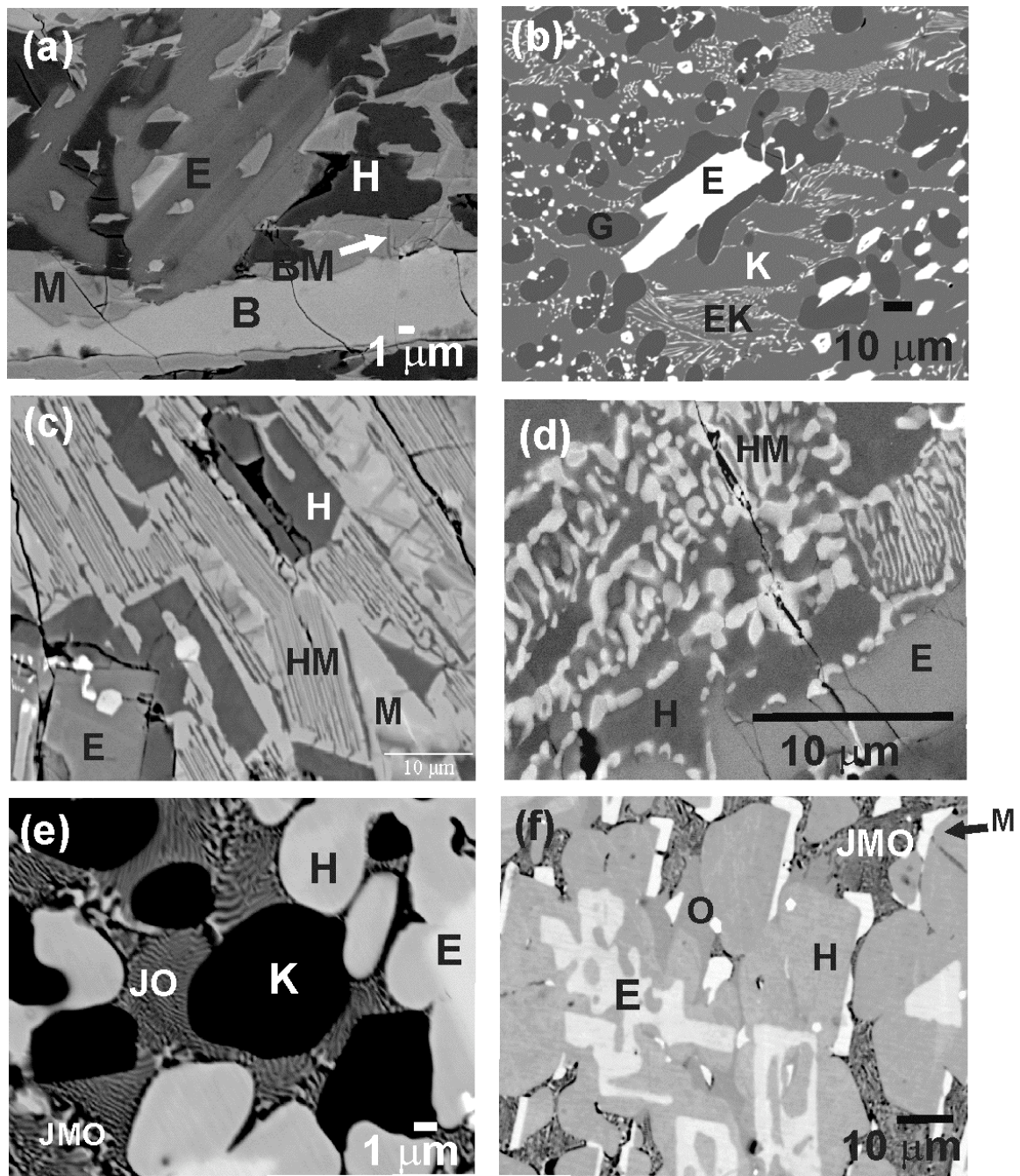


Figure 3.13 – BSE images showing microstructures observed in (a) as-cast 50B:25Fe:25U alloy (Nr.12), (b) as-cast 43B:55Fe:2U alloy (Nr.18), (c, d) respectively, as-cast and annealed 40B:40Fe:20U alloy (Nr.21), (e) as-cast 38B:52Fe:10U alloy (Nr.22), and (f) as-cast 33B:50Fe:17U alloy (Nr.25). The black arrow indicates in (a) the E/M interface and in (f) the M regions. The white arrow in (a) indicates regions BM. The phase labeling is given in Table 3.1.

The microstructure of the as-cast 33B:50Fe:17U ( $\text{UFe}_3\text{B}_2$  stoichiometry) alloy (Nr.25), presents four regions, designated by E, H, O, M and JMO (Figure 3.13 (f)). WDS, EDS and PXRD results indicate that phases E, H, O and M correspond respectively to  $\text{UFeB}_4$ ,  $\text{UFe}_3\text{B}_2$ ,  $\text{UFe}_4\text{B}$  and  $\text{UFe}_2$ , while JMO corresponds to the  $\alpha\text{-Fe} + \text{UFe}_2 + \text{UFe}_4\text{B}$  ternary eutectic mixture. Annealing induced a decrease in the  $\text{UFeB}_4$  volume fraction consistent with the PXRD results.

It should be noticed that the  $\alpha\text{-Fe}$  phase present in the microstructures at room temperature was in fact  $\gamma\text{-Fe}$  at the reactions temperature.

### Transition temperatures

Figure 3.14 presents the DTA curves for the 38B:52Fe:10U and 33B:50Fe:17U ( $\text{UFe}_3\text{B}_2$  stoichiometry) as-cast alloys (respectively, Nr.22 and 25). The assigning of specific transformations to the transitions observed in the DTA curve derivatives was carried out based on the sequential melting of the phases/cotectic mixtures/ternary mixtures present in the microstructures and on their apparent volume fractions.

The DTA curve of the 38B:52Fe:10U (Nr.22) alloy presented three transitions. The major constituents in the microstructure are  $\text{UFe}_3\text{B}_2$  (regions H),  $\text{Fe}_2\text{B}$  (Regions K), and the  $\alpha\text{-Fe} + \text{UFe}_4\text{B}$  *cotectic* mixture (regions JO) (see Figure 3.13 (e)). The first transition, at 1030 °C, corresponds to melting of the  $\gamma\text{-Fe} + \text{UFe}_4\text{B}$  mixture and the transition at 1180 °C, to the succeeding melting of  $\text{Fe}_2\text{B}$ . The last transition occurs at 1230 °C and corresponds to the melting of  $\text{UFe}_3\text{B}_2$  possibly together with melting of  $\text{UFeB}_4$ .

The DTA curve of the 33B:50Fe:17U ( $\text{UFe}_3\text{B}_2$  stoichiometry) alloy (Nr.25) presented three transitions. The major constituent in the microstructure is  $\text{UFe}_3\text{B}_2$ , albeit with minor amounts of  $\text{UFeB}_4$ ,  $\text{UFe}_2$  and  $\text{UFe}_4\text{B}$  (see Figure 3.13 (f)). The first transition, at 990 °C, corresponds to melting of the ternary eutectic mixture  $\gamma\text{-Fe} + \text{UFe}_2 + \text{UFe}_4\text{B}$  and is possibly also associated with melting of the  $\text{UFe}_2$  and  $\text{UFe}_4\text{B}$  individual

patches; the next transition, at 1208 °C, corresponds to melting of  $\text{UFe}_3\text{B}_2$ , and the broad transition at 1265 °C, corresponds to the succeeding melting of  $\text{UFeB}_4$ .

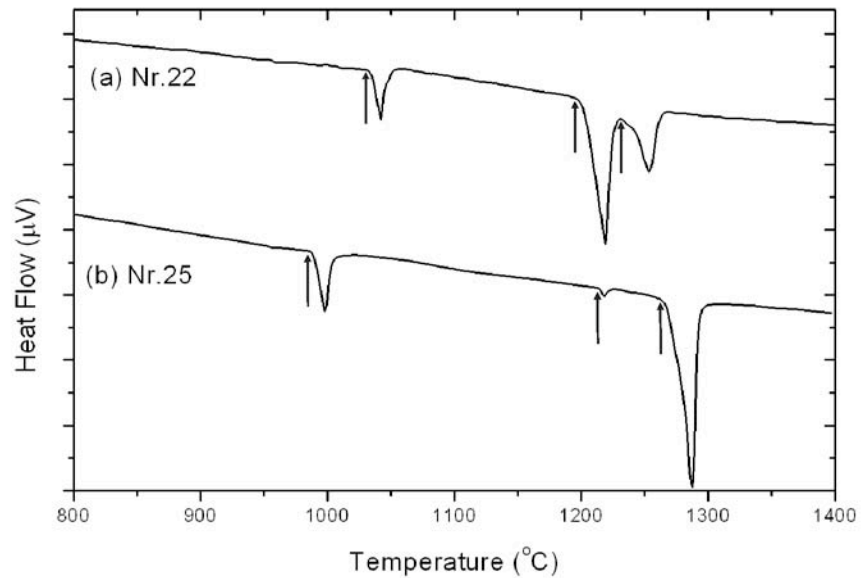


Figure 3.14 – DTA curves for representative 0%>U>30% and 21%>B>50% (at.%) section as-cast: (a) 38B:52Fe:10U and (b) 33B:50Fe:17U ( $\text{UFe}_3\text{B}_2$  stoichiometry) alloys (Nr. 22 and 25).

**UB<sub>2</sub>-UFeB<sub>4</sub>-UFe<sub>2</sub>****Compatibility triangle**

The intimate microstructural contact between UB<sub>2</sub> and UFeB<sub>4</sub> (respectively, regions B and E in Figure 3.13 (a)), UFe<sub>2</sub> and UB<sub>2</sub> (regions BM in Figure 3.13 (a)) and UFeB<sub>4</sub> and UFe<sub>2</sub> (respectively, regions E and M in Figure 3.13 (a)) implies the existence of an UB<sub>2</sub>-UFeB<sub>4</sub>-UFe<sub>2</sub> compatibility triangle and a corresponding ternary reaction involving the three phases.

**R7<sub>II</sub> ternary reaction**

The UB<sub>2</sub>/UFeB<sub>4</sub> boundary line (l<sub>3</sub>) which stems from the higher temperature R1<sub>III</sub>, converges to R7. The UFeB<sub>4</sub>/FeB boundary line (l<sub>8</sub>) must diverge from R7 toward a lower temperature ternary reaction, as there is no higher temperature invariant reaction from where it can originate. A diverging boundary line dismisses a class I ternary reaction and implies that R7 lies outside the UB<sub>2</sub>-UFeB<sub>4</sub>-UFe<sub>2</sub> compatibility triangle. Since UB<sub>2</sub> and UFe<sub>2</sub> are both congruent compounds, the only possible equation for a class III reaction would be:  $L + UB_2 + UFe_2 \rightarrow UFeB_4$ . However, the four-phase equilibrium geometry of this reaction would position R7 close to R3<sub>II</sub> and R2<sub>III</sub>. This fact is not compatible with the previously defined liquidus surface configuration and therefore a class II ternary reaction has been inferred for R7. As a result, the UB<sub>2</sub>/UFe<sub>2</sub> boundary line (l<sub>7</sub>) converges also to R7<sub>II</sub> and the ternary reaction is situated outside the UB<sub>2</sub>-UFeB<sub>4</sub>-UFe<sub>2</sub> triangle.

Since UB<sub>2</sub> and UFe<sub>2</sub> are both congruent compounds that cannot form by *reaction* transitions, the l<sub>7</sub> boundary line must be *cotectic*:



An UFe<sub>2</sub> + UB<sub>2</sub> *cotectic* mixture (regions BM) was indeed evident in the microstructure of the 50B:25Fe:25U alloy (Nr.12) (Figure 3.13 (a)).

The  $l_8$  boundary line can also be assumed as *cotectic*, as (i)  $UFe_2$  is a congruent compound that cannot form through a *reaction* transition involving  $UFeB_4$  consumption; and (ii)  $UFeB_4$  is a high temperature compound, and its solidification through consumption of the low melting point  $UFe_2$  ( $T_m=1228$  °C [3]) is not probable. This is supported by the fact that in all microstructures investigated  $UFeB_4$  solidifies prior to  $UFe_2$ . Consequently:



The boundary line  $l_3$  can have either a *cotectic* or *reaction* nature [21,22], which could not be established from the microstructures.

The proposed equation for the ternary reaction is:

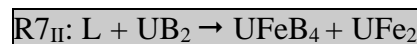


Table 3.3 presents the  $R7_{II}$  ternary reaction equation (left column), the boundary lines at the invariant point (centre column) and the four-phase equilibrium configuration (right column). At the  $R7_{II}$  ternary reaction two phases,  $UB_2$  and  $L(R7_{II})$ , interact and form two other phases,  $UFeB_4$  and  $UFe_2$ . The two three-phase regions,  $UB_2 + UFeB_4 + L$  and  $UB_2 + L + UFe_2$ , descend from higher temperature toward the four-phase reaction plane, where they meet to form a horizontal trapezium in which the four phases,  $UB_2 + UFeB_4 + L + UFe_2$ , are in equilibrium (see right column on Table 3.3). Below the four phase reaction plane two three-phase regions form,  $UB_2 + UFeB_4 + UFe_2$  and  $UFeB_4 + L + UFe_2$ . The  $UB_2$  crystallization field is delimited by the lines converging to  $R7_{II}$  indicating that the ternary reaction is situated across  $UB_2$  below the  $UFeB_4$ - $UFe_2$  Alkemade line to allow the formation of the low temperature  $UFeB_4$ - $UFe_2$ - $L$  triangle. This trapezium configuration shows that  $R7_{II}$  lies in the  $UFeB_4$ - $UFe_3B_2$ - $UFe_2$  compatibility triangle.

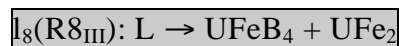
**UFeB<sub>4</sub>-UFe<sub>3</sub>B<sub>2</sub>-UFe<sub>2</sub>****Compatibility triangle**

The intimate microstructural contact between UFeB<sub>4</sub> and UFe<sub>2</sub> (respectively, regions E and M in Figure 3.13 (a)), UFeB<sub>4</sub> and UFe<sub>3</sub>B<sub>2</sub> (respectively regions E and regions H in Figure 3.6 (c)) and UFe<sub>3</sub>B<sub>2</sub> and UFe<sub>2</sub> (respectively, regions HM in Figure 3.6 (c)) implies the existence of an UFeB<sub>4</sub>-UFe<sub>3</sub>B<sub>2</sub>-UFe<sub>2</sub> compatibility triangle and a corresponding ternary reaction involving the three phases. Indeed the microstructure of the annealed 40B:40Fe:20U alloy (Nr.21) points to an equilibrium between these phases (see Figure 3.13 (d)). However, the proportion of UFeB<sub>4</sub> was reduced during the annealing treatment, indicating that the primary solidification resulted in an excessive production of UFeB<sub>4</sub>.

**R8<sub>III</sub> ternary reaction**

The UFeB<sub>4</sub>/UFe<sub>2</sub> boundary line (l<sub>8</sub>), which stems from the higher temperature ternary reaction R7<sub>II</sub>, is therefore converging to R8. The other two boundary lines involving UFe<sub>3</sub>B<sub>2</sub>; UFeB<sub>4</sub>/UFe<sub>3</sub>B<sub>2</sub> (l<sub>9</sub>) and UFe<sub>3</sub>B<sub>2</sub>/UFe<sub>2</sub> (l<sub>10</sub>), must diverge from R8 toward lower temperature ternary reactions, as there are no higher temperature invariant points from where they can originate. As a result, R8 is a class III ternary reaction lying outside the UFeB<sub>4</sub>-UFe<sub>3</sub>B<sub>2</sub>-UFe<sub>2</sub> compatibility triangle.

As discussed for R7<sub>II</sub>, the l<sub>8</sub> boundary line presents a *cotectic* nature. Therefore:



The UFeB<sub>4</sub>/UFe<sub>3</sub>B<sub>2</sub> ragged interface (regions E/regions H) in alloy Nr.25 (Figure 3.13 (f)) suggests that UFe<sub>3</sub>B<sub>2</sub> formation involved UFeB<sub>4</sub> consumption, indicating a *reaction* nature for l<sub>9</sub>:



The microstructure of the 40B:40Fe:20U alloy (Nr.21) shows evidence of an  $\text{UFe}_3\text{B}_2$  +  $\text{UFe}_2$  *cotectic* mixture (regions HM in Figure 3.13 (c)) indicating a *cotectic* nature for  $I_{10}$ :



The proposed equation for the ternary reaction is:

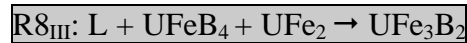


Table 3.3 presents the  $R8_{\text{III}}$  ternary reaction equation (left column), the boundary lines at the invariant point (centre column) and the four-phase equilibrium configuration (right column). At  $R8_{\text{III}}$  three phases interact isothermally upon cooling to form a new phase, i.e.,  $\text{UFeB}_4$ ,  $\text{UFe}_2$  and  $\text{L}(R8_{\text{III}})$  located at the vertices of a horizontal triangular reaction plane, combine to form  $\text{UFe}_3\text{B}_2$ , whose composition lies inside the triangle (see right column of Table 3.2). The three-phase field  $\text{UFeB}_4 + \text{L} + \text{UFe}_2$  descends from higher temperature to the ternary peritectic temperature, and three-phase regions  $\text{UFeB}_4 + \text{UFe}_3\text{B}_2 + \text{L}$ ,  $\text{UFe}_3\text{B}_2 + \text{L} + \text{UFe}_2$  and  $\text{UFeB}_4 + \text{UFe}_3\text{B}_2 + \text{UFe}_2$  are issued beneath and proceed to lower temperatures. The ternary reaction configuration demands the  $\text{UFeB}_4$ - $\text{UFe}_3\text{B}_2$ - $\text{UFe}_2$  triangle to lie inside the  $\text{UFeB}_4$ - $\text{UFe}_2$ - $\text{L}(R8_{\text{III}})$  one, which roughly positions the  $R8_{\text{III}}$  ternary reaction.

**UFeB<sub>4</sub>-FeB-Fe<sub>2</sub>B****Compatibility triangle**

Figure 3.13 (b) presents microstructural evidence of three additional boundary lines; one inferred from the interface between UFeB<sub>4</sub> (regions E) and FeB (regions G), another inferred from the interface between UFeB<sub>4</sub> (regions E) and Fe<sub>2</sub>B (regions K) and another from the interface between FeB (regions G) and Fe<sub>2</sub>B (regions K). These boundary lines imply the existence of an UFeB<sub>4</sub>-FeB-Fe<sub>2</sub>B compatibility triangle and a corresponding ternary reaction involving the three phases.

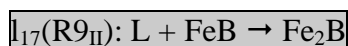
**R<sub>9II</sub> ternary reaction**

The UFeB<sub>4</sub>/FeB boundary line (l<sub>16</sub>) diverges from the higher temperature R<sub>6II</sub> and converges to R<sub>9</sub>. The UFe<sub>3</sub>B<sub>2</sub>/Fe<sub>2</sub>B boundary line (l<sub>18</sub>) must diverge from R<sub>9</sub> towards a lower temperature ternary reaction, as there is no higher temperature invariant point from where it can originate. This fact dismisses a class I ternary reaction and implies that R<sub>9</sub> lies outside the UFeB<sub>4</sub>-FeB-Fe<sub>2</sub>B compatibility triangle. The four-phase equilibrium geometry consistent with a class III reaction of the type L + FeB + UFeB<sub>4</sub> → Fe<sub>2</sub>B or L + FeB + Fe<sub>2</sub>B → UFeB<sub>4</sub> would require R<sub>9</sub> to be situated, respectively, outside the ternary diagram or close to R<sub>1III</sub>. This fact is not compatible with the previously defined liquidus surface configuration and therefore a class II ternary reaction has been inferred for R<sub>9</sub>.

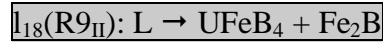
FeB is a congruent compound that cannot be formed by *reaction* transitions. On the other hand, UFeB<sub>4</sub> cannot form by a *reaction* transition through FeB consumption since it solidifies prior to FeB (see Figure 3.13 (b)). As a result, l<sub>16</sub> is of *cotectic* nature:



The l<sub>17</sub> line stems from the binary diagram [1] with a *reaction* nature:



The microstructure of the 43B:55Fe:2U alloy (Nr.18) evidenced an  $\text{Fe}_2\text{B} + \text{UFeB}_4$  *cotectic* mixture, pointing to a *cotectic* nature for  $I_{18}$ :



The proposed equation for the ternary reaction is:



Table 3.3 presents the  $R9_{II}$  ternary reaction equation (left column), the boundary lines at the invariant reaction (centre column) and the four-phase equilibrium configuration (right column). At  $R9_{II}$  two phases,  $\text{FeB}$  and  $L(R9_{II})$ , interact to form two other phases,  $\text{Fe}_2\text{B}$  and  $\text{UFeB}_4$ . Two three-phase regions,  $\text{UFeB}_4 + \text{FeB} + L$  and  $\text{FeB} + \text{Fe}_2\text{B} + L$ , descend from higher temperature toward the four-phase reaction plane, where they meet to form a horizontal trapezium,  $\text{UFeB}_4 + \text{FeB} + \text{Fe}_2\text{B} + L$ , where the four phases are in equilibrium. Below this temperature two other three-phase regions form,  $\text{UFeB}_4 + \text{FeB} + \text{Fe}_2\text{B}$  and  $\text{UFeB}_4 + \text{Fe}_2\text{B} + L$ . The  $\text{FeB}$  crystallization field is delimited by the lines converging to  $R8_{II}$  indicating that the ternary reaction is situated across  $\text{FeB}$  below the  $\text{Fe}_2\text{B}$ - $\text{UFeB}_4$  Alkemade line to allow the formation of the low temperature  $\text{UFeB}_4$ - $\text{Fe}_2\text{B}$ - $L$  triangle. This trapezium configuration shows that  $R9_{II}$  lies in the  $\text{UFeB}_4$ - $\text{Fe}_2\text{B}$ - $\text{UFe}_3\text{B}_2$  compatibility triangle.

**UFeB<sub>4</sub>-UFe<sub>3</sub>B<sub>2</sub>-Fe<sub>2</sub>B****Compatibility triangle**

The intimate microstructural contact between the UFeB<sub>4</sub> (regions E) and Fe<sub>2</sub>B (regions K) (Figure 3.13 (b)), UFeB<sub>4</sub> (regions E) and UFe<sub>3</sub>B<sub>2</sub> (regions H) (Figure 3.13 (f)) and UFe<sub>3</sub>B<sub>2</sub> (regions H) and Fe<sub>2</sub>B (regions K) (Figure 3.13 (e)) implies the existence of an UFeB<sub>4</sub>-UFe<sub>3</sub>B<sub>2</sub>-Fe<sub>2</sub>B compatibility triangle and of a ternary reaction involving the three phases.

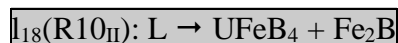
**R10<sub>II</sub> ternary reaction**

The UFeB<sub>4</sub>/Fe<sub>2</sub>B boundary line (l<sub>18</sub>), which stems from the higher temperature R9<sub>II</sub>, together with the UFeB<sub>4</sub>/UFe<sub>3</sub>B<sub>2</sub> boundary line (l<sub>9</sub>), which stems from the higher temperature R8<sub>III</sub>, converge to R10. On the other hand, the UFe<sub>3</sub>B<sub>2</sub>/Fe<sub>2</sub>B boundary line (l<sub>19</sub>) diverges from R10, since there is no higher temperature ternary invariant point from where it can originate. This configuration corresponds to a class II ternary reaction with R10<sub>II</sub> lying outside the UFeB<sub>4</sub>-UFe<sub>3</sub>B<sub>2</sub>-Fe<sub>2</sub>B compatibility triangle.

As discussed for R9<sub>III</sub>, the l<sub>9</sub> boundary line presents a *cotectic* nature:



As discussed for R9<sub>II</sub>, the l<sub>18</sub> boundary line presents a *cotectic* nature:



The l<sub>19</sub> boundary line can have either a *cotectic* or *reaction* nature [21,22], which could not be established from the microstructures.

The proposed equation for the ternary reaction is:

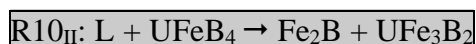


Table 3.3 presents the R10<sub>II</sub> ternary reaction equation (left column), the boundary lines at the invariant reaction (centre column) and the four-phase equilibrium configuration (right column). At R10<sub>II</sub> two phases, UFeB<sub>4</sub> and L(R10<sub>II</sub>), interact to form two other phases, UFe<sub>3</sub>B<sub>2</sub> and Fe<sub>2</sub>B. Two three-phase regions, UFeB<sub>4</sub> + UFe<sub>3</sub>B<sub>2</sub> + L and UFeB<sub>4</sub> + Fe<sub>2</sub>B + L, descend from higher temperature toward the four-phase reaction plane, where they meet to form a horizontal trapezium, UFeB<sub>4</sub> + UFe<sub>3</sub>B<sub>2</sub> + Fe<sub>2</sub>B + L, where the four phases are in equilibrium. Below this temperature two other three-phase regions form, UFeB<sub>4</sub> + UFe<sub>3</sub>B<sub>2</sub> + Fe<sub>2</sub>B and UFe<sub>3</sub>B<sub>2</sub> + Fe<sub>2</sub>B + L. The UFeB<sub>4</sub> crystallization field is delimited by the lines converging to R10<sub>II</sub> indicating that the ternary reaction is situated across UFeB<sub>4</sub> below the Fe<sub>2</sub>B-UFe<sub>3</sub>B<sub>2</sub> Alkemade line to allow the formation of the low temperature Fe<sub>2</sub>B-UFe<sub>3</sub>B<sub>2</sub>-L triangle. This trapezium configuration shows that R10<sub>II</sub> lies in the Fe<sub>2</sub>B-U<sub>2</sub>Fe<sub>21</sub>B<sub>6</sub>-UFe<sub>4</sub>B compatibility triangle.

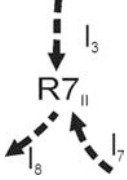
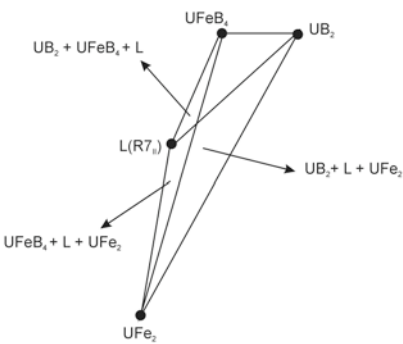
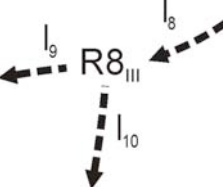
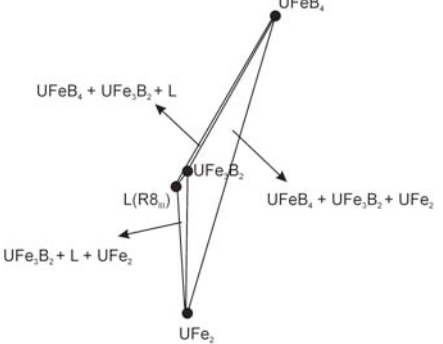
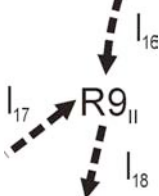
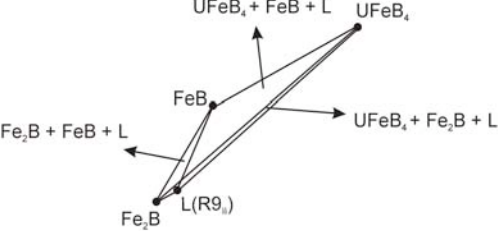
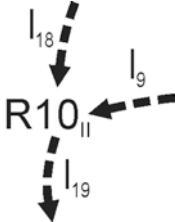
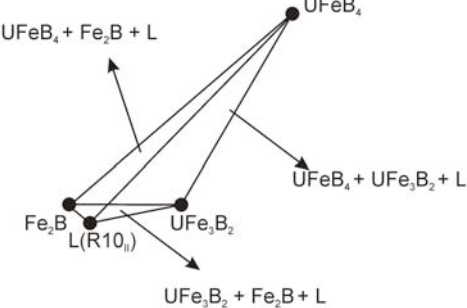
Boundary lines associated with ternary reactions	Four-phase configuration
<p><math>L + UB_2 \rightarrow UFeB_4 + UFe_2</math></p> 	<p><math>I_3(R7_{II}): UB_2/UFeB_4</math> (regions B/regions E)</p> <p><math>I_7(R7_{II}): L \rightarrow UB_2 + UFe_2</math> (regions BM)</p> <p><math>I_8(R7_{II}): L \rightarrow UFeB_4 + UFe_2</math> (regions E + regions M)</p> 
<p><math>L + UFeB_4 + UFe_2 \rightarrow UFe_3B_2</math></p> 	<p><math>I_8(R8_{III}): L \rightarrow UFeB_4 + UFe_2</math> (regions E + regions M)</p> <p><math>I_9(R8_{III}): L + UFeB_4 \rightarrow UFe_3B_2</math> (regions E <math>\rightarrow</math> regions H)</p> <p><math>I_{10}(R8_{III}): L \rightarrow UFe_3B_2 + UFe_2</math> (regions HM)</p> 
<p><math>L + FeB \rightarrow UFeB_4 + Fe_2B</math></p> 	<p><math>I_{16}(R9_{II}): L \rightarrow UFeB_4 + FeB</math> (regions E + regions G)</p> <p><math>I_{17}(R9_{II}): L + FeB \rightarrow Fe_2B</math> (from binary diagram [1])</p> <p><math>I_{18}(R9_{II}): L \rightarrow UFeB_4 + Fe_2B</math> (regions E + regions K)</p> 
<p><math>L + UFeB_4 \rightarrow Fe_2B + UFe_3B_2</math></p> 	<p><math>I_9(R10_{II}): L + UFeB_4 \rightarrow UFe_3B_2</math> (regions E <math>\rightarrow</math> regions H)</p> <p><math>I_{18}(R10_{II}): L \rightarrow UFeB_4 + Fe_2B</math> (regions EK)</p> <p><math>I_{19}(R10_{II}): UFe_3B_2/Fe_2B</math> (regions H/regions K)</p> 

Table 3.3 – Boundary lines for R7<sub>II</sub>, R8<sub>III</sub>, R9<sub>II</sub> and R10<sub>II</sub> ternary reactions associated with the four-phase configuration.

### Liquidus projection

Figure 3.15 shows the liquidus projection of the  $0\% < U < 30\%$  and  $21\% < B < 50\%$  (at.%) section together with the Alkemade lines defining the phase equilibria. Figure 3.16 shows the position of alloys Nr.12, 18, 21, 22, 24 and 25. The grey lettering indicates the primary crystallization fields.

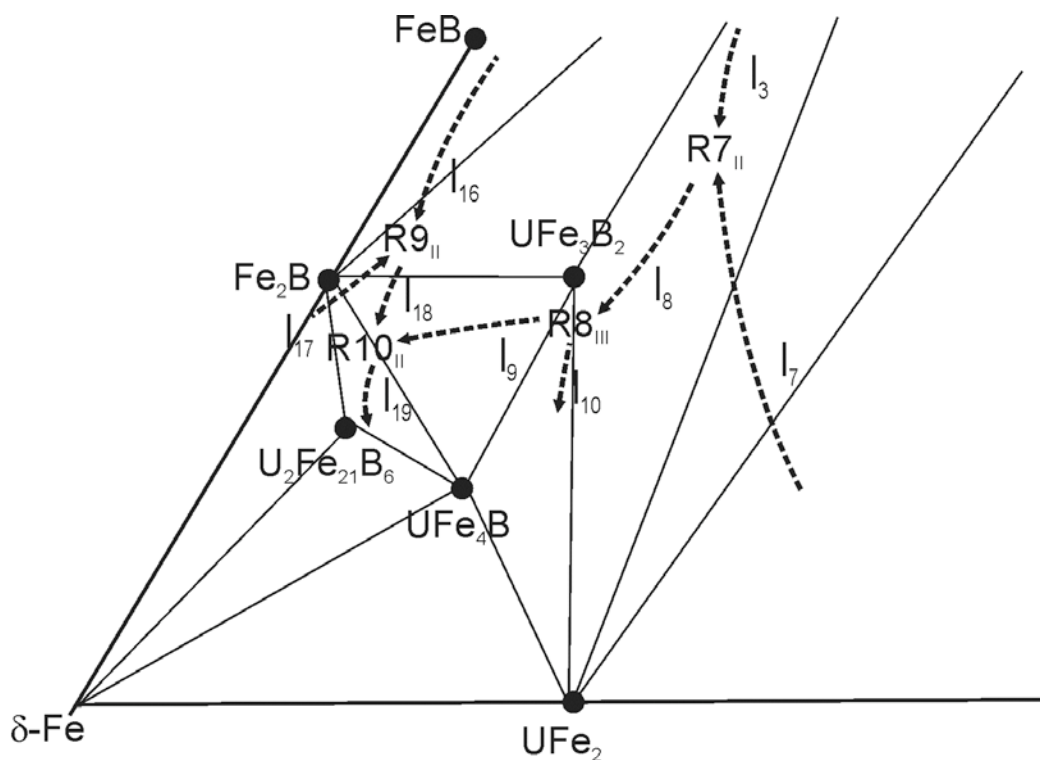


Figure 3.15 – Liquidus projection in the  $0\% < U < 30\%$  and  $21\% < B < 50\%$  (at%) section showing the approximate position of  $R7_{II}$ ,  $R8_{III}$ ,  $R9_{II}$  and  $R10_{II}$ . Solid lines represent the Alkemade lines and dashed lines indicate the liquid composition at the boundary lines.

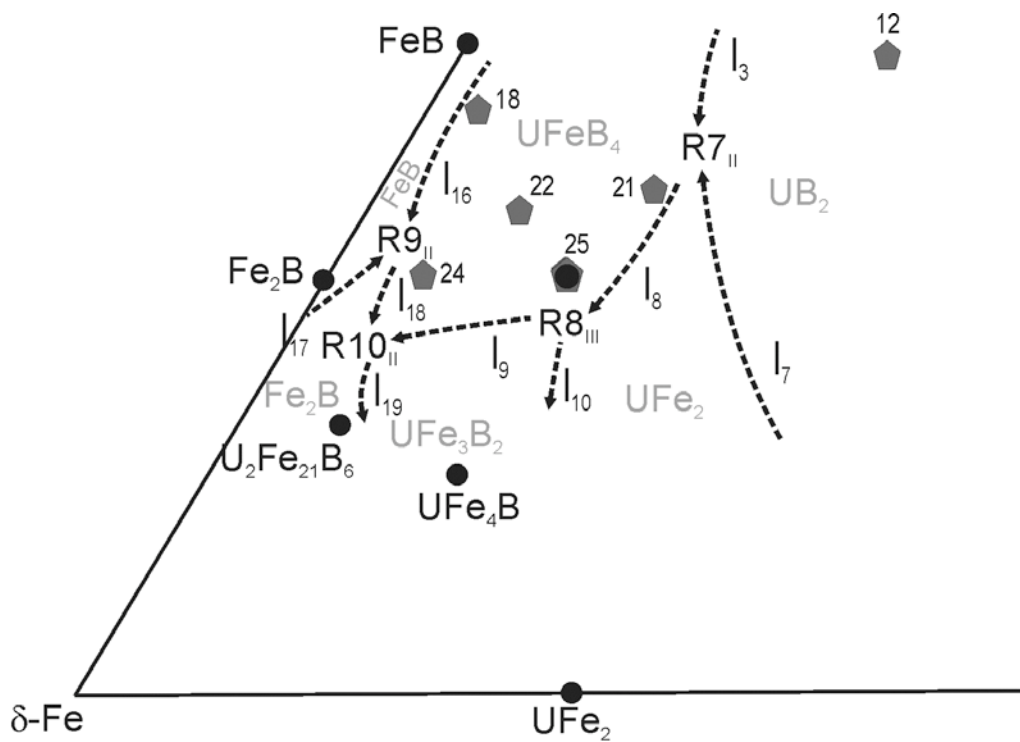


Figure 3.16 – Liquidus projection of the 0%>U>30% and 21%>B>50% (at.%) section showing R7<sub>II</sub>, R8<sub>III</sub>, R9<sub>II</sub> and R10<sub>II</sub> together with the 50B:25Fe:25U, 43B:55Fe:2U, 40B:40Fe:20U, 38B:52Fe:10U, 34B:60Fe:6U and 33B:50Fe:17U (UFe<sub>3</sub>B<sub>2</sub> stoichiometry) (respectively Nr.12, 18, 21, 22, 24 and 25) alloys position. Dashed lines represent the liquid composition at the boundary lines. The grey lettering indicates primary crystallization fields.

### Solidification path

Figure 3.17 shows the solidification paths of the 38B:52Fe:10U and 33B:50Fe:17U ( $\text{UFe}_3\text{B}_2$  stoichiometry) alloys (respectively, Nr. 22 and 25).

The 38B:52Fe:10U alloy (Nr.22) presented the following solidification sequence:  $L \rightarrow \text{UFeB}_4$  (regions E)  $\rightarrow \text{UFe}_3\text{B}_2$  (regions H)  $\rightarrow \text{Fe}_2\text{B}$  (regions K)  $\rightarrow \gamma\text{-Fe} + \text{UFe}_4\text{B}$  (regions JO)  $\rightarrow \gamma\text{-Fe} + \text{UFe}_4\text{B} + \text{UFe}_2$  (regions JMO) (Figure 3.13 (e)). The primary solidification of  $\text{UFeB}_4$  indicates that the alloy is situated in the crystallization field of this compound. According to the transition temperatures (Figure 3.14), formation of  $\text{UFe}_3\text{B}_2$  (below  $l_9$ ) occurred at 1230 °C; formation of  $\text{Fe}_2\text{B}$  (along and below  $l_{19}$ ) occurred at 1180 °C. The fact that  $l_9$  converges to  $R_{10\text{II}}$  and  $l_{19}$  diverges from  $R_{10\text{II}}$  implies that this ternary reaction occurs at  $1180\text{ °C} < T < 1230\text{ °C}$ . Moreover, since  $l_9$  operated at a temperature near 1230 °C ( $\text{UFe}_3\text{B}_2$  formation) and is diverging from  $R_{8\text{II}}$ , this implies that  $R_{8\text{II}}$  occurs at  $T > 1230\text{ °C}$ .

The microstructure of the 33B:50Fe:17U (Nr.25,  $\text{UFe}_3\text{B}_2$  stoichiometry) alloy presents the following solidification sequence:  $L \rightarrow \text{UFeB}_4$  (regions E)  $\rightarrow \text{UFe}_3\text{B}_2$  (regions H)  $\rightarrow \text{UFe}_4\text{B}$  (regions O) +  $\text{UFe}_2$  (regions M)  $\rightarrow \gamma\text{-Fe} + \text{UFe}_4\text{B} + \text{UFe}_2$  (regions JMO) (Figure 3.13 (f)). Solidification started with  $\text{UFeB}_4$  indicating that the alloy is situated inside the primary crystallization field of this compound. According to the transition temperatures (Figure 3.14), the solidification of  $\text{UFeB}_4$  occurred at 1265 °C (above  $l_9$ ) together with and the formation of  $\text{UFe}_3\text{B}_2$  (below  $l_9$ ). The fact that  $l_9$  diverges from  $R_{8\text{III}}$  and converges to  $R_{10\text{II}}$  implies that  $R_{8\text{III}}$  occurs at  $T > 1265\text{ °C}$  and  $R_{10\text{II}}$  occurs at  $T < 1265\text{ °C}$ .

Since  $l_3$  is diverging from  $R_{1\text{III}}$  and converging to  $R_{7\text{II}}$  the latter reaction must occur at  $T < 1660\text{ °C}$ . Additionally, since  $l_{17}$  is diverging from the binary phase diagram where it operates at 1389 °C and is converging to  $R_{9\text{II}}$  the latter reaction must occur at  $T < 1389\text{ °C}$ .

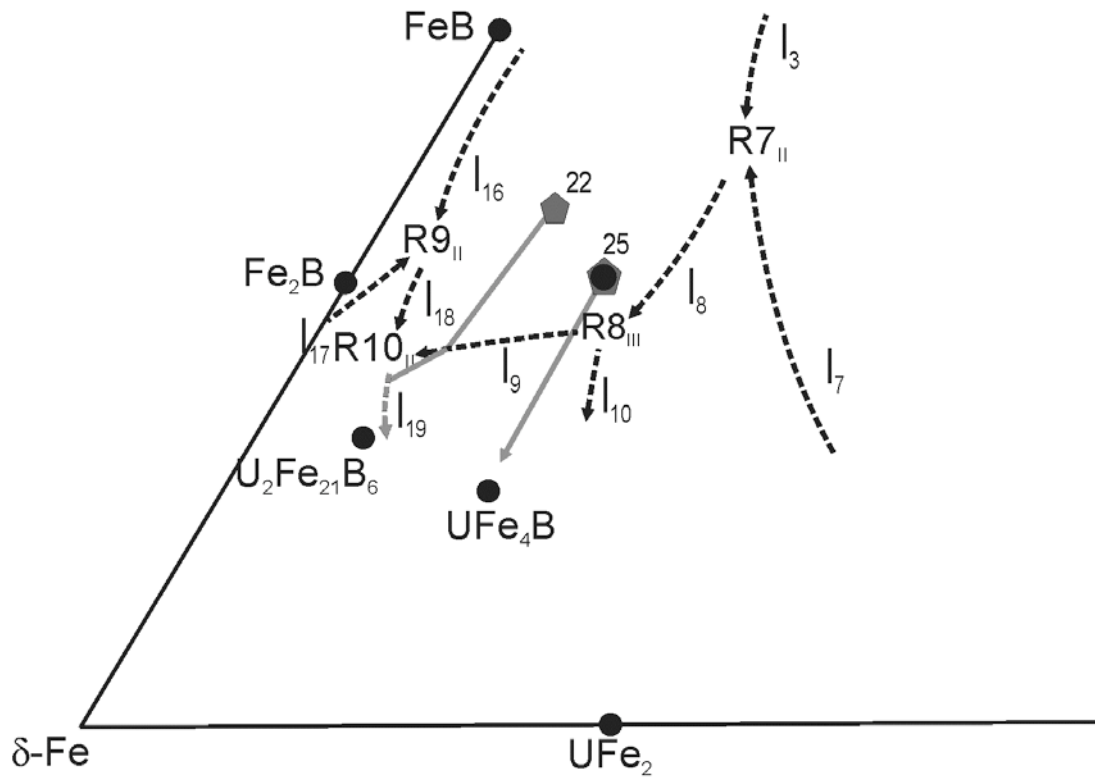


Figure 3.17 – Solidification path for 38B:52Fe:10U and 33B:50Fe:17U alloys (respectively Nr.22 and 25). Dashed lines represent the liquid composition at the boundary lines.



### **3.3.2.3 Fe-rich section**

The Fe- rich section of the ternary phase diagram comprehends two ternary reactions of class III (R11<sub>III</sub> and R13<sub>III</sub>), three ternary reactions of class II (R12<sub>II</sub>, R14<sub>II</sub>, R15<sub>II</sub>) and one ternary reaction of class I (R16<sub>I</sub>).

### **PXRD**

Figure 3.19 shows the experimental diffractograms of representative alloys that best evidence the ternary compounds present in the compatibility triangles of the Fe-rich section.

The PXRD diffractogram of the as-cast 23B:62Fe:15U alloy (Nr.30) points to a significant presence of  $\text{UFe}_3\text{B}_2$  and minor amounts of  $\text{UFe}_4\text{B}$ ,  $\text{UFe}_2$  and  $\alpha\text{-Fe}$ . The diffractogram of the annealed 21B:76Fe:3U alloy (Nr.31) points to  $\alpha\text{-Fe}$  and  $\text{Fe}_2\text{B}$  as the predominant phases, but evidences also the presence of  $\text{U}_2\text{Fe}_{21}\text{B}_6$  and minor amounts of  $\text{UFe}_3\text{B}_2$ ,  $\text{UFe}_4\text{B}$ . The diffractogram of the 10B:80Fe:10U alloy (Nr.43) evidences  $\text{UFe}_4\text{B}$  and  $\alpha\text{-Fe}$  as predominant phases, however,  $\text{UFe}_2$  and  $\text{UFe}_3\text{B}_2$  are also present.

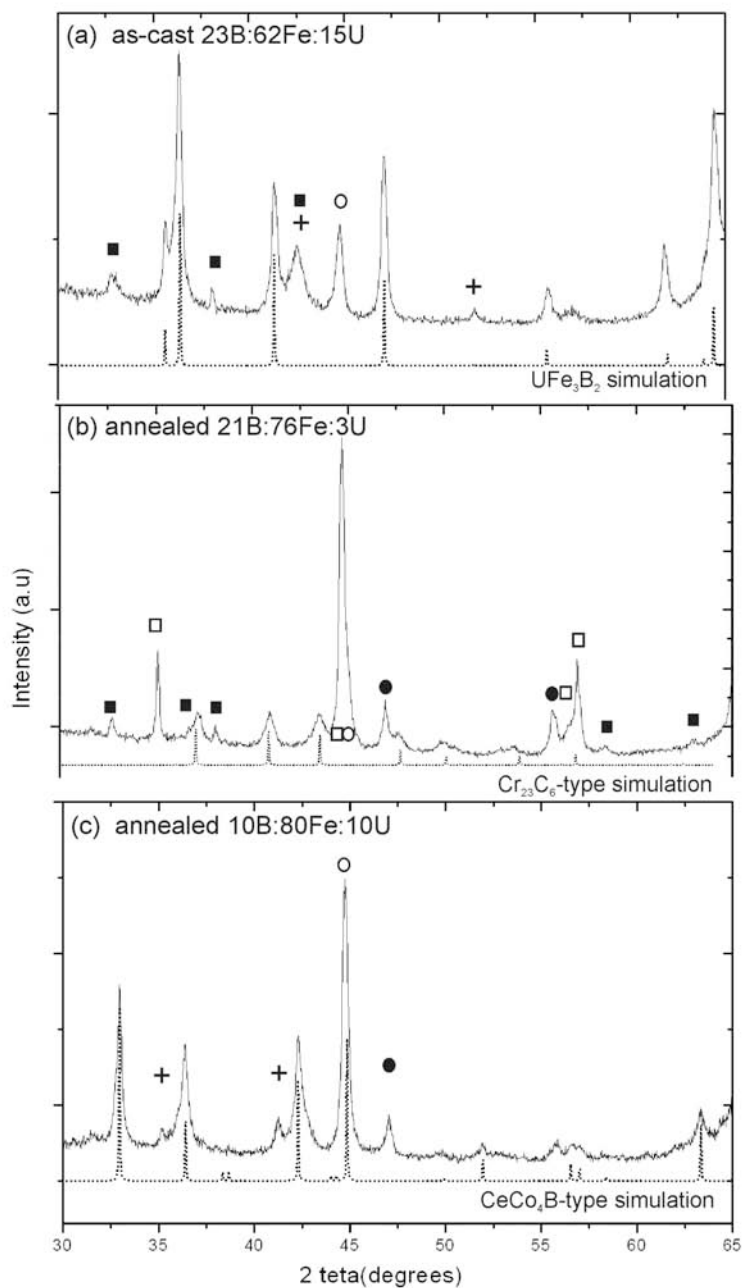


Figure 3.19 – Representative experimental powder X-ray diffractograms of Fe-rich alloys: (a) as-cast 23B:62Fe:15U (Nr.30), (b) annealed 21B:76Fe:3U (Nr.31), (c) annealed 10B:80Fe:10U (Nr.43), where the presence of, respectively,  $\text{UFe}_3\text{B}_2$ ,  $\text{U}_2\text{Fe}_{21}\text{B}_6$  and  $\text{UFe}_4\text{B}$  is evident. The dotted lines represent simulations for these compounds. Dotted lines represent simulations:  $\text{UFe}_3\text{B}_2$  crystallizes with  $\text{CeCo}_3\text{B}_2$ -type structure,  $\text{U}_2\text{Fe}_{21}\text{B}_6$  crystallizes with a  $\text{Cr}_{23}\text{C}_6$  type-structure and  $\text{UFe}_4\text{B}$  crystallizes with a structure related to the  $\text{CeCo}_4\text{B}$  one. Symbols:  $\text{UFe}_2$  - crosses,  $\text{UFe}_4\text{B}$  - solid squares,  $\text{UFe}_3\text{B}_2$  - solid circles,  $\alpha\text{-Fe}$  - open circles,  $\text{Fe}_2\text{B}$  - open squares.

### Microstructures

Microstructures of four alloys in as-cast and/or annealed conditions have been used to evidence the boundary lines and compatibility triangles in this section of the diagram.

The microstructure of the as-cast 17B:73Fe:10U alloy (Nr.36), shown in Figure 3.20 (a), presents four regions, designated by K, H, MO, JO and JMO. WDS, EDS and PXRD results indicated that the phases correspond, respectively, to  $\text{Fe}_2\text{B}$  and  $\text{UFe}_3\text{B}_2$ , while MO is an  $\text{UFe}_2 + \text{UFe}_4\text{B}$  *cotectic* mixture, JO is an  $\alpha\text{-Fe} + \text{UFe}_4\text{B}$  *cotectic* mixture, and JMO corresponds to the  $\alpha\text{-Fe} + \text{UFe}_2 + \text{UFe}_4\text{B}$  ternary eutectic mixture.

The microstructure of the as-cast 17B:66Fe:17U ( $\text{UFe}_4\text{B}$  stoichiometry) alloy (Nr.37), shown in Figure 3.20 (b), presents four regions, designated as H, M, O and JMO. WDS, EDS and PXRD results indicate that these phases correspond, respectively, to  $\text{UFe}_3\text{B}_2$ ,  $\text{UFe}_2$ , and  $\text{UFe}_4\text{B}$ , while JMO corresponds to the  $\alpha\text{-Fe} + \text{UFe}_2 + \text{UFe}_4\text{B}$  ternary eutectic mixture. The annealed microstructure of the same alloy, shown in Figure 3.20 (c), evidences globulization of the *cotectic* and ternary eutectic constituents. Furthermore, both the microstructures and the PXRD results show that during the heat treatment the volume fraction of the  $\text{UFe}_4\text{B}$  compound (regions O) increased at the expenses of an  $\text{UFe}_3\text{B}_2$  (regions H) reduction.

The as-cast 15B:80Fe:5U alloy (Nr.39) microstructure, shown in Figure 3.20 (d) presents five regions, designated as K, J, P, JO and JMO. WDS, EDS and PXRD results indicate that these phases correspond, respectively, to  $\text{Fe}_2\text{B}$ ,  $\alpha\text{-Fe}$ ,  $\text{U}_2\text{Fe}_{21}\text{B}_6$ , while JO is an  $\alpha\text{-Fe} + \text{UFe}_4\text{B}$  *cotectic* mixture and JMO corresponds to the  $\alpha\text{-Fe} + \text{UFe}_2 + \text{UFe}_4\text{B}$  ternary eutectic mixture.

The as-cast 9B:87Fe:4U microstructure (Nr.44), shown in Figure 3.20 (e), presents five regions designated as J, P, PO, JO and JMO. WDS, EDS and PXRD results indicate that these phases correspond, respectively, to  $\alpha\text{-Fe}$ ,  $\text{U}_2\text{Fe}_{21}\text{B}_6$  while PO correspond to an  $\text{U}_2\text{Fe}_{21}\text{B}_6 + \text{UFe}_4\text{B}$  *cotectic* mixture, JO is an  $\alpha\text{-Fe} + \text{UFe}_4\text{B}$  *cotectic* mixture and JMO corresponds to the ternary  $\alpha\text{-Fe} + \text{UFe}_2 + \text{UFe}_4\text{B}$  eutectic mixture.

The annealed microstructure of the same alloy, shown in Figure 3.20 (f), shows an increased volume fraction of the  $\alpha$ -Fe (regions J) and  $\text{UFe}_2$  (regions M) phases in agreement with the PXRD results. The fact that the annealed microstructure presents only  $\alpha$ -Fe (regions J),  $\text{UFe}_2$  (regions M) and  $\text{UFe}_4\text{B}$  (regions O) indicates that this alloy is situated in the  $\gamma$ -Fe- $\text{UFe}_4\text{B}$ - $\text{UFe}_2$  compatibility triangle. It is noteworthy that the  $\alpha$ -Fe phase present in the microstructures at room temperature was in fact  $\gamma$ -Fe at the reaction's temperatures.

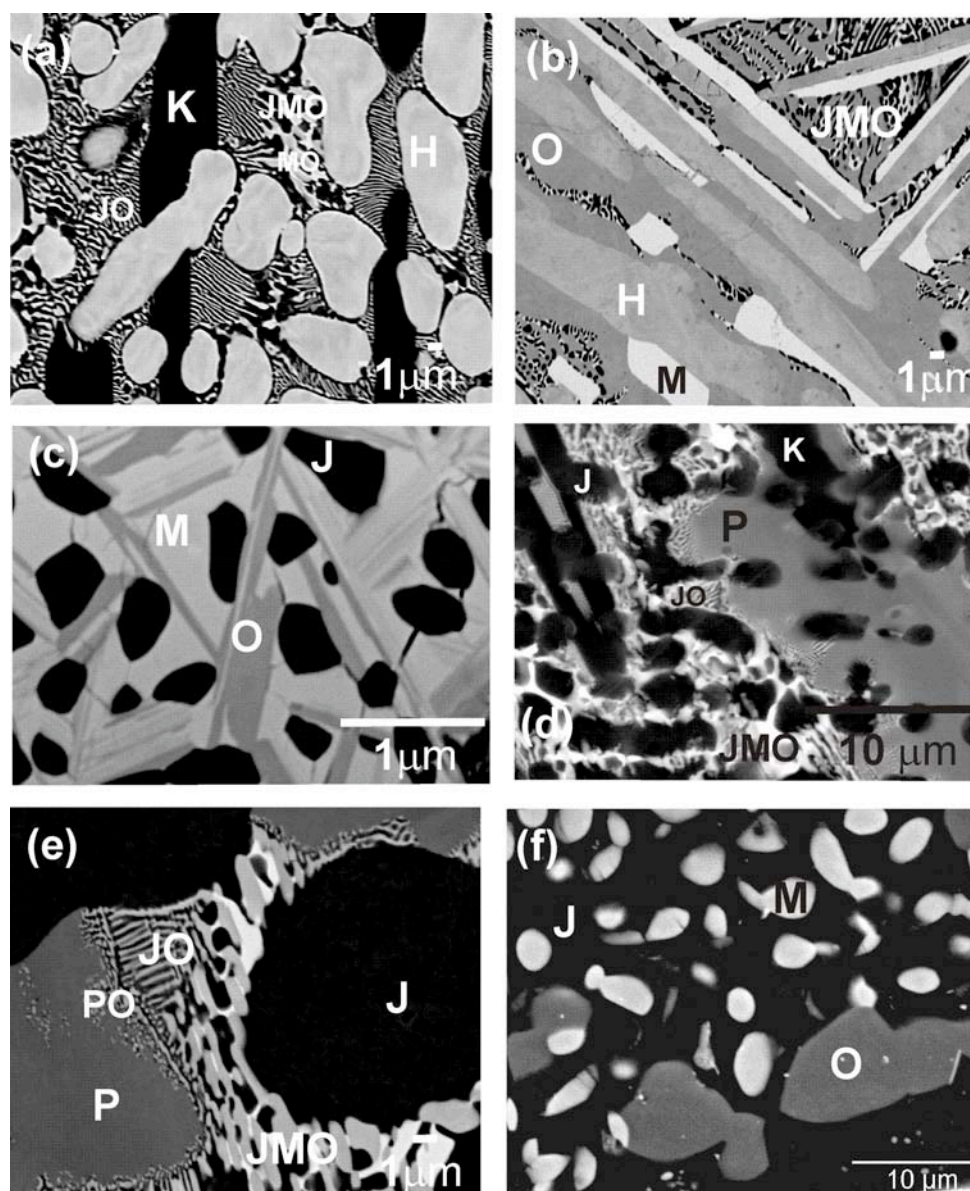


Figure 3.20 – BSE images showing microstructures of the (a) as-cast 17B:73Fe:10U alloy (Nr. 36), (b) as-cast and (c) annealed 17B:66Fe:17U ( $\text{UFe}_4\text{B}$  stoichiometry) alloy (Nr.37), (d) as-cast 15B:80Fe:5U alloy (Nr.39), (e) as-cast and (f) annealed 9B:87Fe:4U (Nr.44) alloy. The phase labeling is given in Table 3.1.

### Transition temperatures

Figure 3.21 presents the transition temperatures determined by DTA for the 17B:73Fe:10U, 17B:66Fe:17U and 9B:87Fe:4U as-cast alloys (respectively, Nr.36, 37 and 44). The assigning of specific phase transformations to the transitions observed in the DTA curve derivatives was based on the sequential melting of the phases/*cotectic* mixtures/*ternary* mixtures present in the microstructures and on their apparent volume fractions.

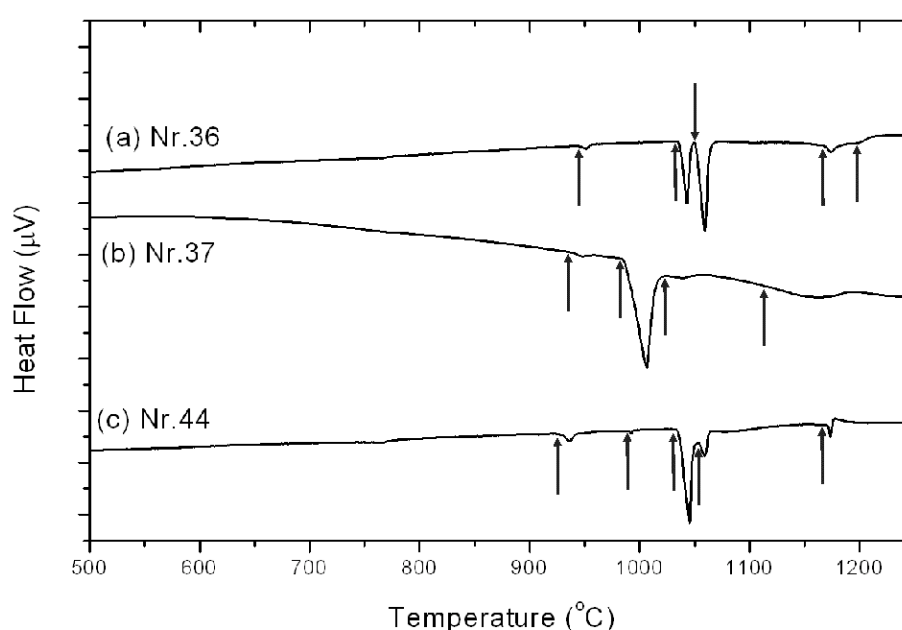


Figure 3.21 – DTA curves for representative Fe-rich as-cast: (a) 17B:73Fe:10U, (b) 17B:66Fe:17U (UFe<sub>4</sub>B stoichiometry) and (c) 9B:87Fe:4U alloys (Nr. 36, 37 and 44).

The DTA curve of 17B:73Fe:10U as-cast alloy (Nr.36), whose microstructure is shown in Figure 3.20 (a), presented five transitions. The first transition, at 945 °C, corresponds to the  $\alpha$ -Fe  $\rightarrow$   $\gamma$ -Fe allotropic transformation (J regions in the ternary eutectic and *cotectic* mixtures). This result was confirmed by HTXRD as can be observed in Figure 3.22, where the peak corresponding to  $\alpha$ -Fe disappears at 930-940 °C and is replaced by the peak corresponding to  $\gamma$ -Fe. Martensite plates were detected inside the  $\alpha$ -Fe dendrites in the post-mortem microstructure, indicating boron supersaturation. The required solute diffusion and the lack of grain boundaries (especially triple joints [23]) are expected to have induced the large overheating detected for the  $\alpha$ -Fe  $\rightarrow$   $\gamma$ -Fe transformation that in

equilibrium occurs at 912 °C. The next transition, at 1030 °C, corresponds to melting of the  $\gamma$ -Fe +  $\text{UFe}_4\text{B}$  *cotectic* mixture (regions JO). The ensuing peak at 1050 °C is likely to correspond to melting of the *cotectic* mixture  $\text{UFe}_2$  +  $\text{UFe}_4\text{B}$  (regions MO) and the other occurring at 1170 °C to melting of the  $\text{UFe}_3\text{B}_2$  phase (regions H). The last broad transition at 1195 °C, corresponds to melting of  $\text{Fe}_2\text{B}$ , the primary crystallization phase (regions K).

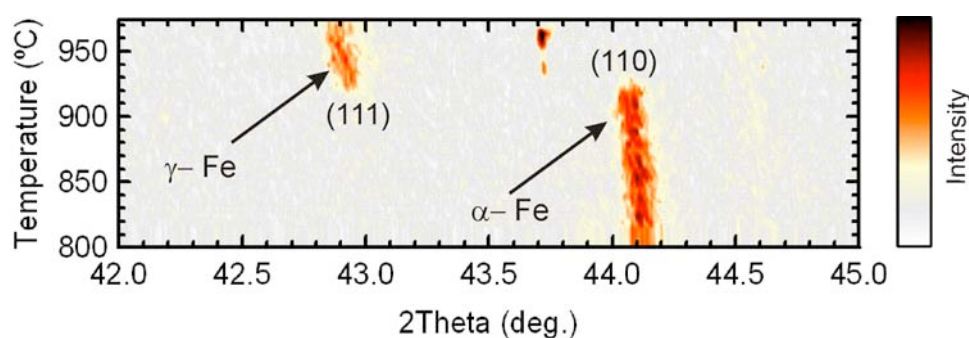


Figure 3.22 – HTXRD results of  $\alpha$ -Fe to  $\gamma$ -Fe transformation.

The DTA curve of 17B:66Fe:17U ( $\text{UFe}_4\text{B}$  stoichiometry) as-cast alloy (Nr.37) whose microstructure is shown in Figure 3.20 (b) exhibited four transitions. The first was detected at 940 °C and corresponds to the  $\alpha$ -Fe  $\rightarrow$   $\gamma$ -Fe allotropic transition (J regions in the ternary eutectic and *cotectic* mixtures). The succeeding transition at 980 °C corresponds to melting of  $\gamma$ -Fe +  $\text{UFe}_2$  +  $\text{UFe}_4\text{B}$  ternary eutectic mixture (regions JMO). The next transformation at 1020 °C corresponds to melting of  $\text{UFe}_4\text{B}$  (regions O) together with melting of  $\text{UFe}_2$  (regions M) and the transition at 1100 °C to the succeeding melting of  $\text{UFe}_3\text{B}_2$  (regions H).

The DTA curve of 9B:87Fe:4U as-cast alloy (Nr.44) whose microstructure is shown in Figure 3.20 (e) presented five transitions. The first transition, at 935 °C, corresponds to the  $\alpha$ -Fe  $\rightarrow$   $\gamma$ -Fe allotropic transformation (J regions in the ternary eutectic and *cotectic* mixtures), which is followed by another reduced signal at 985 °C corresponding to melting of the  $\gamma$ -Fe +  $\text{UFe}_2$  +  $\text{UFe}_4\text{B}$  ternary eutectic mixture (regions JMO). The ensuing transition at 1030 °C corresponds to melting of the  $\gamma$ -Fe +  $\text{UFe}_4\text{B}$  *cotectic* mixture (regions JO). According to the solidification sequence, the next transition at 1050 °C, corresponds to the succeeding melting of  $\text{U}_2\text{Fe}_{21}\text{B}_6$  (regions P). The last transition occurs at 1165 °C and corresponds to melting of  $\gamma$ -Fe (regions J).

**UFe<sub>3</sub>B<sub>2</sub>-Fe<sub>2</sub>B-UFe<sub>4</sub>B****Compatibility triangle**

Figure 3.20 (a) shows an intimate microstructural contact between UFe<sub>3</sub>B<sub>2</sub> and Fe<sub>2</sub>B (respectively, regions H and regions K), and between Fe<sub>2</sub>B and UFe<sub>4</sub>B (respectively, regions K and O). Figure 3.20 (b) presents microstructural evidence of an additional boundary line inferred from the interfaces between UFe<sub>3</sub>B<sub>2</sub> (regions H) and UFe<sub>4</sub>B (regions O). These boundary lines imply the existence of an UFe<sub>3</sub>B<sub>2</sub>-Fe<sub>2</sub>B-UFe<sub>4</sub>B compatibility triangle and a corresponding ternary reaction involving the three phases.

**R11<sub>III</sub> ternary reaction**

The UFe<sub>3</sub>B<sub>2</sub>/Fe<sub>2</sub>B boundary line (l<sub>19</sub>), which stems from the higher temperature ternary reaction R10<sub>II</sub>, converges to R11. The two boundary lines involving UFe<sub>4</sub>B: UFe<sub>3</sub>B<sub>2</sub>/UFe<sub>4</sub>B (l<sub>20</sub>) and UFe<sub>4</sub>B/Fe<sub>2</sub>B (l<sub>21</sub>) must diverge from R11, as there are no higher temperature ternary reactions from where they can originate. As a result R11 is a class III ternary reaction lying outside the UFe<sub>3</sub>B<sub>2</sub>-Fe<sub>2</sub>B-UFe<sub>4</sub>B compatibility triangle.

The boundary lines l<sub>19</sub> and l<sub>21</sub> could have either a *cotectic* or *reaction* nature [21,22], which could not be established from the microstructures.

The microstructure of the as-cast 17B:66Fe:17U (UFe<sub>4</sub>B stoichiometry) alloy (Nr.37) shown in Figure 3.20 (b) shows that UFe<sub>4</sub>B formation (regions O) involved consumption of UFe<sub>3</sub>B<sub>2</sub> (regions H), which demonstrates a *reaction* nature for l<sub>20</sub>:



The proposed equation for the ternary reaction is:

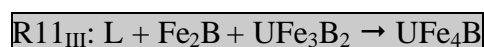


Table 3.4 presents the R11<sub>III</sub> ternary reaction equation (left column), the boundary lines at the invariant reaction (centre column) and the four-phase equilibrium configuration (right column). At R11<sub>III</sub> three phases, UFe<sub>3</sub>B<sub>2</sub>, Fe<sub>2</sub>B and L, located at the vertices of a horizontal triangular reaction plane, combine to form UFe<sub>4</sub>B, whose composition lies inside the triangle. The three-phase field UFe<sub>3</sub>B<sub>2</sub> + Fe<sub>2</sub>B + L descends from higher temperature to the ternary peritectic temperature, and three-phase regions Fe<sub>2</sub>B + L + UFe<sub>4</sub>B, UFe<sub>3</sub>B<sub>2</sub> + L + UFe<sub>4</sub>B and UFe<sub>3</sub>B<sub>2</sub> + Fe<sub>2</sub>B + UFe<sub>4</sub>B are issued beneath and proceed to lower temperatures. The ternary reaction configuration demands the UFe<sub>3</sub>B<sub>2</sub>-Fe<sub>2</sub>B-UFe<sub>4</sub>B triangle to lie inside the UFe<sub>3</sub>B<sub>2</sub>-Fe<sub>2</sub>B-L(R11<sub>III</sub>) one at the ternary reaction temperature, which roughly positions the R11<sub>III</sub> ternary reaction.

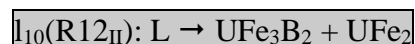
**UFe<sub>3</sub>B<sub>2</sub>-UFe<sub>2</sub>-UFe<sub>4</sub>B****Compatibility triangle**

Figure 3.20 (b) shows an intimate microstructural contact between UFe<sub>3</sub>B<sub>2</sub> (regions H) and UFe<sub>2</sub> (regions M), UFe<sub>3</sub>B<sub>2</sub> (regions H) and UFe<sub>4</sub>B (regions O) and UFe<sub>2</sub> (regions M) and UFe<sub>4</sub>B (regions O). These boundary lines imply the existence of an UFe<sub>3</sub>B<sub>2</sub>-UFe<sub>2</sub>-UFe<sub>4</sub>B compatibility triangle and a corresponding ternary reaction involving the three phases.

**R12<sub>II</sub> ternary reaction**

The UFe<sub>3</sub>B<sub>2</sub>/UFe<sub>4</sub>B boundary line (l<sub>20</sub>), which stems from higher temperature ternary reaction R11<sub>III</sub>, is converging to R12, together with UFe<sub>3</sub>B<sub>2</sub>/UFe<sub>2</sub> boundary line (l<sub>10</sub>), which stems from higher temperature R8<sub>III</sub>. Moreover, the UFe<sub>2</sub>/UFe<sub>4</sub>B boundary line (l<sub>22</sub>) must diverge from R12 toward a lower temperature ternary reaction, as there are no higher temperature ternary reactions from where it can originate. As a result, R12 is a class II ternary reaction that lies outside the compatibility triangle.

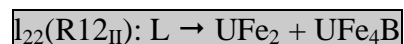
As discussed for R8<sub>III</sub>, the l<sub>10</sub> boundary line presents a *cotectic* nature:



As discussed for R11<sub>III</sub>, the l<sub>20</sub> boundary line presents a *reaction* nature:



The UFe<sub>4</sub>B + UFe<sub>2</sub> (regions MO) *cotectic* mixture (Figure 3.20 (a)) indicates that l<sub>22</sub> assumes a *cotectic* nature:



The proposed equation for the ternary reaction is:

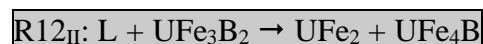


Table 3.4 presents the R12<sub>II</sub> ternary reaction equation (left column), the boundary lines at the invariant point (centre column) and the four-phase equilibrium configuration (right column). At R12<sub>II</sub> two phases, UFe<sub>3</sub>B<sub>2</sub> and L, interact to form two other phases, UFe<sub>2</sub> and UFe<sub>4</sub>B. Two three-phase regions, UFe<sub>3</sub>B<sub>2</sub> + UFe<sub>4</sub>B + L and UFe<sub>3</sub>B<sub>2</sub> + UFe<sub>2</sub> + L, descend from higher temperatures toward the four-phase reaction plane, where they meet to form a horizontal trapezium, UFe<sub>3</sub>B<sub>2</sub> + UFe<sub>2</sub> + UFe<sub>4</sub>B + L, where the four phases are in equilibrium. Below this temperature two other three-phase regions form, UFe<sub>3</sub>B<sub>2</sub> + UFe<sub>2</sub> + UFe<sub>4</sub>B and UFe<sub>2</sub> + UFe<sub>4</sub>B + L. The UFe<sub>3</sub>B<sub>2</sub> crystallization field is delimited by the lines converging to R12<sub>II</sub> indicating that the ternary reaction is situated across UFe<sub>3</sub>B<sub>2</sub> below the UFe<sub>2</sub>-UFe<sub>4</sub>B Alkemade line to allow the formation of the low temperature UFe<sub>2</sub>-UFe<sub>4</sub>B-L triangle. This trapezium configuration shows that R12<sub>II</sub> lies in the UFe<sub>2</sub>-UFe<sub>4</sub>B- $\gamma$ -Fe compatibility triangle.

**UFe<sub>4</sub>B-Fe<sub>2</sub>B-U<sub>2</sub>Fe<sub>21</sub>B<sub>6</sub>****Compatibility triangle**

The intimate microstructural contact between Fe<sub>2</sub>B (regions K) and UFe<sub>4</sub>B (regions O) (Figure 3.20 (a)), Fe<sub>2</sub>B (regions K) and U<sub>2</sub>Fe<sub>21</sub>B<sub>6</sub> (regions P) (Figure 3.20 (d)) and U<sub>2</sub>Fe<sub>21</sub>B<sub>6</sub> (regions P) and UFe<sub>4</sub>B (regions O) (Figure 3.20 (e)) implies the existence of an UFe<sub>4</sub>B-Fe<sub>2</sub>B-U<sub>2</sub>Fe<sub>21</sub>B<sub>6</sub> compatibility triangle and a corresponding ternary reaction involving the three phases.

**R13<sub>II</sub> ternary reaction**

The Fe<sub>2</sub>B/UFe<sub>4</sub>B boundary line (l<sub>21</sub>), which stems from the higher temperature R11<sub>III</sub> ternary reaction, is therefore converging to R13. The other two boundary lines involving U<sub>2</sub>Fe<sub>21</sub>B<sub>6</sub> formation, Fe<sub>2</sub>B/U<sub>2</sub>Fe<sub>21</sub>B<sub>6</sub> (l<sub>23</sub>) and UFe<sub>4</sub>B/U<sub>2</sub>Fe<sub>21</sub>B<sub>6</sub> (l<sub>24</sub>), must diverge from R13 toward lower temperature ternary reactions, as there are no higher temperature reactions from where they can originate. As a result R13 is a class III ternary reaction that lies outside the UFe<sub>4</sub>B-Fe<sub>2</sub>B-U<sub>2</sub>Fe<sub>21</sub>B<sub>6</sub> compatibility triangle.

The UFe<sub>4</sub>B + U<sub>2</sub>Fe<sub>21</sub>B<sub>6</sub> (regions PO) *cotectic* mixture (Figure 3.20 (e)) indicates that l<sub>24</sub> assumes a *cotectic* nature:



The boundary line l<sub>23</sub> and l<sub>21</sub> could have either a *cotectic* or *reaction* nature [21,22], which could not be established from the microstructures.

The proposed equation for the ternary reaction is:



Table 3.4 presents the R13<sub>III</sub> ternary reaction equation (left column), the boundary lines at the invariant point (centre column) and the four-phase equilibrium configuration (right column). At R13<sub>III</sub> three phases, UFe<sub>4</sub>B, Fe<sub>2</sub>B and L, located at

the vertices of a horizontal triangular reaction plane, combine to form  $U_2Fe_{21}B_6$ , whose composition lies inside the triangle. The three-phase field  $Fe_2B + UFe_4B + L$  descends from higher temperature to the ternary peritectic temperature, the three-phase regions  $U_2Fe_{21}B_6 + Fe_2B + L$ ,  $UFe_4B + L + U_2Fe_{21}B_6$  and  $Fe_2B + UFe_4B + U_2Fe_{21}B_6$  are issued beneath and proceed to lower temperatures. The ternary reaction configuration demands the  $Fe_2B-UFe_4B-U_2Fe_{21}B_6$  triangle to lie inside the  $Fe_2B-UFe_4B-L$  (R13<sub>III</sub>) one at the ternary reaction temperature, which roughly positions the R13<sub>III</sub> ternary reaction.

**$\gamma$ -Fe-Fe<sub>2</sub>B-U<sub>2</sub>Fe<sub>21</sub>B<sub>6</sub>****Compatibility triangle**

The intimate microstructural contact between Fe<sub>2</sub>B (regions K) and U<sub>2</sub>Fe<sub>21</sub>B<sub>6</sub> (regions P) (Figure 3.20 (d)),  $\alpha$ -Fe (regions J) and U<sub>2</sub>Fe<sub>21</sub>B<sub>6</sub> (regions P) (Figure 3.20 (e)) and Fe<sub>2</sub>B (regions K) and  $\alpha$ -Fe (regions J) Figure 3.20 (d)) implies the existence of a  $\gamma$ -Fe-Fe<sub>2</sub>B-U<sub>2</sub>Fe<sub>21</sub>B<sub>6</sub> compatibility triangle, and a corresponding ternary reaction involving the three phases.

**R14<sub>II</sub> ternary reaction**

The Fe<sub>2</sub>B/U<sub>2</sub>Fe<sub>21</sub>B<sub>6</sub> boundary line ( $l_{23}$ ) which stems from the higher temperature R13<sub>III</sub> ternary reaction, converges to R14. The  $\gamma$ -Fe/U<sub>2</sub>Fe<sub>21</sub>B<sub>6</sub> boundary line ( $l_{26}$ ) must diverge from R14 toward a lower temperature ternary reaction, as there are no higher temperature ternary reactions from where it can originate. This fact dismisses a class I ternary reaction and implies that R14 lies outside the  $\gamma$ -Fe-Fe<sub>2</sub>B-U<sub>2</sub>Fe<sub>21</sub>B<sub>6</sub> compatibility triangle. The four-phase equilibrium geometry consistent with a class III reaction of the types  $L + \gamma\text{-Fe} + \text{U}_2\text{Fe}_{21}\text{B}_6 \rightarrow \text{Fe}_2\text{B}$  or  $L + \gamma\text{-Fe} + \text{Fe}_2\text{B} \rightarrow \text{U}_2\text{Fe}_{21}\text{B}_6$ , would position R14 outside the ternary diagram or close to R11<sub>II</sub>, respectively. Since this is not compatible with the previously defined liquidus surface configuration, a class II ternary reaction has been inferred R14.

The  $l_{23}$  boundary line can have either a *cotectic* or *reaction* nature [21,22], which could not be inferred from the microstructures.

The  $l_{25}$  boundary line stems from the binary diagram [1] with a *cotectic* nature:



The  $l_{26}$  boundary line can have either a *cotectic* or *reaction* nature [21,22], which could not be established from the microstructures.

The proposed equation for the ternary reaction is:



Table 3.4 presents the R14<sub>II</sub> ternary reaction equation (left column), the boundary lines at the invariant point (centre column) and the four-phase equilibrium configuration (right column). At R14<sub>II</sub> two phases, Fe<sub>2</sub>B and L, interact to form two other phases, U<sub>2</sub>Fe<sub>21</sub>B<sub>6</sub> and  $\gamma$ -Fe. Two three-phase regions,  $\gamma$ -Fe + Fe<sub>2</sub>B + L and  $\gamma$ -Fe + U<sub>2</sub>Fe<sub>21</sub>B<sub>6</sub> + L, descend from higher temperatures toward the four-phase reaction plane, where they meet to form a horizontal trapezium,  $\gamma$ -Fe + Fe<sub>2</sub>B + U<sub>2</sub>Fe<sub>21</sub>B<sub>6</sub> + L, where the four phases are in equilibrium. Below this temperature two other three-phase regions form,  $\gamma$ -Fe + Fe<sub>2</sub>B + U<sub>2</sub>Fe<sub>21</sub>B<sub>6</sub> and  $\gamma$ -Fe + U<sub>2</sub>Fe<sub>21</sub>B<sub>6</sub> + L. The Fe<sub>2</sub>B crystallization field is delimited by the lines converging to R14<sub>II</sub> indicating that the ternary reaction is situated across Fe<sub>2</sub>B below the  $\gamma$ -Fe-U<sub>2</sub>Fe<sub>21</sub>B<sub>6</sub> Alkemade line to allow the formation of the low temperature  $\gamma$ -Fe-U<sub>2</sub>Fe<sub>21</sub>B<sub>6</sub>-L triangle. This trapezium configuration shows that R14<sub>II</sub> lies in the  $\gamma$ -Fe-UFe<sub>4</sub>B-U<sub>2</sub>Fe<sub>21</sub>B<sub>6</sub> compatibility triangle.

**$\gamma$ -Fe-UF<sub>4</sub>B-U<sub>2</sub>Fe<sub>21</sub>B<sub>6</sub>****Compatibility triangle**

Figure 3.20 (e) evidences an intimate microstructural contact between UF<sub>4</sub>B (regions O) and U<sub>2</sub>Fe<sub>21</sub>B<sub>6</sub> (regions P),  $\alpha$ -Fe and (regions J) and U<sub>2</sub>Fe<sub>21</sub>B<sub>6</sub> (regions P). Likewise, Figure 3.20 (a) evidences intimate microstructural contact between  $\alpha$ -Fe (regions J) and UF<sub>4</sub>B (regions O). These boundary lines imply the existence of a  $\gamma$ -Fe-UF<sub>4</sub>B-U<sub>2</sub>Fe<sub>21</sub>B<sub>6</sub> compatibility triangle, and therefore of a ternary reaction involving the three phases.

**R15<sub>II</sub> ternary reaction**

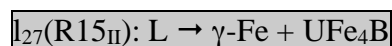
The U<sub>2</sub>Fe<sub>21</sub>B<sub>6</sub>/UF<sub>4</sub>B boundary line (*l*<sub>24</sub>) stems from the higher temperature R13<sub>II</sub> and converges to R15 together with the  $\gamma$ -Fe/U<sub>2</sub>Fe<sub>21</sub>B<sub>6</sub> boundary line (*l*<sub>26</sub>) that stems from the higher temperature R14<sub>II</sub>. The  $\gamma$ -Fe/UF<sub>4</sub>B boundary line (*l*<sub>27</sub>) must diverge from R15 as there are no higher temperature invariant points from where it can originate. As a result, R15 is a class II ternary reaction that lies outside the  $\gamma$ -Fe-UF<sub>4</sub>B-U<sub>2</sub>Fe<sub>21</sub>B<sub>6</sub> compatibility triangle.

As discussed for R13<sub>II</sub>, the *l*<sub>24</sub> boundary line presents a *cotectic* nature:



As discussed for R14<sub>II</sub>, the *l*<sub>26</sub> boundary line can present either a *cotectic* or *reaction* nature.

The  $\gamma$ -Fe + UF<sub>4</sub>B (regions JO) *cotectic* mixture (Figure 3.20 (a)) indicates that *l*<sub>27</sub> assumes a *cotectic* nature:



The proposed equation for the ternary reaction is:



Table 3.5 presents the R15<sub>II</sub> ternary reaction equation (left column), the boundary lines at the invariant reaction (centre column) and the four-phase equilibrium configuration (right column). At R15<sub>II</sub> two phases, U<sub>2</sub>Fe<sub>21</sub>B<sub>6</sub> and L, interact to form two other phases,  $\gamma$ -Fe and UFe<sub>4</sub>B. Two three-phase regions,  $\gamma$ -Fe + U<sub>2</sub>Fe<sub>21</sub>B<sub>6</sub> + L and UFe<sub>4</sub>B + U<sub>2</sub>Fe<sub>21</sub>B<sub>6</sub> + L, descend from higher temperatures toward the four-phase reaction plane, where they meet to form a horizontal trapezium,  $\gamma$ -Fe + UFe<sub>4</sub>B + U<sub>2</sub>Fe<sub>21</sub>B<sub>6</sub> + L, where the four phases are in equilibrium. Below this temperature two other three-phase regions form,  $\gamma$ -Fe + UFe<sub>4</sub>B + U<sub>2</sub>Fe<sub>21</sub>B<sub>6</sub> and  $\gamma$ -Fe + UFe<sub>4</sub>B + L. The U<sub>2</sub>Fe<sub>21</sub>B<sub>6</sub> crystallization field is delimited by the lines converging to R15<sub>II</sub> indicating that the ternary reaction is situated across U<sub>2</sub>Fe<sub>21</sub>B<sub>6</sub> below the  $\gamma$ -Fe-UFe<sub>4</sub>B Alkemade line to allow the formation of the low temperature  $\gamma$ -Fe-UFe<sub>4</sub>B-L triangle. This trapezium configuration shows that R15<sub>II</sub> lies in the  $\gamma$ -Fe<sub>2</sub>-UFe<sub>4</sub>B-UFe<sub>2</sub> compatibility triangle.

$\gamma$ -Fe- $\text{UFe}_4\text{B}$ - $\text{UFe}_2$ **Compatibility triangle**

The microstructural contact between the  $\text{UFe}_2$  (regions M) and  $\text{UFe}_4\text{B}$  (regions O) (Figure 3.20 (a)),  $\alpha$ -Fe (regions J) and  $\text{UFe}_4\text{B}$  (regions O) (Figure 3.20(e)), together with the line between the  $\alpha$ -Fe and  $\text{UFe}_2$  crystallization fields which originates in the Fe-U binary diagram [3] imply the existence of a  $\gamma$ -Fe- $\text{UFe}_2$ - $\text{UFe}_4\text{B}$  compatibility triangle and a corresponding ternary reaction involving the three phases.

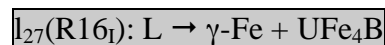
**R16<sub>I</sub> reaction**

The  $\text{UFe}_2/\text{UFe}_4\text{B}$  boundary line ( $l_{22}$ ), which stems from the higher temperature R12<sub>II</sub>, is converging to R16 together with the  $\gamma$ -Fe/ $\text{UFe}_4\text{B}$  boundary line ( $l_{27}$ ), which stems from the higher temperature R15<sub>II</sub>. This dismisses a class III ternary reaction. A class II ternary reaction, with a diverging  $\gamma$ -Fe/ $\text{UFe}_2$  boundary line ( $l_{28}$ ) implies a ternary reaction,  $L + \text{UFe}_4\text{B} \rightarrow \gamma\text{-Fe} + \text{UFe}_2$ , with an impossible geometry since the invariant point would be situated outside the ternary diagram. As a result, R16 is a class I ternary reaction that lies inside the  $\gamma$ -Fe- $\text{UFe}_2$ - $\text{UFe}_4\text{B}$  compatibility triangle.

As discussed for R12<sub>II</sub>, the  $l_{22}$  boundary line presents a *cotectic* nature:



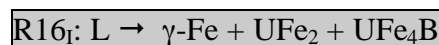
As discussed for R15<sub>II</sub>, the  $l_{27}$  boundary line presents a *cotectic* nature:



The  $l_{28}$  boundary line stems from the binary diagram [3] with a *cotectic* nature:



The proposed equation for the ternary reaction is:



The JMO ternary eutectic mixture was frequently present in the microstructures of Fe-rich alloys (see Figure 3.20). The microstructure of the 7B:79Fe:14U alloy (Nr.47) evidenced a minor volume fraction of  $\text{UFe}_4\text{B}$  primary dendrites in a  $\alpha\text{-Fe} + \text{UFe}_2 + \text{UFe}_4\text{B}$  ternary eutectic matrix. This alloy is therefore situated inside the  $\text{UFe}_4\text{B}$  primary crystallization near the ternary eutectic reaction.

Table 3.5 presents the  $\text{R16}_1$  ternary reaction equation (left column), the boundary lines at the invariant point (centre column) and the four-phase equilibrium configuration (right column). The ternary eutectic reaction  $\text{R16}_1$  occurs by isothermal decomposition of the liquid phase into three different solid phases:  $\gamma\text{-Fe}$ ,  $\text{UFe}_2$  and  $\text{UFe}_4\text{B}$ . The three-phase fields  $\gamma\text{-Fe} + \text{UFe}_4\text{B} + \text{L}$ ,  $\gamma\text{-Fe} + \text{UFe}_2 + \text{L}$  and  $\text{UFe}_2 + \text{UFe}_4\text{B} + \text{L}$  are separated by *cotectic* boundary lines and terminate on the ternary eutectic plane  $\gamma\text{-Fe} + \text{UFe}_2 + \text{UFe}_4\text{B} + \text{L}$ . The three-phase field  $\gamma\text{-Fe} + \text{UFe}_2 + \text{UFe}_4\text{B}$  forms below the ternary eutectic temperature.

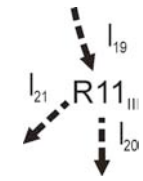
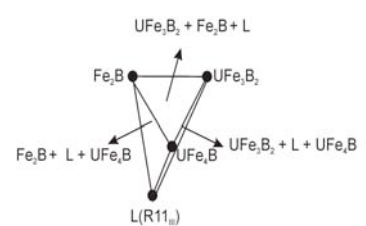
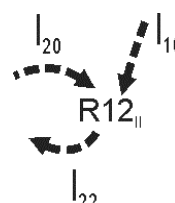
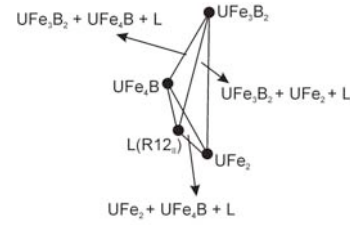
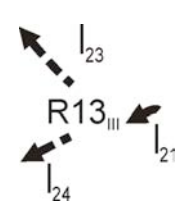
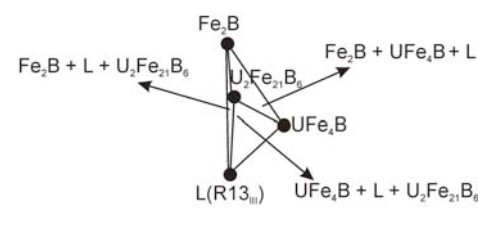
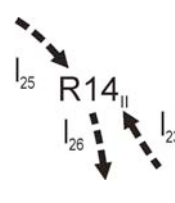
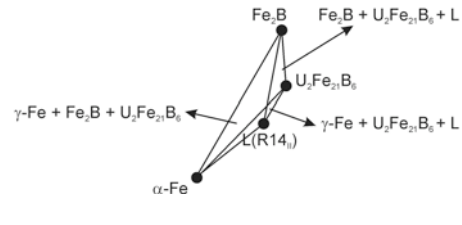
Boundary lines associated with ternary reactions		Four-phase configuration
$L + Fe_2B + UFe_3B_2 \rightarrow UFe_4B$ 	$l_{19}(R11_{III}): UFe_3B_2/Fe_2B$ (regions H + regions K)  $l_{20}(R11_{III}): L + UFe_3B_2 \rightarrow UFe_4B$ (regions H $\rightarrow$ regions O)  $l_{21}(R11_{III}): Fe_2B/UFe_4B$ (regions K + regions O)	
$L + UFe_3B_2 \rightarrow UFe_2 + UFe_4B$ 	$l_{20}(R12_{II}): L + UFe_3B_2 \rightarrow UFe_4B$ (regions H $\rightarrow$ regions O)  $l_{10}(R12_{II}): L \rightarrow UFe_3B_2 + UFe_2$ (regions HM)  $l_{22}(R12_{II}): L \rightarrow UFe_4B + UFe_2$ (regions MO)	
$L + UFe_4B + Fe_2B \rightarrow U_2Fe_{21}B_6$ 	$l_{21}(R13_{III}): Fe_2B/UFe_4B$ (regions K + regions O)  $l_{24}(R13_{III}): L \rightarrow UFe_4B + U_2Fe_{21}B_6$ (regions O + regions P)  $l_{23}(R13_{III}): Fe_2B/U_2Fe_{21}B_6$ (regions K/regions P)	
$L + Fe_2B \rightarrow U_2Fe_{21}B_6 + \gamma\text{-Fe}$ 	$l_{23}(R14_{II}): Fe_2B/U_2Fe_{21}B_6$ (regions K/regions P)  $l_{25}(R14_{II}): L \rightarrow Fe_2B + \gamma\text{-Fe}$ (regions K + regions J)  $l_{26}(R14_{II}): U_2Fe_{21}B_6/\gamma\text{-Fe}$ (regions P/regions J)	

Table 3.4 – Boundary lines for R11<sub>III</sub>, R12<sub>II</sub>, R13<sub>III</sub> and R14<sub>II</sub> ternary reactions associated with the four-phase configuration.

Boundary lines associated with ternary reactions	Four-phase configuration	
<p><math>L + U_2Fe_{21}B_6 \rightarrow UFe_4B + \gamma\text{-Fe}</math></p>	<p><math>l_{26}(R15_{II}): U_2Fe_{21}B_6/\gamma\text{-Fe}</math> (regions P/regions J)</p> <p><math>l_{24}(R15_{II}): L \rightarrow UFe_4B + U_2Fe_{21}B_6</math> (regions O + regions P)</p> <p><math>l_{27}(R15_{II}): L \rightarrow UFe_4B + \gamma\text{-Fe}</math> (regions O + regions J)</p>	
<p><math>L \rightarrow \gamma\text{-Fe} + UFe_2 + UFe_4B</math></p>	<p><math>l_{22}(R16_I): L \rightarrow UFe_2 + UFe_4B</math> (regions MO)</p> <p><math>l_{27}(R16_I): L \rightarrow \gamma\text{-Fe} + UFe_4B</math> (regions JO)</p> <p><math>l_{28}(R16_I): L \rightarrow \gamma\text{-Fe} + UFe_2</math></p>	

Table 3.5 – Boundary lines for R15<sub>II</sub> and R16<sub>I</sub> ternary reactions associated with the four-phase configuration.

### Liquidus projection

Figure 3.23 shows the liquidus projection at the Fe-rich section together with the Alkemade lines defining the phase equilibria. Figure 3.24 shows the position of alloys Nr. 36, 37, 39, 41, 43, 44, and 47. The grey lettering indicates primary crystallization fields.

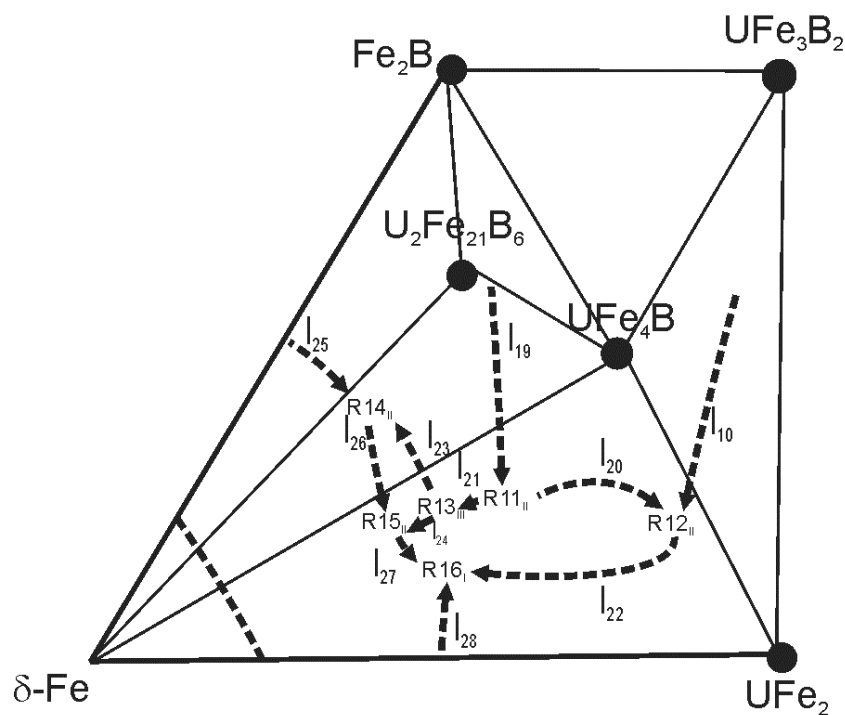


Figure 3.23 – Liquidus projection diagram in the part the Fe-rich section showing R11<sub>III</sub>, R12<sub>II</sub>, R13<sub>III</sub>, R14<sub>II</sub>, R15<sub>II</sub> and R16<sub>I</sub> where solid lines represent Alkemade lines and dashed lines indicate the liquid composition at the boundary lines.

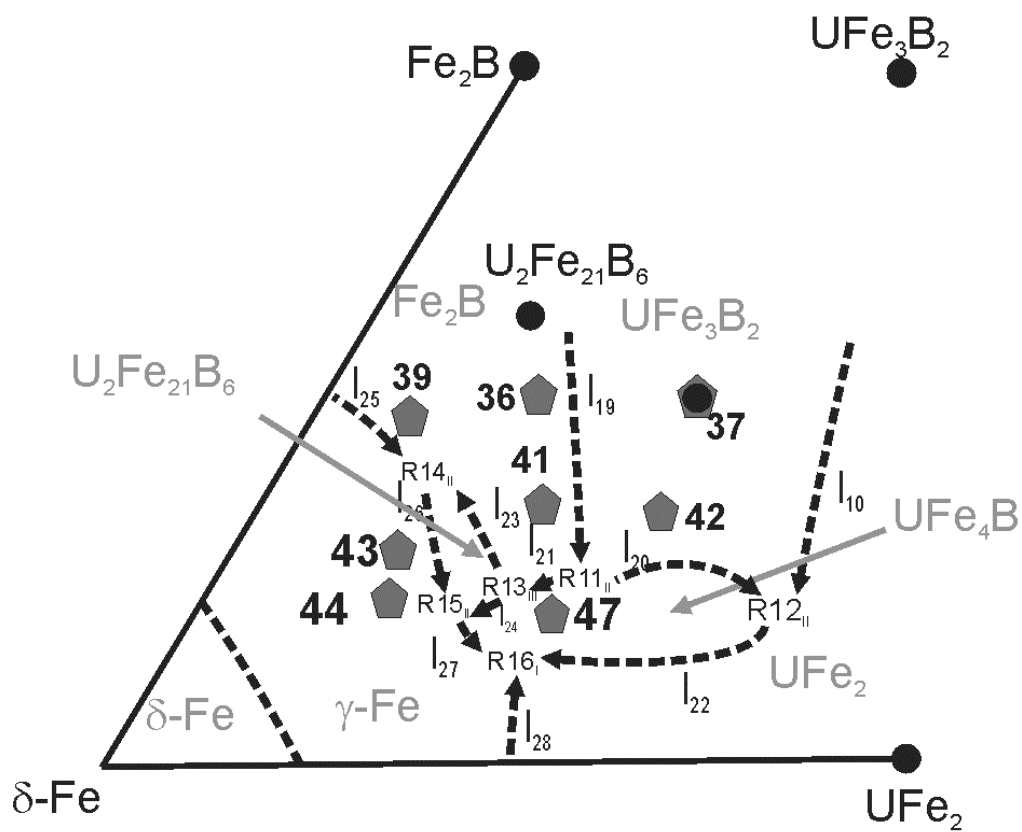


Figure 3.24 – Liquidus projection diagram in the Fe-rich section showing  $R11_{II}$ ,  $R12_{II}$ ,  $R13_{III}$ ,  $R14_{II}$ ,  $R15_{II}$  and  $R16_I$  together with 17B:73Fe:10U, 17B:66Fe:17U ( $\text{UFe}_4\text{B}$  stoichiometry), 15B:80Fe:5U, 11B:78Fe:11U, 10B:80Fe:10U, 9B:87Fe:4U, and 7B:79Fe:14U alloys positions (respectively, Nr. 36, 37, 39, 41, 43, 44 and 47) where the dashed lines represent the liquid composition at the boundary lines. The grey lettering indicates the primary crystallization fields of the compounds.

### Solidification path

Figure 3.25 shows the solidification path for the 17B:73Fe:10U, 17B:66Fe:17U (UFe<sub>4</sub>B stoichiometry) and 9B:87Fe:4U alloys (respectively, Nr. 36, 37 and 44).

The microstructure of the 17B:73Fe:10U (Nr.36) alloy exhibits the following solidification sequence: L → Fe<sub>2</sub>B (regions K) → UFe<sub>3</sub>B<sub>2</sub> (regions H) → UFe<sub>2</sub> + UFe<sub>4</sub>B (regions MO) → γ-Fe + UFe<sub>4</sub>B (regions JO) → γ-Fe + UFe<sub>2</sub> + UFe<sub>4</sub>B (regions JMO) (Figure 3.20 (a)). Therefore, according to the DTA results, solidification started at 1195 °C with the formation of Fe<sub>2</sub>B and this indicates that the alloy is situated inside the primary crystallization field of this compound. Solidification of UFe<sub>3</sub>B<sub>2</sub> (along or below l<sub>19</sub>) occurred at 1170 °C; solidification of the UFe<sub>2</sub> + UFe<sub>4</sub>B *cotectic* mixture (along l<sub>22</sub>) occurred at 1050 °C; and solidification of γ-Fe + UFe<sub>4</sub>B (along l<sub>27</sub>) occurred at 1030 °C. The fact that U<sub>2</sub>Fe<sub>21</sub>B<sub>6</sub> phase is not present in the microstructure suggests that nucleation of this phase was hindered by kinetic reasons. The fact that l<sub>27</sub> diverges from R15<sub>II</sub> enables to infer that this ternary reaction occurs at T > 1030 °C. Since l<sub>19</sub> converges to R11<sub>II</sub> this ternary reaction occurs at T < 1170 °C.

The microstructure of the 17B:66Fe:17U (UFe<sub>4</sub>B stoichiometry) alloy (Nr.37) evidences the following solidification sequence: L → UFe<sub>3</sub>B<sub>2</sub> (regions H) → UFe<sub>4</sub>B (regions O) → UFe<sub>2</sub> (regions M) → UFe<sub>4</sub>B + UFe<sub>2</sub> (regions MO) → γ-Fe + UFe<sub>2</sub> + UFe<sub>4</sub>B (regions JMO) (Figure 3.20 (b)). Therefore, solidification initiated at 1100 °C with the formation of UFe<sub>3</sub>B<sub>2</sub>, indicating that the alloy is situated inside the primary crystallization field of this compound. The solidification of UFe<sub>4</sub>B (below l<sub>20</sub>) together with the solidification of the UFe<sub>2</sub> + UFe<sub>4</sub>B *cotectic* mixture (along l<sub>22</sub>) occurred at 1020 °C. The solidification ended in R16<sub>I</sub> with the γ-Fe + UFe<sub>2</sub> + UFe<sub>4</sub>B ternary eutectic mixture at 980 °C. Since l<sub>20</sub> is converging to, and l<sub>22</sub> is diverging from, R12<sub>II</sub>, this ternary reaction occurs in the 1020 °C < T < 1100 °C temperature range. Consequently the lower temperature R13<sub>II</sub> occurs at T < 1100 °C.

The microstructure of the 9B:87Fe:4U alloy (Nr.44) presents the following solidification sequence: L → γ-Fe (regions J) → U<sub>2</sub>Fe<sub>21</sub>B<sub>6</sub> (regions P) → γ-Fe + UFe<sub>4</sub>B

(regions JO)  $\rightarrow$   $\gamma$ -Fe +  $\text{UFe}_2$  +  $\text{UFe}_4\text{B}$  (regions JMO) (Figure 3.20 (e)). The primary solidification of  $\gamma$ -Fe occurred at 1165 °C; the solidification of  $\gamma$ -Fe and  $\text{U}_2\text{Fe}_{21}\text{B}_6$  (along  $l_{26}$ ) occurred at 1050 °C; solidification of  $\gamma$ -Fe +  $\text{UFe}_4\text{B}$  *cotectic* mixture (along  $l_{27}$ ) occurred at 1030 °C. The solidification ended at 985 °C in  $\text{R16}_I$  with the  $\gamma$ -Fe +  $\text{UFe}_2$  +  $\text{UFe}_4\text{B}$  ternary eutectic mixture. The fact that  $l_{26}$  diverges from  $\text{R14}_{II}$  and converges to  $\text{R15}_{II}$  implies that  $\text{R14}_{II}$  occurs at  $T > 1050$  °C and that  $\text{R15}_{II}$  occurs at  $T < 1050$  °C. On the other hand,  $l_{27}$  diverges also from  $\text{R15}_{II}$ , which enables to infer that this ternary reaction occurs at  $T > 1030$  °C. The configuration of  $\text{R14}_{II}$  implies the convergence of  $l_{25}$ , which diverges from the binary phase diagram at  $T = 1174$ °C [1] without crossing the respective Alkemade line. This points to a monotonic temperature decrease in  $l_{25}$  and as a result,  $\text{R14}_{II}$  occurs at  $T < 1174$  °C.

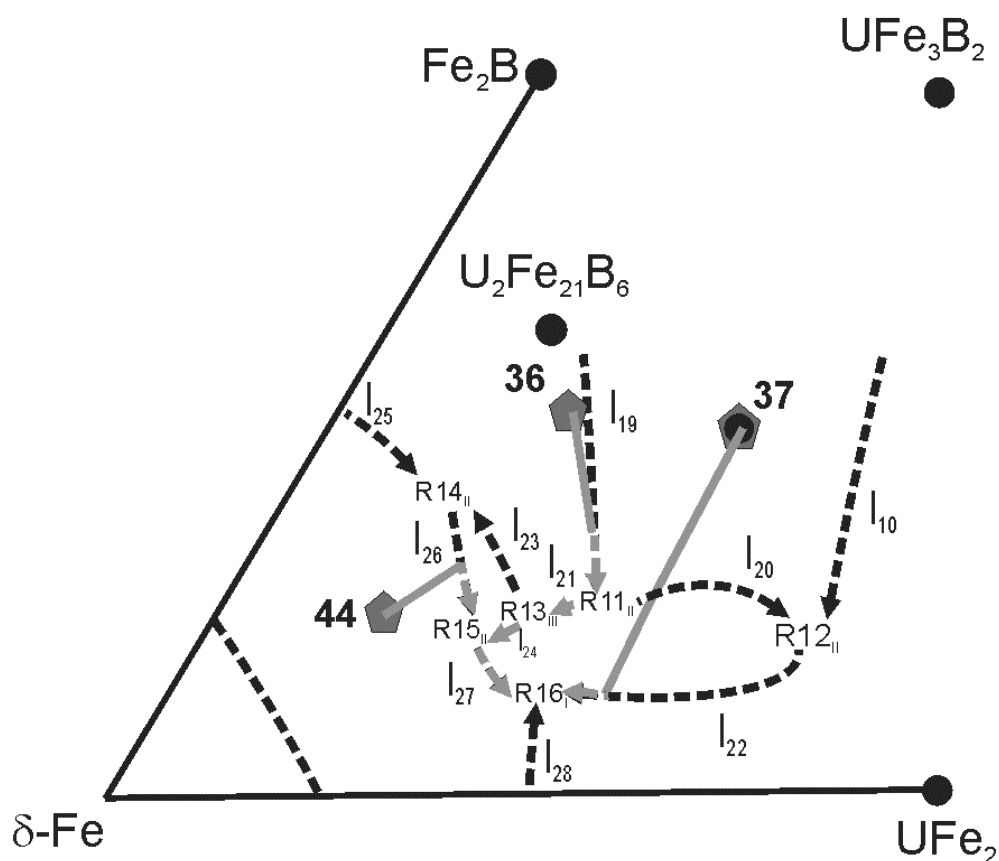


Figure 3.25 – Solidification path for alloys 17B:73Fe:10U, 17B:66Fe:17U ( $\text{UFe}_4\text{B}$  stoichiometry) and 9B:87Fe:4U alloys (respectively, Nr. 36, 37 and 44).

**Reaction scheme**

Figure 3.26 shows the reaction scheme in the Fe-rich section with indication of the transition temperatures. The ternary reactions are presented by decreasing temperature order, together with the binary reactions stemming from the B-Fe and Fe-U binary diagrams. U-B binary reactions do not converge to the ternary reactions discussed in this section, and therefore have not been represented. The arrowed lines represent the boundary lines that diverge/converge from the ternary reactions. The low temperature regions issued from the ternary reactions are listed underneath each ternary reaction equation.

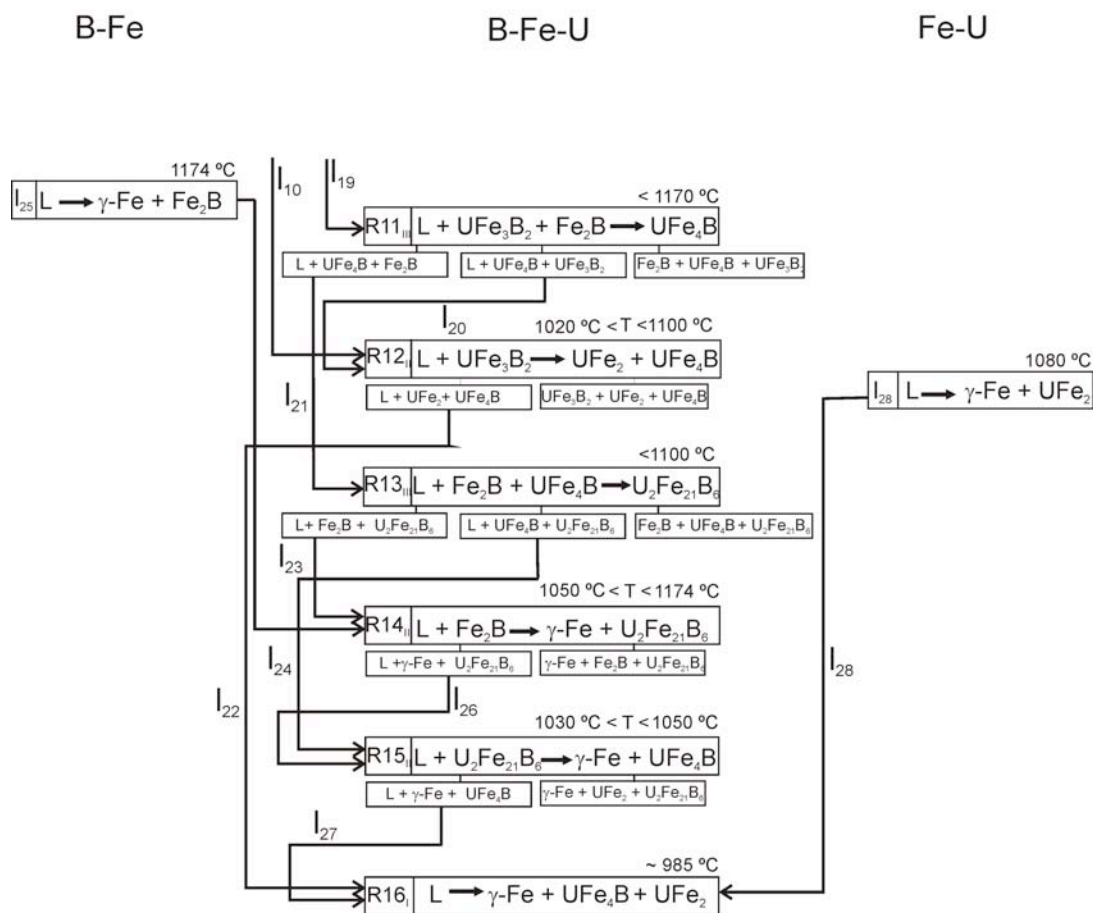


Figure 3.26 – Reaction scheme corresponding to the Fe-rich section of the liquidus projection.

### 3.3.2.4 U-rich section

The U-rich section of the ternary phase diagram comprehends one ternary reaction of class II (R17<sub>II</sub>) and one ternary reaction of class I (R18<sub>I</sub>).

#### PXRD

Figure 3.27 shows the experimental diffractograms of representative alloys that best evidence the phases present in the compatibility triangles of the U-rich region.

The PXRD diffractogram obtained for the annealed 30B:4Fe:66U alloy (Nr.27) shows a significant presence of  $UB_2$  and minor peaks of  $UFe_2$  and  $U_6Fe$ . The PXRD diffractogram of the as-cast 9B:6Fe:85U alloy (Nr.46) evidences a significant presence of  $UB_2$  and  $\alpha$ -U and a minor peaks of  $U_6Fe$ . The PXRD diffractogram of the as-cast 5B:50Fe:45U alloy (Nr.50) evidences a significant presence of  $UFe_2$ , however  $U_6Fe$  and  $UO_2$  peaks are also observed.

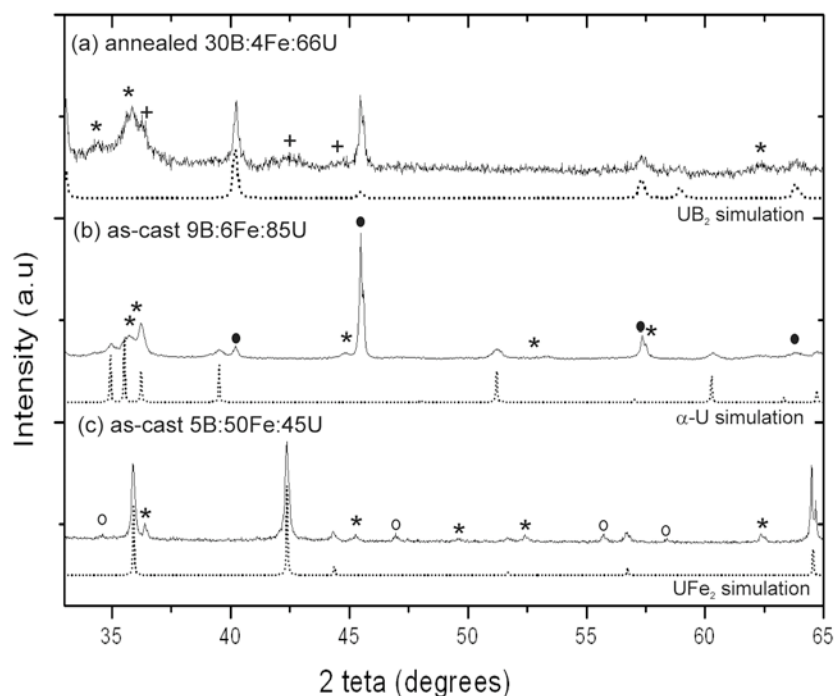


Figure 3.27 – Representative experimental powder X-ray diffractograms of U-rich alloys: (a) annealed 30B:4Fe:66U (Nr.27) (b) as-cast 9B:6Fe:85U (Nr.46), (c) as-cast 5B:50Fe:45U (Nr.50) where  $UB_2$ ,  $\alpha$ -U and  $UFe_2$  are clearly evident. The dotted lines represent the simulations for  $UB_2$ ,  $\alpha$ -U and  $UFe_2$ . Symbols:  $U_6Fe$ -stars;  $UFe_2$ - crosses,  $UO_2$  - open circles and  $UB_2$  – close circles.

### Microstructures

Microstructures of three as-cast alloys were used to evidence the boundary lines associated with each ternary reaction.

The microstructure of the 16B:44Fe:40U alloy (Nr.38), shown in Figure 3.28 (c) presents four regions, designated as B, M, Q and MQ. WDS, EDS and PXRD results indicate that these phases correspond, respectively, to  $UB_2$ ,  $UFe_2$ , and  $U_6Fe$ , while MQ corresponds to the  $UFe_2 + U_6Fe$  *cotectic* mixture.

The microstructure of the 9B:12Fe:79U: alloy (Nr.45), shown in Figure 3.28 (a) and (b) presents three regions, designated as B, Q and BMQ. WDS, EDS and PXRD results indicate that these phases correspond, respectively, to  $UB_2$  and  $U_6Fe$ , while BMQ corresponds to the  $UB_2 + UFe_2 + U_6Fe$  ternary eutectic mixture (see Figure 3.28 (b)).

The microstructure of the 9B:6Fe:85U: alloy (Nr.46), shown in Figure 3.28 (d) and (e) presents three regions, designated as B, N and Q. WDS, EDS and PXRD results indicate that these phases correspond, respectively, to  $UB_2$ ,  $\alpha$ -U and  $U_6Fe$ . The annealed microstructure of this alloy, shown in Figure 3.28 (f), evidences coarsening of  $U_6Fe$  (regions Q). Furthermore the  $UB_2$  dendrites show lower aspect ratios as a result of a globulization process.

It should be noticed that the  $\alpha$ -U phase present in the microstructures at room temperature was  $\gamma$ -U at the reactions temperature.

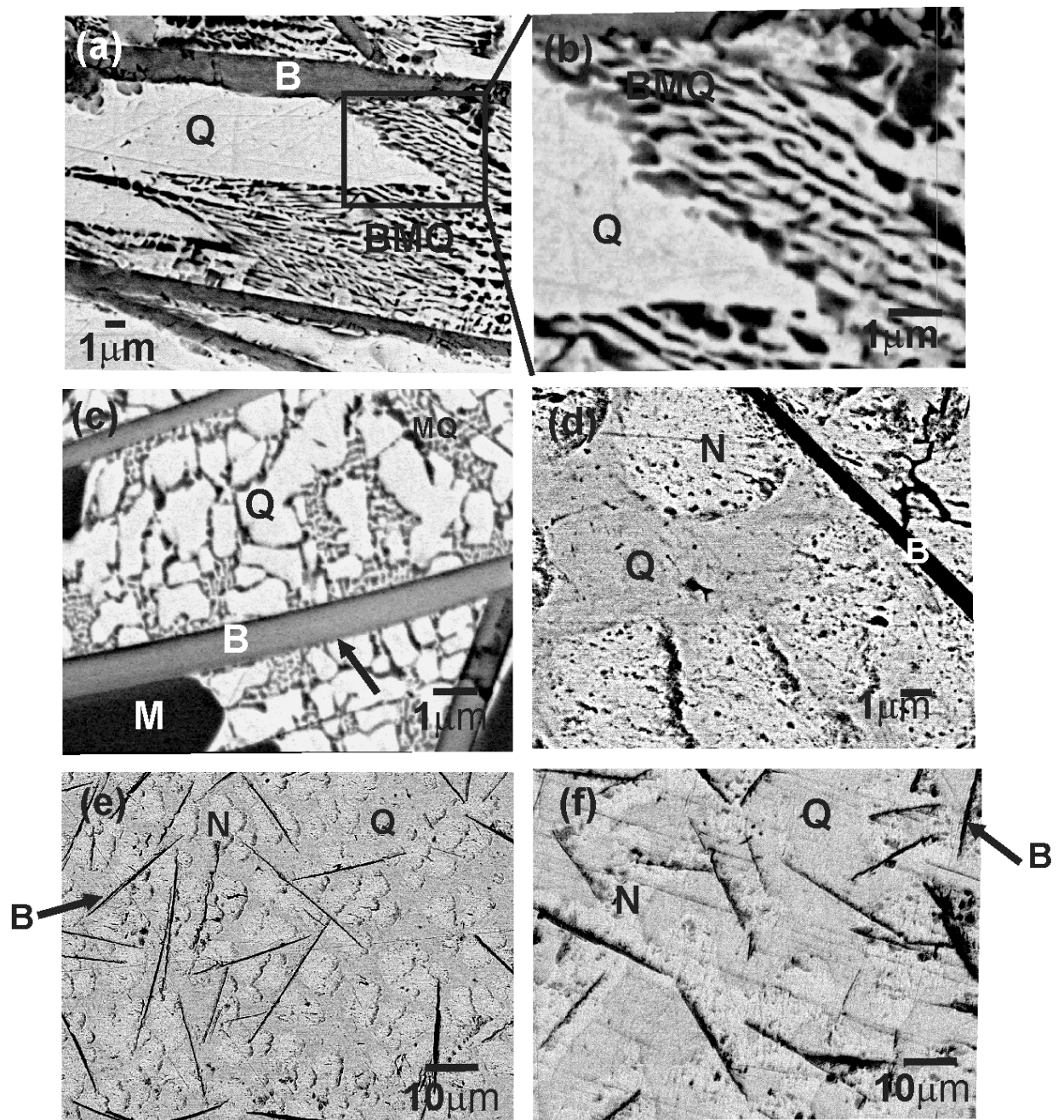


Figure 3.28 – BSE images showing microstructures observed in (a) as-cast 9B:12Fe:79U alloy (Nr.45), (b) is a magnified detail of 9B:12Fe:79U alloy (Nr.45), (c) as-cast 16B:43Fe:40U alloy (Nr.38), (d) low and (e) high magnification of as-cast 9B:6Fe:85U alloy (Nr.46) and (f) annealed 9B:6Fe:85U alloy (Nr.46). The pits observed in the U dendrites in (d) and (e) (regions N) result from a slight overetching.

### Transition temperatures

The assigning of specific phase transformations to the transitions observed in the DTA curve derivatives (Figure 3.29) was carried out based on the sequential melting of the phases/cotectic mixtures/ternary mixtures present in the microstructures and on their apparent volume fractions.

The DTA curve of the 16B:44Fe:40U alloy (Nr.38) alloy shows two transitions. The first signal was detected at 710 °C and corresponds to melting of  $UF_2$ . The ensuing transition at 1060 °C corresponds to melting of the  $UB_2$  compound.

The DTA curve of the 9B:12Fe:79U alloy (Nr.45) alloy shows two transitions. The first signal was detected at 710 °C and corresponds to melting of  $U_6Fe$ . The ensuing transition at 780 °C corresponds to the melting of the  $UB_2$  compound.

The DTA curve of the 9B:6Fe:85U alloy (Nr.46) alloy shows three transitions. The first signal was detected at 670 °C and corresponds to the allotropic transformation of  $\alpha$ -U  $\rightarrow$   $\beta$ -U [2]. The ensuing transition at 760 °C corresponds to melting of the interdendritic  $U_6Fe$  closely followed by the  $\beta$ -U  $\rightarrow$   $\gamma$ -U allotropic transition [2]. The last transition occurred at 815 °C and corresponds to melting of  $\gamma$ -U dendrites probably associated with melting of  $UB_2$ .

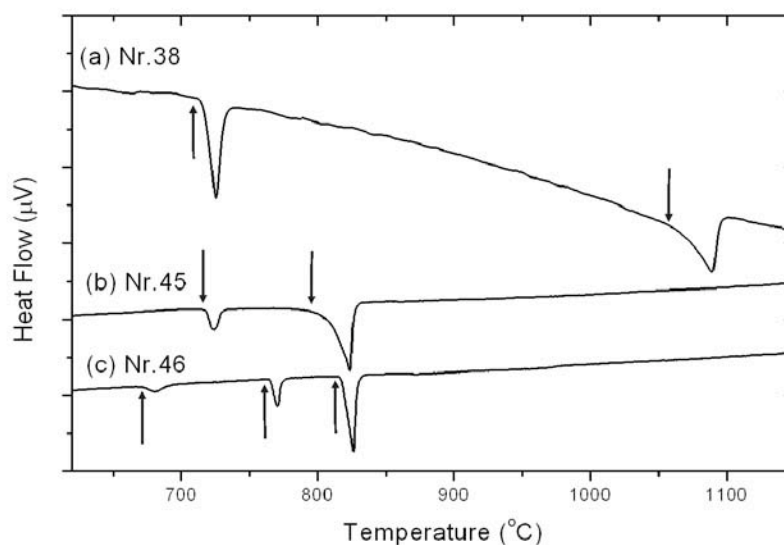


Figure 3.29 – DTA curves for representative U-rich section (a) as-cast 16B:44Fe:40U alloys (Nr. 38), (b) as-cast 9B:12Fe:79U alloys (Nr. 45), (c) as-cast 9B:6Fe:85U alloys (Nr. 46).

$\gamma$ -U-UB<sub>2</sub>-U<sub>6</sub>Fe**Compatibility triangle**

Figure 3.28 (c) and (d) evidences an intimate microstructural contact between UB<sub>2</sub> (regions B) and U<sub>6</sub>Fe (regions Q) (see black arrow), UB<sub>2</sub> (regions B) and  $\alpha$ -U (regions N) and  $\alpha$ -U (regions N) and U<sub>6</sub>Fe (regions Q), which implies the existence of an UB<sub>2</sub>- $\gamma$ -U-U<sub>6</sub>Fe compatibility triangle and a corresponding ternary reaction involving the three phases.

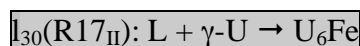
**R17<sub>II</sub> ternary reaction**

The binary UB<sub>2</sub> +  $\gamma$ -U eutectic in the B-U phase diagram occurs at a temperature (1107 °C [2]) higher than the transition temperatures detected for U-rich alloys. Therefore the UB<sub>2</sub>/ $\gamma$ -U boundary line (l<sub>29</sub>) converges to the lower temperature R17 from the binary diagram. The UB<sub>2</sub>/U<sub>6</sub>Fe boundary line (l<sub>31</sub>) must diverge from R17 toward a lower temperature ternary reaction, as there are no higher temperature ternary reactions from where it can originate. This fact dismisses a class I ternary reaction and implies that R17 lies outside the UB<sub>2</sub>-U<sub>6</sub>Fe- $\gamma$ -U compatibility triangle. The four-phase equilibrium geometry consistent with a class III reaction of the type L + UB<sub>2</sub> +  $\gamma$ -U → U<sub>6</sub>Fe would position R17 outside the ternary diagram. As a result, a class II ternary reaction has been inferred for R17.

The l<sub>29</sub> boundary line stems from the binary diagram [2] with a *cotectic* nature:



The l<sub>30</sub> boundary line stems from the binary diagram [3] with a *cotectic* nature:



The l<sub>31</sub> boundary line can have either a *cotectic* or *reaction* nature [21,22], which could not be established from the microstructures.

The proposed equation for the ternary reaction is:

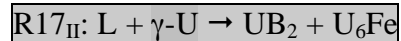


Table 3.6 presents the R17<sub>II</sub> ternary reaction equation (left column), the boundary lines at the invariant point (centre column) and the four-phase equilibrium configuration (right column). At R17<sub>II</sub> two phases, L and  $\gamma$ -U, interact and form two other phases, U<sub>6</sub>Fe and UB<sub>2</sub>. Two three-phase regions,  $\gamma$ -U + U<sub>6</sub>Fe + L and  $\gamma$ -U + UB<sub>2</sub> + L, descend from higher temperature toward the four-phase reaction plane, where they meet to form a horizontal trapezium, UB<sub>2</sub> +  $\gamma$ -U + U<sub>6</sub>Fe + L, where the four phases are in equilibrium. Below this temperature two other three-phase regions form, UB<sub>2</sub> +  $\gamma$ -U + U<sub>6</sub>Fe and UB<sub>2</sub> + U<sub>6</sub>Fe + L. The  $\gamma$ -U crystallization field is delimited by the lines converging to R17<sub>II</sub> indicating that the ternary reaction is situated across  $\gamma$ -U below the UB<sub>2</sub>-U<sub>6</sub>Fe Alkemade line to allow the formation of the low temperature UB<sub>2</sub>-U<sub>6</sub>Fe-L triangle. This trapezium configuration shows that R17<sub>II</sub> lies in the UB<sub>2</sub>-UFe<sub>2</sub>-U<sub>6</sub>Fe compatibility triangle.

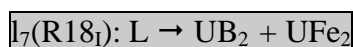
**UB<sub>2</sub>-UFe<sub>2</sub>-U<sub>6</sub>Fe****Compatibility triangle**

The intimate microstructural contact between UB<sub>2</sub> (regions B) and UFe<sub>2</sub> (regions M) (see Figure 3.28 (c)) and UB<sub>2</sub> (regions M) and U<sub>6</sub>Fe (regions Q) (see arrow in Figure 3.28 (c)) together with the boundary line between UFe<sub>2</sub> and U<sub>6</sub>Fe, which stems from the binary diagram [3], imply the existence of an UB<sub>2</sub>-UFe<sub>2</sub>-U<sub>6</sub>Fe compatibility triangle and a corresponding ternary reaction involving the three phases.

**R18<sub>I</sub> ternary reaction**

Alloy Nr.38 presents a primary solidification of UB<sub>2</sub> (regions B) (see Figure 3.28 (c)), which implies that its composition is situated inside the UB<sub>2</sub> crystallization field. Subsequently the liquid followed the UB<sub>2</sub>/UFe<sub>2</sub> boundary line (l<sub>7</sub>) forming a (divorced) *cotectic* mixture of these congruent compounds (see Figure 3.28 (c)). Low magnification images demonstrated that formation of the primary phase was relatively modest (~20% volume fraction) indicating that l<sub>7</sub> passes near alloy Nr.38 position. Therefore the l<sub>7</sub> boundary line that converges to R7<sub>II</sub> crosses the corresponding Alkemade line, where it achieves a temperature maximum, before converging to R18. The UB<sub>2</sub>/U<sub>6</sub>Fe boundary line (l<sub>31</sub>), which stems from R17<sub>II</sub> converges to the lower temperature R18. The fact that both l<sub>7</sub> and l<sub>31</sub> are converging to R18 dismisses a class III ternary reaction. A class II ternary reaction, with a diverging UFe<sub>2</sub>/U<sub>6</sub>Fe boundary line (l<sub>29</sub>) implies a ternary reaction, L + UB<sub>2</sub> → γ-U + U<sub>6</sub>Fe, with an impossible geometry as the invariant point would be situated outside the ternary diagram. As a result, R18 is a class I ternary reaction that lies inside the UB<sub>2</sub>-UFe<sub>2</sub>-U<sub>6</sub>Fe compatibility triangle.

As discussed for R17<sub>II</sub>, the l<sub>7</sub> boundary line presents a *cotectic* nature:

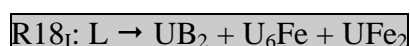


The  $l_{31}$  boundary line can have either a *cotectic* or *reaction* nature [21,22], which could not be established from the microstructures.

The boundary line  $l_{32}$  stems from the binary diagram [3] with a *cotectic* nature:



The proposed equation for the ternary reaction is:



The microstructure of the 9B:12Fe:79U alloy (Nr.45) evidences the  $UB_2 + UFe_2 + U_6Fe$  ternary eutectic mixture (regions BMQ, see magnified detail in Figure 3.28 (b)). Since the  $R18_I$  is far from the  $UB_2$  stoichiometric composition, the volume fraction of this compound (regions B) in the ternary eutectic mixture is low.

Table 3.6 presents the  $R18_{II}$  ternary reaction equation (left column), the boundary lines at the invariant point (centre column) and the four-phase equilibrium configuration (right column). The ternary eutectic reaction  $R18_I$  occurs by isothermal decomposition of the liquid phase into three different solid phases,  $UB_2$ ,  $UFe_2$  and  $U_6Fe$ . The three three-phase fields  $L + UB_2 + U_6Fe$ ,  $L + UB_2 + UFe_2$  and  $L + UFe_2 + U_6Fe$  terminate on the ternary eutectic plane  $L + UB_2 + U_6Fe + UFe_2$ . Below the ternary eutectic temperature the three-phase field  $UB_2 + U_6Fe + UFe_2$  is formed.

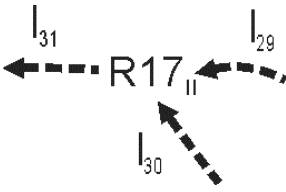
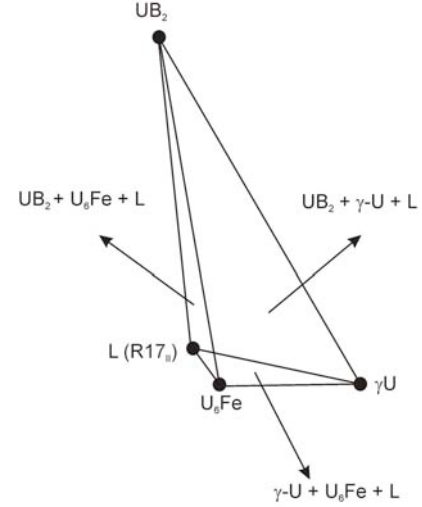
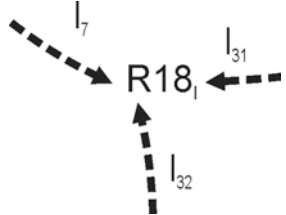
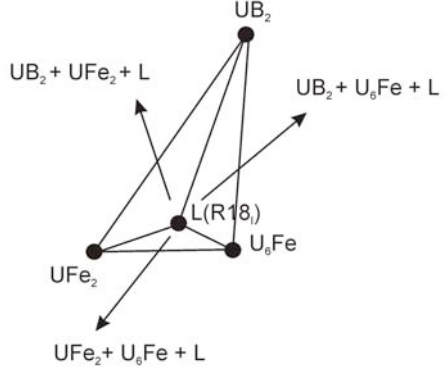
Boundary lines associated with ternary reactions	Four-phase configuration
<p><math>L + \gamma\text{-U} \rightarrow \text{UB}_2 + \text{U}_6\text{Fe}</math></p> <p><math>I_{29}(\text{R17}_{\text{II}}) : L \rightarrow \text{UB}_2 + \gamma\text{-U}</math> (from binary diagram [2])</p> <p><math>I_{30}(\text{R17}_{\text{II}}) : L + \gamma\text{-U} \rightarrow \text{U}_6\text{Fe}</math> (from binary diagram [3])</p> <p><math>I_{31}(\text{R17}_{\text{II}}) : \text{UB}_2/\text{U}_6\text{Fe}</math> (regions B/regions Q)</p> 	
<p><math>L \rightarrow \text{UB}_2 + \text{U}_6\text{Fe} + \text{UFe}_2</math></p> <p><math>I_7(\text{R18}_I) : L \rightarrow \text{UB}_2 + \text{UFe}_2</math> (regions M + regions B)</p> <p><math>I_{31}(\text{R18}_I) : \text{UB}_2/\text{U}_6\text{Fe}</math> (regions B/regions Q)</p> <p><math>I_{32}(\text{R18}_I) : L \rightarrow \text{UFe}_2 + \text{U}_6\text{Fe}</math> (from binary diagram [3])</p> 	

Table 3.6 – Boundary lines for R17<sub>II</sub> and R18<sub>I</sub> ternary reactions associated with the four-phase configuration.



### Solidification path

Figure 3.31 shows the solidification path for 16B:44Fe:40U, 9B:12Fe:79U and 9B:6Fe:85U alloys (Nr. 38, 45 and 46).

The microstructure of the 16B:44Fe:40U (Nr.38) alloy shown in Figure 3.28 (a) evidences the following solidification path:  $L \rightarrow UB_2$  (regions B)  $\rightarrow UFe_2$  (regions M)  $\rightarrow UFe_2 + U_6Fe$  (regions MQ). Since the two major phases are  $UB_2$  and  $UFe_2$ , the two transitions observed in the DTA curves should involve these compounds. Solidification started at 1060 °C with formation of  $UB_2$  (above  $l_7$ ). Solidification of  $UFe_2$  (along  $l_7$ ) occurred at 710 °C. Since  $l_7$  converges to  $R18_I$  this ternary reaction occurs at  $T < 710$  °C.

The microstructure of the 9B:12Fe:79U alloy (Nr.45) alloys exhibits the following solidification sequence:  $L \rightarrow UB_2$  (regions B)  $\rightarrow U_6Fe$  (regions Q)  $\rightarrow UB_2 + UFe_2 + U_6Fe$  (regions BMQ) (Figure 3.28 (a) and (b)). Solidification begins with  $UB_2$  (above  $l_{29}$ ) at 780 °C and the alloy is therefore situated inside the primary crystallization field of this compound. Formation of  $U_6Fe$  (along  $l_{31}$ ) occurred at 710 °C. The fact that  $l_{31}$  diverges from  $R17_{II}$  enables to infer that this ternary reaction occurs at  $T > 710$  °C. Since  $l_{30}$  stems from the binary diagram at 795 °C [3] and converges to  $R17_{II}$  this ternary reaction occurs hence at  $710$  °C  $< T < 795$  °C. Since the volume fraction of ternary eutectic mixture is reduced (see Figure 3.28 (a)), the ternary eutectic formation was not detected in the DTA curves.

The microstructure of the 9B:6Fe:85U alloy (Nr.46) alloy exhibits the following solidification sequence:  $L \rightarrow UB_2$  (regions B)  $\rightarrow \gamma-U$  (regions N)  $\rightarrow U_6Fe$  (regions Q) (Figure 3.28 (d)). The primary solidification of  $UB_2$  together with the formation of  $\gamma-U$  occurred at 815 °C (along  $l_{29}$ ); the solidification of  $U_6Fe$  (along  $l_{31}$ ) together with the allotropic transformation of  $\gamma-U \rightarrow \beta-U$  [2] occurred at 760 °C; the last transition occurred at 670 °C and corresponds to the allotropic transformation of  $\beta-U \rightarrow \alpha-U$  [2]. Since  $l_{29}$  is converging and  $l_{31}$  is diverging from  $R17_{II}$ , this ternary reaction should occurs at  $760$  °C  $< T < 815$  °C.

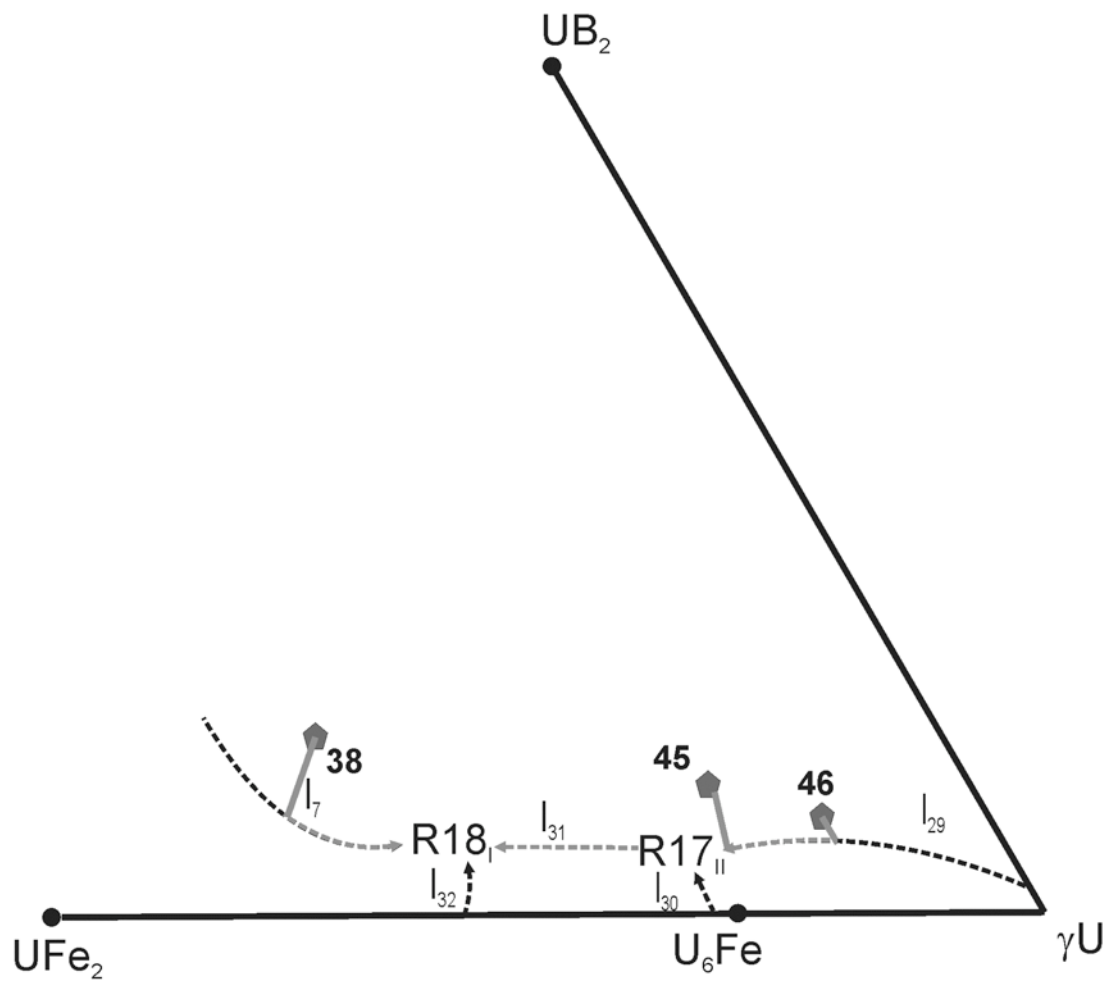


Figure 3.31 – Solidification path for alloys 16B:43Fe:40U, 9B:12Fe:79U and 9B:6Fe:85U alloys position (respectively, Nr. 38, 45 and 46).



### 3.3.3 Complete liquidus projection

Figure 3.33 shows the complete liquidus projection of the B-Fe-U ternary phase diagram with 32 boundary lines and 18 invariant reactions: 5 of class III; 9 of class II and 4 of class I.

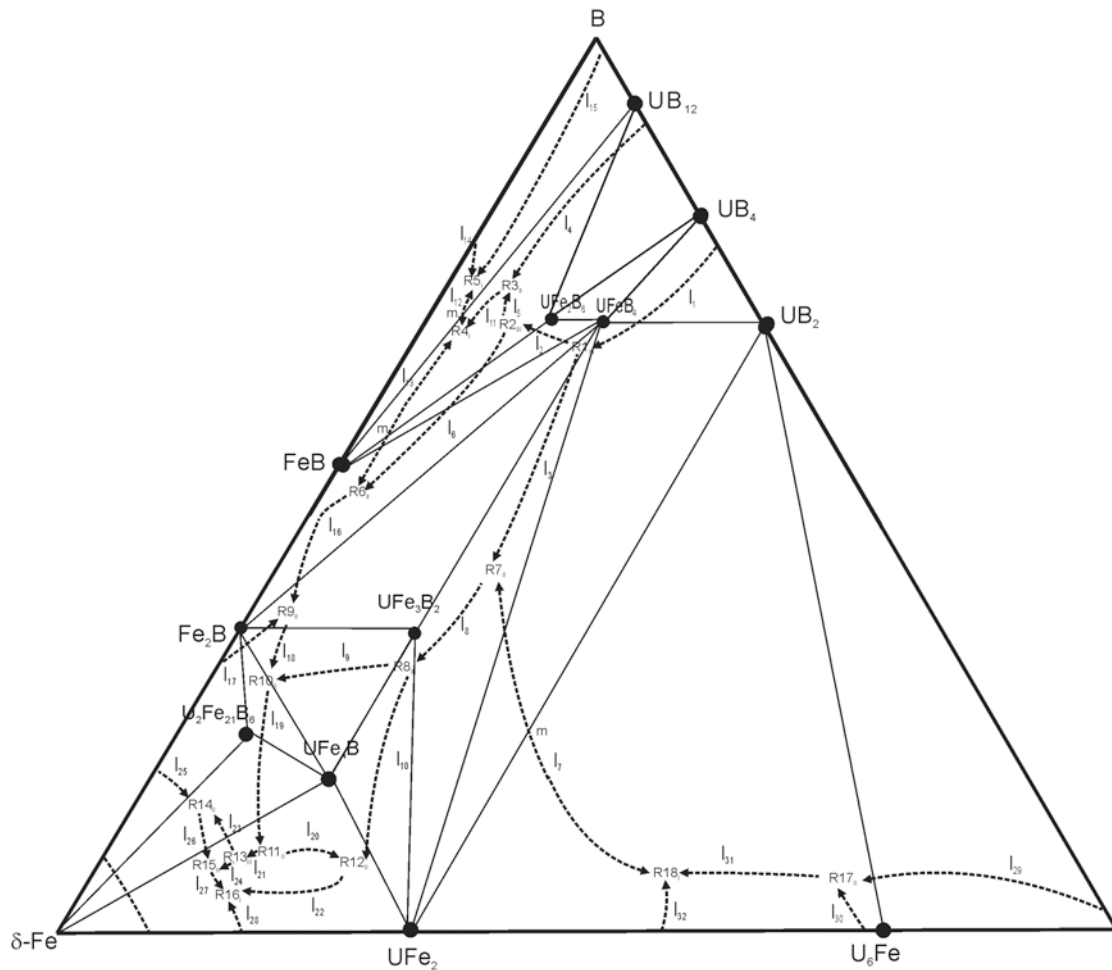


Figure 3.33 – Liquidus projection diagram in the B-Fe-U ternary diagram showing all the ternary reactions, where solid lines represent the solid phases in equilibrium and dashed lines indicate the liquid composition (see appendix 1).

## 3.3.3.1 Total reaction scheme

The total reaction scheme (Figure 3.34) presents the ternary reactions by decreasing temperature order, together with the binary reactions. The low temperature regions issued from the ternary reactions are listed underneath each ternary reaction equation. Temperature maxima in the boundary lines is represented by 'm'.

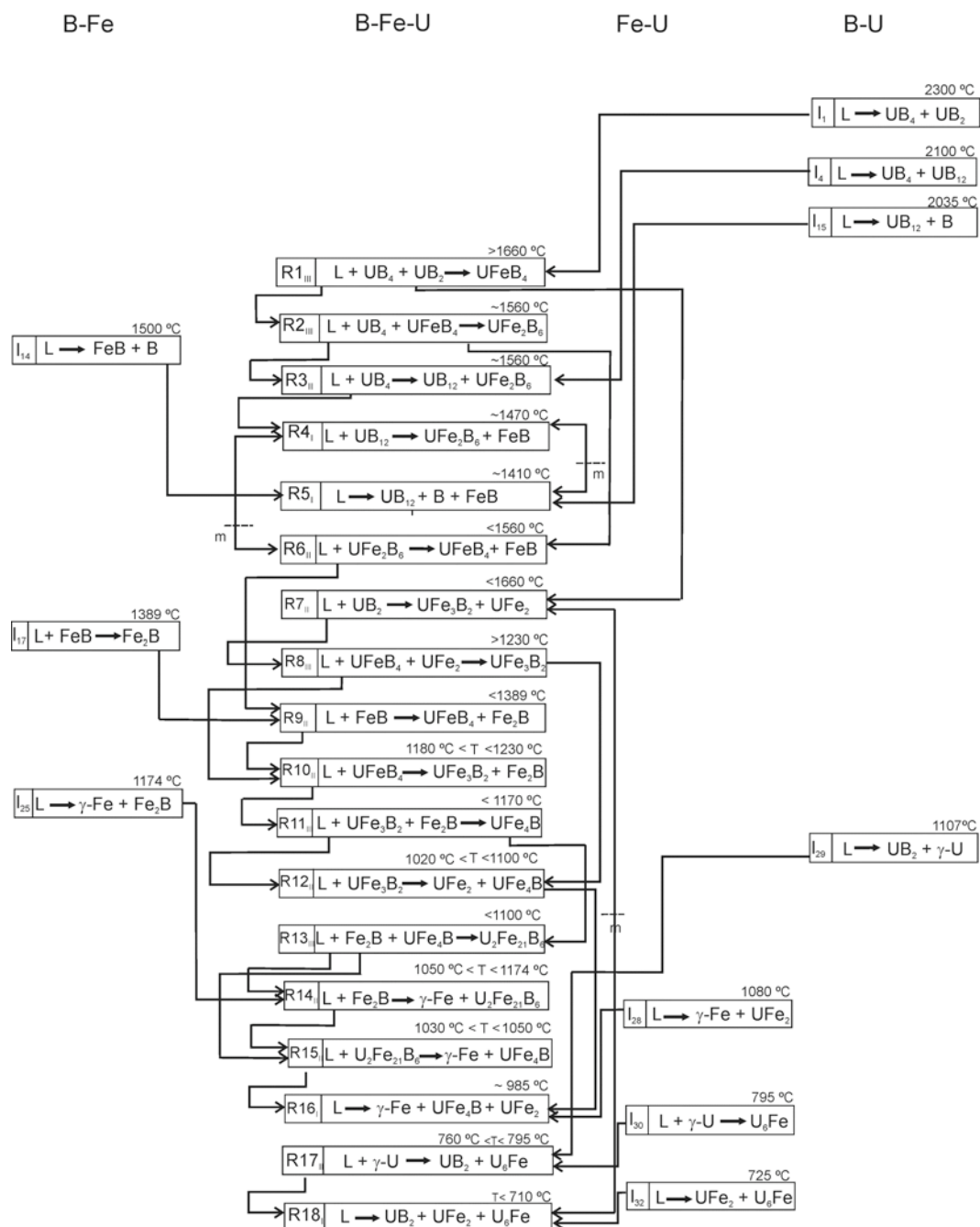


Figure 3.34 – Reaction scheme of the liquidus projection of the B-Fe-U diagram.

### 3.3.4 Isothermal sections

The isothermal section at 780 °C is presented in Figure 3.35. At this temperature 26 phase fields have been identified.

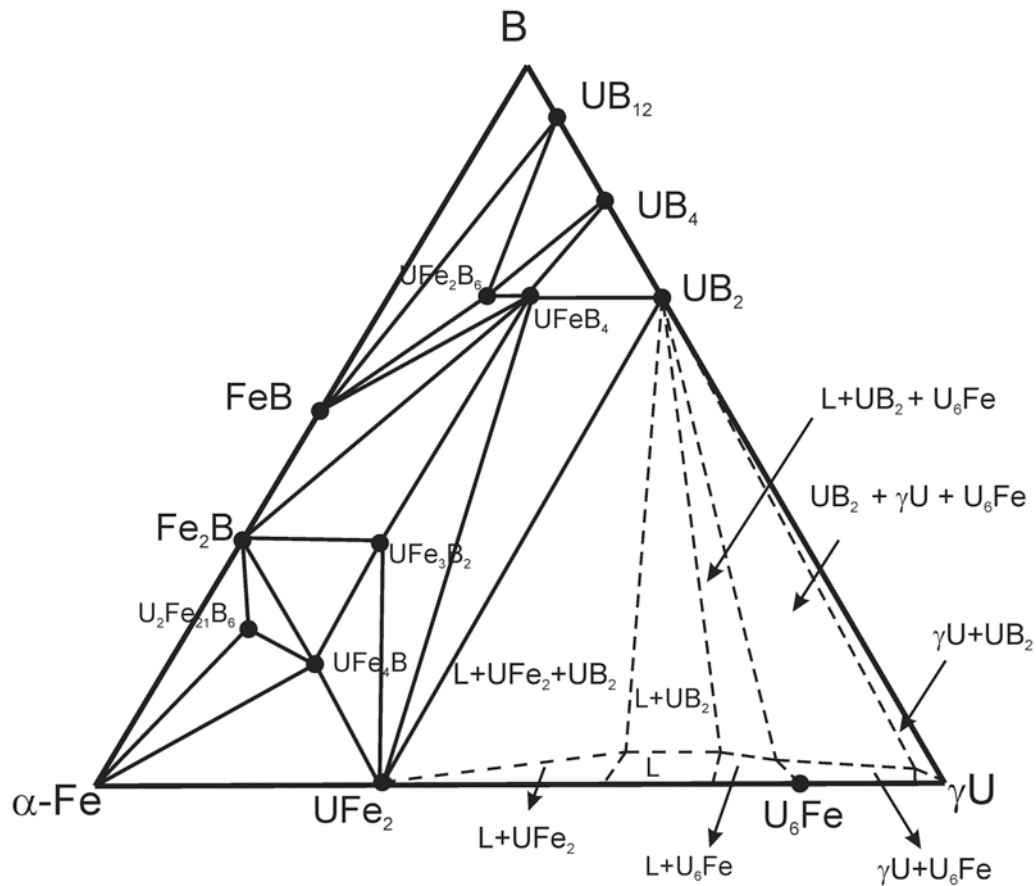


Figure 3.35 – Isothermal section at 780 °C of the B-Fe-U ternary phase diagram showing the Alkemade lines.

The isothermal section at 950 °C is presented in Figure 3.36. At this temperature 24 phase fields have been identified.

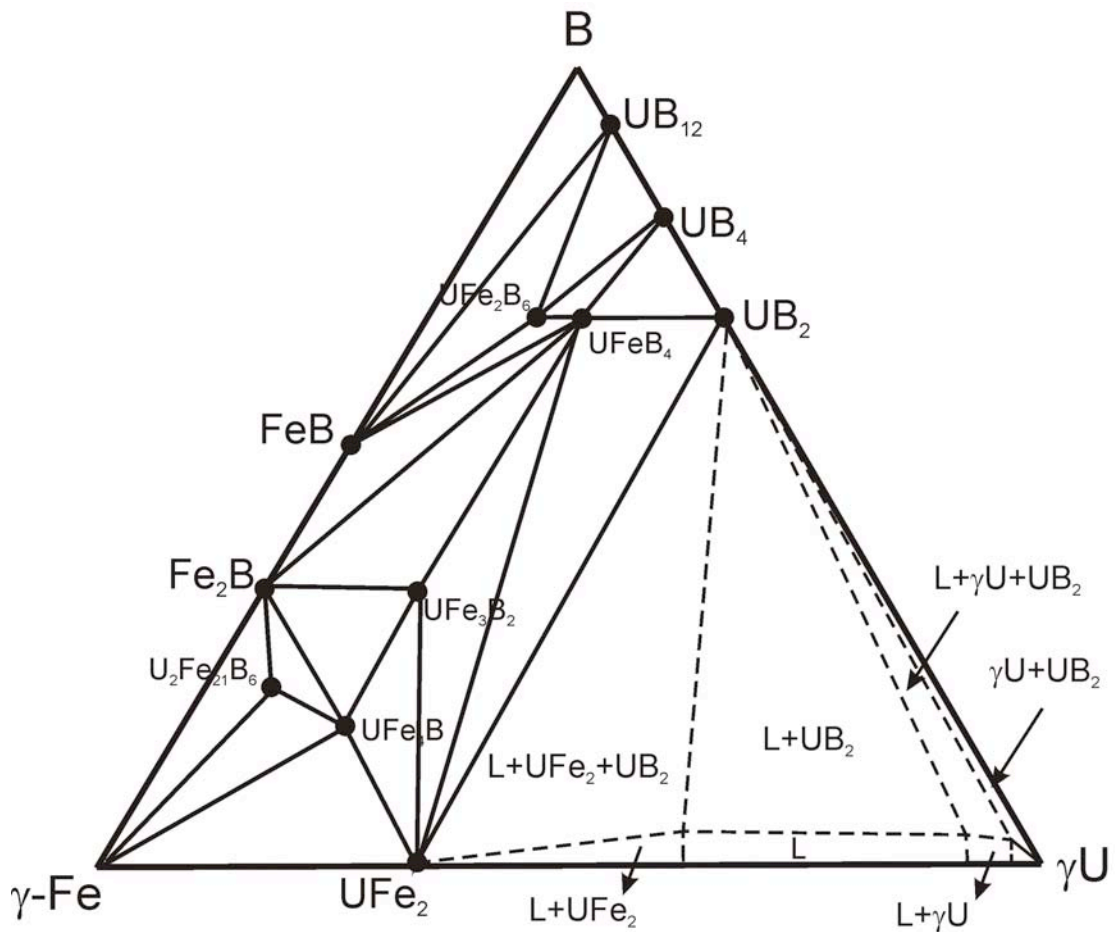


Figure 3.36 – Isothermal section at 950 °C of the B-Fe-U ternary phase diagram showing the Alkemade lines.

The isothermal section at 1100 °C is presented in Figure 3.37. At this temperature 29 phase fields have been identified.

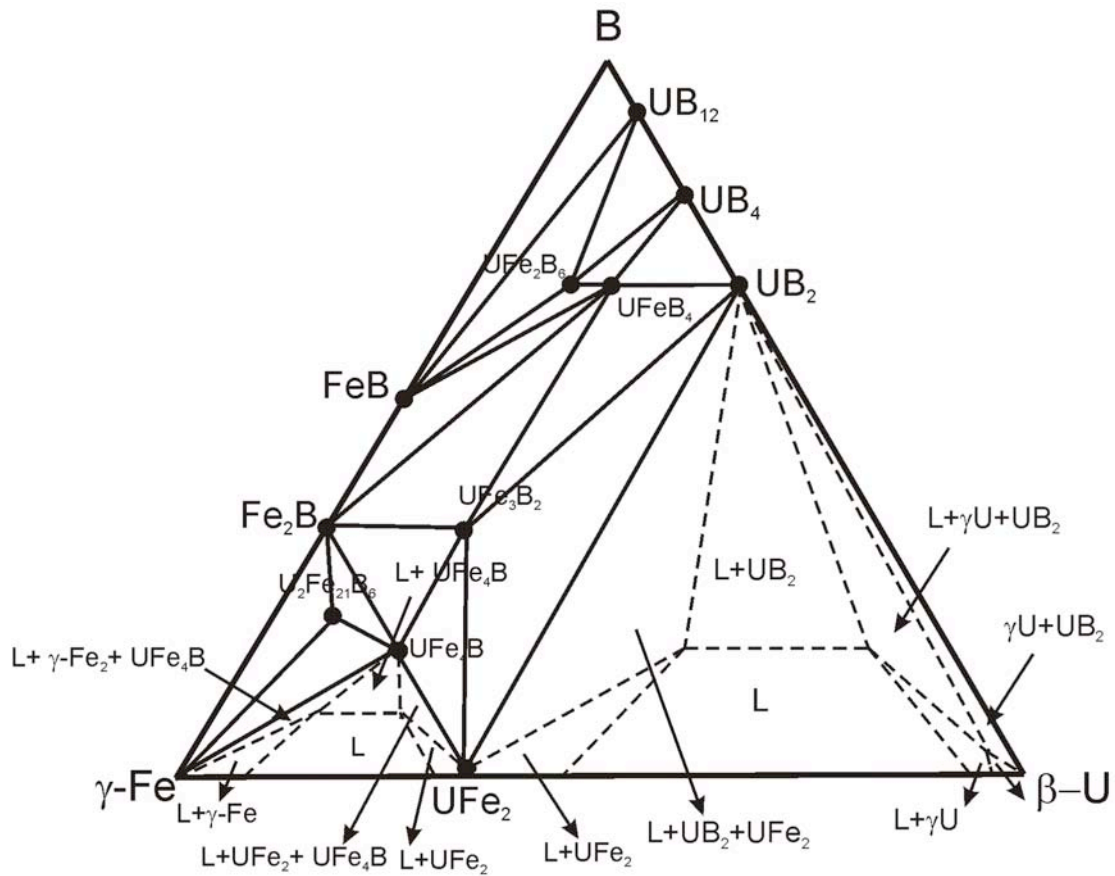


Figure 3.37 – Isothermal section at 1100 °C of the B-Fe-U ternary phase diagram showing the Alkemade lines.

### 3.3.5 Vertical section along the U:(Fe,B) = 1:5 line

A vertical section across the U:(Fe,B) = 1:5 is proposed in Figure 3.38. Alloys with an U:(Fe,B) proportion of 1:5 and primary solidification above R1<sub>III</sub> (both in B content and temperature) show a deviation of the liquid composition to the left due to UB<sub>4</sub> crystallization. As a result, these alloys exhibit phases situated on the left of the 1:5 line, such as the iron-rich phases. Alloys with 1:5 proportion situated below R1<sub>III</sub> present primary crystallization of UB<sub>2</sub>. In these cases, due to UB<sub>2</sub> solidification the liquid composition crosses l<sub>3</sub> and enters the UFeB<sub>4</sub> primary crystallization field. Subsequently, the liquid composition crosses the l<sub>9</sub> boundary line when the compound UFe<sub>3</sub>B<sub>2</sub> forms. After this point the liquid composition crosses l<sub>20</sub>, where UFe<sub>4</sub>B starts to crystallize. The congruent compound UFe<sub>2</sub> forms when the liquid crosses l<sub>22</sub> and follows to the eutectic valley. The solidification ends at the R16<sub>I</sub> ternary eutectic, positioned to the left of the 1:5 line. In the base of the diagram, the vertical section crosses the l<sub>28</sub> boundary line. In summary, the U:(Fe,B) = 1:5 vertical section intercepts one four-phase reaction plane at 1660 °C (R1<sub>III</sub>: L + UB<sub>4</sub> + UB<sub>2</sub> → UFeB<sub>4</sub>) and crosses five boundary lines, l<sub>3</sub>, l<sub>9</sub>, l<sub>20</sub>, l<sub>22</sub> and l<sub>28</sub>.

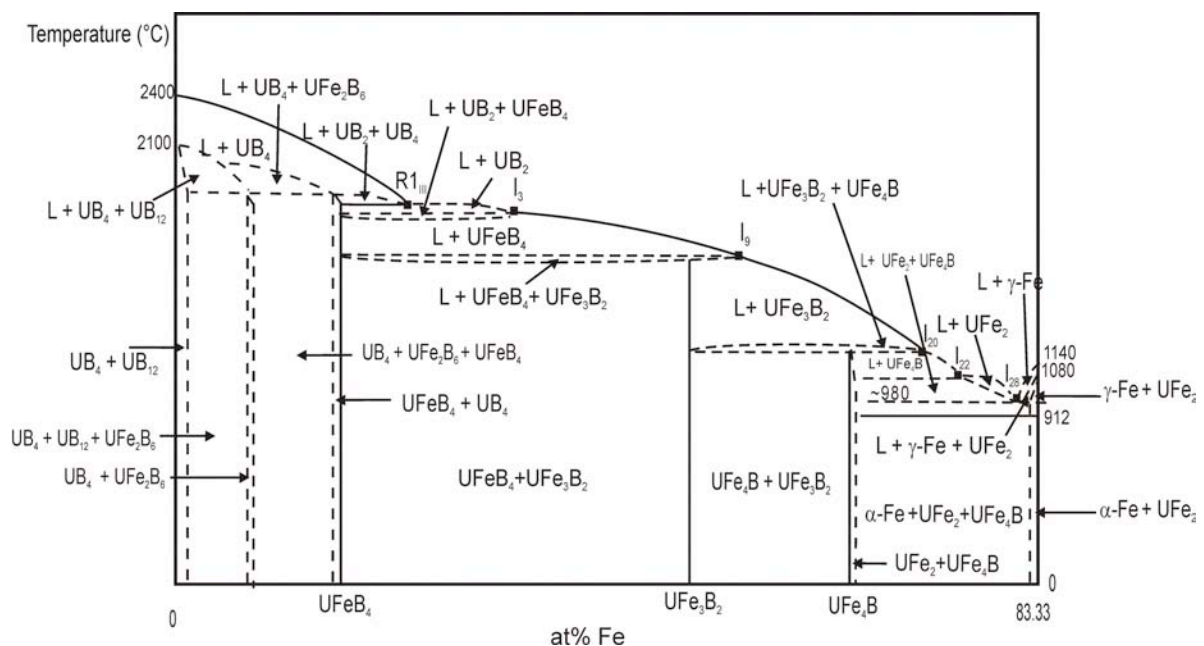


Figure 3.38 – Isopleth at 16.67 at.% U. The squares indicate intersections with boundary lines in the liquidus projection.

### **3.4 References**

- [1] ASM International, Binary Alloy Phase Diagrams B-Fe, 2nd edition Plus Updates.
- [2] ASM International, Binary Alloy Phase Diagrams B-U, 2nd edition Plus Updates.
- [3] ASM International, Binary Alloy Phase Diagrams Fe-U, 2nd edition Plus Updates.
- [4] H. Okamoto, Binary alloy phase diagrams updating service. In: Okamoto H, editor. Ohio, Metals Park: ASM International, (1991).
- [5] Y. Bkurstöm, Ark Kemi Mineral Geology, 11A (1933) 1.
- [6] Y. Khan, E. Kneller, M. Sostarich, Zeitschrift für Metalkunde, 73 (1982) 624.
- [7] Q. Zhi-Cheng, W. Wen-Kui, H. Shou-An., Acta Physica Sinica, 36 (1987) 769.
- [8] F. H. Sanchez, J. I. Bdnick, Y. D. Zhang, W. A. Hines, M. Choi, R. Hasegawa. Physics Review B, 34 (1986) 4738.
- [9] L. G. Voroshin, L. S. Lyakhovich, G. G. Panich, G. F. Protasevich, Metal Science and Heat Treatment, 9 (1970) 732.
- [10] B. W. Howlett, Journal of the Institute Metals, 88 (1959-1960) 91.
- [11] R. W. Mar, Journal of American Ceramic Society, 58 (1975) 145.
- [12] L. Toth, H. Nowotny, F. Benesovsky, E. Rudy, Monatshefte für Chemie, 92 (1961) 794.
- [13] F. Bertaut, P. Blum, Comptes Rendus de l'Académie des sciences, 229 (1949) 666.
- [14] L. R. Chapman, C. F. Jr. Holcombe, Journal of Nuclear Materials, 126 (1984) 323.
- [15] K. Yoshihara, M. Kanno, Journal of Inorganic Nuclear Chemistry, 36 (1974) 309.
- [16] M. Kanno, Journal of Nuclear Materials, 51 (1974) 24.
- [17] V. A. Lebedev, N. V. Kazarov, V. I. Pyarkov, I. F. Nichkov, S. P. Raspopin., Izvestiya Akademii Nauk SSSR Metal, 2 (1973) 212.
- [18] I. P. Valyovka, YuB. Kuzma, Dopovidi Akademii Nauk Ukrainhoi, RSR Ser A, (1975) 652.
- [19] I. P. Valyovka, YuB. Kuzma, Dopovidi Akademii Nauk Ukrainhoi RSR Ser A (1974) 1029.

[20] W. Kurz, D.J. Fisher, “Fundamentals of solidification”, 3rd edition, Trans Tech Publications, USA, (1992) Appendix 3.

[21] F. N. Rhines, “Phase Diagrams in Metallurgy Their Development and Application”, McGraw-Hill, USA, (1956) 159.

[22] A. Prince, “Alloy phase equilibria”, Elsevier Pub.Co., Amsterdam, New York, (1966).

[23] R. Angers, A. Couture, Metallurgical Transactions A, 17A (1986) 37.

---

## **Chapter 4**

---



### **Chapter 4 – Ternary compounds characterization**

This chapter presents the structural and magnetic characterization of the ternary compounds present in the B-Fe-U system, i.e.,  $\text{UFeB}_4$ ,  $\text{UFe}_2\text{B}_6$ ,  $\text{UFe}_3\text{B}_2$ ,  $\text{UFe}_4\text{B}$  and  $\text{U}_2\text{Fe}_{21}\text{B}_6$ . As demonstrated in Chapter 3, all ternary compounds melt incongruently and are formed by peritectic-like transitions. This implies that, in practice, due to encapsulation other phases are typically present in alloys with the compounds composition.

The boron-rich alloys were sufficiently brittle, and the grain sizes were sufficiently large, to allow extraction of macroscopic  $\text{UFeB}_4$ ,  $\text{UFe}_2\text{B}_6$  and  $\text{UFe}_3\text{B}_2$  single crystals through cleavage and intergranular fracture. Structural information on the  $\text{UFe}_2\text{B}_6$  and  $\text{UFe}_3\text{B}_2$  compounds could then be retrieved from single crystal diffraction, which however was not successful for the  $\text{UFeB}_4$  compound due to the consistently poor quality of the extracted crystals. Careful selection of the alloys composition, solidification method and annealing treatment allowed also producing the  $\text{UFeB}_4$ ,  $\text{UFe}_2\text{B}_6$ ,  $\text{UFe}_3\text{B}_2$  compounds as (nearly) single-phase polycrystalline materials suitable for magnetic measurements.

In contrast, the toughness of the iron-rich alloys hindered the extraction of  $\text{UFe}_4\text{B}$  and  $\text{U}_2\text{Fe}_{21}\text{B}_6$  single crystals, impeding the structural refinement of these compounds from single-crystal diffraction data. In addition, owing to the reduced primary solidification fields of the  $\text{UFe}_4\text{B}$  and  $\text{U}_2\text{Fe}_{21}\text{B}_6$  compounds and, especially, due to the remote localization of these primary fields in relation to the compounds composition (see Figure 3.24), the alloys with a significant presence of  $\text{UFe}_4\text{B}$  and  $\text{U}_2\text{Fe}_{21}\text{B}_6$  exhibited a high volume fraction of other phases. Long annealing treatments have not been successful in eliminating these spurious phases due to the relatively high melting point of the borides, the low U diffusivity and the existence of low melting temperature phases/eutectic mixtures, which prevented heat treatments at high temperatures. As a result, structural characterization by Rietveld refinement using PXRD data, as well as magnetic measurements, could not be carried out for these multiphasic materials. Nevertheless, the crystalline structures of the  $\text{UFe}_4\text{B}$  and  $\text{U}_2\text{Fe}_{21}\text{B}_6$  compounds could be investigated by local electron diffraction using SEM coupled with EBSD. This method

was also employed to study the high-boron content  $\text{UFeB}_4$  compound to determine the cause of its poor crystalline quality. It is worth mentioning that the U radioactivity limited the use of transmission electron microscopy due to contamination issues during sample preparation.

#### 4.1 $\text{UFeB}_4$

Compounds with the  $\text{RTB}_4$  and  $\text{ATB}_4$  stoichiometry (R = rare earth, A = actinide and T = transition metal) generally crystallize with the orthorhombic  $\text{YCrB}_4$ -type structure [1], although compounds with the  $\text{ThTB}_4$  stoichiometry (T = V, Mo) have been found to crystallize with the orthorhombic  $\text{ThMoB}_4$ -type structure [1]. Ternary  $\text{RTB}_4$  (R = rare earth, T = Ru, Os) and  $\text{GdTB}_4$  (T = Cr, Mn, Fe, Co) compounds exhibit a paramagnetic behavior in the 80-300 K range [2]. A similar compound,  $\text{TmAlB}_4$ , where Al replaces T and which consists of a random intergrowth of  $\text{YCrB}_4$  and  $\text{ThMoB}_4$ -type layers [3], presents an antiferromagnetic transition at 9.5 K.

Uranium borides with the  $\text{UTB}_4$  stoichiometry (T = Cr, Mn, Co) have been shown to crystallize with the orthorhombic  $\text{YCrB}_4$ -type structure [4,5] and to exhibit paramagnetic behavior in the 80-300K range [2]. Results on the  $\text{UFeB}_4$  compound indicate that this compound crystallizes also with the  $\text{YCrB}_4$ -type structure ( $a = 0.5877(3)$  nm,  $b = 1.1389(6)$  nm and  $c = 0.3438(2)$  nm [2]) and presents a paramagnetic behavior in the 80-300 K range [2].

The following section reports specific characteristics of the  $\text{UFeB}_4$  ternary compound based on powder X-ray diffraction (PXRD), scanning electron microscopy (SEM), complemented with electron-backscattered diffraction (EBSD) and energy dispersive spectroscopy (EDS), as well as magnetic measurements.

### 4.1.1 Results and discussion

#### XRD

Single-crystal extraction was accomplished, however structural information could not be retrieved due to the low crystalline quality of compound. As a result, the materials were only characterized in the polycrystalline form. As-cast alloys have not been thoroughly investigated by PXRD due to the massive presence of other phases. The 66B:17Fe:17U (UFeB<sub>4</sub> stoichiometry) alloy annealed at 1100°C for 60 days has been selected for that purpose due to the low volume fraction of impurity phases. Figure 4.1 presents the corresponding diffractogram, which demonstrates that UFeB<sub>4</sub> is the predominant phase with minor peaks corresponding to the UB<sub>4</sub> compound. Assuming an orthorhombic YCrB<sub>4</sub>-type structure [2] the following lattice parameters:  $a = 0.5877(3)$  nm,  $b = 1.1389(6)$  nm and  $c = 0.3438(2)$  nm, have been determined from the PXRD data for the UFeB<sub>4</sub> compound. Assuming the other possible orthorhombic structure, ThMoB<sub>4</sub>-type, the lattice parameters would be:  $a = 0.7198(6)$  nm,  $b = 0.93280(8)$  nm and  $c = 0.3424(3)$  nm. The absence of diffracted intensity at  $2\theta = 24.8$ ,  $32.3$  and  $36.1^\circ$  points to an YCrB<sub>4</sub>-type rather than a ThMoB<sub>4</sub>-type structure. Nevertheless, the experimental intensity of the peaks in the  $21$ - $33^\circ$  range differs significantly from the expected for an YCrB<sub>4</sub>-type structure, while the intensity relation of the higher peaks in this range is similar to the one expected for the ThMoB<sub>4</sub>-type structure. This effect should not have resulted from preferential crystallographic orientation, since the materials are brittle and could be easily reduced to fine powder. Furthermore, similar intensity variations were generally observed for the UFeB<sub>4</sub> peaks in all the alloys investigated. Therefore, the intensity inversions observed experimentally have most probably structural causes.

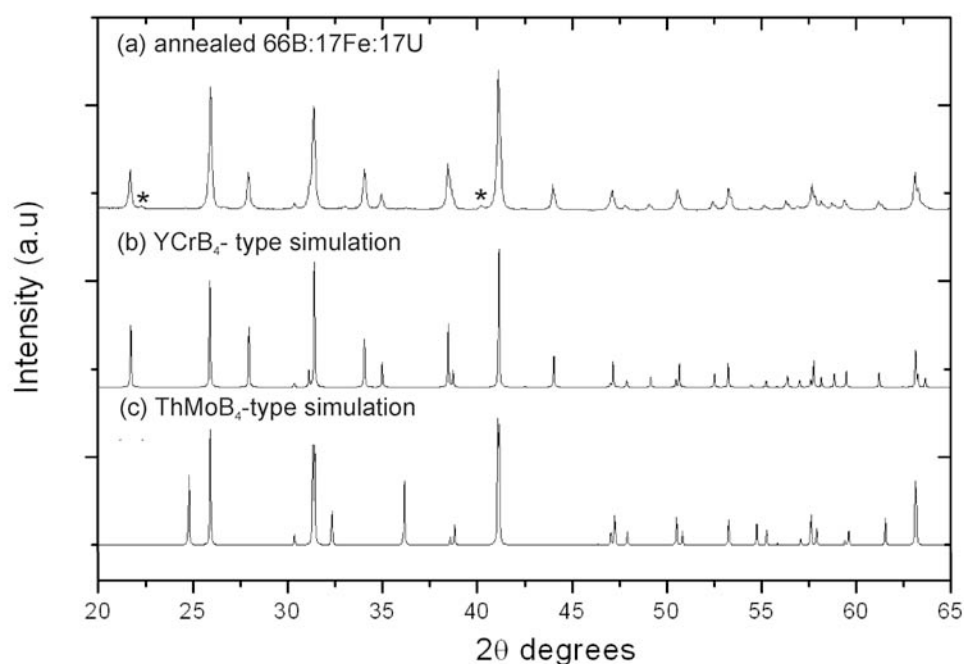


Figure 4.1 – (a) Experimental powder X-ray diffraction pattern of the annealed an 66B:17Fe:17U ( $\text{UFeB}_4$  stoichiometry) alloy, (b) simulation for the  $\text{YCrB}_4$ -type structure and (c) simulation for the  $\text{ThMoB}_4$ -type structure (the stars indicate reflections indexed to  $\text{UB}_4$ ).

### SEM/EDS and EBSD

In as cast alloys the  $\text{UFeB}_4$  compound exhibited frequently a BSE contrast characteristic of a random intergrowth imaged edge-on (see Figure 4.2). A previous high-resolution transmission electron microscopy study on  $\text{TmAlB}_4$  evidenced an intergrowth between the two orthorhombic  $\text{YCrB}_4$  and  $\text{ThMoB}_4$ -type structures, with a  $(010)_{\text{YCrB}_4} // (\bar{1}10)_{\text{ThMoB}_4}$  and  $[001]_{\text{YCrB}_4} // [001]_{\text{ThMoB}_4}$  orientation relation [3]. In the present study, the radioactivity of U limited the use of transmission electron microscopy due to contamination issues during sample preparation; nevertheless, the  $\text{UFeB}_4$  structure could be investigated by EBSD.

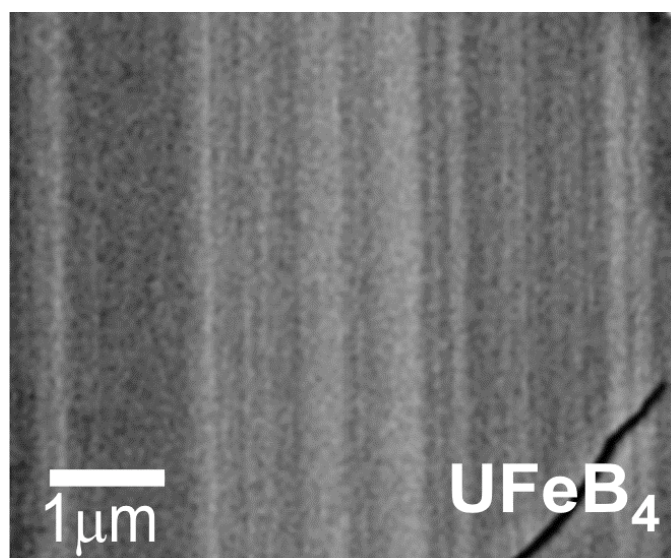


Figure 4.2 – BSE image showing light and dark layers in the  $\text{UFeB}_4$  phase (as-cast 50B:25Fe:25U alloy) characteristic of a random intergrowth when observed edge-on.

EBS D patterns obtained in regions displaying the intergrowth contrast showed that the crystallographic plane parallel to the layers presented intense HOLZ rings around low-index zone axes (see Figure 4.3). The mechanism that leads to diffraction rings can be interpreted as a transmission resonance along the respective zone axis [6, 7]. The experimental EBS D patterns could be indexed to either an  $\text{YCrB}_4$  or a  $\text{ThMoB}_4$ -type structure (see Figure 4.4). However, in both cases some of the simulated bands are absent from the experimental patterns, while a few experimental bands emanating from the intense HOLZ rings are not present in the simulations. This may have been induced by the symmetry breakdown resulting from a fine mixture of the  $\text{YCrB}_4$  and  $\text{ThMoB}_4$  structure types. The crystallographic plane associated with the strong HOLZ rings corresponds to  $(010)_{\text{YCrB}_4}$  and  $(1\bar{1}0)_{\text{ThMoB}_4}$  with  $[001]_{\text{YCrB}_4} // [001]_{\text{ThMoB}_4}$ . The results indicate therefore that the  $\text{UFeB}_4$  compound tends to adopt a random intergrowth structure analogous to the one previously reported for  $\text{TmAlB}_4$  and suggest that the formation of intense HOLZ rings around the principal directions of a specific crystallographic plane is a sign of a random distribution of planar defects. The intergrowth contrast has not been so clearly detected in the annealed  $\text{UFeB}_4$  compound, which probably is an indication of a higher predominance of the  $\text{YCrB}_4$ -type phase. Nevertheless, the intensity inversions observed in the PXR D data (see Figure 4.1), and

the fact that intense rings centered on the low-index zone axes of the  $(010)_{\text{YCrB}_4} // (110)_{\text{ThMoB}_4}$  plane could also be detected in annealed alloys, suggest the presence of a residual intergrowth in the annealed  $\text{UFeB}_4$  compound.

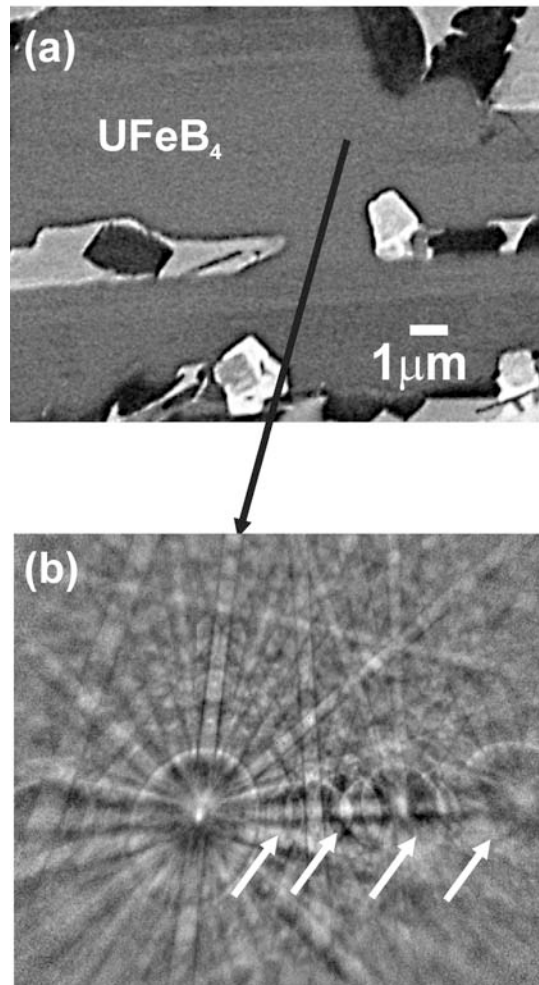


Figure 4.3 – (a) BSE image showing light and dark layers in the  $\text{UFeB}_4$  phase (as-cast 50B:25Fe:25U alloy), (b) Experimental EBSD pattern of the  $\text{UFeB}_4$  phase. The arrows indicate diffraction rings centered on low-index zone axes of a crystallographic plane parallel to the planar defects.

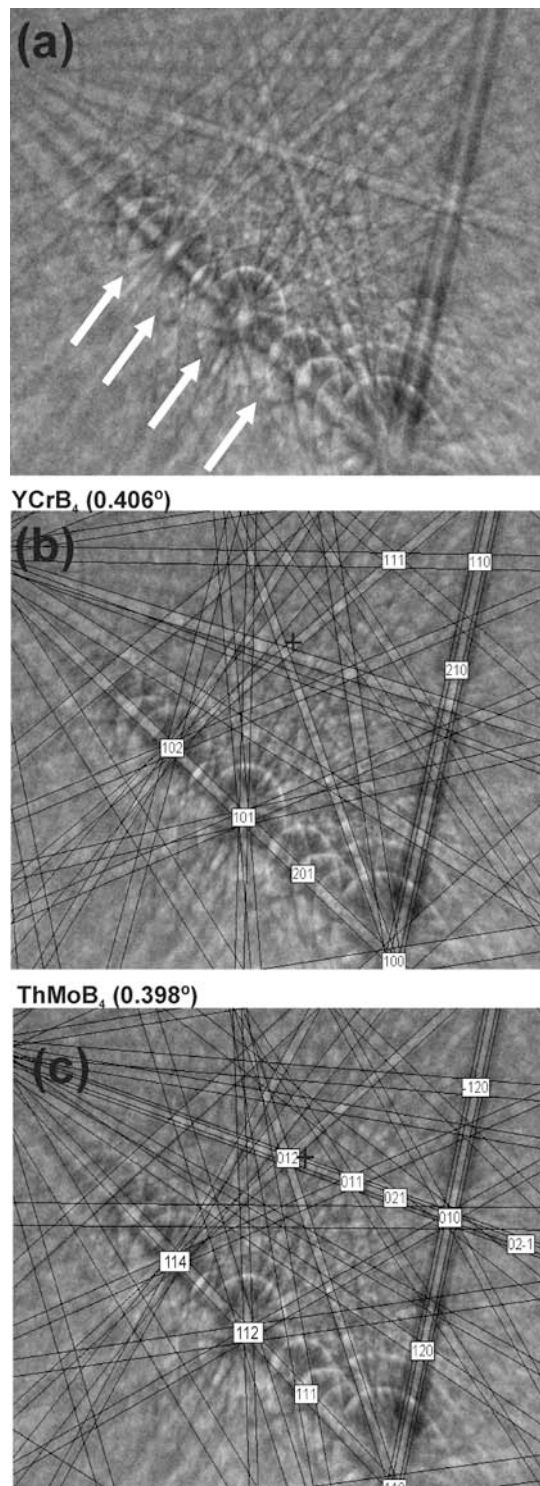


Figure 4.4 – (a) Experimental EBSD pattern of the  $UFeB_4$  compound and simulations with 40 indexed planes for (b)  $YCrB_4$ -type and (c)  $ThMoB_4$ -type structures (MAD = 0.406 and 0.398°, respectively). The arrows indicate concentric diffraction rings associated with the crystallographic plane corresponding to the planar defects.

### **Magnetic properties**

The dependence of the inverse susceptibility on the temperature,  $1/\chi$  (T), for a powdered polycrystalline 66U:17Fe:17B (UFeB<sub>4</sub> stoichiometry) alloy annealed at 1100°C for 60 days is shown in Figure 4.5. No magnetic transitions were observed between 2 and 300 K. The tail detected at low temperatures (see arrow) is most probably due to minute amounts of ferromagnetic impurities. Hence, contrarily to TmAlB<sub>4</sub>, no anti-ferromagnetic transition has been observed at low temperatures for UFeB<sub>4</sub>, which invalidates the hypothesis that the intergrowth between the YCrB<sub>4</sub> and ThMoB<sub>4</sub>-type structures originates low temperature anomalies in the physical properties of this class of compounds [3].

The dependence of magnetization on the applied field,  $M(B)$ , up to 6 T and at 2 K is shown in Figure 4.6. The curve shows essentially the linear behavior characteristic of paramagnetic materials, with the steep magnetization increase at low fields resulting probably from ferromagnetic impurities. These results complement at low temperatures the previous measurements reported for UFeB<sub>4</sub> [2] and are in agreement with the behavior observed for other UTB<sub>4</sub> compounds (T = Cr, Mn and Co) between 80-300K [2]. As demonstrated by the PXRD data (see Figure 1) and SEM observations, the alloy used for the magnetic properties investigation presented a minor fraction of UB<sub>4</sub> that would have affected the magnetic behavior of the material. However, research on UB<sub>4</sub> revealed a paramagnetic behavior between 2 and 800 K [8], discarding any possible influence on the measurements carried out for the predominantly UFeB<sub>4</sub> material.

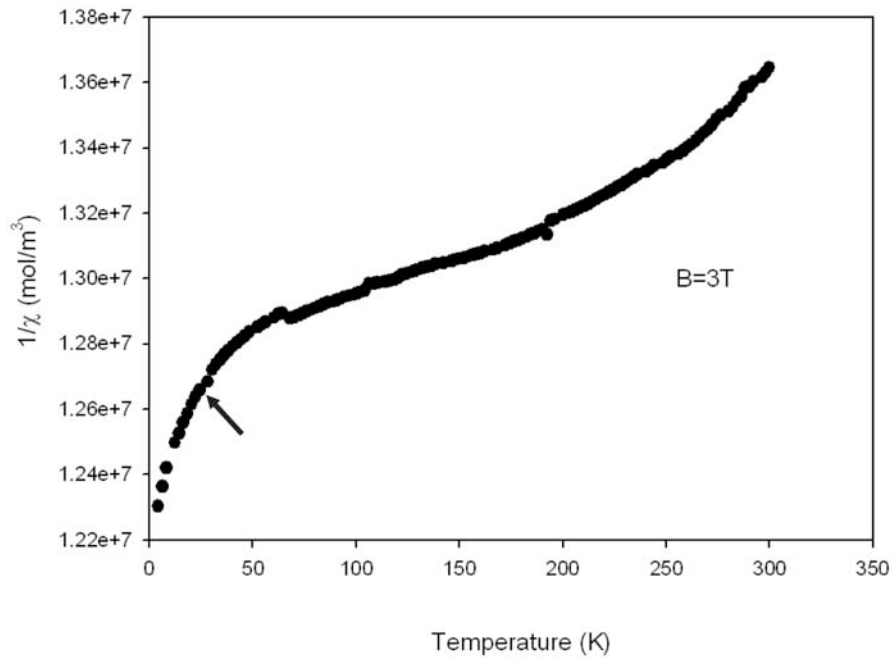


Figure 4.5 – Temperature dependence of the inverse susceptibility for the annealed 66U:17Fe:17B alloy (UFeB<sub>4</sub> stoichiometry) at 3T. The upturn at 30K results most likely from ferromagnetic impurities.

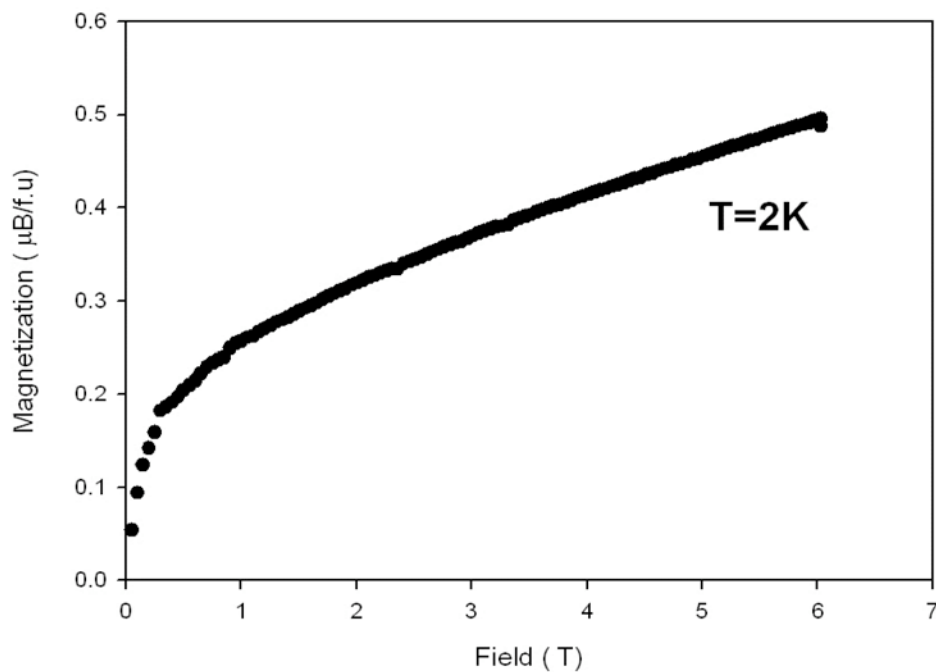


Figure 4.6 – Magnetic field dependence of the magnetization for the annealed 66U:17Fe:17B alloy (UFeB<sub>4</sub> stoichiometry) at 2K.

## 4.2 UFe<sub>2</sub>B<sub>6</sub>

Literature reports on R<sub>x</sub>T<sub>y</sub>B<sub>z</sub> compounds with 1:2:6 stoichiometry are limited to RCr<sub>2</sub>B<sub>6</sub> (R = Pr, Nd, Sm) [9, 10], RCu<sub>2</sub>B<sub>6</sub> (R = Sm, Nd) [1] and ThCr<sub>2</sub>B<sub>6</sub> [11], which crystallize with the orthorhombic CeCr<sub>2</sub>B<sub>6</sub>-type structure. Magnetic measurements on CeCr<sub>2</sub>B<sub>6</sub> and ThCr<sub>2</sub>B<sub>6</sub> compounds evidenced a paramagnetic behavior in the 2-300K temperature range [11].

The following section presents PXRD results obtained from polycrystalline material, together with structure refinement and magnetic characterization of UFe<sub>2</sub>B<sub>6</sub> single crystals.

### 4.2.1 Results and discussion

#### XRD

PXRD showed that the UFe<sub>2</sub>B<sub>6</sub> compound is the predominant phase in the 67B:22Fe:11U (UFe<sub>2</sub>B<sub>6</sub> stoichiometry) alloy annealed at 1700°C for 5h. However, the UB<sub>4</sub> compound is also present with a 15%, volume fraction as determined with the powder cell software package [12] from the intensity relations.

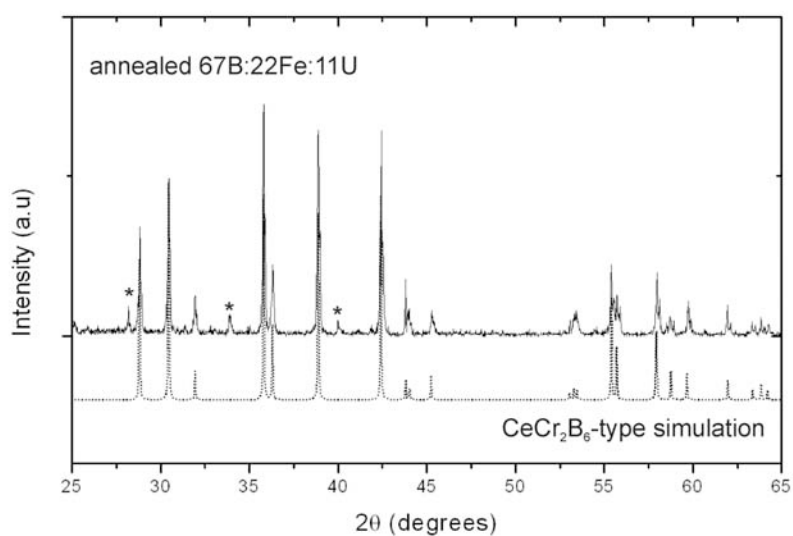


Figure 4.7 – Experimental PXRD of the annealed 67B:22Fe:11U (UFe<sub>2</sub>B<sub>6</sub> stoichiometry) alloy, and simulation for the CeCr<sub>2</sub>B<sub>6</sub>-type structure (stars – UB<sub>4</sub>).

Single crystals have been extracted from the 67B:22Fe:11U (UFe<sub>2</sub>B<sub>6</sub> stoichiometry) alloy annealed at 1700°C for 5h. Single crystal X-ray diffraction data indicates that the UFe<sub>2</sub>B<sub>6</sub> compound crystallizes with the CeCr<sub>2</sub>B<sub>6</sub>-type structure that belongs to the *Immm* space group (Nr.71). Details on the single crystal data collection and structural refinement are listed in Table 4.1. The anisotropic displacement parameters ( $U_{xx}$ ) for all atoms are also given in Table 4.2. Selected interatomic distances and coordination numbers for the different atoms are presented in Table 4.3.

Space group	<i>I</i> /mmm (Nr.71)
Lattice parameters (nm)	
a	0.31372(6)
b	0.61813(11)
c	0.82250(17)
Cell volume (nm <sup>3</sup> )	0.15950(5)
Formula per unit cell	2
Calculated density (Mg/m <sup>3</sup> )	4.316
Temperature (K)	150 (2)
Absorption coefficient (mm <sup>-1</sup> )	29.668
Data collection	CCD Mo K $\alpha$ , 0.71073
Theta range for data collection (°)	4.12-35.98
Data set	-5 ≤ h ≤ 5, -10 ≤ k ≤ 10, -13 ≤ l ≤ 13
Number of measured reflections	1325
Number of unique reflections	246
Number of reflections with I > 2 $\sigma$ (I <sub>0</sub> )	246
Number of refined parameters	18
R <sub>1</sub> , wR <sub>1</sub> (I > 2 $\sigma$ (I <sub>0</sub> ))	0.0106 0.0252
R <sub>2</sub> , wR <sub>2</sub> all data	0.0106 0.0252
Goodness of fit on F <sup>2</sup>	1.124
Highest/lower peaks of electron density (e/Å <sup>3</sup> )	2.377 – 1.990
Refinement method, software	Full matrix least squares on F <sup>2</sup>

Table 4.1 – Crystal data and structure refinement for UFe<sub>2</sub>B<sub>6</sub> single crystal.

Atom	Wyckoff position	x	y	z	U <sub>11</sub>	U <sub>22</sub>	U <sub>33</sub>	U <sub>23</sub>	U <sub>13</sub>	U <sub>12</sub>
U1	2 <i>d</i>	0	1/2	0	0.0252(8)	0.0165(8)	0.0076(8)	0.000	0.000	0.000
Fe1	4 <i>i</i>	1/2	1/2	0.65308	0.0344(18)	0.0206(19)	0.0075(18)	0.000	0.000	0.000
B1	4 <i>h</i>	0	0.3544(6)	1/2	0.049(12)	0.031(14)	0.013(12)	0.000	0.000	0.000
B2	8 <i>l</i>	0	0.2604(5)	0.3044(3)	0.042(9)	0.034(10)	0.030(9)	-0.004(8)	0.000	0.000

Table 4.2 – Atomic positions and thermal parameters (nm<sup>2</sup>) for the UFe<sub>2</sub>B<sub>6</sub> compound obtained from single X-ray crystal diffraction.

Atom	Neighbor	Distance	Atom	Neighbor	Distance
U1 :	4B1	0.2695(3)	B1:	2B2	0.1711(3)
	8B2	0.2764(2)		1B1	0.1799(8)
	4B2	0.2909(1)		4Fe1	0.2203(2)
	4Fe1	0.3257(1)	2U1	0.2695(3)	
	4Fe1	0.3337(3)	B2:	2B2	0.1810(3)
	2U1	0.3137(2)		1Fe1	0.2034(3)
Fe1:	2B2	0.2034(3)	2Fe1	0.2186(2)	
	4B2	0.2186(2)	1B1	0.1711(3)	
	4B1	0.2203(2)	2U1	0.2764(2)	
	2Fe1	0.2518(1)	1U1	0.2909(1)	
	1Fe1	0.3815(1)			
	2U1	0.3256(7)			
	2U1	0.3337(3)			

Table 4.3 – Selected interatomic distances (d, nm) for atoms in the UFe<sub>2</sub>B<sub>6</sub> compound.

In the UFe<sub>2</sub>B<sub>6</sub> structure the boron atoms form a three-dimensional infinite network in which rings with fourteen-, eight-, and ten- atoms are discernible along the directions [100], [010] and [001], respectively (Figure 4.8). Along the [010] direction (Figure 4.8 (b)) two types of layers, **A** and **A'**, in which **A'** is  $\frac{1}{2}$  **a** shifted in relation to **A**, can be found.

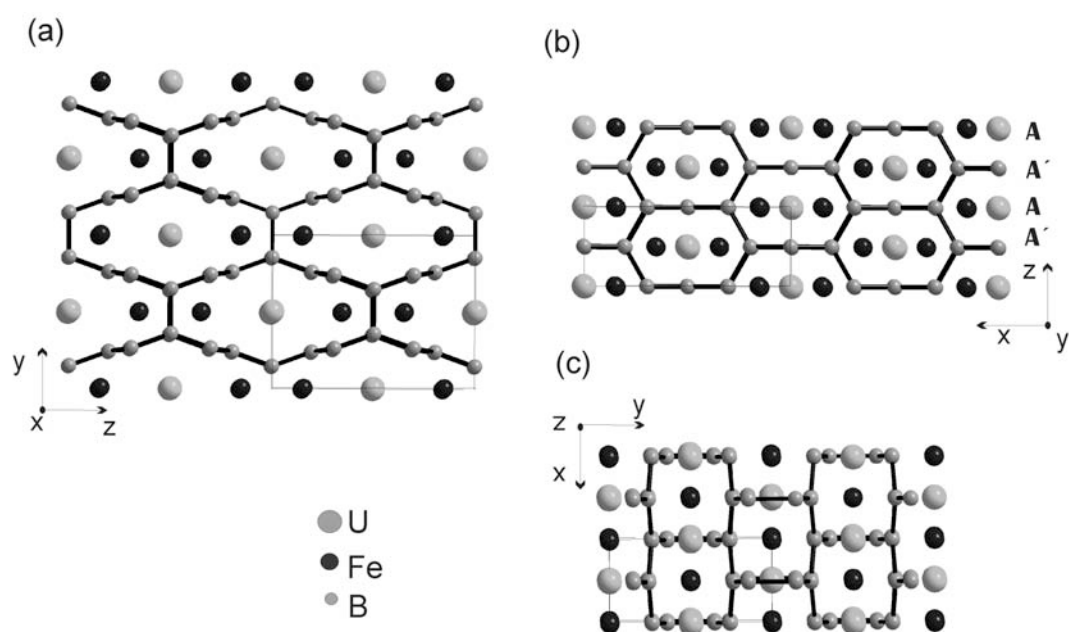


Figure 4.8 – Projections of the  $\text{UFe}_2\text{B}_6$  on along (a) [100], (b) [010] and (c) [001].

The coordination polyhedra for  $\text{UFe}_2\text{B}_6$  are shown in Figure 4.9. The uranium atoms (Figure 4.9 (a)) occupy the  $2d$  positions and have a coordination polyhedron composed by 16 boron, 8 iron and 2 uranium atoms. The iron atoms occupy the  $4i$  positions and have as nearest neighbors 4 uranium, 10 boron and 3 other iron atoms (Figure 4.9 (b)). The  $4h$  (B1) and  $8l$  (B2) boron positions are represented in Figure 4.9 (c) and (d) respectively, both with a coordination number of 9 and different atomic environments. In B1, the coordination polyhedron is composed by 3 boron, 2 uranium and 4 iron atoms. The environment of B2 consists of the same number of boron atoms, but with an iron atom less and an uranium atom more. All boron atoms have therefore three boron neighbors with B-B distances in the 0.171-0.181 nm range. The uranium atoms have sixteen boron neighbors and an average U-B interatomic distance of 0.278 nm, which is significantly higher than the sum of the U and B radii (0.244 nm, for a coordination number of 12 [13]) however this can be explained by the higher coordination number of U in  $\text{UFe}_2\text{B}_6$  (20). Iron atoms have 10 boron neighbors with Fe-B distances in the 0.203-0.220 nm range. It is worth noticing that the Fe-B2 distance (0.203 nm) is remarkably shorter than the sum of the two radii (0.217 nm [13]), pointing to electronic

interactions between these two atoms. The short Fe-Fe distance of 0.252 nm is also noteworthy, as it suggests metallic bond character. The U-U distance (0.314 nm), is above the sum of the metallic radii (0.304 nm [13]) contrarily to the Th-Th and Ce-Ce distances in, respectively, the  $\text{ThCr}_2\text{B}_6$  and  $\text{CeCr}_2\text{B}_6$  isostructural borides, which are both well below the sum of the respective metallic radii in agreement with a metallic bond character [11,13]. The U-U distance in  $\text{UFe}_2\text{B}_6$  is nonetheless below the Hill limit for uranium (0.340 nm [14]), which denotes a significant delocalization via direct  $5f$ - $5f$  orbital overlapping (itinerant state) and points to non-magnetic ordering of the U sublattice in  $\text{UFe}_2\text{B}_6$ .

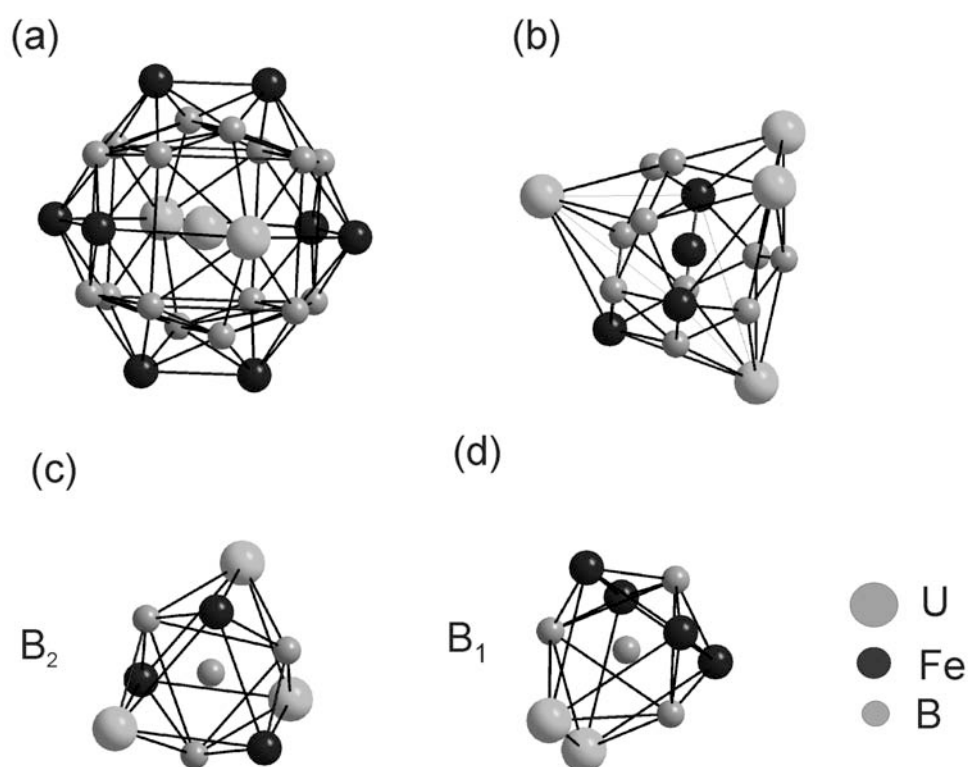


Figure 4.9 – Coordination polyhedra for (a) U atom, (b) Fe atom and (c)  $\text{B}_2$  atom and (d)  $\text{B}_1$  atom.

### Magnetic properties

The magnetic measurements have been carried out on the powdered polycrystalline annealed 67B:22Fe:11U ( $\text{UFe}_2\text{B}_6$  stoichiometry) alloy (see Figure 4.7). The  $\chi(T)$  curve shown in Figure 4.10 evidences a susceptibility signal inversely proportional to the temperature characteristic of a paramagnetic behavior. Albeit a contribution from the  $\text{UB}_4$  impurity phase is expected, its paramagnetic character [8] indicates that the  $\text{UFe}_2\text{B}_6$  compound is also paramagnetic.

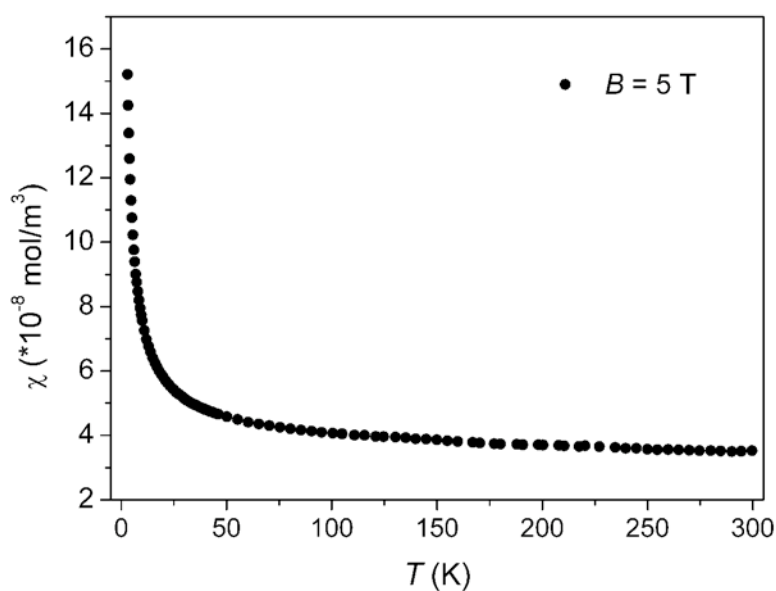


Figure 4.10 – Temperature dependence of the magnetic susceptibility of  $\text{UFe}_2\text{B}_6$  at compound at 5 Tesla.

### 4.3 UFe<sub>3</sub>B<sub>2</sub>

The crystal structures and physical properties of a series of RT<sub>3</sub>B<sub>2</sub> compounds (R = rare earth and T = transition metal) have been previously reported [15, 16]. The hexagonal CeCo<sub>3</sub>B<sub>2</sub>-type structure has been observed for LaIr<sub>3</sub>B<sub>2</sub>, LuOs<sub>3</sub>B<sub>2</sub>, RRh<sub>3</sub>B<sub>2</sub> (R = La-Gd) and for RRu<sub>3</sub>B<sub>2</sub> (R = La, Ce, Pr, Nd, Sm, Gd, Tb, Dy, Ho, Er, Tm, Yb, Lu, Y) compounds [15,16]. However, RIr<sub>3</sub>B<sub>2</sub> compounds (R = Ce, Nd, Sm, Gd, Tb, Dy, Ho, Er, Tm, Yb, Lu, Sc, Y), RRh<sub>3</sub>B<sub>2</sub> (R = Tb - Lu), and R<sub>1-x</sub>Rh<sub>3</sub>B<sub>2</sub> (x = 0.5; R = La, Ce, Pr, Nd) crystallize with other structure types, such as ErIr<sub>3</sub>B<sub>2</sub> [16], ErRh<sub>3</sub>B<sub>2</sub> [17] and La<sub>1-x</sub>Rh<sub>3</sub>B<sub>2</sub> [18], respectively. In these cases, the first two structure types belong to the monoclinic system and the latter is a distorted variant of the hexagonal CeCo<sub>3</sub>B<sub>2</sub>-type structure, yet all the structures adopted by RT<sub>3</sub>B<sub>2</sub> compounds show similar X-ray diffractograms. Reports on ThT<sub>3</sub>B<sub>2</sub> (T = Ru, Ir) and UT<sub>3</sub>B<sub>2</sub> (T = Os, Co) borides have shown that these CeCo<sub>3</sub>B<sub>2</sub>-type compounds exhibit a paramagnetic behavior in the 2-300 K temperature range [16].

PXRD studies on UFe<sub>3</sub>B<sub>2</sub> point to crystallization with the hexagonal CeCo<sub>3</sub>B<sub>2</sub>-type structure [5, 19], nevertheless no single crystal diffraction has been performed and the possibility of crystallization with other structure types has not been discarded. Furthermore, to the author's best knowledge the magnetic properties of this specific compound have not yet been determined, although a <sup>57</sup>Fe Mössbauer study reported non-order of the Fe magnetic moments at room temperature, suggesting therefore a paramagnetic behavior [20]. However, RFe<sub>4</sub>B (R = 4*f*-element) compounds, with higher iron concentration, have been described to be magnetically ordered at room temperature [21]. Moreover, uranium-iron compounds with lower iron content, such as UFe<sub>2</sub>, have also a magnetically ordered iron sublattice, albeit with some 5*f*-3*d* hybridization and a consequent low magnetic moment [22]. These issues raise questions on the actual magnetic nature of UFe<sub>3</sub>B<sub>2</sub>.

The following section presents a detailed crystallographic and magnetic investigation of the UFe<sub>3</sub>B<sub>2</sub> compound based on X-ray diffraction (powder and single-crystal) and

magnetic measurements, with the objective of refining the crystal structure and clarifying the magnetic behavior.

### 4.3.1 Results and discussion

#### **XRD**

PXRD data obtained from the 33B:50Fe:17U ( $\text{UFe}_3\text{B}_2$  stoichiometry) alloy annealed at 950°C for 60 days is shown in Figure 4.11 (a). A predominance of the  $\text{UFe}_3\text{B}_2$  phase, with a  $\text{CeCo}_3\text{B}_2$ -type or closely related structure, is observed. Nevertheless, minor amounts of  $\text{UFeB}_4$  and  $\text{UFe}_4\text{B}$  could be detected. The diffractogram obtained from a material pulled by the Czochralski method from the 23B:62Fe:15U alloy is presented in Figure 4.11 (b). This material consists essentially of  $\text{UFe}_3\text{B}_2$  with a minute contamination of  $\alpha$ -Fe (<3% wt). The intensity inversions are expected to have resulted from preferred crystallographic orientation since powdering of these high-iron content alloys was difficult.

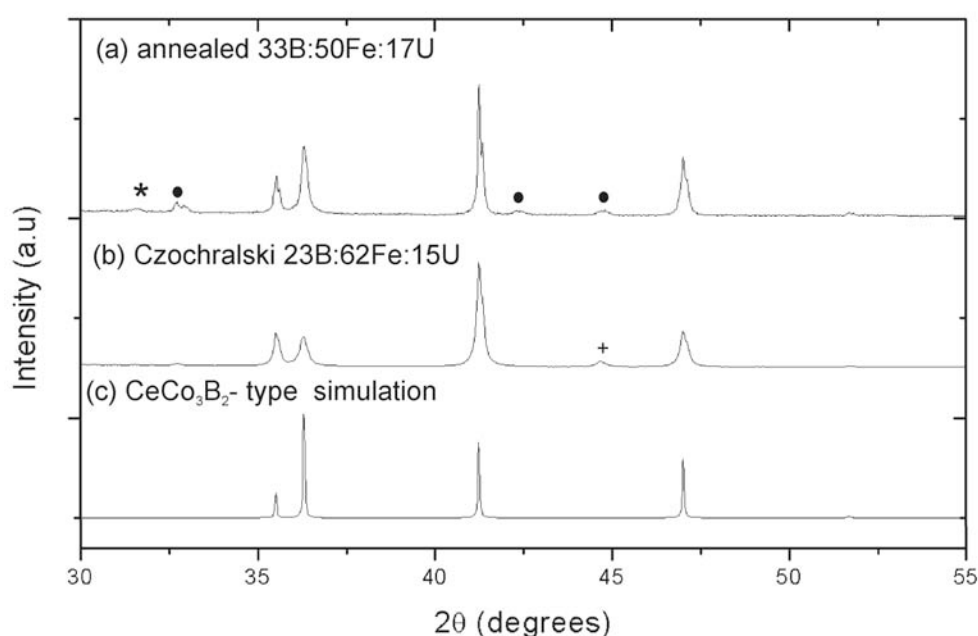


Figure 4.11 – Experimental powder X-ray diffraction patterns of (a) annealed 33B:50Fe:17U ( $\text{UFe}_3\text{B}_2$  stoichiometry) alloy, (b) Czochralski pulled 23B:62Fe:15U alloy, and (c) simulation for  $\text{UFe}_3\text{B}_2$  phase with the  $\text{CeCo}_3\text{B}_2$ -type structure (star –  $\text{UFeB}_4$ , black circles –  $\text{UFe}_4\text{B}$  and cross –  $\alpha$ -Fe).

Single crystal X-ray diffraction experiments performed on a crystal extracted from the annealed 33B:50Fe:17U (UFe<sub>3</sub>B<sub>2</sub> stoichiometry) alloy confirmed that the UFe<sub>3</sub>B<sub>2</sub> compound adopts the CeCo<sub>3</sub>B<sub>2</sub>-type structure belonging to the *P6/mmm* space group (Nr.191). Details on single crystal data collection and structural refinement are listed in Table 4.4. The atomic positions and anisotropic displacement parameters ( $U_{xx}$ ) are given in Table 4.5. Selected interatomic distances and coordination numbers are presented in Table 4.6.

Space group	P6/mmm (Nr.191)
Lattice parameters (nm)	
<i>a</i>	0.5052(1)
<i>c</i>	0.3002(1)
Cell volume (nm <sup>3</sup> )	0.664
Formula per unit cell	1
Calculated density (g/m <sup>3</sup> )	10.709
Absorption coefficient (mm <sup>-1</sup> )	76.663
Data collection	Kappa-CCD, Mo, K $\alpha$
Theta range for data collection (°)	4.66-49.86
Data set	-10≤h≤10, -9≤k≤9, -6≤l≤6
Number of measured reflections	2711
Number of unique reflections	172
Number of reflections with I>2 $\sigma$ (I <sub>0</sub> )	172
Number of refined parameters	9
R <sub>1</sub> , wR <sub>1</sub> (I>2 $\sigma$ (I <sub>0</sub> ))	0.0222 0.0517
Goodness of fit on F <sup>2</sup>	1.146
Highest/lower peaks of electron density (e/ Å <sup>3</sup> )	6.069–3.954
Refinement method, software	Full matrix least squares on F <sup>2</sup> , Shelxl

Table 4.4 – Crystal data and structure refinement for the UFe<sub>3</sub>B<sub>2</sub> single crystals extracted from the annealed 33B:50Fe:17U (UFe<sub>3</sub>B<sub>2</sub> stoichiometry) alloy.

Atom	Wyckoff	x	y	Z	$U_{11}$	$U_{22}$	$U_{33}$	$U_{23}$	$U_{13}$
U1	1a	0	0	0	0.0049(1)	0.0049(1)	0.0076(1)	0.000	0.000
Fe1	3g	1/2	1/2	1/2	0.0067(2)	0.0067(2)	0.0066(2)	0.000	0.000
B1	2c	1/3	2/3	0	0.0083(1)	0.0083(1)	0.0039(2)	0.000	0.000

Table 4.5 – Atomic positions and thermal parameters ( $\text{nm}^2$ ) for the  $\text{UFe}_3\text{B}_2$  compound obtained from single X-ray crystal diffraction.

U:	6B	0.2915
	12Fe	0.2937
	2U	0.3002
Fe:	4B	0.2091
	4Fe	0.2525
	3U	0.2937
B:	5Fe	0.2091
	2U	0.2154

Table 4.6 – Interatomic distances (nm) for atoms in the  $\text{UFe}_3\text{B}_2$  crystal.

Figure 4.12 presents the projections of the  $\text{UFe}_3\text{B}_2$  crystal structure along the  $[100]$  and  $[001]$  directions. Two types of layers, one with only iron atoms and the other with uranium and boron atoms, can be found stacked along the  $[001]$  direction (see Figure 4.12 (a)). A network with six iron rings can be observed perpendicular to  $[001]$  (Figure 4.12 (b)).

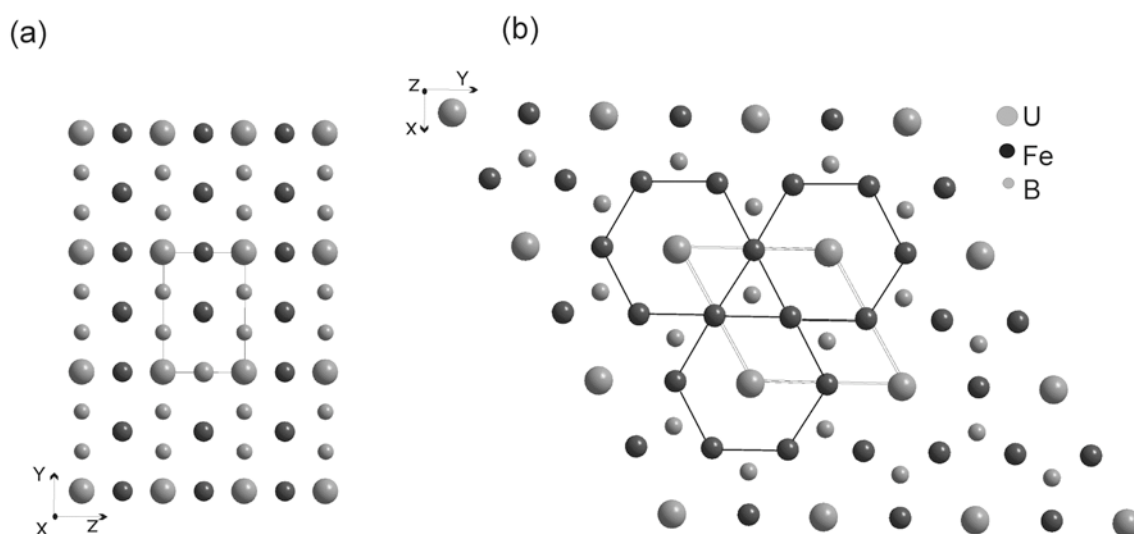


Figure 4.12 – Projections of the  $\text{UFe}_3\text{B}_2$  structure along (a)  $[100]$  and (b)  $[001]$  showing the unit cell.

The  $\text{CeCo}_3\text{B}_2$  structure is an ordered variant of the  $\text{CaCu}_5$  structure, with cerium replacing calcium, and cobalt and boron replacing copper in the  $3g$  and  $2c$  positions, respectively. The coordination polyhedras for uranium, iron and boron atoms in  $\text{UFe}_3\text{B}_2$  are shown in Figure 4.13. Uranium atoms have a coordination number of 20 (Figure 4.13 (a)). The U-U distance (0.300 nm) is only slightly lower than the sum of the metallic radii (0.308 nm, for a coordination number of 12 [13]). This value is below the Hill limit [14], which would predict a delocalization via direct  $5f$ - $5f$  orbital overlapping, leading to a non-magnetic behavior for the uranium atoms. The same situation has been described for  $\text{CeRh}_3\text{B}_2$  [23]. The coordination number of iron is 14 and its coordination sphere is similar to that of cobalt in  $\text{CeCo}_3\text{B}_2$  [24, 25], corresponding to a deformed cubooctahedron with two additional atoms of iron situated against the faces, which are formed by two uranium and boron atoms (Figure 4.13 (b)). The U-Fe distance (0.294 nm) is higher than the sum of the respective metallic radius (0.279 nm, for a coordination number of 12 [13]), however this can be explained by the higher coordination number of iron (14) in  $\text{UFe}_3\text{B}_2$  and probably to a hybridization of the  $5f$ - $3d$  orbitals. It is noteworthy that the Fe-B distance (0.209 nm) is shorter than the sum of the two radii (0.217 nm [13]), pointing to electronic interactions between these two atoms. The Fe-Fe distance of 0.252 nm is identical to what is observed in  $\alpha$ -Fe, suggesting a metallic bonding character. The coordination polyhedron of boron has the shape of a trigonal prism with three additional atoms, resulting in a coordination number of 9 (Figure 4.13 (c)).

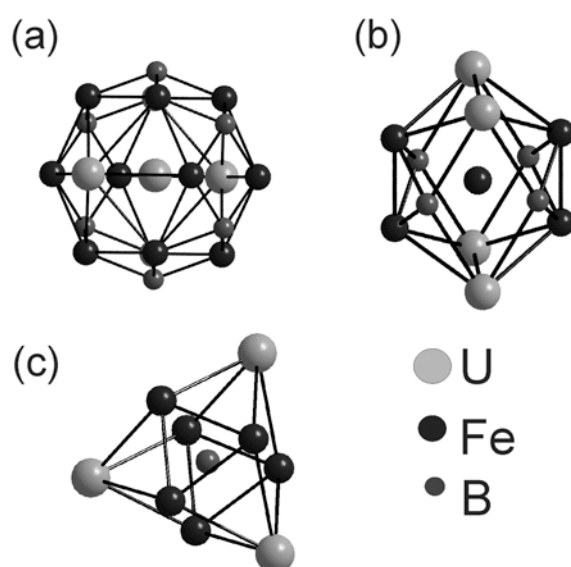


Figure 4.13 – Coordination polyhedra for (a) U atom, (b) Fe atom and (c) B atom.

### Magnetic properties

Since the annealed 33B:50Fe:17U alloy presented  $\text{UFeB}_4$  and  $\text{UFe}_4\text{B}$  as impurity phases (see Figure 4.10 (a)), and the magnetic properties of the latter compound are unknown, the Czochralski pulled 23B:62Fe:15U alloy (see Figure 4.11 (b)) was selected for the magnetic investigations. The temperature dependence of magnetization,  $M(T)$ , measured at 1 T, is shown in Figure 4.14. No magnetic transitions are observed within the studied temperature range. However, a convex curvature can be seen close to room temperature, which is an indication of a ferromagnetic-like transition with a Curie temperature just above 300 K. The inset in Figure 4.14 shows the field cooled (FC) and zero-field cooled (ZFC) magnetization at 0.01 T. The mild magnetization increase in the ZFC curve at low temperatures indicates domain wall pinning and therefore magnetic irreversibility. This behavior has been observed for other compounds with structures deriving also from the  $\text{CaCu}_5$ -type, as  $\text{UFe}_{5.8}\text{Al}_{6.2}$  [26] and  $\text{SmCo}_{5.85}\text{Si}_{0.90}$  [27].

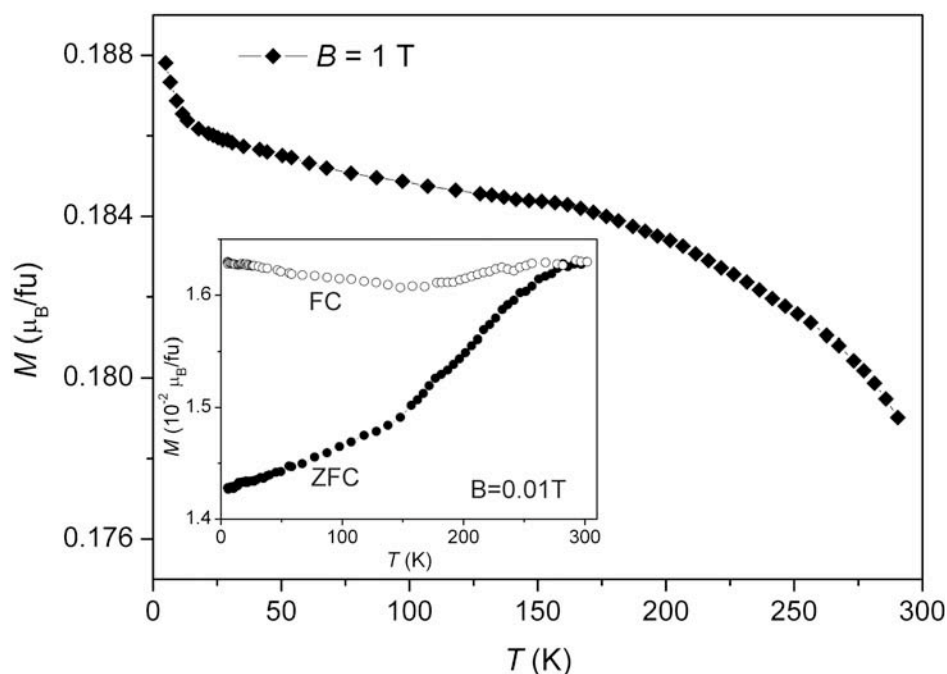


Figure 4.14 – Temperature dependence of the magnetization  $M(T)$  for the  $\text{UFe}_3\text{B}_2$  compound taken in a field of 1 T. The inset shows the ZFC and FC curves in a field of 0.01 T.

The isothermal magnetization curves,  $M(B)$ , recorded at different temperatures, confirm the ferromagnetic behavior, with the magnetization saturating at  $\sim 1.5$  T (Figure 4.15). However, the measured saturation moment,  $0.21 \mu_B/\text{f.u.}$ , is low (and the real value for  $\text{UFe}_3\text{B}_2$  should be even lower due to the contribution of the iron contamination). This low magnetization points to a significant degree of hybridization between iron and uranium and, consequently, to an iron-based magnetism. Assuming (i) a nearly random crystallographic orientation of the grains in the polycrystalline material (similar to a randomly oriented fixed powder) and (ii) the least favored situation of just an easy magnetization axis for  $\text{UFe}_3\text{B}_2$ , then the ratio between the measured magnetization of the polycrystalline sample and the maximum expected magnetization (correspondent to a oriented single crystal with the easy axis parallel to the magnetic field or to a fine powder free to rotate) can be considered to be 0.5 [28]. Consequently, the  $0.21 \mu_B/\text{f.u.}$  saturation magnetization points to a maximum of  $0.42 \mu_B/\text{f.u.}$  magnetization value for  $\text{UFe}_3\text{B}_2$ . Since  $\text{UFe}_3\text{B}_2$  has 3 Fe atoms, the maximum magnetic moment for each Fe atom should be  $\sim 0.14 \mu_B/\text{Fe}$ , which is considerably lower than that obtained for  $\text{UFe}_2$  ( $\sim 0.6 \mu_B/\text{Fe}$  [29]). This may justify why the iron magnetic ordering has been missed in the  $\text{UFe}_3\text{B}_2$  Mössbauer study [20] contrarily to what has been reported in the  $\text{UFe}_2$  Mössbauer studies [30].

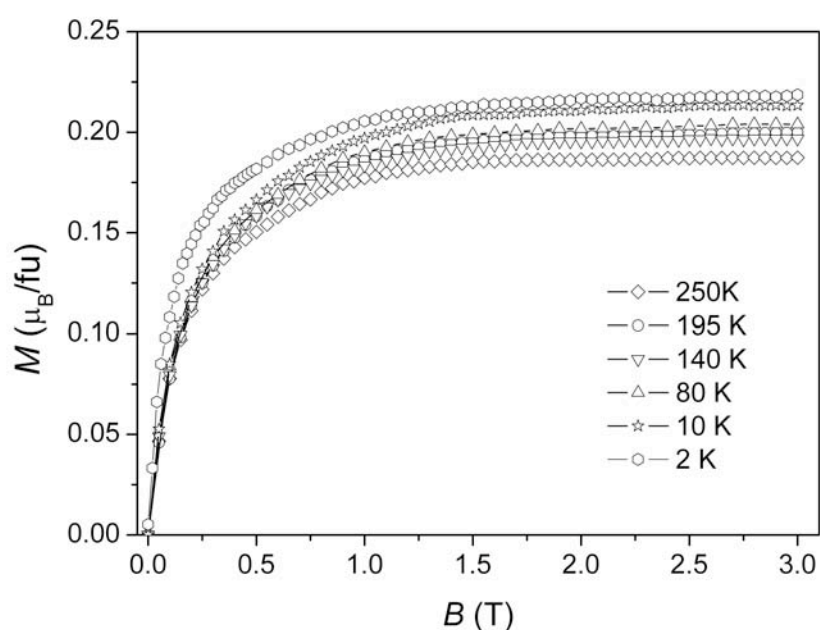


Figure 4.15 – Magnetization dependence on applied field for  $\text{UFe}_3\text{B}_2$  at different temperatures.

#### **4.4 UFe<sub>4</sub>B**

There are several structure prototypes reported in the literature for  $R_xT_yB_z$  and  $A_xT_yB_z$  compounds with  $x:y:z$  ratios similar to 1:4:1, namely  $Ce_3Co_{11}B_4$ ,  $CeCo_4B$ ,  $Ce_2Co_7B_3$ ,  $Nd_3Ni_{13}B_2$ ,  $Lu_5Ni_{19}B_6$  [31-35], yet among them the  $CeCo_4B$ -type is the most commonly adopted structure. Nevertheless, the other structure types are based on a hexagonal subcell of the  $CeCo_4B$  structure and present similar diffractograms.

$RNi_4B$  compounds with  $R = Sm, Tb, Ho$  and  $Er$  adopt the  $CeCo_4B$ -type structure and evidence ferromagnetic behavior below, respectively, 38, 21, 6 and 21 K [36], whereas the  $PrNi_4B$  compound with the same structure type has a paramagnetic behavior in the 2-300 K temperature range [36].  $ThCo_4B$  and  $UCo_4B$  crystallize also with a hexagonal  $CeCo_4B$ -type structure, the first shows a ferromagnetic behavior below 303 K [37], whereas the latter is paramagnetic between 2 and 300 K [38].

The next section investigates the crystal structure of the  $UFe_4B$  ternary boride using PXRD, and SEM complemented with EDS, WDS and, especially, EBSD.

##### **4.4.1 Results and discussion**

###### **XRD and WDS**

Figure 4.16 presents an experimental diffractogram of the 10B:80Fe:10U alloy annealed at 950°C for 60 days, where a compound with an atomic arrangement related to the  $CeCo_4B$ -type structure could be detected among other phases. A systematic comparison between PXRD data and WDS results showed that this compound exhibits an  $U_{1.00}Fe_{5.37(9)}B_{1.14(8)}$  average composition (Table 3.1), which roughly agrees with an 1:4:1 stoichiometry. The lattice parameters determined for  $UFe_4B$  assuming a  $CeCo_4B$ -type structure are:  $a = 0.493(1)$  nm and  $c = 0.704(2)$  nm.

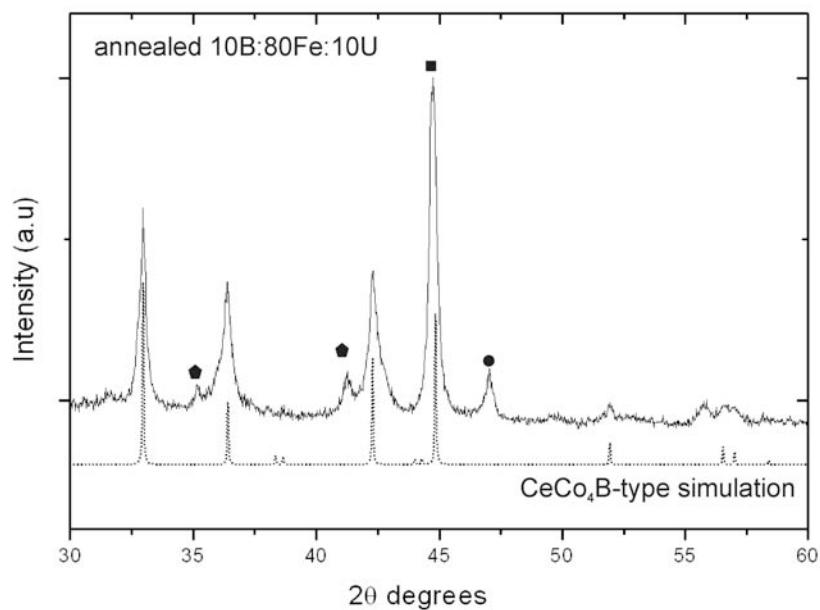


Figure 4.16 – Experimental powder X-ray diffraction pattern of the annealed 10B:80Fe:10U alloy together with a simulation for  $\text{UFe}_4\text{B}$  with the  $\text{CeCo}_4\text{B}$ -type structure (pentagons -  $\text{UFe}_2$ , circle -  $\text{UFe}_3\text{B}_2$ ; square -  $\alpha\text{-Fe}$ ).

The complexity of the iron-rich microstructures hindered the extraction of  $\text{UFe}_4\text{B}$  single crystals and the production of single-phase polycrystalline material. As a result, structural information could not be retrieved from single crystal diffraction nor could Rietveld analysis be performed.

### SEM/EDS and EBSD

BSE imaging associated with EDS maps showed that the microstructure of the annealed 10B:80Fe:10U alloy presented globular  $\alpha$ -Fe and faceted  $\text{UFe}_2$  grains dispersed in a  $\text{UFe}_4\text{B}$  matrix (see Figure 4.17).

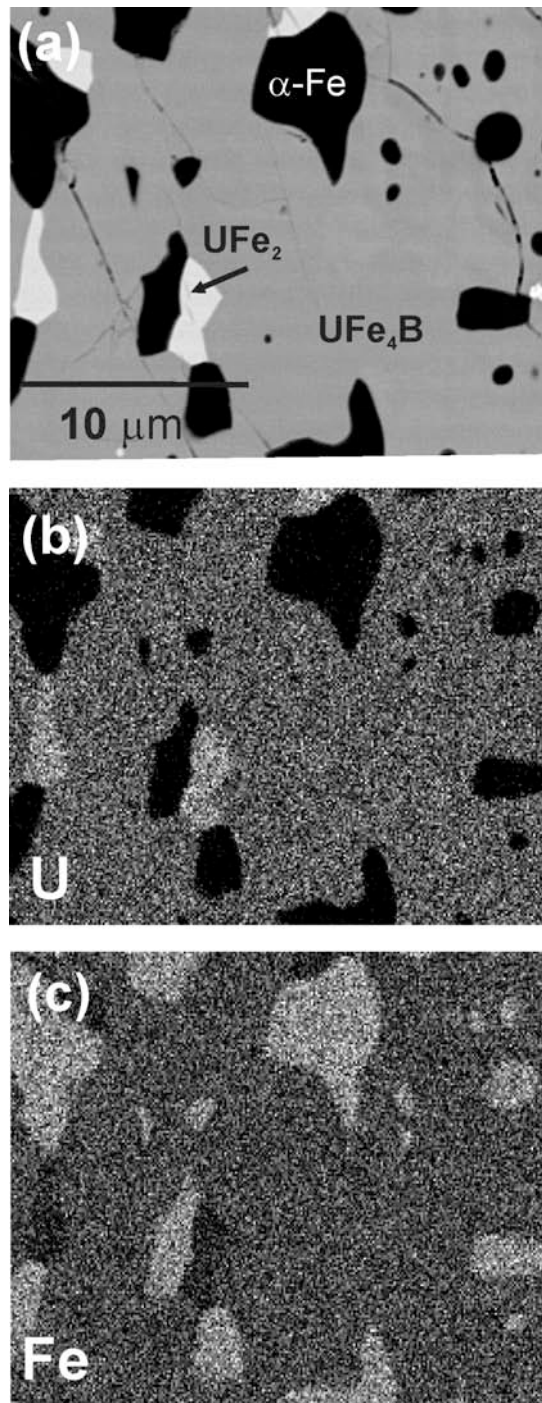


Figure 4.17 – (a) BSE image of the annealed 10B:80Fe:10U alloy and (b) U and (c) Fe X-ray maps.

The PXRD results indicated that the  $UFe_4B$  structure is related to the hexagonal  $CeCo_4B$ -type structure, therefore five closely related structures with a stoichiometry similar to 1:4:1 and belonging to the  $P6/mmm$  (Nr.191) space group;  $CeCo_4B$ ,  $Ce_3Co_{11}B_4$ ,  $Ce_2Co_7B_3$ ,  $Nd_3Ni_{13}B_2$  and  $Lu_5Ni_{19}B_6$ , have been considered for the EBSD simulations. The lattice parameters for the five phases have been established by adjusting simulated diffractograms to the experimental PXRD data using the PowderCell software [12]. Crystallographic information of the candidate structures [39] has been loaded into the Channel 5 software database [40]. The experimental patterns shown in Figures 4.18 to 4.20 were acquired in three different  $UFe_4B$  grains and are presented together with simulations for the candidate structures. Table 4.7 lists the cell parameters adjusted to the PXRD data and the list of simulated bands absent from the experimental patterns for each structure.

Overall the results show that none of the candidate structures is a perfect match for the  $UFe_4B$  compound, since in all cases some of the simulated planes (albeit with relatively high indexes) are absent from the experimental EBSD patterns. A close inspection to the PXRD data of alloys containing the  $UFe_4B$  compound showed that the same peaks appear in the diffractogram although with low intensity. Under the point of view of mean angular deviation, and therefore of  $c/a$  ratio, a better match has in general been obtained for the  $CeCo_4B$ -type structure (see MAD values in the legends of Figures 4.18 to 4.20).



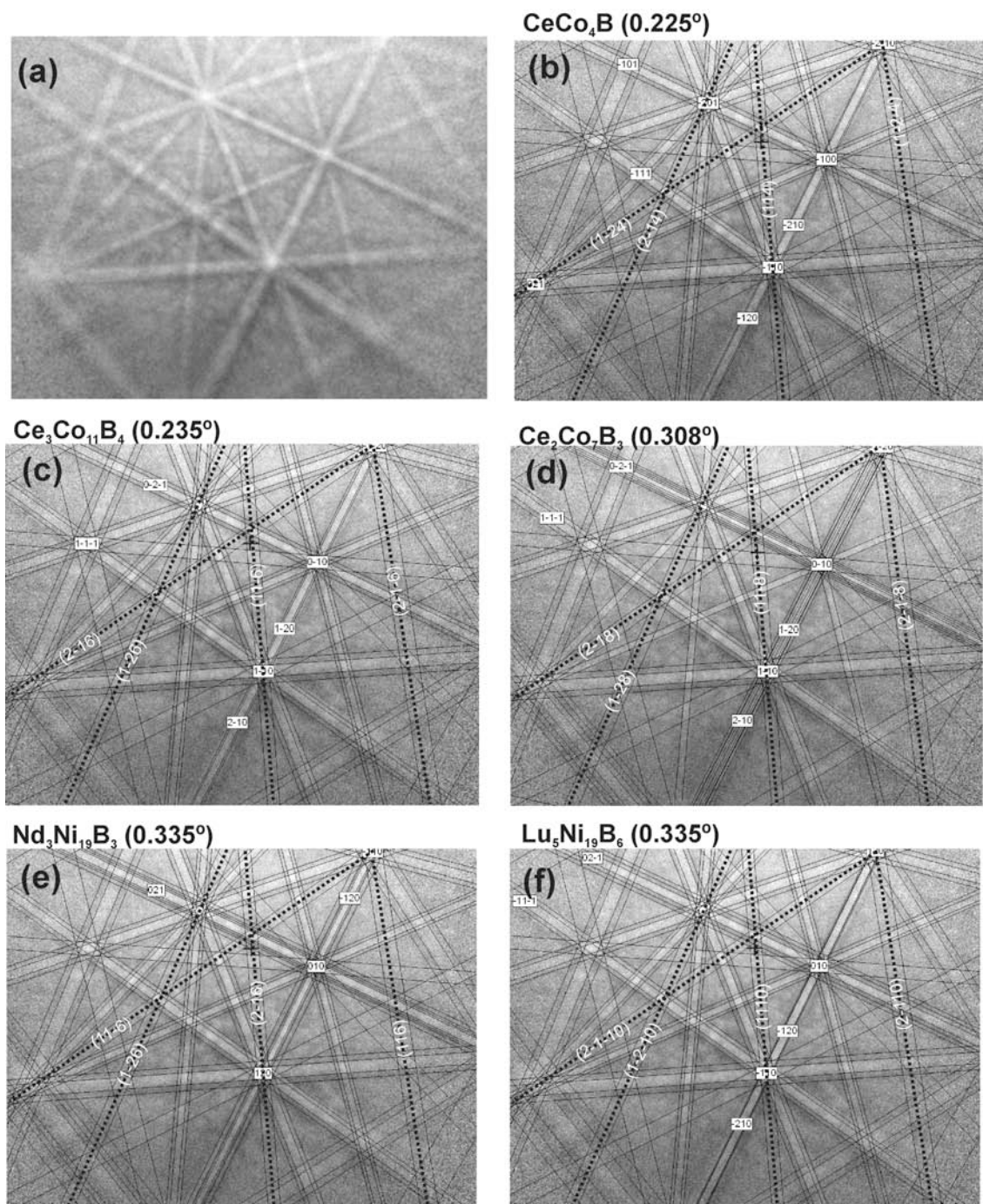


Figure 4.19 – (a) Experimental  $UFe_4B$  EBSD pattern of grain 2 and simulations for (b)  $CeCo_4B$ -type structure (MAD = 0.225°), (c)  $Ce_3Co_{11}B_4$ - type structure (MAD = 0.235°), (d)  $Ce_2Co_7B_3$ - type structure (MAD = 0.308°), (e)  $Ni_3Nd_3B_2$ -type structure (MAD = 0.335°) and (f)  $Lu_5Ni_9B_6$ -type structure (MAD = 0.335°). The simulations were performed for 60 reflecting planes. The dashed lines indicate simulated bands absent in the experimental patterns.



Structure type	PXRD adjusted cell parameters	Absent plane family	EBSD Intensity	XRD Intensity	2 $\theta$
CeCo <sub>4</sub> B	a=0.493(1) nm c=0.704(3) nm	$\{032\}$	36%	21%	71.42°
		$\{214\}$	20%	8%	80.91°
Ce <sub>3</sub> Co <sub>11</sub> B <sub>4</sub>	a=0.493(3) nm c=1.053(8) nm	$\{033\}$	31%	18%	71.40°
		$\{\bar{1}2\bar{6}\}$	17%	8%	80.81°
Ce <sub>2</sub> Co <sub>7</sub> B <sub>3</sub>	a=0.493(7) nm c=1.406(2) nm	$\{3\bar{3}4\}$	38%	16%	71.46°
		$\{\bar{2}18\}$	31%	8%	80.77°
Nd <sub>3</sub> Ni <sub>13</sub> B <sub>2</sub>	a=0.492(1) nm c=1.050(8) nm	$\{033\}$	41%	24%	71.43°
		$\{\bar{1}2\bar{6}\}$	23%	8%	80.91
Lu <sub>5</sub> Ni <sub>19</sub> B <sub>6</sub>	a=0.493(2) nm c=1.761(2) nm	$\{0\bar{3}5\}$	33%	20%	71.55
		$\{\bar{1}210\}$	15%	7%	81.73°

Table 4.7 – Lattice parameters adjusted from the PXRD data for the CeCo<sub>4</sub>B-, Ce<sub>3</sub>Co<sub>11</sub>B-, Ce<sub>2</sub>Co<sub>7</sub>B<sub>3</sub>-, Ni<sub>3</sub>Nd<sub>13</sub>B<sub>2</sub>- and Lu<sub>5</sub>Ni<sub>19</sub>B<sub>6</sub>-type structures together with simulated planes absent in experimental patterns.

## **4.5 U<sub>2</sub>Fe<sub>21</sub>B<sub>6</sub>**

R<sub>2</sub>T<sub>21</sub>B<sub>6</sub> (R = Ho, Er, Tm, Yb, Lu, T = transition metal) compounds have been shown to crystallize with an atomic arrangement based on the Cr<sub>23</sub>C<sub>6</sub>-type structure,  $Fm\bar{3}m$  (Nr.225) space group [41]. Uranium compounds with the U<sub>2</sub>T<sub>21</sub>B<sub>6</sub> (T = Co, Ni) composition crystallize also with the same type of structure [42]. In this family of compounds the *f* element is located in the 8*c* position replacing the Cr atom, while the *d* element occupies the 4*a*, 32*f* and 48*h* sites also replacing Cr, and boron is in the 24*e* position replacing the C atom [42]. Magnetic studies on these compounds have not been reported to the best of the author's knowledge.

The next section investigates the crystal structure of the U<sub>2</sub>Fe<sub>21</sub>B<sub>6</sub> ternary boride using PXRD, and SEM complemented with EDS, WDS and, especially, EBSD.

### **4.5.1 Results and discussion**

#### **XRD and WDS**

Figure 4.21 presents an experimental diffractogram of the 15B:80Fe:5U alloy annealed at 950°C for 60 days, where a compound with an atomic arrangement related to the Cr<sub>23</sub>C<sub>6</sub>-type structure could be detected among other phases. A systematic comparison between PXRD data and WDS results showed that this compound exhibits an U<sub>1.00</sub>(Fe<sub>13.75(5)</sub>B<sub>4.54(1)</sub>) average composition (Table 3.1), which roughly agrees with an 2:21:6 stoichiometry. The lattice parameter determined for U<sub>2</sub>Fe<sub>21</sub>B<sub>6</sub> is:  $a = 1.0766(4)$  nm. Due to their toughness the material could not be easily reduced to powder, leading to peak intensity inversions in the PXRD data. Furthermore, due to the complexity of the iron-rich alloys microstructure, the UFe<sub>4</sub>B compound could not be extracted as single crystal nor could single-phase polycrystalline material be produced. As a result, structural information could not be retrieved from single crystal diffraction nor could Rietveld analysis be performed.

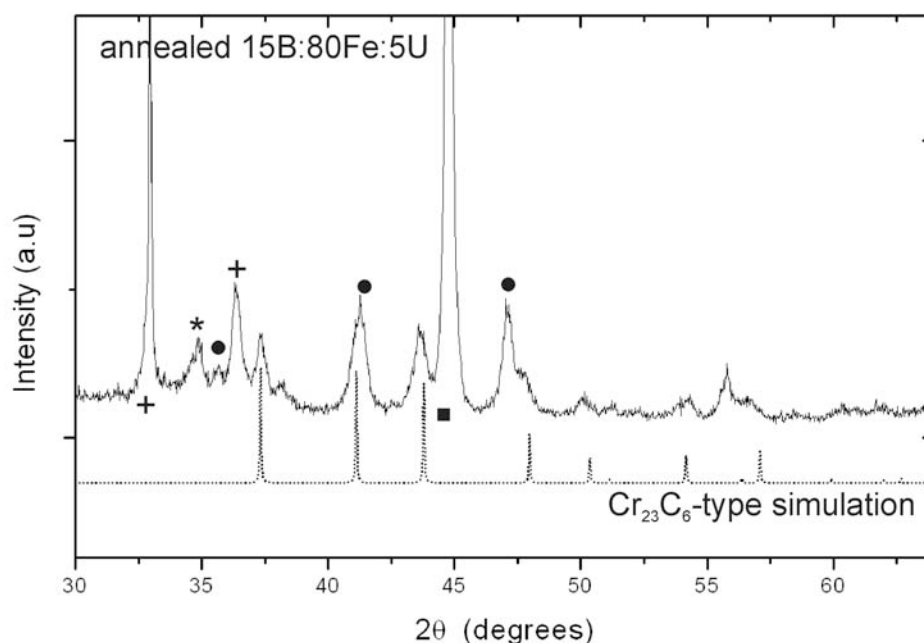


Figure 4.21 – Experimental powder X-ray diffraction pattern of annealed 15B:80Fe:5U alloy together with a simulation for  $U_2Fe_{21}B_6$  with the  $Cr_{23}C_6$ -type structure (crosses -  $UFe_4B$ ; star -  $Fe_2B$ ; circles -  $UFe_3B_2$ ; square -  $\alpha$ -Fe).

### SEM/EDS and EBSD

BSE imaging associated with EDS maps showed that the microstructure of the annealed 15B:80Fe:5U alloy consisted of  $\alpha$ -Fe and  $UFe_3B_2$  globules in a  $U_2Fe_{21}B_6$  matrix (see Figure 4.22).

Typical experimental EBSD patterns obtained for the  $U_2Fe_{21}B_6$  phase are shown in Figure 4.23 (a) to (c). In present case, the modified  $Cr_{23}C_6$ -type structure was the only candidate atomic arrangement and reasonable matches have been obtained between the experimental and simulated patterns (see Figure 4.23 (e) to (g)). For quality comparison purposes a typical EBSD pattern of the  $UFe_3B_2$  compound obtained from the same sample is shown in Figure 4.23 (d). The consistently lower quality observed for the experimental EBSD patterns of the  $U_2Fe_{21}B_6$  phase points to a degree of disorder in the crystal structure.

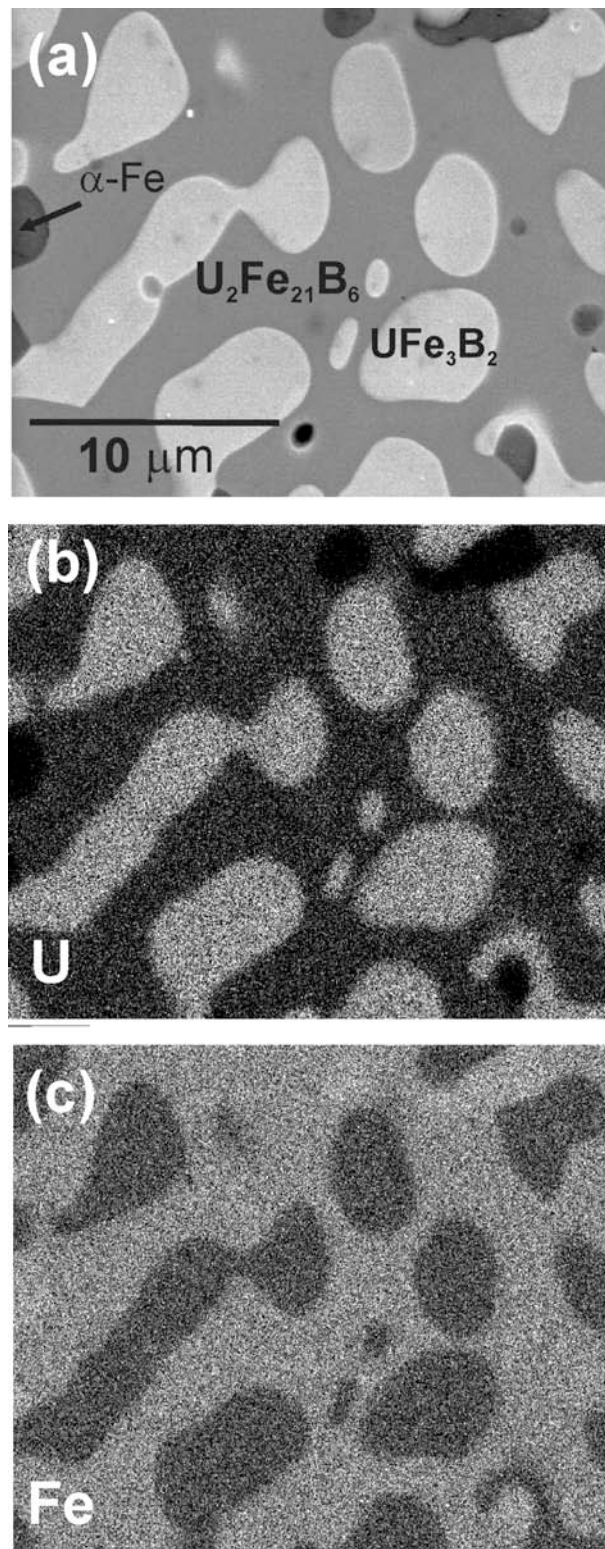


Figure 4.22 – (a) BSE image of the annealed 15B:80Fe:5U alloy and (b) U and (c) Fe X-ray maps.



#### **4.6 References**

- [1] YuB. Kuzma, N.F. Chaban, “Binary and ternary systems containing boron” handbook, (eds. Metallurgy), Moscow, (1990) (in Russian) 317.
- [2] R. Sobczak and P. Rogl, *Journal of Solid State*, 27 (1979) 343.
- [3] K. Yubuta, T. Mori, A. Leithe-Jasper, Y. Grin, S. Okada, T. Shishido, *Materials Research Bulletin*, 44 (2009) 1743.
- [4] P. Rogl, H. Nowotny, *Monatshefte für Chemie*, 106 (1975) 381.
- [5] I. P. Valyovka and Yu. B. Kuz`ma. *Dopovidi Akademii Nauk Ukrainskoi RSR Ser A*, (1975) 652.
- [6] A. Winkelmann, *Dynamical Simulation of Electron Backscatter Diffraction Patterns*, *Electron Backscatter Diffraction in Materials Science*, Adam J. Schwartz, Mukul Kumar (eds.), Springer series 2000.
- [7] J. R. Michael, J. A. Eades. *Ultramicroscopy*, 81 (2000) 67.
- [8] A. Galatanu, E. Yamamoto, H. Yoshinori, O. Yoshichika, *Physica B*, 378-380 (2006) 999.
- [9] YuB. Kuz`ma and S.I Svarichevskaya, *Soviet Physics Crystallography*, 17 (1973) 830.
- [10] S. I. Mikhailenko, YuB. Kuz`ma, *Dopovidi Akademii Nauk Ukrainskoi RSR Ser. A*, (1975) 465.
- [11] T. Konrad, W. Jeitschko, E Danebrock, C. Evers, *Journal of Alloys and Compounds*, 234 (1996) 56.
- [12] G. Nolze, W. Kraus, *Powder Cell for Windows, Version 2.2*, Federal Institute for Materials Research and Testing, Berlin, 1999.
- [13] B. K. Vainshtein, V. M. Fridkin, V. L. Indenbom, *Modern Crystallography II, Structure of Crystals*, Vol. 21, Springer-Verlag, Berlin, (1982) 71.
- [14] H. H. Hill, “Plutonium 1970 and Other Actinides”, (ed. W.N. Miner), AIME, New York, (1970).
- [15] H. C. Ku, G.P.Meisner, F.Acker, D.C Jonston, *Journal of Solid State Chemistry*, 35 (1980) 91.
- [16] H. C. Ku, G.P. Meisner, *Journal of Less-Common Metals* 78 (1981) 99.

- [17] J. Bernhard , H. Kitazawa , I. Higashi , T. Shishido , T. Fukuda , H. Takei , Boron-rich solids. AIP Conference Proceedings, 231(1991) 212.
- [18] H. C. Ku, L. J. Ma, M. F. Tai, Y. Wang, H. E. Horng, Journal of Less-Common Metals, 109 (1985) 219.
- [19] I. P. Valyovka, Yu.B. Kuzma, Dopovidi Akademii Nauk Ukrainskoi RSR Ser A (1974) 1029.
- [20] S. I. Yushuk, YuB. Kuzma, A. S. Kamzin, I. P. Valovka, M. M. Zakharko, I.I. Adamenko, Fizika Tverdogo Tela, 22 (1980) 612.
- [21] P. P Vaishnava, C. W. Kimball, A. M. Umarji, S. K. Malik, G. K. Shenoy, Journal of Magnetic Materials 49 (1985) 286.
- [22] M. Wulff, B. Lebech, A. Delapalme, G. H. Lander, J. Rebizant, J. C. Spirlet, Physica B: Condensed Matter, 156-157 (1989) 836.
- [23] S. K. Dhar, S. K. Malik, R. Vijayaraghavan, Journal of Physics C 14 (1981) L321.
- [24] Y.B. Kuz'ma, Crystal Chemistry Borides, Vyscha Shkola Press, Lviv, 1983.
- [25] E. Parthé, B. Chabot, in: K. Gschneider, L. Eyring (Eds.), Handbook on Physics and Chemistry of Rare Earths, Vol. 6, Elsevier, The Netherlands, Chapter 48 (1984).
- [26] A. P. Gonçalves, P. Estrela, J. C. Waerenborgh, J. A. Paixão, M. Bonnet, J. C. Spirlet, M. Godinho, M. Almeida, Journal of Magnetic Materials 189 (1998) 283-292.
- [27] J. Luo, J. K. Liang, Y. Q. Guo, Q. L. Liu, L. T. Yang, F. S. Liu, G. H. Rao, Applied Physics Letters, 84 (2004) 3094.
- [28] V. Sechvosky, H. Havela, Handbook of Magnetic Materials, Vol.11, Chapter 1, (ed. K. H. J Buschow) Elsevier Science, (1996) 20.
- [29] B. Lebech, M. Wulff, G. H. Lander, J. Rebizant, J. C. Spirlet, A. Delapalme Journal of Physics: Condensed Matter 1 (1989) 10229.
- [30] S. Tsutsui, M. Nakada, Y. Kobayashi, S. Nasu, Y. Haga, Y. Onuki, Hyperfine Interactions 133, (2001) 17.
- [31] N. S. Bilonizhko, YuB. Kuzma, Inorganic Materials, 10 (1974) 227.
- [32] YuB. Kuzma, O. M. Dub, N. F. Chaban, Dopovidi Akademii Nauk Ukrainskoi SSR, Ser B, 7 (1985) 36.

- [33] YuB. Kuzma, N. S. Bilonizhko, *Dopovidi Akademii Nauk Ukrainskoi RSR Ser A*, 43 (1981) 87.
- [34] YuB. Kuzma, M. P. Khaburkaya. *Inorganic Materials*, 10 (1975) 1625.
- [35] R. Nagarajan, L. C. Gupta, C. Mazumbar, Z. Hossain, Dhar SK, C. Godart, B. D. Padalia, R. Vijayaraghavan, *Journal of Alloys and Compounds*, 225 (1995) 571.
- [36] T. Tolinski, A. Kowalczyk, A. Szaferek, B. Andrzejewski, J.Kovac, M. Timko, *Journal of Alloys and Compounds*, 347, (2002) 31-35.
- [37] O. Isnard, V. Pop, J. C. Toussaint, *Journal of Physics: Condensed Matter*, 15 (2003) 791.
- [38] H. Nakotte, L. Havela, J.P. Kuang, F.R. deBoer, K. H. J. Buschow, J. H. V. J. Brabers, T. Kuroda, K. Sugiyama, M. Date, *Int. Journal of Modern Physics B* 7 (1993) 838.
- [39] E Villars, L.D. Calvert, “Pearson's Handbook of Crvstallographic Data for Intermetallic Phases”, ASM International, Materials Park, OH, 2nd. edn., 1991.
- [40]<http://www.oxinst.eu/products/microanalysis/ebsd/ebsd-acquisition-software/Pages/channel5.aspx>
- [41] YuB. Kuzma, N. F. Chaban, “Binary and ternary systems containing boron” *Handbook*, (eds. Metallurgy), Moscow, (1990), (in Russian).
- [42] E. Ganlberger, H. Nowonty, F. Benesowsky, *Monatshefte für Chemie*, 96 (1965) 1144.

---

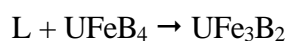
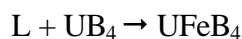
## **Chapter 5**

---



### **5.1 Concluding remarks and future work**

The B-Fe-U ternary diagram comprehends seven binary compounds and five ternary compounds which form 32 boundary lines, 18 compatibility triangles and corresponding 18 ternary reactions. The B-rich section of the ternary phase diagram exhibits 18 boundary lines and six invariant reactions; two ternary reactions of class III (R1<sub>III</sub>, R2<sub>III</sub>); two ternary reactions of class II (R3<sub>II</sub>, R6<sub>II</sub>) and two ternary reaction of class I (R4<sub>I</sub>, R5<sub>I</sub>). The 0% >U>30% and 21% >B>50% (at.%) section of the ternary phase diagram comprehends one ternary reaction of class III (R8<sub>III</sub>) and three ternary reactions of class II (R7<sub>II</sub>, R9<sub>II</sub>, R10<sub>II</sub>). The Fe-rich section of the ternary phase diagram comprehends two ternary reactions of class III (R11<sub>III</sub> and R13<sub>III</sub>), three ternary reactions of class II (R12<sub>II</sub>, R14<sub>II</sub>, R15<sub>II</sub>) and one ternary reaction of class I (R16<sub>I</sub>). The U-rich section exhibits one ternary reaction of class II (R17<sub>II</sub>) and one ternary reaction of class I (R18<sub>I</sub>). The isothermal section at 780°C of the B-Fe-U diagram presents 26 phase fields and nowhere can liquid be found. The isothermal section at 950°C exhibits 24 phase fields. The isothermal section at 1100°C presents 29 phase fields. A cascade of peritectic-like transitions exists along the U:(Fe,B)=1:5 vertical section:



The U:(Fe,B)=1:5 vertical section intercepts one four-phase reaction plane at 1660 °C (R1<sub>III</sub>:  $L + UB_4 + UB_2 \rightarrow UFeB_4$ ) and crosses also five boundary lines  $l_3$ ,  $l_9$ ,  $l_{20}$ ,  $l_{22}$  and  $l_{28}$ .

Scarcity and toxicity are some of the problems associated with uranium compounds investigation. An additional limitation of the current work has been the difficulty to produce single-phase materials, since the compounds melt incongruently and their primary crystallization fields are distant from the compounds composition. For this reason the physical properties of the compounds cannot be easily measured, hindering possible theoretical calculations for the B-Fe-U ternary phase diagram. Furthermore, the Fe-rich alloys present a high toughness and cannot be easily reduced to powder with a perfectly random crystallographic orientation. This leads to some degree of

---

texture in the PXRD patterns, which together with the unavoidable presence of impurity phases renders Rietveld refinement of polycrystalline samples unviable. Moreover, U radioactivity limits the use of transmission electron microscopy especially due to contamination issues during the sample preparation. Nevertheless, structural characterization has been performed for the five compounds existing in the B-Fe-U ternary diagram;  $\text{UFeB}_4$ ,  $\text{UFe}_2\text{B}_6$ ,  $\text{UFe}_3\text{B}_2$ ,  $\text{UFe}_4\text{B}$  and  $\text{U}_2\text{Fe}_{21}\text{B}_6$ . High-quality  $\text{UFe}_2\text{B}_6$  and  $\text{UFe}_3\text{B}_2$  single crystals have been successfully extracted. Furthermore, the magnetic properties of the  $\text{UFeB}_4$ ,  $\text{UFe}_2\text{B}_6$  and  $\text{UFe}_3\text{B}_2$  compounds have been effectively measured from (nearly) single-phase polycrystalline materials.

Powder X-ray studies suggested that the  $\text{UFeB}_4$  compound crystallizes essentially with the  $\text{YCrB}_4$ -type structure although with peak intensity inversions. BSE images of this compound evidenced consistent contrast variations that are characteristic of a random intergrowth. The crystallographic plane parallel to the layers displayed intense HOLZ rings in the EBSD patterns of as-cast  $\text{UFeB}_4$ . The EBSD results showed that  $\text{UFeB}_4$  consists of an intergrowth between  $\text{YCrB}_4$  and  $\text{ThMoB}_4$  type-structures with the  $a(010)_{\text{YCrB}_4} // (\bar{1}10)_{\text{ThMoB}_4}$  and  $[001]_{\text{YCrB}_4} // [001]_{\text{ThMoB}_4}$  orientation relation. Magnetic measurements indicate that the  $\text{UFeB}_4$  compound has a paramagnetic behavior in the 2-300 K temperature range.

PXRD and single crystal diffraction showed that the  $\text{UFe}_2\text{B}_6$  compound crystallizes with the orthorhombic  $\text{CeCr}_2\text{B}_6$ -type structure ( $Immm$  space group Nr.71,  $a = 0.31372(6)$  nm,  $b = 0.61813(1)$  nm,  $c = 0.82250(2)$  nm. Magnetic measurements indicate that this compound is paramagnetic in the 2-300 K temperature range.

Single-crystal X-ray diffraction confirmed that the  $\text{UFe}_3\text{B}_2$  boride crystallizes with the hexagonal  $\text{CeCo}_3\text{B}_2$ -type structure. The U-U interatomic distances point to magnetic non-order of the uranium sublattice resulting from direct hybridization of the  $5f$ - $5f$  orbitals. The magnetization measurements demonstrated a ferromagnetic-like behavior at room temperature with a Curie temperature just above 300 K, which is therefore originating from ordering of the iron moments, and a very low saturation

magnetization for the compound. This reduced magnetic moment of the iron-sublattice, is probably due to  $5f-3d$  hybridization.

The structural identification of the  $UFe_4B$  and  $U_2Fe_{21}B_6$  compounds was performed using PXRD and EBSD analysis. The results indicate that the  $U_2Fe_{21}B_6$  structure is consistent with a  $Cr_{23}B_6$ -type structure,  $Fm\bar{3}m$  space group (Nr.225), while  $UFe_4B$  crystallizes with an unknown structure closely related with the  $CeCo_4B$ -type structure,  $P6/mmm$  space group (Nr.191).

In summary, the present work revealed three novel ternary compounds ( $UFe_2B_6$ ,  $UFe_4B$  and  $U_2Fe_{21}B_6$ ) and contributed for the description of the crystal structures and magnetic properties of all ternary compounds present in the B-Fe-U system. Furthermore, the overall configuration of the liquidus surface has been established. Nevertheless, further work on the same line of research is required:

- Additional alloys should be produced to confirm the particular configuration proposed for each ternary reaction.
- Since a ferromagnetic behavior has been found for the  $UFe_3B_2$  compound, the  $UFe_4B$  and  $U_2Fe_{21}B_6$  compounds, with higher iron content, are expected to present interesting magnetic properties. Further studies on the iron-rich compounds of the B-Fe-U ternary diagram should hence be carried out in order to produce single-phase samples and perform physical characterizations. Techniques as induction furnace and the Czochralski method can be used to process the materials.
- Similar studies on ternary systems, such as B-T-U (T= Cr, Co, V, Ni, Mo, W), are necessary for ternary phase diagram determination and physical characterization of the respective ternary compounds.

